SATURATION MAGNETIZATION OF IRON SIXTEEN NITROGEN TWO, A 40-YEAR MYSTERY

A DISSERTATION
SUBMITTED TO THE FACULTY OF THE GRADUATE SCHOOL
OF THE UNIVERSITY OF MINNESOTA
BY

NIAN JI

IN PARTIAL FULFILLMENT OF THE REQUIREMENTS
FOR THE DEGREE OF
DOCTOR OF PHILOSOPHY

PROF. JIAN-PING WANG, ADVISOR

MARCH 2012

Acknowledgements

I am very much delighted to have this chance to thank those people who supported and helped me. First of all, I would like to thank my advisor, Professor Jian-Ping Wang, for his sharing of scientific mind, introducing me to the research field of magnetic materials and supervising me to do this exciting project. The discussion with him was invaluable and guided me to passionately explore amazing science in this topic.

I would also like to acknowledge the input and advice from Professors Randall Victora, Beth Stadler and Jack Judy during my work and stay in the center for Micromagnetic and Information Technollogies (MINT), which builds a solid foundation for me in the field of magnetism and magnetic materials.

I am thankful to my dissertation committee members Professors Dan Dahlberg, Oriol Valls and Anand Gobinath for their time, help and effort of serving in my committee.

I also want thank other faculty members in Physics and Material Science Department of University of Minnesota, who have provided help on discussions and experimental measurements. Special acknowledge goes to Professors Chris Leighton, Paul Crowell, and Boris Shklovskii.

Many of my collaborators provided valuable help to my research. Special acknowledgement goes to Dr. Valeria Lauter (SNS, ORNL), Dr. Chengjun Sun (XSD, ANL), Dr. Larry Allard (HTML, ORNL), Dr. Edgar Lara-Curzio (HTML ORNL), Prof. Frank de Groot (Utrecht University).

I would also like to acknowledge Seagate Technology, Dr. Mark Kief (Seagate), Michael Kausky (Seagate), Sabeswar Sahoo (Seagate), Western Digital

Co, Dr. Dehua Han (WDC), SVTA Inc., Dr. Peter Chow (SVTA) and Dr. Feng Niu (SVTA) for the funding and collaborating on this project.

It has been an enjoyable experience with the past and current members of Professor Wang's group. I would like to thank Xiaoqi Liu, Yunhao Xu, Jiaoming Qiu, Hao Meng, Xiaofeng Yao, Haibao Zhao, Hao Wang, Yisong Zhang, Yuanpeng Li, Ying Jing, Liang Tu, Shihai, He, Hui Zhao, Xuan Li, Meiyin Yang, Wei Wang, Shaoqian Yin, Yi Wang, Xiaowei Zhang, Yinglong Feng, Andrew Lyle, Todd Klein and many other students from MINT Center for their valuable discussion and friendly feedback.

Finally, I would like to express my love and thanks to my parents and my lovely girlfriend. Without their love, support and advice, I would have never gone so far.

Dedication

With gratitude to my parents

Abstract

While the material α"-$Fe_{16}N_2$ and its interesting magnetic behavior were discovered decades ago, there is still no unified answer to the question on whether this phase has a giant saturation magnetization (M_s). There are three important "missing pieces" that emerge upon examination of the magnetization and discussing the magnetism of this system

1) *There is lack of direct measure of the saturation magnetization on $Fe_{16}N_2$.* Conventional magnetometer-based (VSM or SQUID) methods can only measure the total magnetic moment of the samples. The evaluation of the M_s value involves the challenging estimation of the thin film sample volume and the subtle assessment of magnetic contributions from underlayers, substrates or possible impurity phases, resulting in unpredictable errors.
2) *There is no convincing theory/model to rationalize the existence of giant M_s.* The conventional band theory based first-principles calculations only predicts an M_s value similar to that of pure Fe.
3) *There is lack of experiments to explore the underlying physics of the magnetism in $Fe_{16}N_2$ from an electronic state viewpoint l.* The previous investigations only focus on the saturation magnetization measurement. Fundamental physics experiments using advanced tools such as polarized neutron and synchrotron x-rays were seldom reported, which may provide unique and independent information on understanding the magnetism in this material system.

On the purpose of addressing these three issues mentioned above. We first picked up a unique facing-target sputtering approach to synthesize $Fe_{16}N_2$ epitaxial thin films. A detailed structure and chemical analysis confirmed the crystallinity and epitaxial quality of fabricated $Fe_{16}N_2$ films.

In terms of magnetic characterization, in addition to systematically study the

saturation magnetization of the prepared films using a vibrating sample magnetometer (VSM) based method., for the first time,we have discovered the partial localization behavior of 3d electrons in $Fe_{16}N_2$ thin film samples by using polarized synchrotron x-rays. Furthermore, we have used polarized neutron reflectometry (PNR) to directly measure the saturation magnetization in absolute unit, which confirms the presence of giant saturation magnetization. The observed saturation magnetization of $Fe_{16}N_2$ phase is up to 2500 emu/cm^3, which is significantly larger than that of the currently known limit ($Fe_{65}Co_{35}$ with saturation magnetization of 1900 emu/cm^3)

To understand the origin of the giant magnetization, we proposed a “cluster + atom” model, which pointeded out a possible scenario to develop this unusual magnetism in this Fe-N system. Synchrotron x-ray experiments also provided supporting evidences of the charge transfer from the itinerant iron atom to the Fe_6N cluster, which is consistent with the proposed model.

We further discussed the perpendicular anisotropy and the relatively large spin polarization ratio of these $Fe_{16}N_2$ films, which will be very useful for future magnetoresistive devices with perpendicular anisotropy and low damping constant.

Table of Contents

List of Figures

Chapter 4

Publications

Nian Ji, M. S. Osofsky, Valeria Lauter, Lawrence F. Allard, Xuan Li, Kevin L. Jensen, Hailemariam Ambaye, Edgar Lara-Curzio, and Jian-Ping Wang, "Perpendicular magnetic anisotropy and high spin-polarization ratio in epitaxial Fe-N thin films" *Phys. Rev. B* 84, 245310 (2011)

Nian Ji, Lawrence F. Allard, Edgar Lara-Curzio and Jian-Ping Wang, "N site Ordering Effect on Partially $Fe_{16}N_2$" *Appl. Phys. Lett.* 98, 092506 (2011)

Nian Ji, Yiming Wu, Jian-Ping Wang, "Epitaxial High Magnetization Fe-N thin films on Fe(001) seeded GaAs(001) single crystal wafer using facing target sputtering" *J. Appl. Phys*. 109, 07B767 (2011)

Nian Ji, Xiao Qi Liu and Jian-Ping Wang, "Theory of giant saturation magnetization in α"-Fe16N2: role of partial localization in ferromagnetism of 3d transition metals" *New J. Phys*. 12, 063032 (2010)

Nian Ji, Mengkun Liu, Jihao Zhou, Zhifang Lin, and S. Chui, *Optics Express* 13, 5192 (2005)

Mengkun Liu, **Nian Ji,** Zhifang Lin, and S. Chui, *Phys. Rev. E* 72, 056610 (2005)

Yuanyuan Na, Cong Wang, Lihua Chu, Lei Ding, **Nian Ji**, Jian-Ping Wang, Xiaolong Chen, "Magnetic and electronic transport properties of antiperovskite Mn3Cu(Ge)N thin films" *Mater. Lett.* 65, 2401 (2011)

Yuanyuan Na, Cong Wanga, Ying Sun, Lihua Chu, Man Nie, **Nian Ji**, Jian-Ping Wang, "Structure and properties of ternary manganese nitride Mn3CuNy thin films fabricated by facing target magnetron sputtering" *Mater. Res. Bull.* 46, 1022 (2011)

Sample IDs for each figure showing experimental data

Figure number	Sample ID
Figure 2.6	NJ05122010
Figure 2.7	NJ09022010
Figure 2.8	NJ04122010
Figure 2.9	NJ09022010
Figure 2.10	NJ09022010
Figure 2.13a	NJ05122010
Figure 2.13b	NJ04122010; NJ05122011
Figure 2.14	NJ04162010; NJ05152010; NJ06022010
Figure 2.15	NJ01172011
Figure 2.16	NJ01162011
Figure 2.17	NJ01172011
Figure 2.18	NJ04122010
Figure 2.19	NJ04122010
Figure 2.20	NJ05102010
Figure 2.21	NJ04122010
Figure 2.22	NJ05122010
Figure 2.23	NJ05102010

Chapter I Introduction

1.1 Ferromagnetism in a material

Magnetism originates from the orbital and spin motions of electrons (magnetic moment). Depending on how they interact with one another and respond to the external magnetic field, they can be classified into the following five major categories: 1) Diamagnetism, 2) Paramagnetism, 3) Ferromagnetism, 4) Ferrimagnetism, 5) Antiferromagnetism. Materials in the first two categories are those that exhibit no collective magnetic interactions and are not magnetically ordered. Last three groups exhibit long-range magnetic order below a certain temperature. And they can be distinguished by the adjacent atomic magnetic moments parallel (ferromagnetism) or anti-parallel (ferri- or antiferromagnetism) to one another. Throughout this thesis, our discussion will be concentrated on the ferromagnetic material.

When it comes to ferromagnetic materials, iron, nickel and cobalt are elements that immediately come to mind. Because for 3d transition metal and their alloys, the d electrons typically present itinerant features. Unlike paramagnetic materials, the atomic moments in these materials exhibit very strong interactions between one another and result in a parallel alignment of atomic moments and subsequently a large net magnetization (Figure 1.1(a)). This interaction is a quantum mechanical phenomenon due to the relative orientation of the spins of two electrons.

In the absence of external magnetic field, ferromagnetic materials form magnetic domains (inset in Figure 1.1(b)) to minimize the magneto-static energy. Within the domains, the material exhibit long range order and net magnetic moments. In this case, the magnetization response to the external field produces a hysteresis. When the field is large enough, the magnetic moment of the material saturates itself in the sense that all the domains are aligning along the same direction. Therefore, the total magnetic moment of a material can be measured in this approach.

In a ferromagnetic material, since a net magnetization comes from the parallel alignment of all the magnetic moments, an interesting question to ask is how high this net magization can achieve in unit volume, which is by definition, the saturation magnetization of a material.

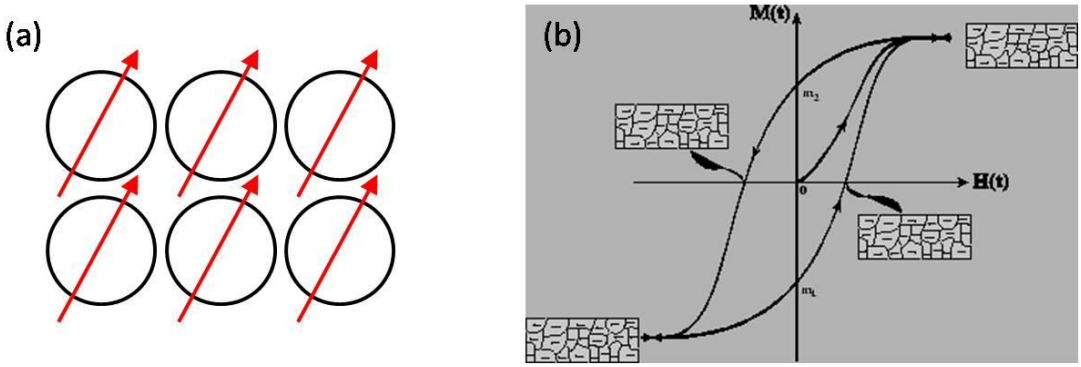

Figure 1.1 (a) An illustration of the atomic magnetic order. Arrows denotes the magnetic moment direction. Circles represent atomic radius. All the moments aligned in parallel along the same direction due to strong inter-atomic exchange interaction. (b) A typical M-H loop for a ferromagnetic material (hyerphysics.phys-astr.gsu.edu/hbase/solids/hyst.html)

1.2 Fundamental limit of saturation magnetization

The atomic magnetic moment of a Fe atom can be up to 7 μ_B[1], largely due to the orbital magnetic moment and the spin moment configuration within the atomic obitals following Hund's first rule[2]. However, in a ferromagnetic Fe metal solid, first of all, the orbital moment is quenched due to the cubic symmetry of the crystal field[3]. Secondly, to favor the ferromagnetic order, the inter-atomic distance has to be small enough to allow the exchange between spins of atoms, in which case, the atomic moment can be strongly reduced. In body centered cubic Fe, the average magnetic moment per atom is 2.2 μ_B in Fe atom. In this case, Hund's rule may not be suitably applied.

To enable the description of the electron overlapping and net magnetic behaviors, an electron band magnetism can be used to depict all the essential

features. The spin-up and spin-down 3d electrons occupy the spin-resolved band with a energy shift described as the exchange splitting, which causes the imbalanced occupation of these two states below Fermi level. Therefore, the net moment can be calculated by subtracting the total occupation of electrons between the two states.

The question regarding "how magnetic a material can possible be" given this band magnetism description is related to the definition of the saturation magnetization, namely, the total magnetic moment that a material can possibly produce given an unit volume. Since individual atoms may produce large moment as predicted by Hund's first rule, as the inter-atomic distance becomes closer, the electrons develops band structure with a spin resolved density of state as schematically shown in figure 1.2. The bandwidth is related to the inter-atomic distance of the material in the sense that lower mass density (ρ) causes relatively narrower bandwidth and subsequently larger magnetic moment per atom (m). In this case, it is immediately noticed that in principle there is a upper limit for the value of the product (ρm), which is equivalent to the definition of saturation magnetization (magnetic moment per volume).

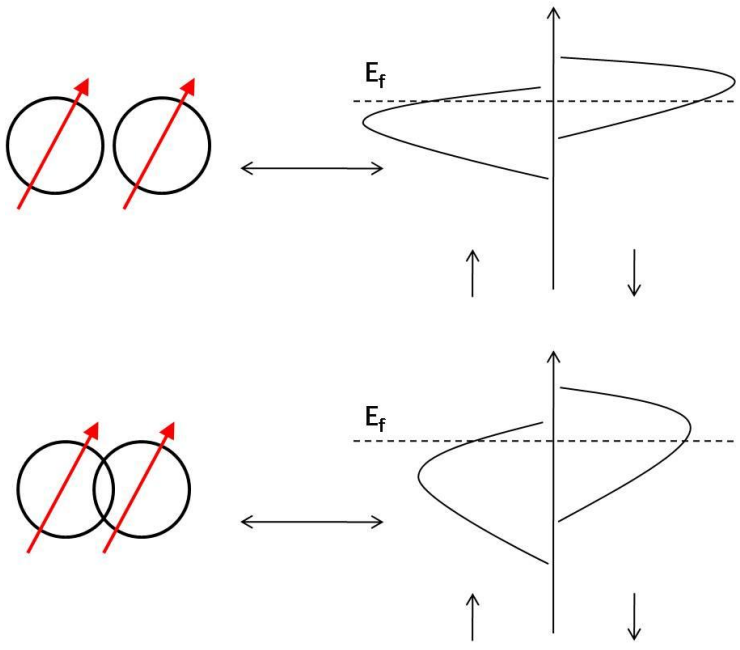

Figure 1.2 An illustration of the correlation between inter-atomic distance in solids and the

bandwidth of spin resolved density of state in typical 3d ferromagnetic metals.

1.3 Seeking Material with High Saturation Magnetization

Magnetic materials with a giant saturation magnetization (M_s) have been a "holy grail" for magnetic researchers and condensed matter physicists for decades because of its great scientific and technological impacts. For example, any improvement of M_s in the magnets used in motors of electric cars and wind-mill generators will increase their energy product and thus generate huge economic impact.

A typical example of its application can be found in magnetic recording industry. The evolutionary path of magnetic data storage has experienced substantial progress in recording areal density and data rate ever since its invention. In 1956, IBM built the first commercially available hard disk drive which was leased as part of the random access method of accounting and control (RAMAC) system. It had an areal density of 2 kbit/in2, a data rate of 70 kbit/s, and stored 5 Mbytes of information on fifty 24-in disks. The material used in the magnetic disks was aluminum coated with particulate γ–iron oxide in an epoxy base. The NRZI (non return to zero) code and amplitude detector combination was utilized for the signal process method. The invention of the RAMAC system marked the beginning of a long history of new technologies and applications for providing the nonvolatile and inexpensive data storage. Meanwhile, research efforts were underway for the development of new magnetic recording physics, new magnetic materials, advanced signal process methods and head-media interface techniques, which led to a steady increase in storage density. As of 2010, the commercial hard disk drive has an areal density above 500 Gbit/in2, a burst data rate of 3.0 Gbits/s, and stored up to 3 Tbytes of information on five 3.5-in disks. This represents a radical increase in the disk capacity by a factor of about 600,000. Fig. 1.3 shows how areal density has increased from when magnetic storage was first developed (1956 RAMAC) through the present time 2010. The overall growth rate has been around 41% per annum

from 1956 to 2010. Thanks to new technologies such as Giant magneto-resistive head (GMR head) and perpendicular recording technology, the areal density achieved for products grew at the rate of 91% per annum from 1995 to 2001. During 2000's, the increase in areal density tended to slow down to 37% per annum but the progress is still substantial.

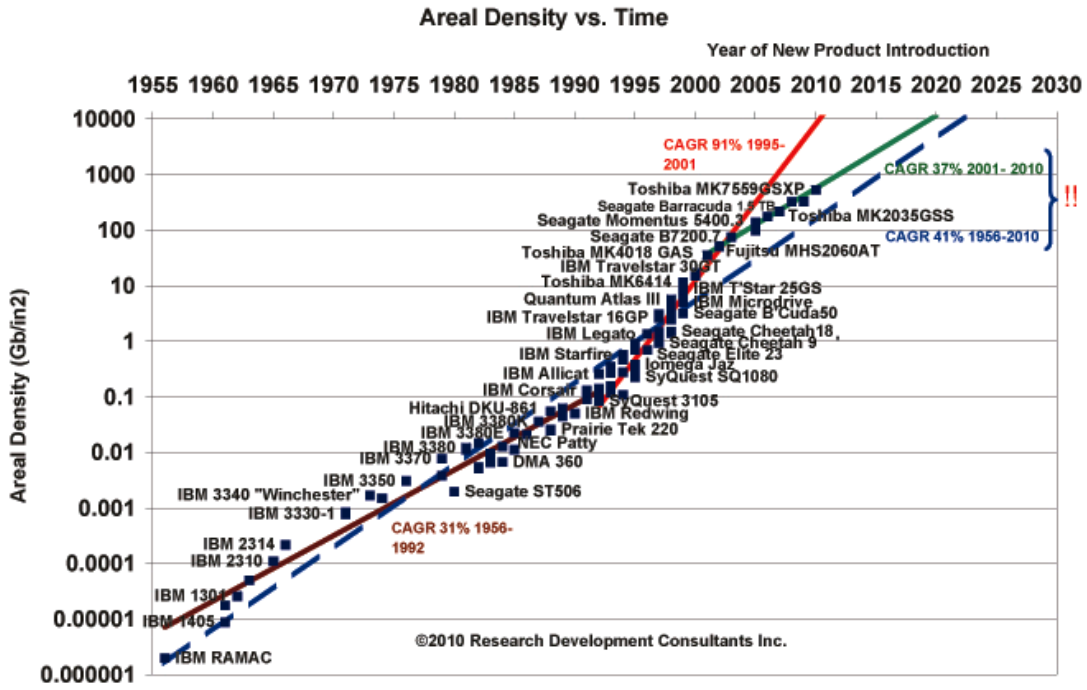

Figure 1.3 Evolution of recording area density of magnetic hard drive disc industry (reproduced from http://rondennison.com/services.htm)

Fig. 1.4 shows all the basic components of a magnetic recording scheme When it comes to magnetic storage, to pursuit higher recording area density, as all the components progressively scale down, it is essential to require the write-head material to produce large enough magnetic field to switch the magnetization of underlying recording media within certain volume, which, by definition, demands the material of the write head to be of high saturation magnetization.

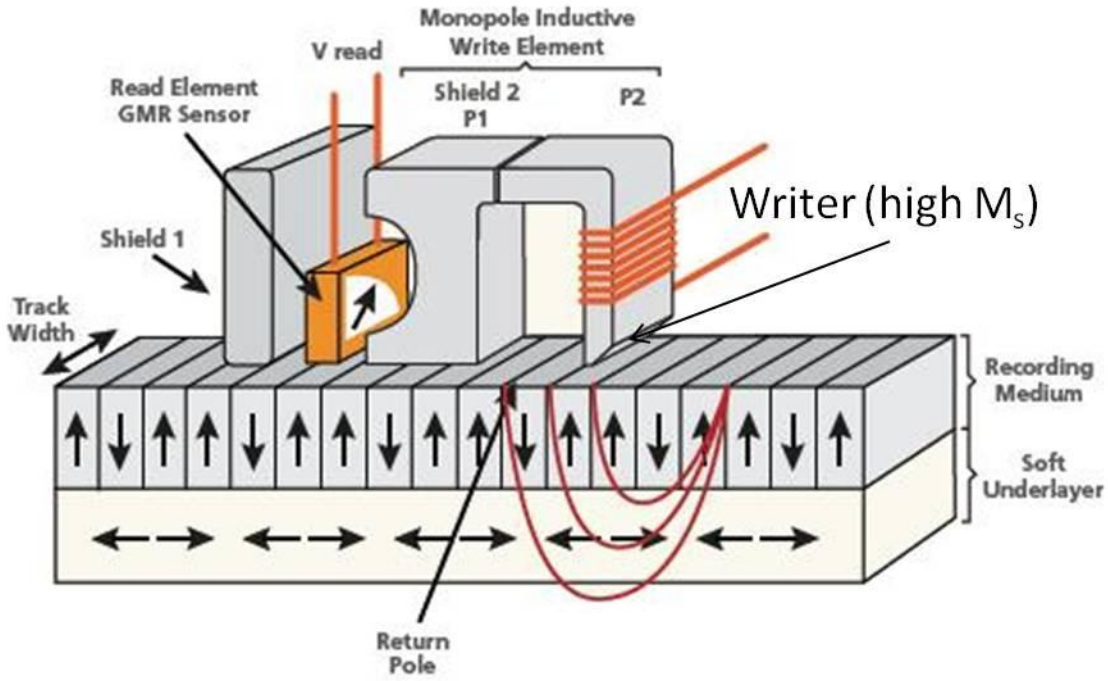

Figure 1.4 A sketch of perpendicular magnetic recording mechanism. The key components (writer, reader and media) are outlined. The write-head requires the material to produce large M_s. (source: www1.hitachigst.com/hdd/technolo/overview/chart13.html)

However, as described earlier, there are limits to just how high the saturation magnetization a material can be. At least many researchers believed so. To increase the magnetic moment per atom without sacrificing the volume, one efficient approach is described in figure 1.5. It is seen that starting from pure metal Fe and progressively doping Co into Fe metal, FeCo alloy can be formed. Since Fe and Co are close to each other in periodic table, the resulting product will have similar band structure and spin resolved density of states as that of Fe metal. The doping of Co effectively only introduces modification of Fermi level since adding Co into Fe essentially increases the total number of electrons. By controlling the doping concentration, it is always possible to find an optimized Fermi level so that the net magnetic moment can be maximized.

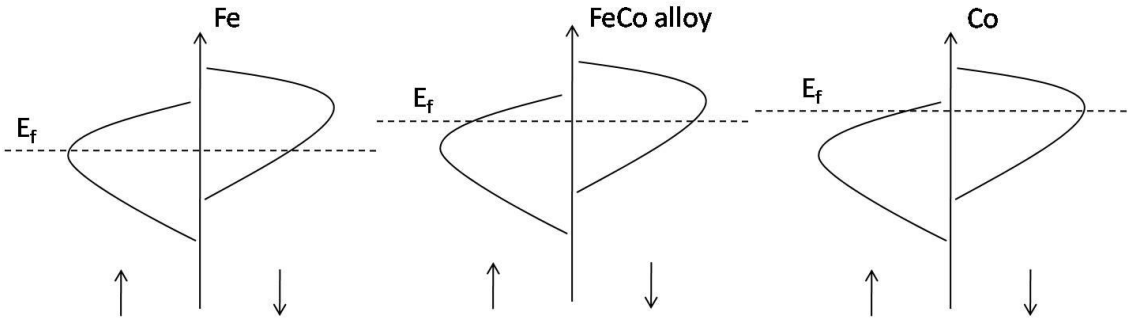

Figure 1.5 a schematic illustration of the idea of increase M_s. The difference of density of state for Fe, FeCo alloy and Co is the Fermi level position. If an optimized FeCo atomic ratio is reached, the E_f can be optimized so that the spin-up and spin-down electrons occupying the bands below the Fermi level can produce highest net magnetic moment.

Following this idea, in early 1930s, researchers found a way to *engineer* ferromagnetic materials with very large saturation magnetization, which was known as Slater-Pauling curve. Figure 1.6 shows the famous Slater-Pauling curve[4,5,6], which describes the variation of average atomic moment with electron concentration for Fe, Co, Ni based ferromagnetic 3d elements and their relevant alloys. This curve gives an excellent account of the experimentally determined magnetic moment in 3d alloy systems and shows a maximum average magnetic moment of around 2.5 μ_B per atom achieved in $Fe_{65}Co_{35}$ and is regarded as the highest bulk saturation magnetization so far. Though in ionic systems, transition elements such as Fe^{3+} may possess local magnetic moment up to 5 μ_B per iron atom (high spin configuration), they usually exist in solids with ferrimagnetic or antiferromagnetic order and are always accompanied with large volume percentage of non-magnetic ions such as O^{2-} or S^{2-}, which significantly reduces the saturation magnetization.

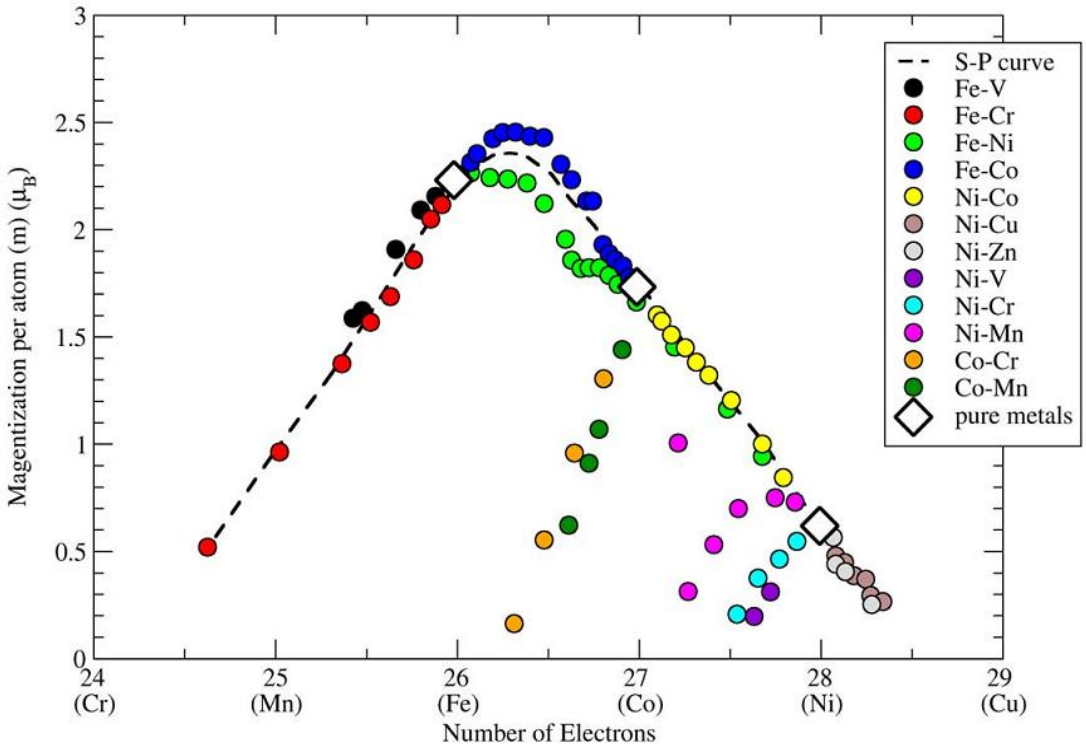

Figure 1.6 Slater-Pauling curve showing average magnetic moment versus electron concentration in the transition metal series (reproduced from Reference. (R. M. Bozorth, Phys. Rev. 79, 887 (1950)))

1.4 $Fe_{16}N_2$, the 40-year mystery

1.4.1 History of the controversy

Almost 40 years ago, a candidate material with saturation magnetization beyond $Fe_{65}Co_{35}$ was found to be $Fe_{16}N_2$, which was intrigued by Kim and Takahashi's giant saturation magnetization report[7] on this material back in 1970s'. Based on the conventional magentometer measurement that measured the bulk average magnetization, they claimed a saturation magnetization of $4\pi M_s$ = 2.58 T[8] on their Fe-nitride thin films prepared through an evaporation method, corresponding to an average magnetic moment of 3.0 μ_B per Fe atom. This is substantially larger than that of FeCo alloy system and directly challenges the well-established itinerant ferromagnetism. Surprisingly little notice was taken of this

claim, likely due to the unshakable faith in the Slater-Pauling Curve or more likely due to the well-known difficulties in determining the magnetization of thin films with high accuracy.

In 1990s', Sugita's and co-workers[9] from Hitachi research group in Japan published a series of studies that were based on their single crystal $Fe_{16}N_2$ thin film samples prepared by molecular beam epitaxy (MBE), showed again that this material has giant saturation magnetization, and in particular a magnetic moment of 3.5 μ_B per Fe atom was revealed. These results draw an immediate attention in the magnetic research society. At the annual conference on Magnetism and Magnetic Materials in 1996, a symposium[10] was held on the topic of $Fe_{16}N_2$, on which both theorists and experimentalists presented their work. However, since the reported saturation magnetization value of the $Fe_{16}N_2$ by different research groups covered a broad range and first-principles calculations based on conventional band magnetism failed to rationalize the existence of the giant magnetization, no decisive conclusion could be drawn on whether it has giant saturation magnetization. The $Fe_{16}N_2$ remains to be a mystery in magnetic materials and magnetism community. Since then, researchers gradually dropped this topic.

1.4.2 The metastable phase α"-$Fe_{16}N_2$

α"-$Fe_{16}N_2$ is a metastable phase, which was discovered by Jack in 1950's[11]. The bulk samples were reported to be successfully prepared from a rapid quenching process from γ'-N-austenite (Ref. 11). From the iron nitride phase diagram as shown in Figure 1.3, it is clear that at high temperature (above 590 °C), the γ-phase (a symbol for face center cubic Fe) dominates. The introduction of N atoms allows the random occupation in the octahedral interstices and consequently form γ-Fe-N phase over a wide N concentration. By quenching it from high temperature, the system undergoes a face-center-cubic (fcc) to body-center-cubic (bcc) phase transformation with N atoms "frozen" at the interstitial sites given the rapid process. As a result, a tetragnally distorted body-centered (bct) structure is formed and

so-called as α'-FeN martensite.

In this iron-nitride martensite, before it collapses into fcc phase, the N concentration can vary from 0 up to 13 at.%, with N atoms randomly occupies the interstitial sites of a preferred lattice direction as shown schematically in Figure 1.4(a). Particularly, at a specific stoichiometry with Fe/N~8/1, upon a suitable heat treatment, the α'-Fe_8N forms α''-$Fe_{16}N_2$ with N being self-arranged in an ordered fashion. As shown in Figure 1.4(b), its unite cell comprises eight distorted bcc cell of α-Fe with N occupying two of the 48 available octahedral interstices with bulk lattice parameters a = 5.72 Å and c = 6.28 Å.

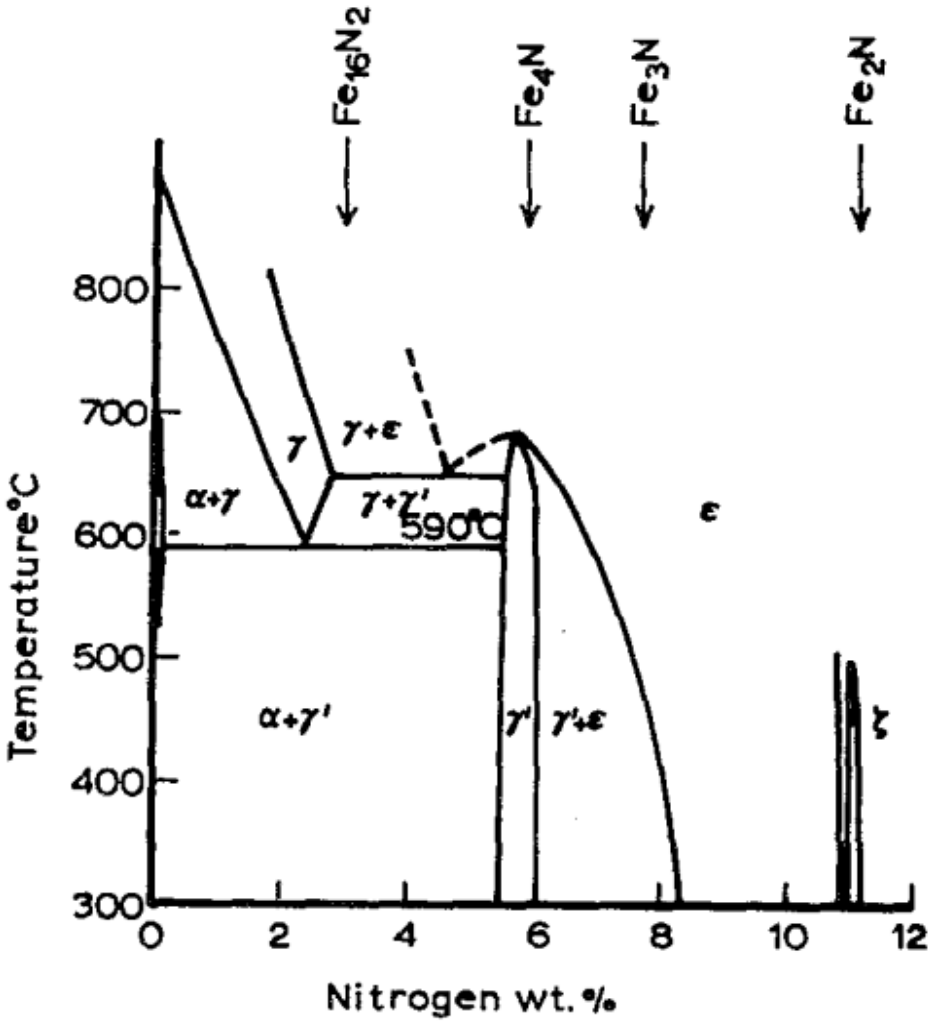

Figure 1.7 The Fe-N phase diagram. (Reproduced from Ref. (K. H. Jack, Proc. R. Sot.

London, Ser. A 208,200 (1951))

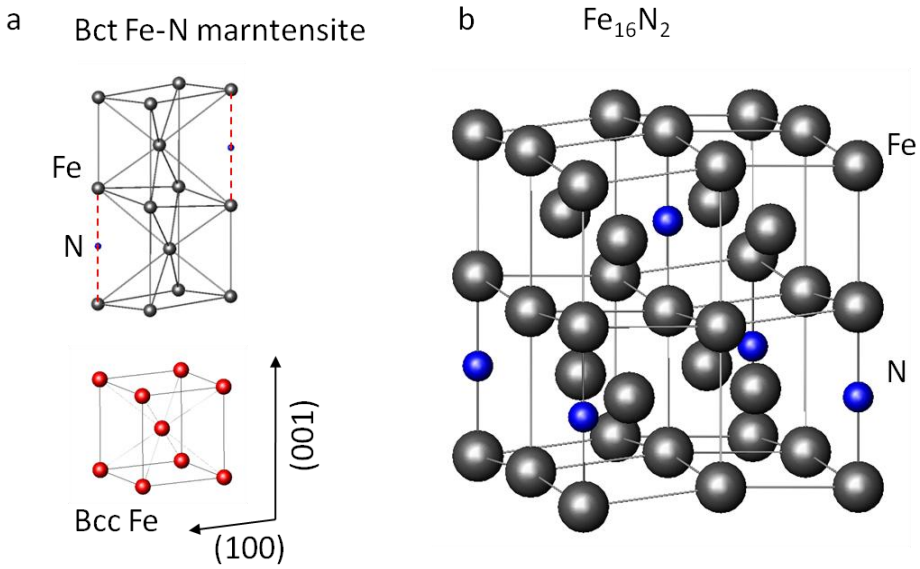

Figure 1.8 (a) a sketch of α'-Fe-N, in which the N atom occupies the interstices with a preferred direction ((001) in this case) and causes the lattice distortion. (b) Crystal structure of $Fe_{16}N_2$ (unit cell), the N site is seen to possess a highly ordered feature.

1.4.3 Experimental and theoretical survey

The production of bulk sample $Fe_{16}N_2$ as powders or foils has followed essentially the 1951 synthesis route, in which case, all the laboratories have produced mixtures of multiple phases that contain $Fe_{16}N_2$ phase. The phase compositions and their corresponding percentage of which have been determined by either XRD or Mossbauer spectroscopy. Since the discovery of this phase, people studied its magnetic properties but found nothing unusual on their bulk samples[12], which contained substantial amount of other iron nitride phases. The 1972 claim by Kim and Takahashi was based on the polycrystalline thin film samples produced by evaporating Fe in N_2 atmosphere on glass substrate, which were announced to be only consisted of α-Fe and α"-$Fe_{16}N_2$. Though the obtained M_s value was dramatically large, achieving $4\pi M_s$ = 2.76 T from their evaluation, this work did not draw immediate attention given the ambiguities on the M_s determinations on thin

film samples that contain multiple phases.

In 1991, Sugita and his team at Hitachi central lab reported the fabrication of $Fe_{16}N_2$ single crystal films by using a MBE process (Ref. 9). They also reported the existence of the giant saturation magnetization in $Fe_{16}N_2$. Following the Hitachi's work, enormous efforts were dedicated to experimentally reproduce or theoretically explain their results. However, the M_s values of the obtained $Fe_{16}N_2$ samples by different researchers covered a broad range. Table I selectively summarizes the typical M_s evaluated in the past several decades. As noted by Metzger et. al[13], these data fall into two camps: those supporting the giant moment claim and those who are against them. A serious issue upon examining the magnetization of $Fe_{16}N_2$ phase is that except the samples from the Hitachi's group, many of other samples reported contained significant amount of phases with much lower saturation magnetization value (such as Fe and γ-FeN). In that case, even the $Fe_{16}N_2$ does exhibit giant M_s, the average magnetization measured by VSM or SQUID may not necessarily produce encouraging results.

Table I average saturation magnetization (M_s (tesla)) and inferred M_s of $Fe_{16}N_2$ prepared by various methods

Ave. $4\pi M_s$ (T)	$4\pi M_s$ of $Fe_{16}N_2$ (T)	Sample and methods	Ref.
2.9	>2.9	Thin film	9
2.58	2.76	Thin film (Evap.)	7
2.4	> 2.6	Thin film (Sputt)	14
2.9	2.9	Thin film (Sputt)	15
2.51	--	Thin film (Sputt)	16
2.4	2.9	Thin film (Evap)	17
2.8~2.9	--	Powder (+Mn)	18
2.66	--	Powder	19
2.1~2.2	< 2.3	Foil	20

2.25	< 2.3	Thin film (Sputt.)	21
2.24	< 2.3	Thin film (Sputt.)	22

To explain these experimental results, theoreticians conducted first-principles calculation using different methods and approximations. In Table II, we summarized some typical results of these calculations. Almost all the obtained average moment per Fe fall in the range 2.3 ~ 2.5 μ_B (expect for the Lai's results[23], which we will comment in our "cluster+atom" model section), which does not show the existence of giant magnetization in $Fe_{16}N_2$.

Table II Average Fe magnetic moments in α"-$Fe_{16}N_2$ from first-principles band structure calculation

Method	**Calculated ave μ_{Fe} (μ_B)**	Ref.
LMTO	2.39	24
LMTO	2.42	25
LMTO	2.50	26
ASW	2.42	27
FLAPW	2.37	28
DV-Xα	2.27	29
LMTO	2.45	20
APW	2.40	30
LMTO (LDA+U)	2.85	23
OLCAO	2.44	31
SIC-LDA	2.39	32

From the band theory, the origin of the net magnetic moment comes from the unequal population of spin up and spin down electrons. Irons which have no

nitrogen neighbors undergo a lattice expansion, giving rise to a moderate enhancement of net moment. Irons with nitrogen neighbors have their moment reduced due to the hybridization between its 3d electrons with nitrogen 2p electrons, ultimately resulting in a little increase of the average magnetic moment comparing to pure Fe metal.

1.5 The scope of this thesis

To place this work in context, we realize there are three important aspects, which we regard as "missing pieces"[33] to cause the chaotic situation in this topic.

1) It is extremely difficult to prepare $Fe_{16}N_2$ bulk sample with pure phase. In that case, the uncertainty introduced by the volume percentage evaluation of $Fe_{16}N_2$ and the magnetic contribution of any other impurity phases can easily introduce a large error bar. For thin film samples, even epitaxial films are prepared in many previous studies, the successful samples usually demand a delicate choice of substrate or underlayer, in which case, their magnetic contributions are subtle to assess based on any conventional magnetometry (VSM, SQUID, etc.) approaches, which only measure the bulk average magnetization.

2) There is lack of experimental studies on the origin of the magnetism in $Fe_{16}N_2$ system from a fundamental physics level. For example, the valance states of the three Fe sites in $Fe_{16}N_2$, the bonding nature between Fe and N, the role of N atom, the degree of site ordering and the possible correlation between extrinsic properties (strain, defects) and its magnetism remain unexplored.

3) Theoretical calculation based on the conventional band magnetism yields disappointing results on rationalizing the high magnetic moment as observed experimentally. However, the local spin density approximation (LSDA) based calculation, has a tendency to underestimate the Coulomb interaction and associated

localized feature of 3d electrons, which may provide inaccurate descriptions on physical parameters such as magnetic moment. Therefore, the magnetism of the $Fe_{16}N_2$ remains unknown given the obvious discrepancy between theory and experiments.

In a purpose of tackling the problems listed above, this thesis presents a systematic study on epitaxial $Fe_{16}N_2$ thin film samples, which includes sample processing, multiple structural characterizations, a variety of techniques to evaluate the saturation magnetization, elemental specific fundamental magnetism study as well as a model study that was based on the first-principles calculation. The chapters are organized as the following.

In Chapter 2, we describe a novel synthesis route to produce epitaxial $Fe_{16}N_2$ thin films based on a facing target sputtering method. Structural and morphology information of the prepared samples are systematically characterized by a combination of techniques such as x-ray diffraction, transmission electron microscopy, etc.

In Chapter 3, we present the saturation magnetization characterization including magnetometry, e.g. VSM. More importantly, we introduce a novel technique to evaluate the magnetization of thin films, the polarized neutron reflectometry (PNR), which directly measures the in-depth profile of magnetization in absolute unit.

In Chapter 4, we provided a theoretical investigation based on our recently proposed "cluster + atom" model to rationalize the giant saturation magnetization in $Fe_{16}N_2$, in which the LDA+U calculation method is used. The proposed model is confirmed by a set of synchrotron based x-ray experiments. In addition, other effects such as N site ordering and epitaxial constrain are also discussed based on the proposed model in this context

In Chapter 5, we described the studies on the perpendicular magnetic anisotropy

developed and spin polarization ratio in $Fe_{16}N_2$. The simultaneous realization of both properties allows its application in future GMR and MTJ devices.

In Chapter 6, we conclude our work and discuss the future outlook of artificially building magnetic materials with giant saturation magnetization.

Reference

[1] H. Beckmann and G. Bergmann, Phys. Rev. Lett. 83, 2417 (1999)

[2] http://en.wikipedia.org/wiki/Hund%27s_rules

[3] http://dpwww.epfl.ch/cours/ansermet/magweb/crystal_field.pdf

[4] J. C. Slater, J. Appl. Phys. 8, 385 (1937).

[5] L. Pauling, Phys. Rev. 54, 899 (1938)

[6] R. M. Bozorth, Phys. Rev. 79, 887 (1950)

[7] T. K. Kim, and M. Takahashi, Appl. Phys. Lett., 20 492 (1972)

[8] In CGS unit, the magnetization is expressed in emu/cm^3. For ferromagnetic material, this is equivalent to the value of magnetization inductance ($4\pi M_s$) in Tesla (T). In this thesis, we have used both magnetic units but they represent the equivalent measure of the same physical parameter

[9] Y. Sugita, et al., *J. Appl. Phys.* 70 (10), 5977 (1991)

[10] The papers were published in J. Appl. Phys. 79 5564-5581 (1996)

[11] K. H. Jack, Proc. R. Sot. London, Ser. A 208,200 (1951)

[12] J. M. D. Coey, Phys. World 6 (August) 25

[13] R. M. Metzger, X. H. Bao and M. Carbucicchio, J. Appl. Phys. 76 (10), 6626 (1994) and references therein

[14] S. Okamoto, O. Kitakami and Y. Shimada, Journal of Applied Physics 79 (3), 1678-1683 (1996).

[15] D. C. Sun and et al., Journal of Physics: Condensed Matter 7 (18), 3667 (1995)

[16] M. A. Russak, C. V. Jahnes, E. Kiohkolm, J.-W. Lee, M. E. Re, and B. C. Webb, J. Appl. Phys. 70, 6427 (1991).

[17] C. Gao, W. D. Doyle, and M. Shamsuzzoha, J. Appl. Phys. 73, 6579 (1993).

[18] X. Bao, R. M. Metzger, and W. D. Doyle, J. Appl. Phys. 73,6734 (1993)

[19] Huang, M. Q., Wallace, W. E., Simizu, S., Pedziwiatr, A. T., Obermyer, R. T., and Sankar,

S. G. (1994a). J. Appl. Phys. 75, 6574.

[20] Coey, J. M. D. (1994). *J. Appl. Phys.* 76, 6632.

[21] M. Takahashi, H. Shoji, H. Takahashi, H. Nashi, T. Wakiyama, M. Doi and M. Matsui, Journal of Applied Physics 76 (10), 6642-6647 (1994).

[22] C. Ortiz, G. Dumpich and A. H. Morrish, Applied Physics Letters 65 (21), 2737-2739 (1994).

[23] Lai, W. Y., Zheng, Q. Q., and Hu, W. Y. (1994). *J. Phys.* C 6, L259

[24] Sakuma, A. (1996). J. Appl. Phys. 79, 5570

[25] Ishida, S., Kitawatase, K., Fujii, S., and Asano, S. (1992). *J. Phys.* C 4, 765.

[26] Min, B. I. (1992). *Phys. Rev.* B 46, 8232.

[27] Matar, S. (1992). *Z. Phys.* B 87, 91.

[28] Coehoorn, R., Daalderop, G. H. O., and Jansen, H. J. F. (1993). *Phys. Rev.* B 48, 3830.

[29] Miura, K., Imanaga, S., and Hayafuji, Y. (1993). *J. Phys.* C 5, 9393.

[30] Sawada, H., Nogami, A., Matsumiya, T., and Oguchi, T. (1994). *Phys. Rev.* B 50, 10004

[31] Huang, M. Z., and Ching, W. Y. (1995). *Phys. Rev.* B 51, 3222.

[32] Umino, K., Nakajima, H., and Shiiki, K. (1996). *J. Mag. Magnet. Mater.* 153, 323.

[33] J. P Wang, INSIC Meeting 2010; APS Meeting 2010; ScienceNOW March 19th 2010; PMRC 2010;

Chapter II Growth Control and Structure Characterization of $Fe_{16}N_2$

2.1 Introduction

To grow epitaxial thin films with high quality, it usually involves the techniques such as molecular beam epitaxy (MBE), pulse laser deposition (PLD) and etc. However, these are not the only approaches to produce single crystal films and are not suitable for industrial application. Here we will introduce another thin film deposition technique based on a physical vapor deposition method – facing target sputtering process. We will illustrate its unique advantage in synthesizing metastable ferromagnetic epitaxial thin films as opposed to other sputtering techniques (such as DC magnetron sputtering). In this chapter, we will show that the facing target sputtering process can repeatedly and reliably produce epitaxial $Fe_{16}N_2$. A collection of thin film structural and chemical characterization technologies were applied to investigate these films in an systematic effort .

2.2 Facing target sputtering process

We start our introduction of the facing target sputtering method by first discussing the working principle of a conventional magnetron sputtering process. In Figure 2.1, a sketch of DC magnetron sputtering method is presented. In this figure, gas ions (Ar in most cases) out of a plasma are accelerated towards the target, resulting in the target material being sputtered from the target surface to the substrate and realize the deposition. However, to synthesize $Fe_{16}N_2$ using such conventional DC sputter, there are two critical drawbacks that could substantially influence the quality of the final products.

1) Given the geometry of the DC sputtering, the substrate is directly exposed to the plasma. In this case, the plasma radiation and bombardment could largely influence the film quality. For the material we study here, $Fe_{16}N_2$ is known as meta-stable. It

requires very precise and delicate treatment to develop favorable growth conditions, which is challenge to realize by using DC magnetron sputtering.

2) When generating self-sustained plasma, if the sputtering targets are consisted of ferromagnetic material (Fe in this case), there is a tendency for the magnetic flux to go interior rather than come out of the target surface for the DC sputtering geometry. In this case, it will require relatively high threshold Ar pressure, which will subsequently influence the texture quality. It is also known that high pressure Ar usually play a negative role on crystallizing films. It will introduce another drawback for the epitaxial growth of the metastable $Fe_{16}N_2$.

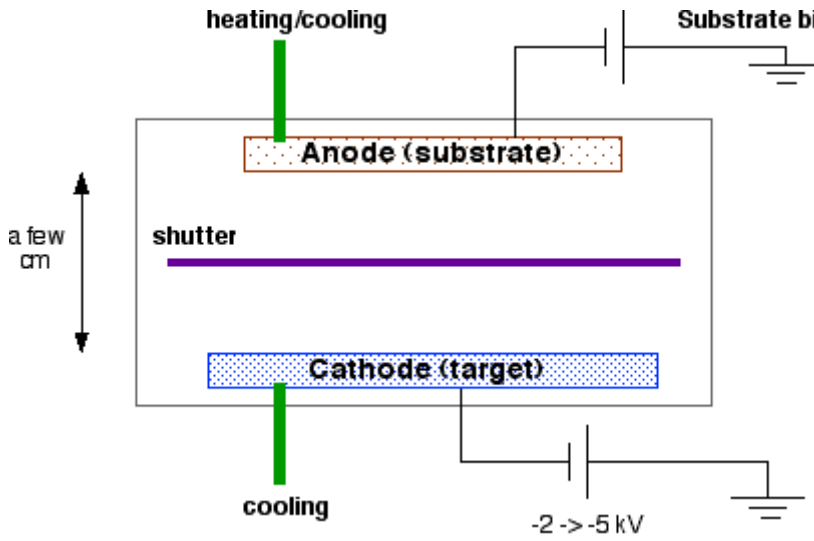

Figure 2.1 A sketch of a conventional magnetron sputtering process.

To overcome these intrinsic issues and synthesize this metastable phase using sputtering technique, we picked up a unique sputtering technique-facing target sputtering method[34, 35]. In Figure 2.2, we show the schematic set-up of this sputtering method. Different from the conventional magnetron sputter, the cathodes are consisted of two targets placed face to face, with magnets placed behind each target, generating a magnetic field as specified in the figure. The substrate is vertically installed by side of the target surface. During the discharging process, electrons oscillate in the space between two targets in helix motion due to the combining effect of both the magnetic and the electrical fields, which effectively

improves the collision efficiency. More importantly, given this geometry, rather than charged ions, neutral atoms are more tentative to reach the substrate, which largely reduces the radiation and bombardment damage of the film due to the plasma. We tested the substrate temperature in-situ during sputtering without heating the substrate purposely (room temperature, 25 ^{o}C). We found the substrate temperature is stabilized at 32 - 35 ^{o}C. As a reference, the substrate temperature can easily go up to 70 – 100 ^{o}C for typical magnetron sputtering without substrate heating. This is of particular importance for the synthesis of metastable phases that sensitive to temperature. Furthermore, the current configuration allows the magnetic field to exist with much lower surface field given this particular geometry, which provides much reduced threshold Ar pressure and is especially important to favor epitaxial growth using sputtering method.

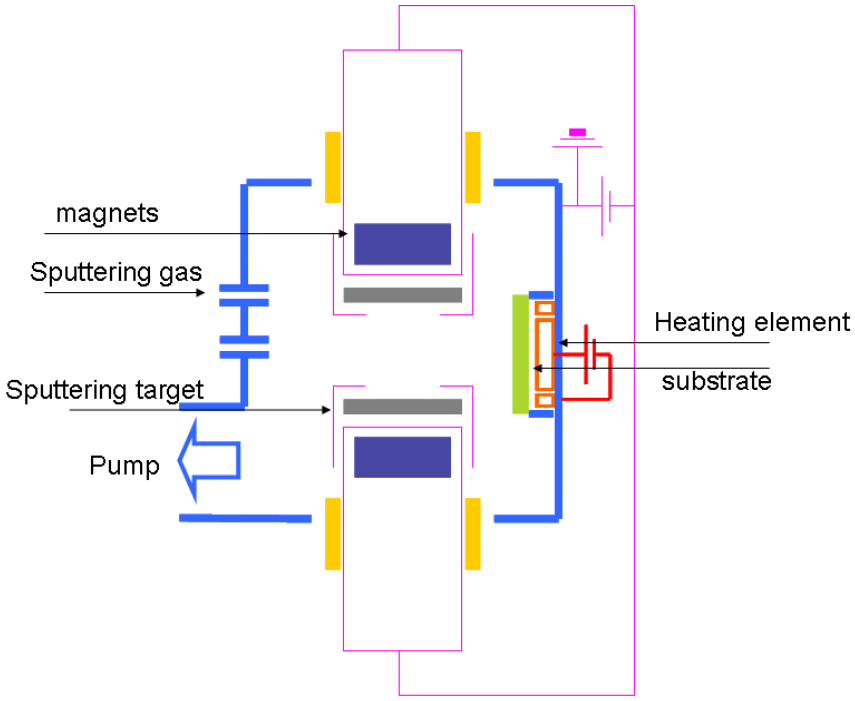

Figure 2.2 A schematic drawing of the facing target sputtering geometry.

Figure 2.3 shows the real image of the facing target sputtering system used in my research. The load-lock and sample transfer system allow the preparation and exchange of samples without breaking the vacuum of the main chamber. In our study,

coupon samples with typical size of 1x1 cm^2 are used. The chamber vacuum is maintained by a cryo-pump (Cryogenic CT08, MODEL CT10) which gives a typical base pressure of $5x10^{-8}$ Torr. The long gas inlet allows Ar and N_2 to ground thoroughly during sputtering. Our facing target sputtering deposition system is consisted of two 4" Fe targets (99.95%), which are placed face to face at a distance of ~10cm. Two cylindrical permanent magnets are installed directly behind the water cooling cathodes, generating a magnetic field around 100~200Oe between targets, with field direction perpendicular to the target surface. The substrate with substrate heater is vertically installed by side of the facing targets with the 12 cm distance from the center of the substrate to the center of the target pairs.

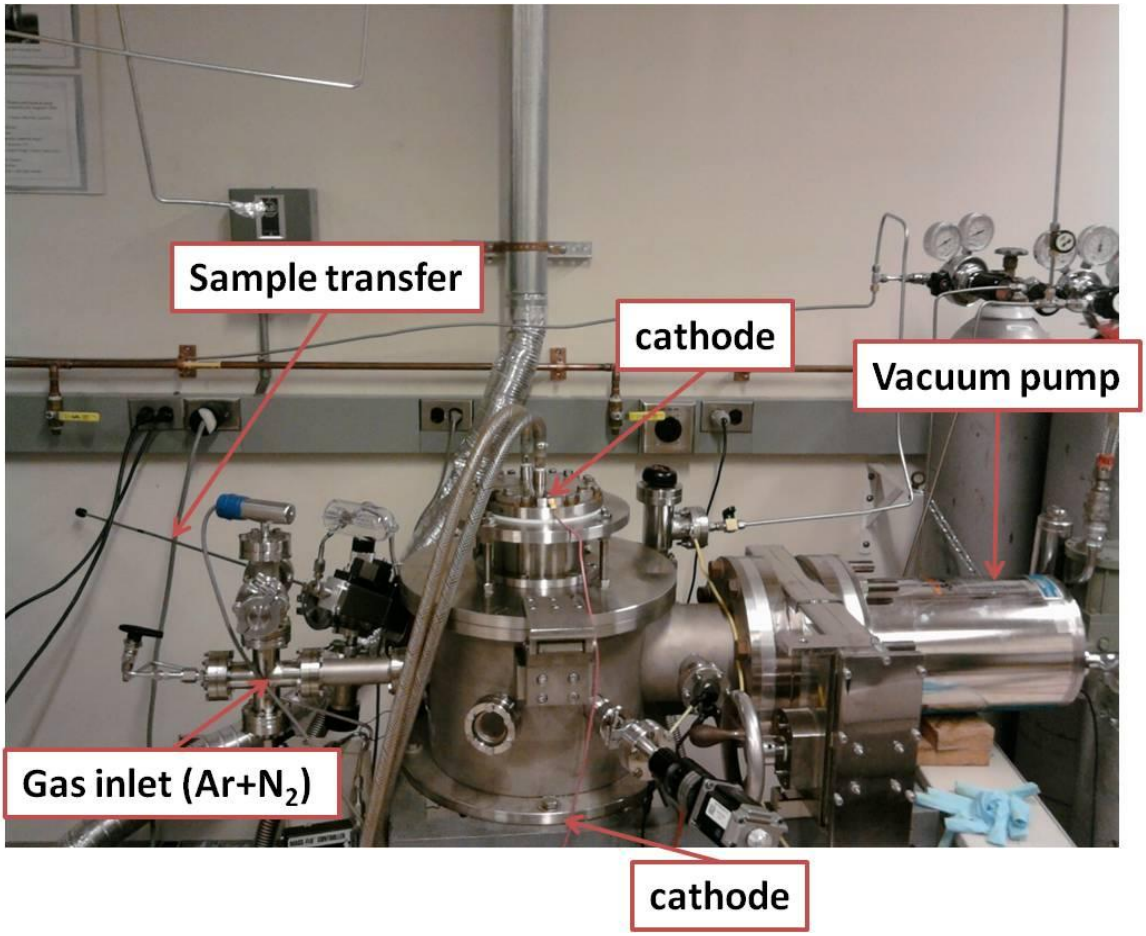

Figure 2.3 An image of facing target deposition system. The key components are outlined on the figure

In a reactive sputtering process, the reaction between inlet gases and target material will effectively "poison" the targets. A signature feedback for this to occur is the observation of target hysteresis. Due to the interaction between the target material and inlet gas during the sputtering process, a hysteresis behavior should be expected if one plots the chamber pressure as a function of inlet gas flow. As shown in Figure 2.4a, we monitored the target pressure as a function of N_2 flow with and without turning on the plasma. In this process, the Ar flow was kept constant of 15sccm and sputtering power was kept constant. From the figure, a slight decrease of chamber pressure is seen after triggering the plasma. However, no obvious hysteresis is observed. Thissuggests the "poisoning" effect is really weak. To further examine the plasma quality, in Figure 2.4b, we plot the target voltage as a function of N_2 partial pressure while fixing the sputtering power at 150W and kept Ar flow as constant (15 sccm). In this case, a clear linear dependence is shown. This indicates the plasma condition is in the current-saturation region.

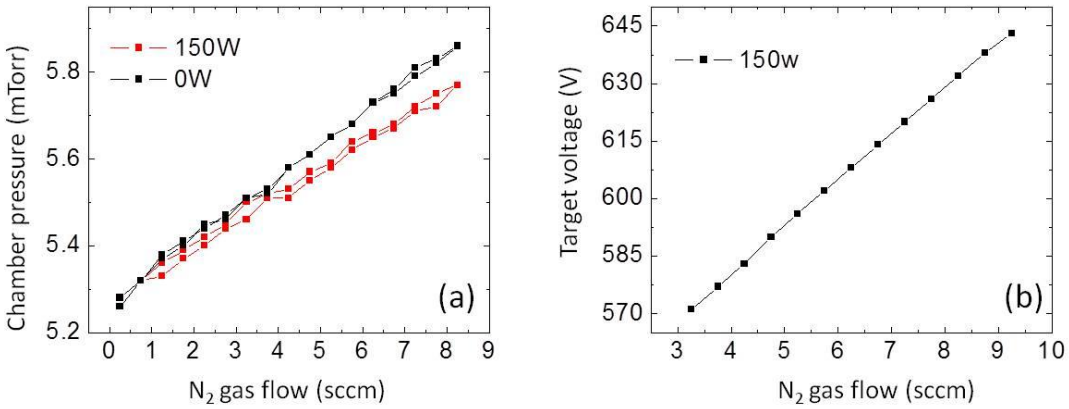

Figure 2.4 (a) chamber pressure as a function of N_2 gas with and without triggering the plasma. (b) Target voltage as a function of N_2 gas flow. In both figure, the Ar flow was kept constant at 15sccm.

2.3 Growth and characterization of iron nitrides

2.3.1 A brief introduction of techniques for structural characterization

To study the structural information of our Fe-N films, we have used a collection of techniques including x-ray diffraction (XRD) and transmission electron microscopy (TEM) techniques. Other measurements such as Auger electron spectroscopy (AES) depth-profile, x-ray photoemission spectroscopy (XPS) are also utilized. A brief introduction and working principles of these techniques are provided below.

X-ray diffraction

The diffracted x-rays from different atoms can interfere with each other and the resultant intensity distribution is strongly modulated by this interaction. If the atoms are arranged in a periodic fashion, as in crystals, the diffracted waves will be consisted of sharp interference maxima (peaks) with the same symmetry as in the distribution of atoms as governed by Bragg Law.

$$2d\sin\theta = \lambda$$

Where d is the spacing between atoms, θ is the angle between the incident beam and the diffraction plane, λ is the x-ray wave length. The angles referred in this study are defined in figure. 2.5.

ω – angle between incident x-rays and sample surface
2θ – angle between incident x-rays and detector
ψ – sample tilt
φ – in-plane sample rotation
x,y – in-plane displacement of sample
z – vertical displacement of sample

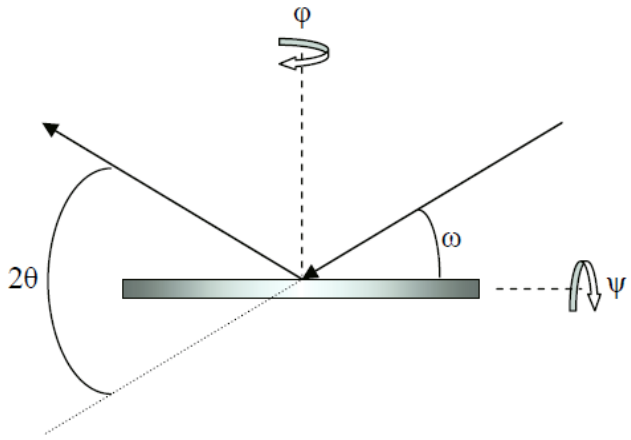

Figure 2.5 A schematic illustration of the x-ray diffraction geometry and the angles used in this study are outlined in this figure.

Precise lattice constants measurements

We scan 2θ over a wide angle range while keeping the ω to be equal to θ during the scan (coupled scan). In this case, the inter-plane distance can be determined by the diffraction peaks according to the Bragg Law.

Rocking curve measurements

This is made by doing a ω scan at a fixed 2θ angle (usually at the diffraction peak position of the films), the width of which is inversely proportionally to the dislocation density in the film and is therefore used as a gauge of the texture quality of the film.

Glancing incidence x-ray diffraction (coupled scan) measurements

This is done by making the incident and diffraction plane parallel to the film surface.

In this geometry, when aligning the scattering vector to the substrate diffraction peak, the peaks yielded from a coupled scans are indexed to the diffractions from in-plane directions.

Glancing incidence x-ray diffraction (Φ scan) measurements

This measurement is done by fixing the 2θ at certain diffraction peak position (in-plane) and rotating the sample stage 360° along a rotating axis perpendicular to the film plane (angle Φ). The results can be used to determine the symmetry of the crystal and also as a gauge of the texture quality of the films along the in-plane direction.

Reciprocal space mapping

This measurement is done by performing a 2θ-ω coupled scan with a fixed ω offset. The map is formed by progressively change the ω offset and run the 2θ-ω coupled scan each time when changing the ω offset. This is therefore useful in determining the lateral structure and texture quality of the films in question.

Instruments used in this study

The wide angle X-ray diffraction measurement is conducted on an X-ray Diffractometer – Bruker-AXS (Siemens) D5005. Rocking curve, reciprocal space mapping, grazing incident x-ray diffractions are conducted on Panalytical X'Pert Pro diffractometer.

Transmission electron microscopy

Samples for analysis via methods of aberration-corrected high-resolution electron microscopy and electron diffraction were prepared from small pieces of the as-sputtered Fe-N samples using a focused-ion-beam (FIB) milling technique. An Hitachi NB-5000 FIB-SEM instrument was used to prepare thin-foil specimens via a standard lift-out technique. Prior to the FIB process, a thin (10nm) Ir layer was

deposited onto the wafer surfaces, as protection for the sputtered films during the initial stages of the FIB sectioning. In the FIB, a layer of carbon about 700 nm thick was laid down by decomposition of phenanthrene with the Ga beam, and a final "strap" of tungsten about 2 μm thick was laid over the carbon. The FIB samples were further thinned using a Fischione Model 1040 Nanomill instrument, with Ar-ion milling at 900 V and a 15 ° angle first to one surface then the other, in order to remove FIB damage and ultimately produce better sections for high-resolution imaging. A final milled cross-section sample is shown in Figure 2.6. The FIB samples were examined in an Hitachi HF-3300 cold-field-emission TEM operated at 300 kV, for bright-field (BF) imaging and for electron diffraction pattern acquisition by selected-area-diffraction and microbeam diffraction methods. In the latter case, a 10 μm condenser aperture was used and the incident beam set at a diameter of 30 to 75 nm to restrict the area from which diffraction patterns were generated; the larger-diameter beam conditions yielded convergent-beam patterns with reflections sharp enough for precision measurements of d-spacings. Images and diffraction patterns were acquired using a Gatan Ultrascan Model 1000 multiscan CCD camera with a 2k x 2k imaging chip.

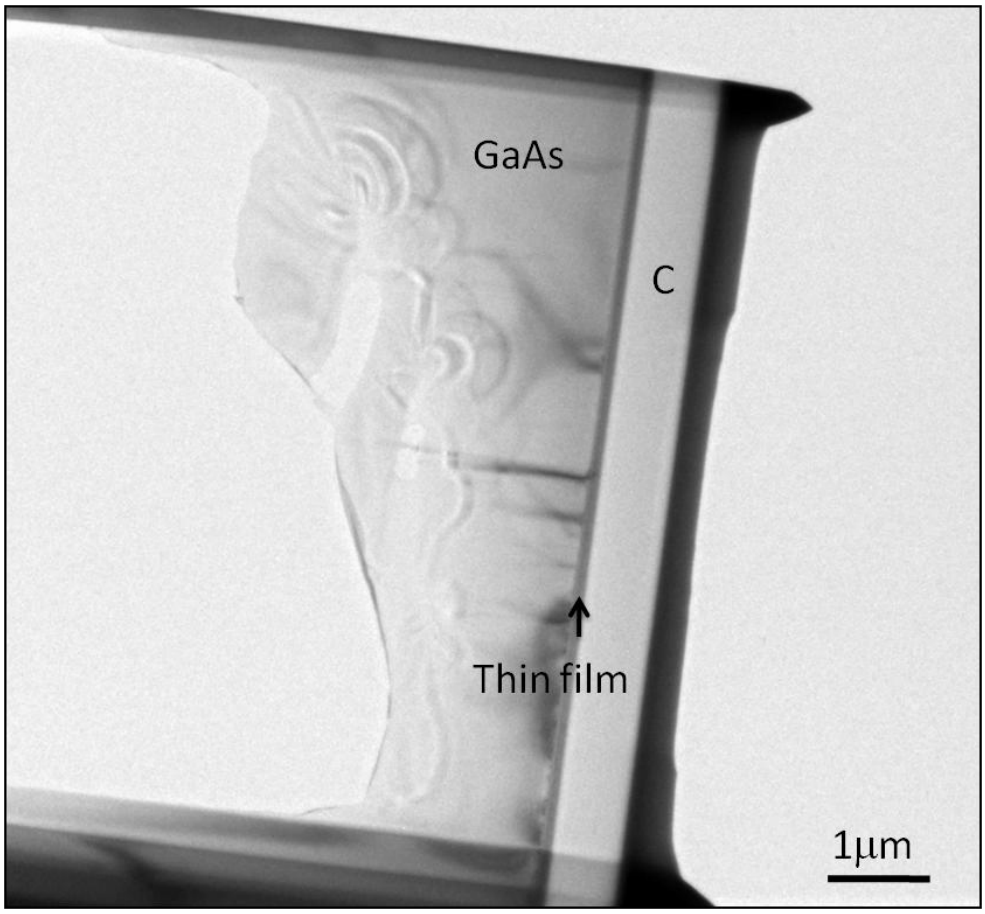

Figure 2.6 Final milled cross-section TEM sample

2.3.2 Characterization of Fe (001) template

As discussed in the previous chapter, the $Fe_{16}N_2$ is metastable phase with body center tetragonal (bct) crystal structure. Therefore, it requires the doping of N atoms along a preferred direction (c-axis) to realize the bct structure. In thin films, an efficient way to facilitate the directional doping is to provide constraint through epitaxy process. Following this discussion, we have chosen to use single crystal GaAs with (100) orientation as the substrate to grow the Fe-N thin films, for which, the in-plane lattice constants are closely matching that of $Fe_{16}N_2$[36].

However, prior to the Fe-N growth, an Fe buffer layer was first deposited on GaAs (001) substrate at 250 ℃, which was demonstrated to induce (001) texture over a relatively large window of deposition conditions as feedback from the X-ray

diffraction (XRD). In our early samples, the Fe underlayer thickness is controlled at 20 ~ 24 nm, which was found to produce good texture quality and smooth surface without introducing large roughness[37]. The texture deviation (full width of half maximum (FWHM)) as measured by Rocking Curve falls typically into the region of (1~2 °), which is of high quality comparing to other sputtered Fe films. As shown in Figure 2.7(a), the XRD measurement indicates that the peak observed of a Fe film grown on GaAs can only be indexed to Fe (002) . This suggests the Fe is of (001) texture. In addition, the rocking curve measured on Fe (002) suggests a FWHM of 1.5 °after Gaussian fitting the experimental data.

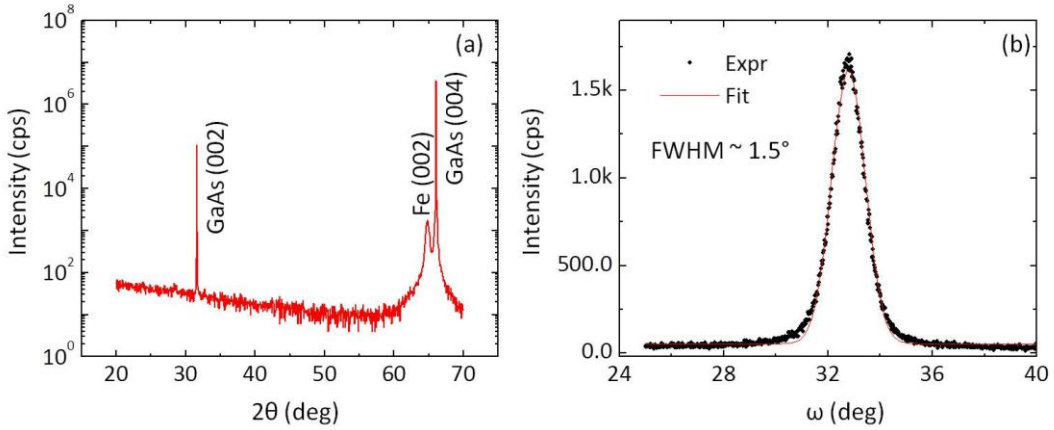

Figure 2.7 (a) x-ray diffraction pattern of Fe (~24nm) deposited on GaAs (001) substrate with conditions outlined in the text. (b) Rocking curve measured on 2θ at Fe (002) with Gaussian fitting.

To confirm that the Fe is indeed epitaxially adapted on GaAs, we used a transmission electron microscopy (TEM) to study a cross-section sample, paying special attention at the Fe/GaAs interfacial region. Figure 2.8a shows a high resolution lattice image taken under high-angle annular dark-field (HAADF) mode. In this figure, the coherency between Fe and GaAs is clearly resolved. From the lattice symmetry analysis, it is noted that Fe and GaAs share a common [110] zone axis with its epitaxial relationship as outlined in figure 2.8b.

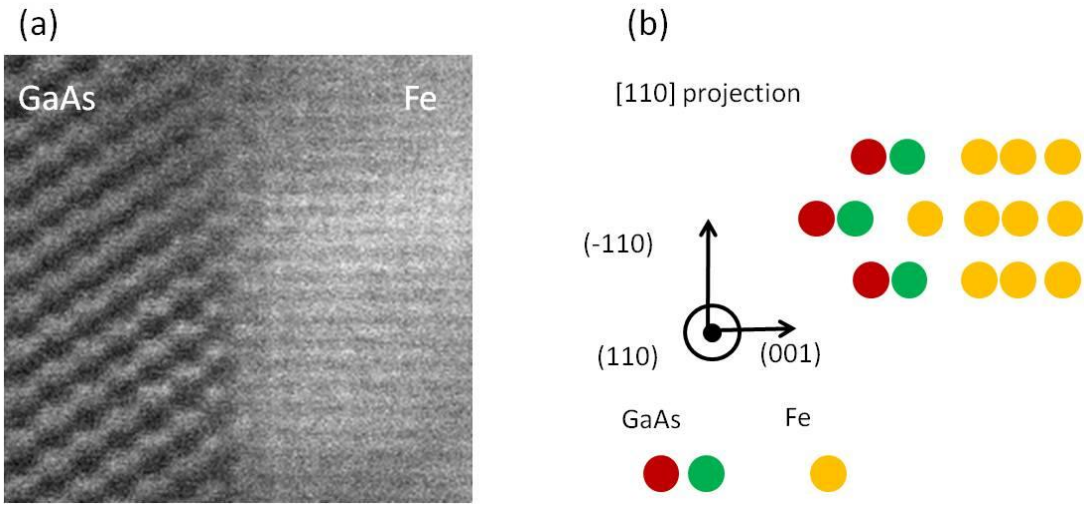

Figure 2.8 (a) A HAADF image at the interface between Fe and GaAs. (b) A sketch of the epitaxial relationship between Fe and GaAs according to the lattice analysis.

A chemical analysis based upon Auger electron spectroscopy depth-profile measurement was conducted on these samples as shown in figure 2.9. Elements including Fe, As, N and O are monitored during each measuring circle. It is seen the Fe layer is of high purity with no observable contamination of O expect for a few nm towards the top interface. Also, no significant As diffusion is seen based on the Auger observation.

We further conducted x-ray photoemission spectroscopy (XPS) measurement to verify the chemical state of the prepared Fe films. After milling away the surface oxides, high resolution scans were performed at both Fe L_2 and L_3 edges. As shown in figure 2.10, single peaks are observable on both edges, suggesting the expected metallic state.

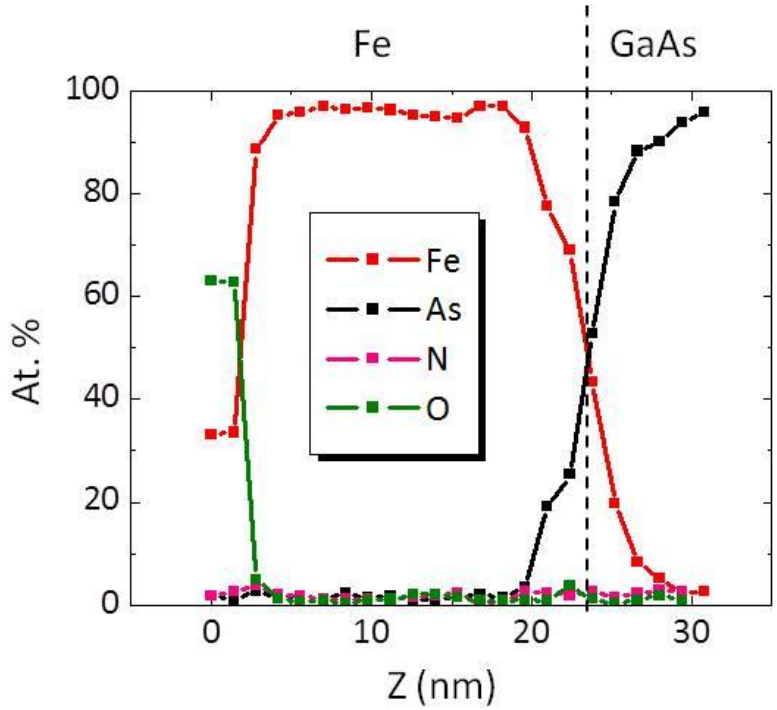

Figure 2.9 Auger electron depth profile on a Fe/GaAs sample for four elements (Fe, As, N, O), Z denotes the distance to the surface along sample normal.

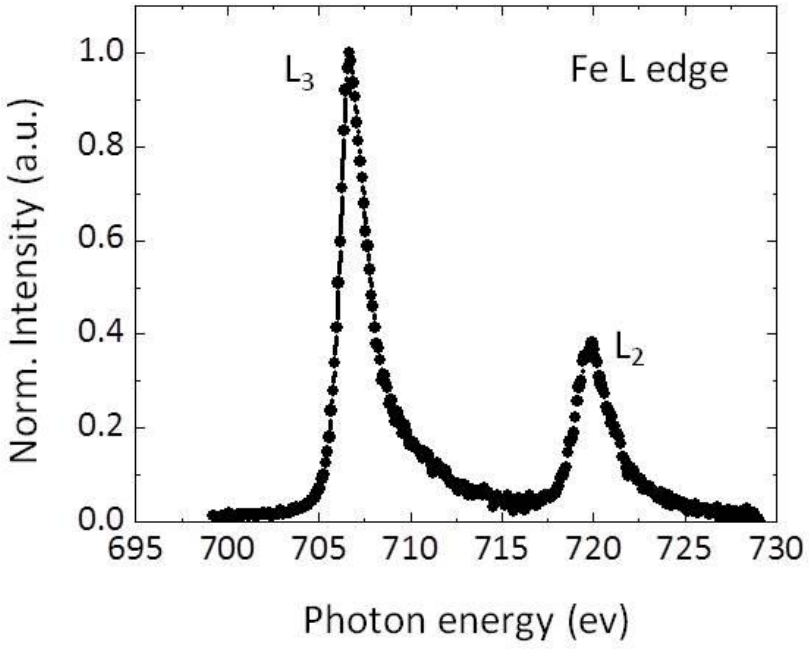

Figure 2.10 Fe L edge HR-XPS measured on a Fe grown on GaAs.

2.3.3 Growth control of iron nitrides using Fe (001) template

So far, we have verified that the Fe underlayer is of expected quality. We now systematically deposit iron nitride films with varying N_2 partial pressure and substrate temperature to optimize the conditions and realize directional doping to produce designated stoichiometry α'-Fe-N (Fe/N ~ 8/1). In Figure 2.11, we plot the obtained phase diagram of Fe-N films deposited using Fe(001)/GaAs(001) as a template. The samples with different phases were determined by the XRD measurement. In this study, we have fixed the sputtering power to be 150 w and Ar working pressure was kept at 5 mTorr. From this figure, it is seen that with the underlayer providing epitaxy constrain, the obtained iron nitrides compounds fall into two main phases. Namely, α'-Fe-N martensites and thermodynamically more stable N-rich γ'-Fe_4N phase.

The phase diagram obtained here can be appreciated by the following. When fixing the N_2 partial pressure and progressively increasing the substrate temperature during growth, the resulting product transferred from metastable α'-Fe-N to a more stable phase γ'-Fe_4N due to the exctra energy provided by the heating, which enhances the mobility of the adatoms. When fixing the substrate temperature while enhancing the N_2 concentration during deposition, the resulting products initially are stabilized at α'-Fe-N with bct crystal symmetry and eventually broken down to form fcc phase that the additional N atoms occupy in-plane interstitial regions and uniformly expend the lattice along the in-plane direction, causing the phase transition from bct to fcc.

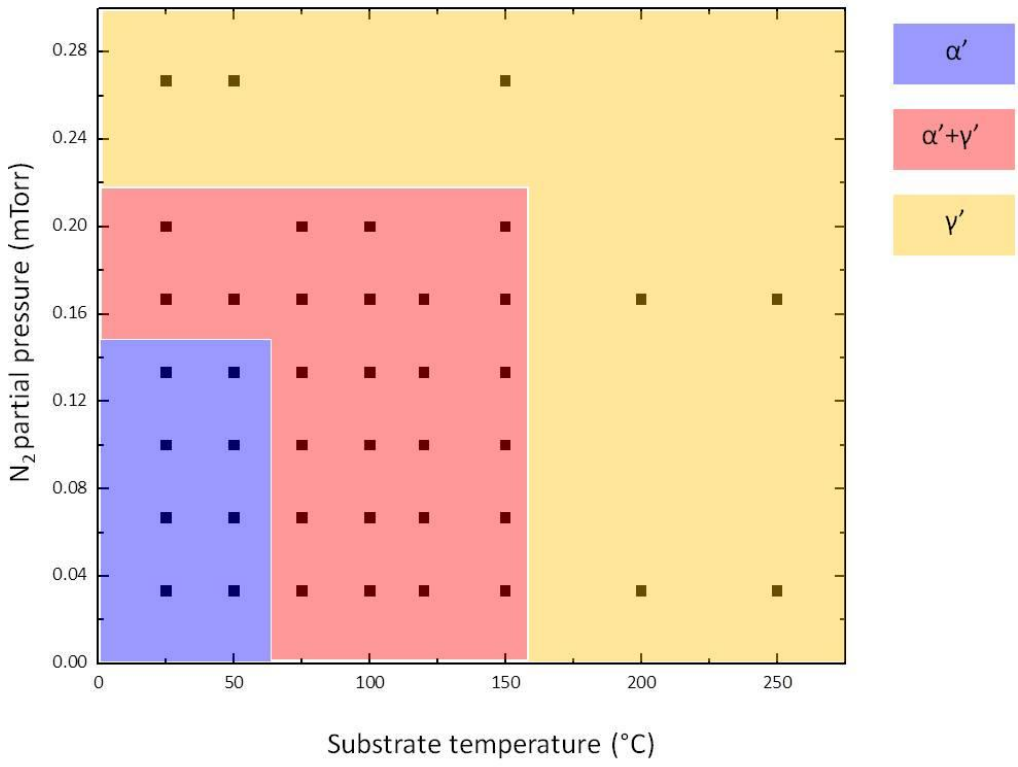

Figure 2.11 Fe-N film phase diagram prepared on Fe(001)/GaAs(001) in this study as a function of N_2 pressure and substrate temperature; the total working pressure and sputtering power were kept constant at 4 mTorr and 150W respectively

2.3.4 Growth control of $Fe_{16}N_2$

Consistent with previous studies using sputtering method, it is unlikely to directly synthesize $Fe_{16}N_2$ without a post-annealing treatment[38, 39, 40, 41]. However, encouraged by the above discussion, it is understood that since α"-$Fe_{16}N_2$ belongs to the family of Fe-N martensites, to obtain α"-$Fe_{16}N_2$, there are two key criteria to be fulfilled.

1) A precise stoichiometry control

It is known that α'-Fe-N martensite is formed through the interstitial doping of N atoms along certain lattice direction (c-axis) and its tetragnality is

correlated with the doping concentration. Therefore, a measure of lattice constant along c-axis is a good indicator of the N doping rate. Plotted in Figure 2.12a are the XRD results of iron nitride films deposited at different N_2 partial pressure ranging from 0.02–0.25 mTorr. Ar partial pressure was kept at 5 mTorr with sputtering power fixed at 150 W. By using the Fe(001)/GaAs(001) template, epitaxial growth of individual Fe–N martensite phases can be obtained with the c-axis perpendicular to the template surface. As the N_2 concentration increases, the α'-(002) peak shifts from high angle to lower value, indicating an enlarged d-spacing along the c-axis due to the increased atomic concentration of N in the interstitial voids. As the N_2 concentration continues to increase, the system eventually experiences bct to fcc phase transition, resulting in the presence of the γ'-Fe_4N phase. Therefore, the optimized N_2 partial pressure to synthesize α'-Fe-N with Fe/N=8/1 (Fe_8N) is determined according to the comparison between measured and expected c-lattice constant of the prepared samples. In Figure 2.12b, we have plotted the calculated c-lattice constant according to XRD results. The dashed horizontal lines correspond to the nominal c-lattice constant values of Fe and Fe_8N respectively.

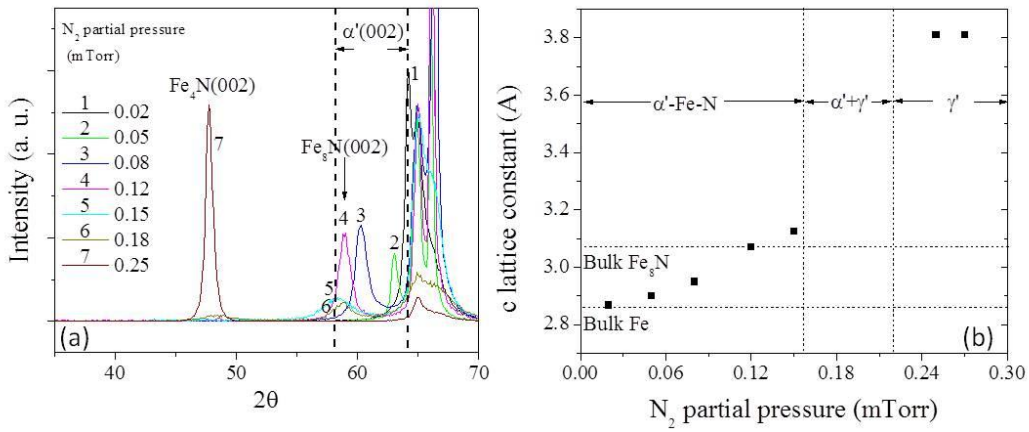

Figure 2.12 (a) X-ray diffraction pattern of epitaxial α'–Fe-N phase films deposited at different N_2 partial pressure (mTorr). (b) Calculated c-lattice constant as a function of N2 partial pressure measured by XRD

2) Control of the degree of N site ordering

From the previous discussion, it is seen that the although a variety of Fe-N compounds can be grown on Fe(001)/GaAs(001) template using the facing target sputtering method. However, the chemically ordered $Fe_{16}N_2$ is not favored even stoichiometry is controlled precisely. This is due to the challenge to facilitate the N atoms to occupy ordered sites in the sputtering process.

Our idea of realizing the chemical ordering in this study is through a post-growth annealing process. In Fig. 2.13a, we showed the XRD results of two samples before and after post annealing treatment at the substrate temperature of 120 ℃. It is immediately noticed that for the annealed sample, at 2θ ~28.5°, there is a diffraction peak developed. The d-spacing of this peak corresponds to the $Fe_{16}N_2$ (002), which is coming from the super-lattice diffraction due to the N occupying the ordered interstitial sites. This is the signature indication of the presence of $Fe_{16}N_2$ phase.

It is also worth mentioning that the annealing temperature is very sensitive to the final product. In Figure 2.13b, we show that when we annealed the as-deposited sample at 130 ℃ for one hour, the obtained sample show N-rich phases, typically Fe_4N. Further increase the annealing temperature results in the formation of more N-rich phase.

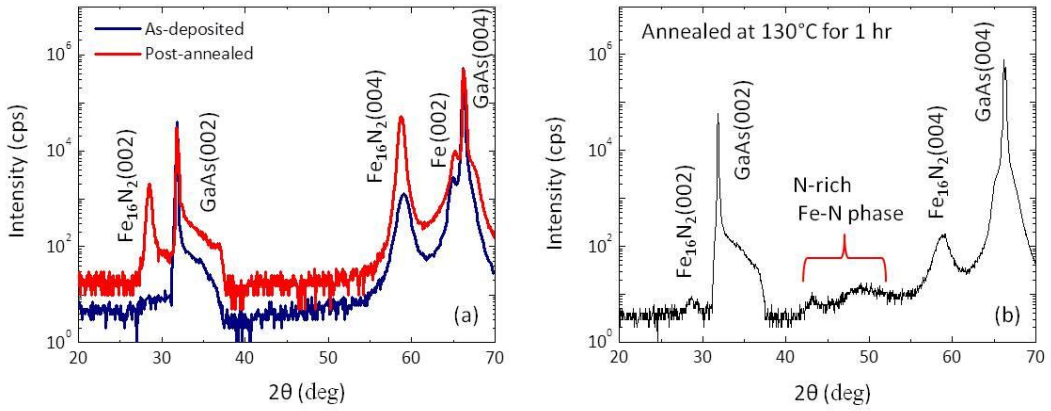

Figure 2.13 (a) X-ray diffraction pattern of as-deposited and post-annealed Fe-N sample (at

substrate temperature of 120 ℃ for 20 hrs. with similar layer structure Fe-N(40nm)/Fe(10nm)/GaAs. (b) X-ray diffraction result of post-annealed sample (same structure as samples in (a)) at substrate temperature of 130 ℃ for 1 hour.

It is also found by post-annealing the as-deposited Fe_8N films for different amount of time at substrate temperature of 120 ℃. The final product can be considered as partially ordered $Fe_{16}N_2$ + Fe_8N phase. In this case, a degree of N site ordering (D) can be defined by comparing the integrated intensity ratio of $I^{obs}(002)/I^{obs}(004)$. This degree of N site ordering[42] can be quantitatively investigated using what is defined as

$$D = \frac{I^{obs}(002)/I^{obs}(004)}{I^{cal}(002)/I^{cal}(004)}$$

where $I^{obs}(002)$ and $I^{obs}(004)$ denote the integrated intensity of peaks according to the measurement. $I^{cal}(002)$ and $I^{cal}(004)$ represent integrated intensity these two peaks calculated from ordered $Fe_{16}N_2$.

Figure 2.14 shows XRD results of Fe-N samples that have been annealed for different amount of time, ranging from 0, 5 to 20 hours. It is seen as the annealing time progressively increases, the D value enhances accordingly and saturates at D~0.36. Further increasing the annealing time up to 50 hrs did not improve the D value significantly.

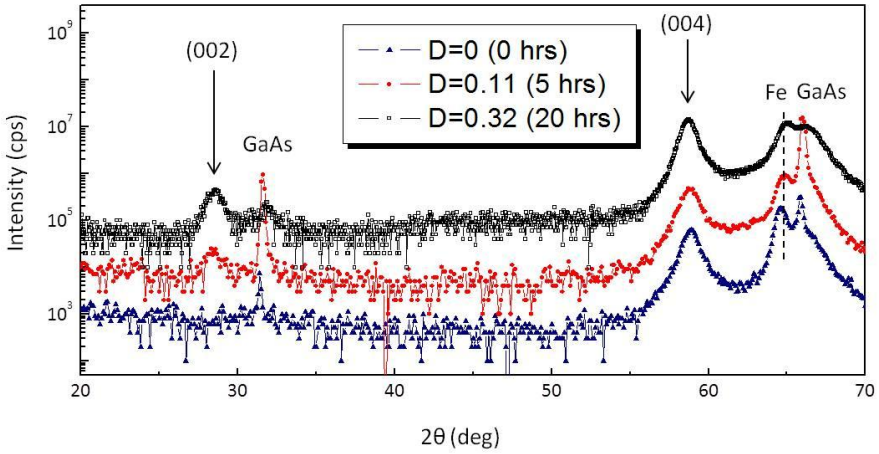

Figure 2.14 X-ray diffraction patterns of partially ordered $Fe_{16}N_2$ samples with different N ordering parameter (D) as calculated. Number in the parenthesis is the amount of annealing time.

2.3.5 Structural characterization of $Fe_{16}N_2$ epitaxial films

1) High angle X-ray diffraction and rocking curve

As previously shown, we have obtained chemically ordered $Fe_{16}N_2$. To further examine the crystal quality and confirm the layer epitaxy, we first conducted a variety of x-ray diffraction measurements on samples with high ordering (D>0.3). Besides the high angle XRD as shown in Fig. 2.13, we examined the rocking curve of the Fe-N peaks as shown in Figure 2.15. With 2θ value fixed at the $Fe_{16}N_2$ (002) and (004) respectively, the ω scan shows expected peak feature. The full width of half maximum (FWHM) were obtained from Gaussian fitting of ~1.56 ° and 0.77 ° respectively for the (002) and (004) peaks, which is of high texture quality for sputtered films. It is interesting to notice that the texture deviation of the super-lattice diffraction (002) is of roughly twice as large as that of (004) diffractions.

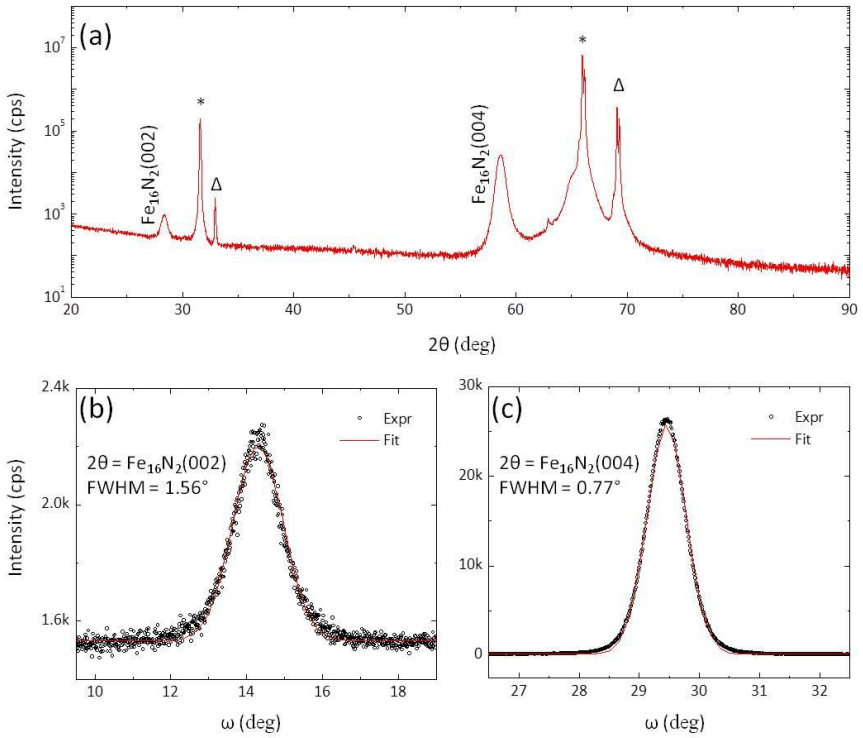

Figure 2.15 (a) A 2θ-ω coupled XRD scan of $Fe_{16}N_2$ grown on GaAs substrate and bonded on a Si wafer during the measurement. The symbols (* and Δ) represents the diffractions from GaAs and Si wafer, respectively. (b) and (c) shows the rocking curves measured on 2θ at $Fe_{16}N_2$ (002) and (004) respectively, the texture deviation of the (002) diffraction is about twice as large as that of (004), as indicated by the FWHM.

2) Grazing incident x-ray diffraction (GIXRD)

To further examine the eptaxial quality, we carried out GIXRD measurement to study the in-plane texture of our thin films. In Figure 2.16, it is shown that with scattering vector perfectly aligned with the substrate GaAs (220), a 2θ-ω coupled scan shows the expected diffraction at 44.8 °, which can be indexed to $Fe_{16}N_2$ (220). After rotating the sample in-plane, the scattering vector is aligned with GaAs (400), similar 2θ-ω coupled scan was performed and the diffraction of $Fe_{16}N_2$ (400) develops coherently. Φ scans at both $Fe_{16}N_2$ (220) and (400) show regularly spaced diffractions with a distance of 90 degree, suggesting a four-fold crystal symmetry along the in-plane direction.

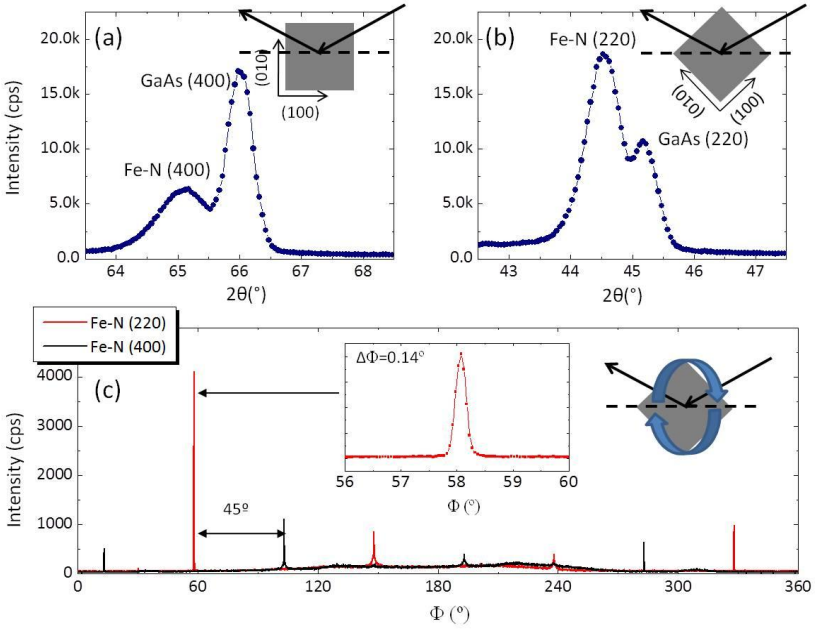

Figure 2.16 (a) and (b) GIXRD 2θ-ω coupled scan with scattering vector aligned along GaAs (400) and (220) respectively. (c) Φ scans with 2θ fixed at Fe-N (220) and Fe-N (400). The inset shows a zoom-in look of a typical Φ scan peak.

3) Reciprocal space mapping (RSM)

We used RSM to study the film morphology along the lateral direction. In Figure 2.17, we show a typical RSM near the substrate diffraction GaAs (002) as outlined. From the shape of the signature diffraction - $Fe_{16}N_2$ (002), the Δω is around 1.5 °, which is a measure of out-plane texture deviation and is consistent with the rocking curve observation. The Δ2θ as outlined in the figure is around 1.4°, which is correlated with the average grain size along the lateral direction.

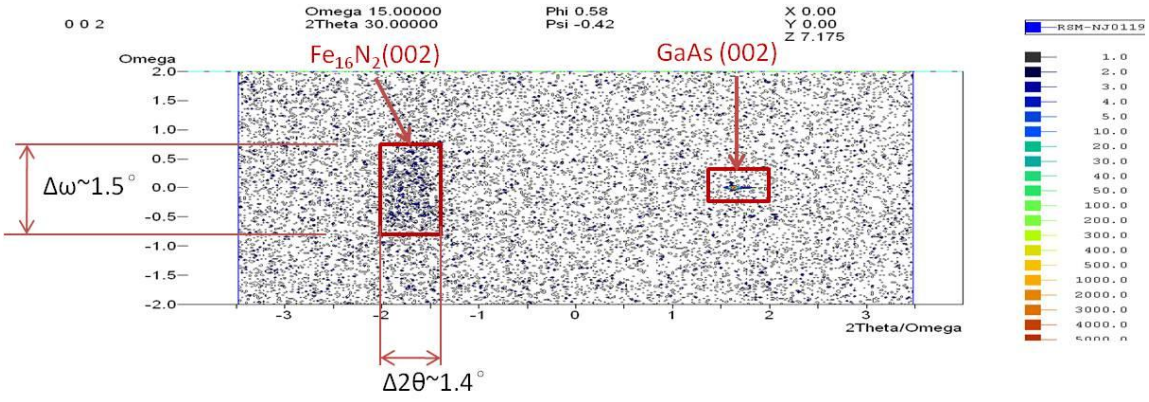

Figure 2.17 A reciprocal space map close to the substrate diffraction GaAs (002). The diffraction from the ordered $Fe_{16}N_2$ (002) is outlined.

4) Low-magnificationag bright field (BF) TEM images

To investigate the thin film morphology, we carried out TEM analysis on the prepared Fe-N samples. Figure 2.18 show a bright field and a dark field images of a cross section sample. It is seen the Fe and Fe-N layer structures are resolved by the morphology contrast given the difference on the growth condition for each layer. This contrast becomes much robust in the dark field image mode, which is mainly due to the different scattering contributions of the light element N in the Fe-N layer. The layers show brighter contrast for higher average atomic number. So Fe layer, for example, is the brightest layer in this image.

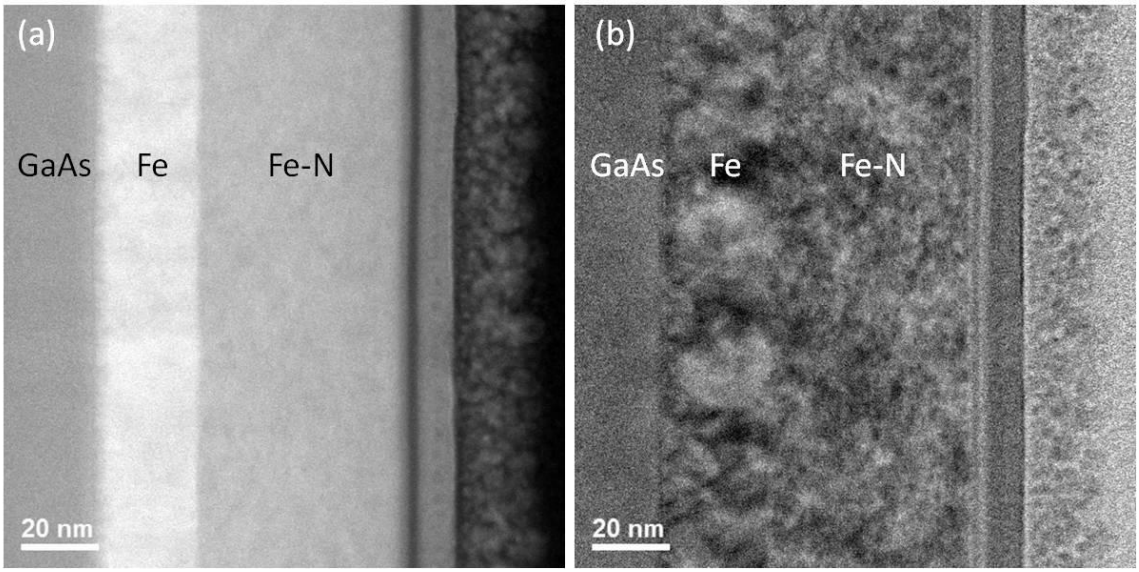

Figure 2.18 (a) Dark field and (b) bright field images of a cross-sectional iron nitride sample. The layer structures are resolved by morphology difference and grayness contrast.

5) High resolution lattice imaging and FFT analysis

After carefully aligning the sample, the scanning TEM allows the direct imaging of lattice structure. In figure 2.19a, we show the lattice image of the GaAs substrate. The dumbbell structure of the GaAs lattice is resolved (region 1),

indicating the imaging resolution is under sub nm. Moving the beam to the Fe-GaAs interface (region 2), it is clear that the substrate and Fe underlayer are highly coherent with a zone axis of <110>. Looking at the Fe-N/Fe interface (region 3), the epitaxy of the tetragonal Fe-N is effectively coherent with the buffer layer. The body-centered cubic Fe layer is in a <110> zone axis orientation, and the tetragonal Fe-N layer is in a <1-10> zone axis orientation, as determined by prior electron diffraction results .

To analyze the periodicities in the lattice images, figure 2.20 shows a diffractogram computed from a 128 x 128px region (i.e. region A). The X and Y scan directions are calibrated so that the peak positions for the [110] and [002] intensities (as determined using the script "Peak" in the Gatan DigitalMicrograph imaging software) closely matched the known d-spacings for the α-Fe structure. Two regions (B and C) as outlined in the Fe-N layer gave the diffractograms with associated periodicities as shown in figure 2.20b middle and bottom. Region B shows only the "spots" corresponding to a disordered ($N < 0.125$) Fe-N structure (where $Fe_{16}N_2$ is equivalent to $FeN_{0.125}$). In comparison, region C shows additional spots corresponding to periodicities that match reasonably well with the d-spacings from $Fe_{16}N_2$, as indicated in the computed pattern for region C. The lattice structure shown within and just above the outline for region C is also consistent with an ordered structure that generates the ordering spots in the diffractogram. These measurements and others from similar images are effectively equivalent to "nanodiffraction" patterns within the respective crystalline layers, and suggest that there are domains on the order of 4nm in extent that are consistent with the ordered $Fe_{16}N_2$ structure, within the generally disordered Fe-N layer. These imaging results therefore support the XRD results described previously.

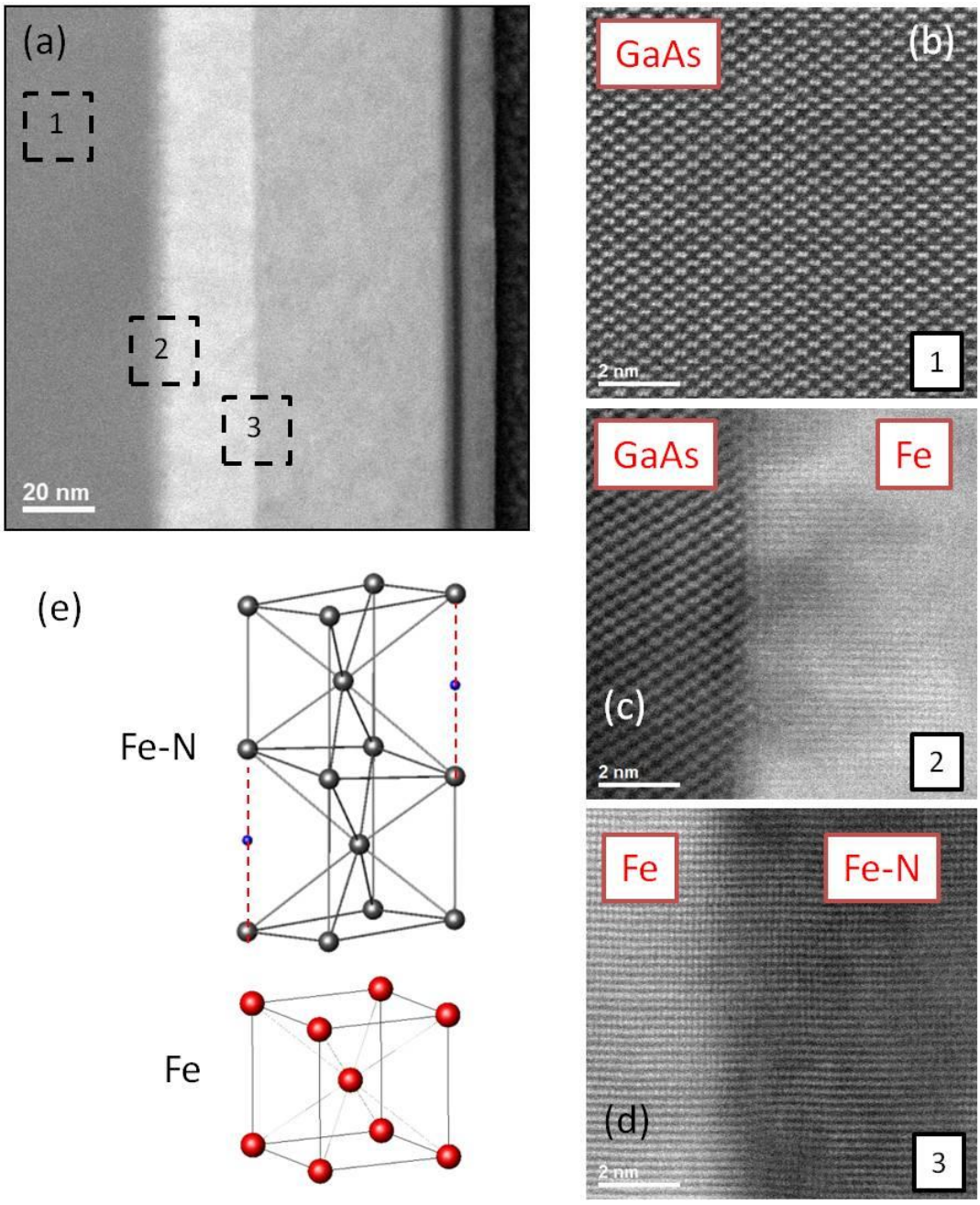

Figure 2.19 (a) same dark-field low-mag image of a cross-sectional Fe-N sample. (b) (c) and (d) show the zoom-in look of regions 1, 2 and 3 as outlined in figure (a). (e) an illustration of the epitaxial relationship as determined by HR lattice image.

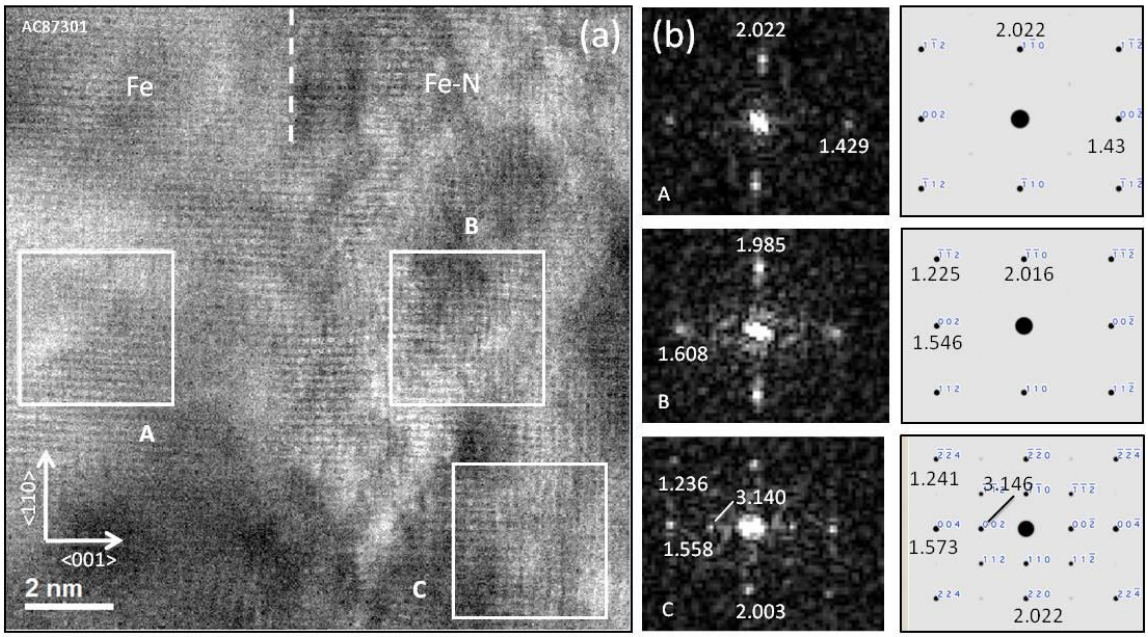

Figure 2.20 (a) Cross-section TEM image of partially ordering Fe-N sample with layer structure Fe-N(/Fe/GaAs; High resolution BF-STEM lattice image of the Fe-N layer showing Fe{110} zone axis; (b) computed diffractograms with associated periodicities identified, from the respective areas a-c shown in (a), along with the computed diffraction patterns for area A: α-Fe, area B: $FeN_{0..125}$, and area C: $Fe_{16}N_2$ (see text for details).

6) Electron Diffraction Analysis

A high-angle annular dark-field scanning transmission electron microscopy (HAADF-STEM) image from a cross-sectional multilayer sample was recorded in Figure 2.21(a). Both microbeam and selected-area diffraction patterns (SADP) were recorded in different regions (Figure 2.21b~e). They correspond in general position to the labeled areas in the HAADF image. These diffraction results reveal the overall crystalline quality of the film and the epitaxy of the lattice structure of the Fe-N layer, which is highly coherent with the Fe buffer layer. With the sample oriented to the [110] zone axis of the GaAs substrate, the α-Fe layer is in a precise [110] orientation. Using the exact d-spacings for the Fe reflections to calibrate a camera factor for further indexing of the rest of the pattern, the d-spacings for the FeN layer are shown to closely match a [1-10] zone axis of Fe lattice that has the same

tetragonal space group (*I4/mmm*) as the stoichiometric $Fe_{16}N_2$. In particular, in region (1) at the GaAs and Fe interface, two diffraction patterns are shown, which can only be indexed to GaAs and Fe with a zone axis of <110>. In region (2), only one Fe diffraction pattern is in presence, corresponding to a cubic symmetry with a 45 ° rotation out of plane. In region (3) at the Fe-N/Fe interface, along the (-110) direction, only one periodicity is shown, which is different from that along its perpendicular direction (001) that two distinguished periodicities are shown. This suggests that the lattice constant of Fe and Fe-N layer are highly coherent along the in-plane (a-axis) direction but deviates substantially along the out-of-plane direction (c-axis).

A microbeam diffraction pattern with the beam spread to cover a 75 nm diameter area, was recorded in figure 2.22b, covering primarily the Fe and FeN layers, with a small contribution from the Ir capping layer and the C layer deposited by the focused ion beam (FIB) process. To bring out additional diffraction information, the contrast of this pattern was expanded as shown in Figure 2.22c. Faint diffuse rings from the amorphous C layer are seen, and a few sharp, irregularly spaced reflections from the crystals in the as-deposited Ir capping layer are also present. The predominant feature of the pattern is, however, the periodic array of diffuse reflections that match the ordering reflections of the $Fe_{16}N_2$ compound. These reflections are circled in Fig. 2.22b. The measured spacings and indexing of the diffuse pattern are consistent with the computed [1-10] $Fe_{16}N_2$ pattern shown in Fig. 2.22d.

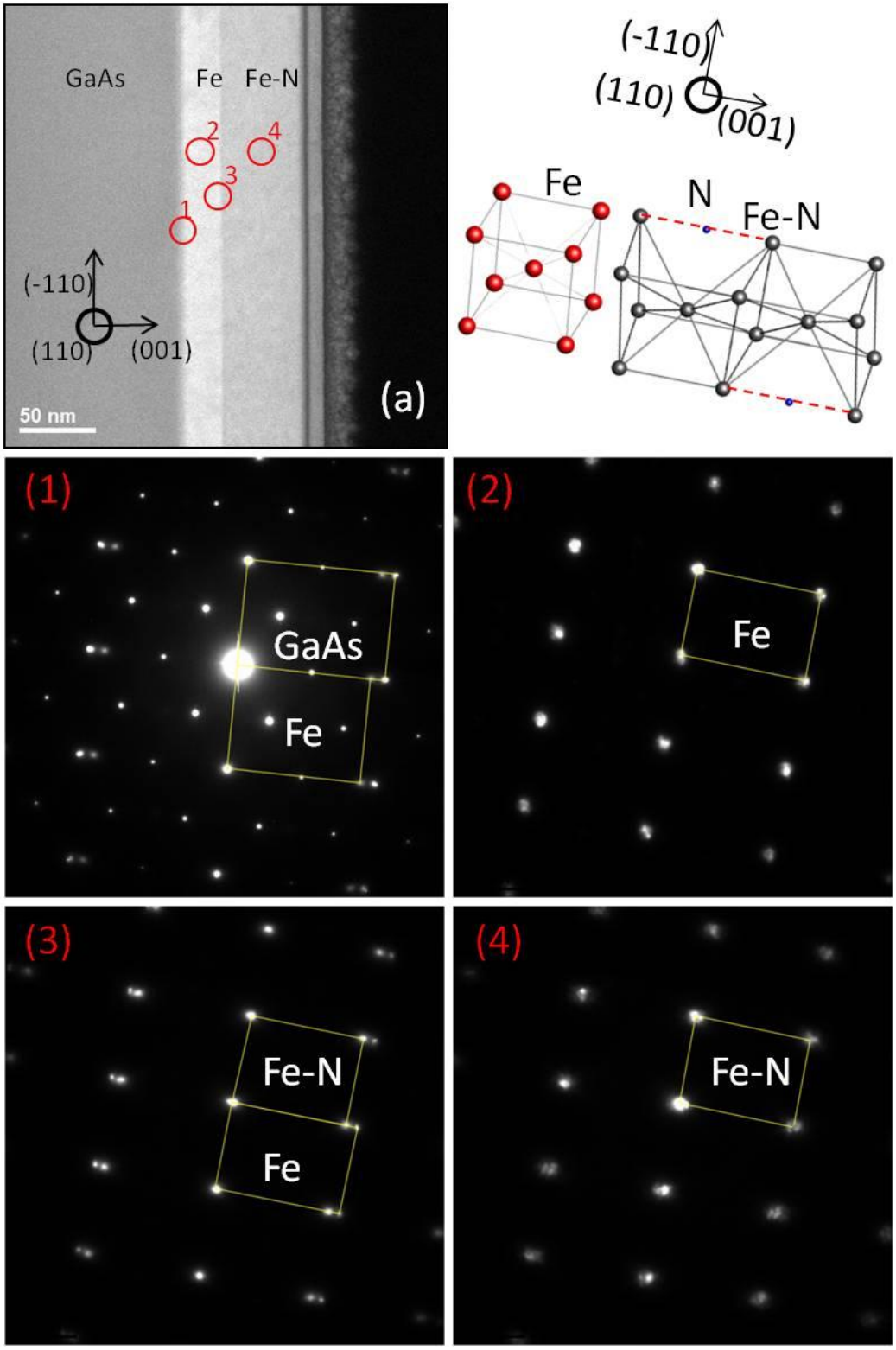

Figure 2.21 (a) HAADF-STEM image and diffraction patterns of epitaxial $Fe_{16}N_2$ cross-sectional sample. A HAADF image of a layered Fe-N sample. (b)-(e) diffraction patterns from the general positions located by the outlined areas in (a).

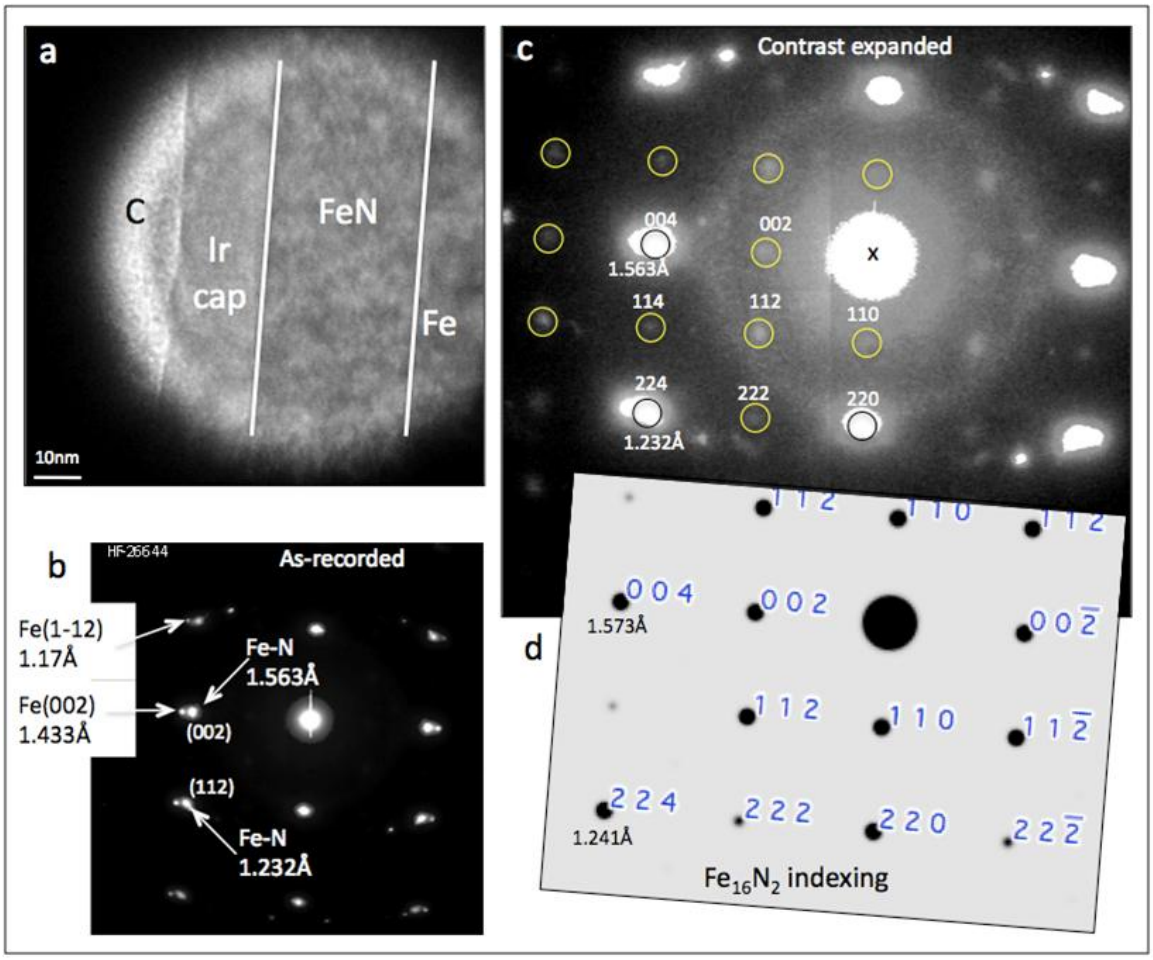

Figure 2.22 TEM/DP study on cross-section partially ordered $Fe_{16}N_2$ sample. (a) Bright-field image of the FIB-milled cross section of an as-deposited multilayer film, showing the area covered by a small convergence electron beam; (b) Electron diffraction pattern (DP) from the area of a), showing Fe in a [110] zone axis orientation; the sharp Fe reflections were used to calibrate the d-spacings for the FeN layer (see text for details); (c) Same DP with contrast expanded, showing periodic array of reflections consistent with the ordering reflections shown in (d), the indexed computed pattern for the $Fe_{16}N_2$ structure.

To determine the lattice constant, we first used the diffraction pattern from the Fe layer indexed to the zone axis of <110> with nominal lattice constant to calibrate the precise camera factor (Figure 2.23). The lattice constant obtained from the Fe-N layer reasonably matches that of bulk $Fe_{16}N_2$.

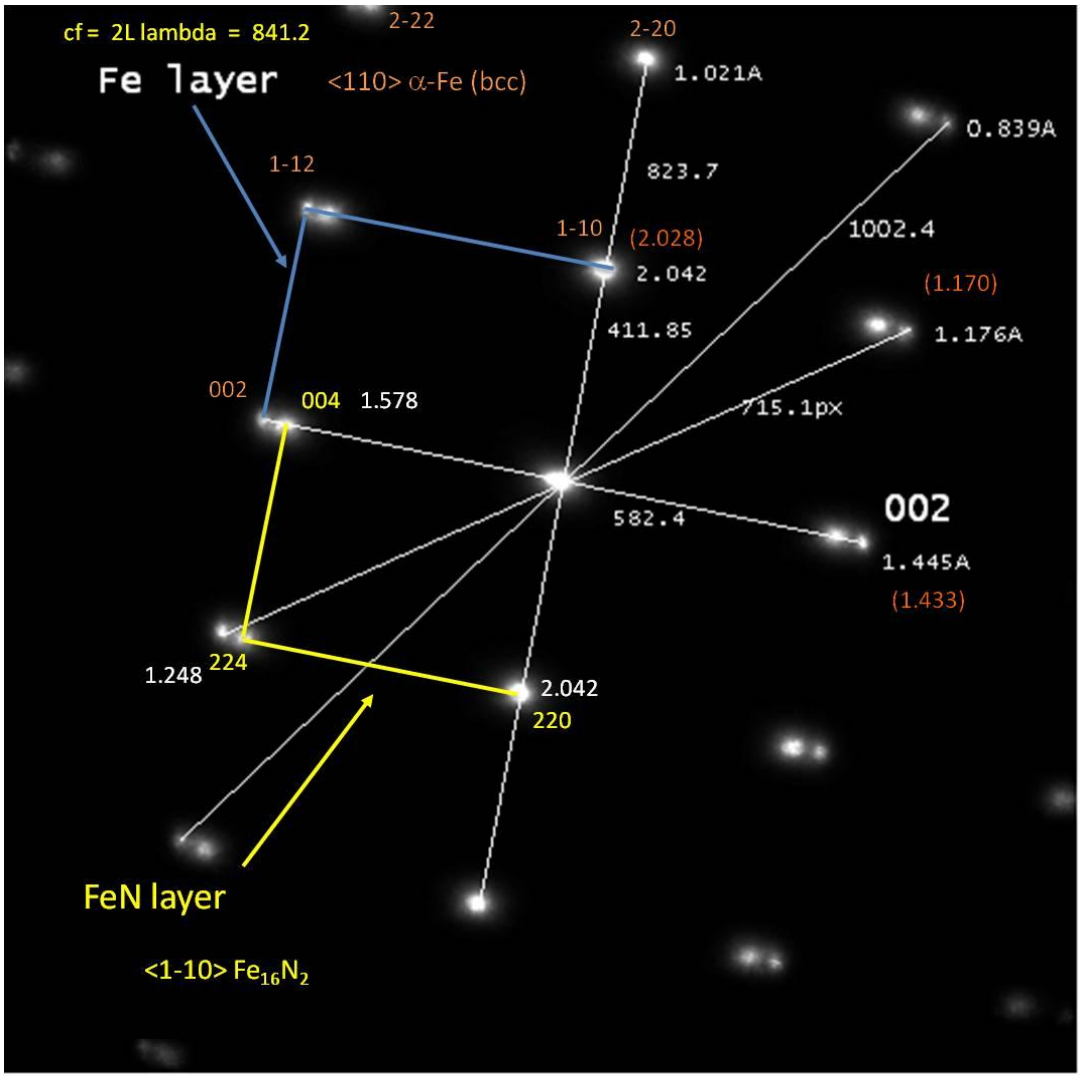

Figure 2.23 A TEM/DP at Fe-N/Fe on a Fe-N sample with lattice constant of each layer calculated and outlined. The camera factor is calibrated using a Fe <110> zone axis with its nominal lattice values.

7) Conversion Beam Electron Diffraction

To confirm the $Fe_{16}N_2$ phase is distributed uniformly and rule out the possible phase segregation. We further conducted conversion beam electron diffraction (CBED) analysis on a cross-sectional film (Figure 2.24). Shrinking the electron beam size to approximately 5 nm and looking at the GaAs/Fe interface (area B), only two diffraction patterns were observed corresponding to GaAs and Fe, respectively. Moving the beam to the Fe layer (region C), only one diffraction

pattern is observable, which can be indexed to the Fe with <110> zone axis. At the Fe-N layer (region D), similar diffraction pattern with different d-spacing along (001) direction is present, while the periodicity along the (110) direction remains the same as that in Fe layer, suggesting the Fe and Fe-N layers are of high epitaxy along the (001) direction.

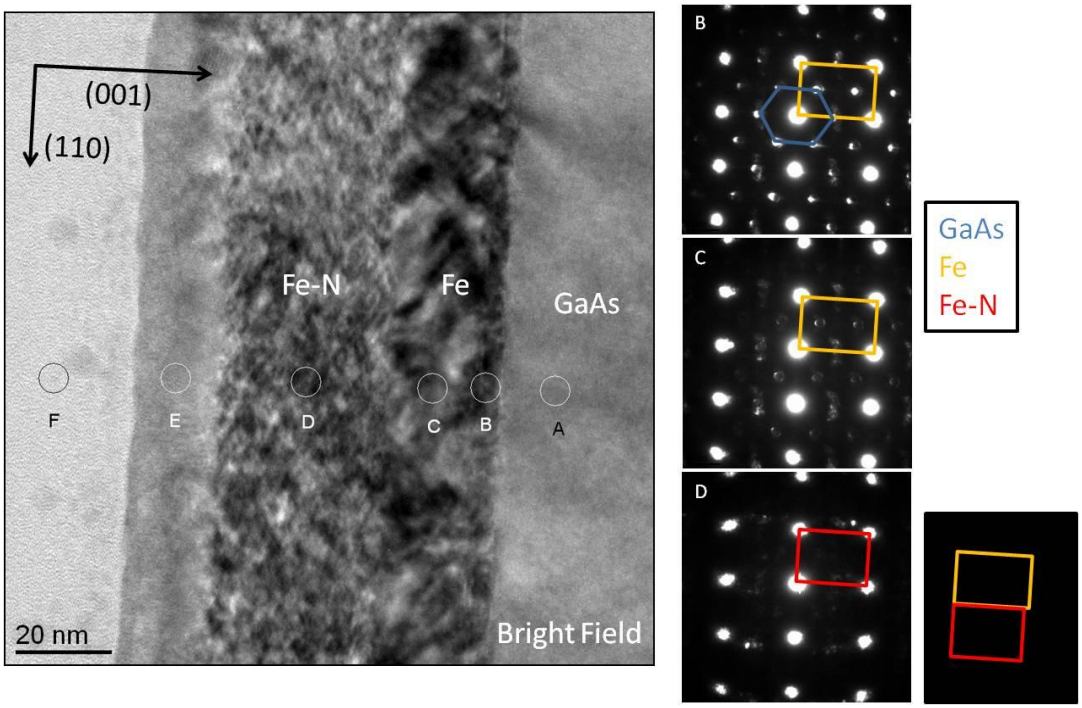

Figure 2.24 CBED analysis of a cross-sectional Fe-N sample. The left figure shows a bright field image and the right panel shows the diffraction patterns at corresponding regions C-D. The diffractions coming from different materials are highlighted correspondingly.

8) Chemical analysis of $Fe_{16}N_2$

To examine the N distribution and verify the stoichiometry of the Fe-N layer, we conducted energy dispersion x-ray (EDX) mapping and Auger electron spectroscopy (AES) depth-profile analysis. Figure 2.25 shows a bright-field STEM imaging and the corresponding energy-dispersive x-ray mapping for each constituent element. These data reveal that N and Fe atoms were distributed homogeneously inside the thin-film region without any segregation at the surface or interface.

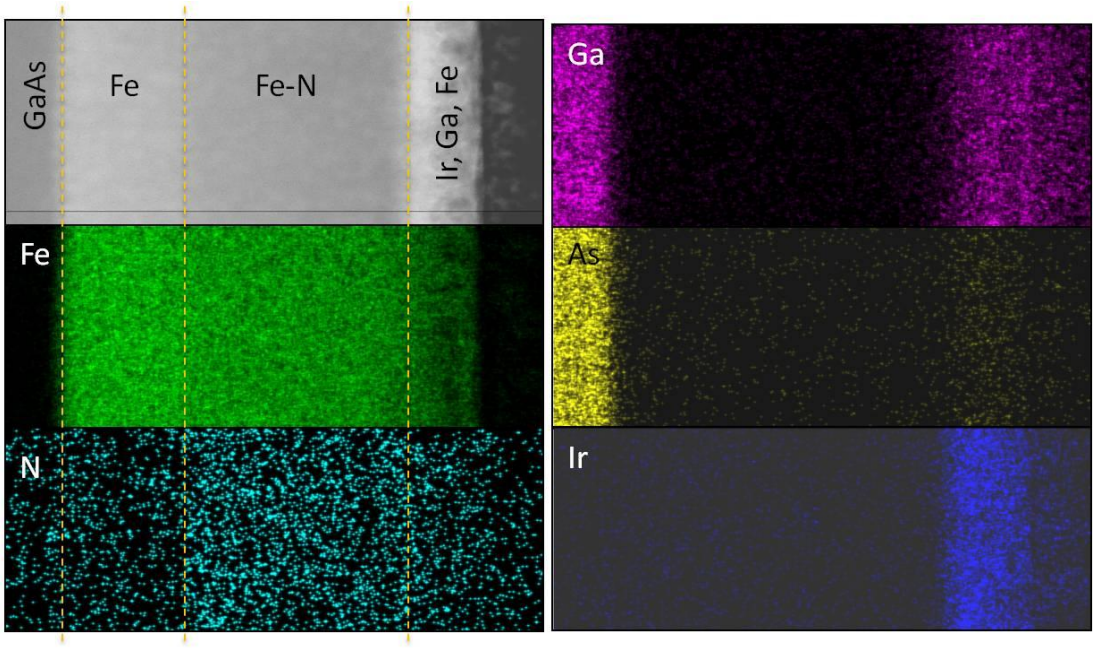

Figure 2.25 Bright field image of a cross-section sample and the corresponding energy-dispersive x-ray spectroscopy mappings for Fe, N, Ga, As and Ir. The presence of a uniform distribution of N in the Fe-N layer is clearly evident.

This observation is essentially consistent with the AES depth-profile measured on a Fe-N sample (Figure 2.26) that Fe and N atoms are distributed uniformly with a relative atomic ratio of Fe/N~8/1. The experiment was conducted on an Auger spectroscopy (Physical Electron Model 545). The element depth profile is measured in UHV condition with a typical sputtering rate of 4 nm/circle. It is also worth mentioning that no impurity elements such as C, O are seen inside the films and no significant inter-diffusion of Fe and GaAs is observable.

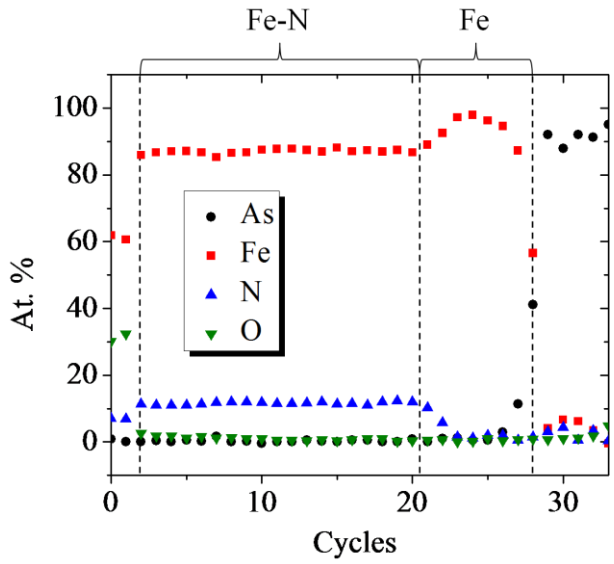

Figure 2.26 Auger electron depth profile on a Fe-N/Fe/GaAs sample for four elements (Fe, As, N, O)

6) XPS study of $Fe_{16}N_2$

We further conducted x-ray photoemission spectroscopy (XPS) measurement on an as-deposited (Fe_8N) sample and a post-annealed sample (partially $Fe_{16}N_2$) in Fe-N layer (figure 2.23), respectively. The experiment was done on a instrument with model Surface Science SSX‑100. The data presented here are measured after sputtering surface oxidizes. The sputtering spot sizes were set to be sufficiently large comparing to the X-ray spot size. The emission current for sputtering was 20 mA and the beam energy was 3 keV. An initial survey scan was recorded prior to the sputtering. The survey scans were also collected after 40 and 70 min sputtering. High resolution scans were recorded after there were no substantial composition changes after the two consecutive sputtering. The overall spectra show single peak at each edge which resembles that of metal Fe. However, the zoom-in look at the L_3 edge resolves differences. In particular, a broader maximum is seen on the $Fe_{16}N_2$ sample, which is different from either the Fe_8N sample or Fe sample. This suggests the presence of multiple Fe valance state in $Fe_{16}N_2$ and will be discussed in detail in chapter IV.

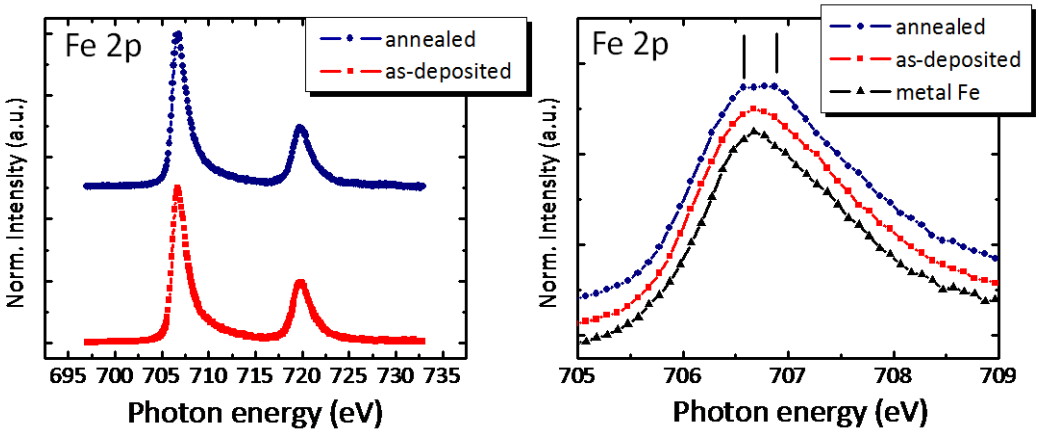

Figure 2.27 XPS measured at Fe2p edge of annealed (Fe16N2) and as-deposited Fe-N samples. It is clear that the absorption spectra of the annealed sample show additional features in contrast to both Fe metal sample and as-deposited nitride sample.

Reference

---

[34] Y. Nimura and M. Naoe. J. Vac. Sci. Technol. A **5** 109 (1987)

[35] Z. H. Qian, Geng Wang, J. M. Sivertsen, J. H. Judy; *IEEE Trans. Magn.*, 33, 3748 (1997)

[36] In-plane lattice constant of $Fe_{16}N_2$ a= 5.72Å, the lattice constant of GaAs is a=5.65Å.

[37] N. Ji, Y. Wu, and J.-P. Wang, *J. Appl. Phys.* **109**, 07B767 (2011)

[38] S. Okamoto, et. al., J. Magn. Magn. Mater., 208 102 (2000)

[39] M. Takahashi, et. al., J. Appl. Phys. 79 (8), 5576 (1996).

[40] C. Ortiz, G. Dumpich, and A. H. Morrish., Appl. Phys. Lett., **65,** 2737 (1994)

[41] M. A. Brewer, K. M. Krishnan and C. Ortiz, J. Appl. Phys. **79,** 5321 (1996)

[42] N. Ji, et. al, Appl. Phys. Lett. 98, 092506 (2011)

Chapter III Magnetic characterization of $Fe_{16}N_2$

3.1 Introduction

The saturation magnetization (M_s) of a bulk material can be easily measured with high accuracy in laboratories using a magnetometer such as vibrating sample magnetometer (VSM) and a superconducting quantum interference device (SQUID). However, for thin films, large error bars are expected for this method. Since the conventional magnetometer based techniques only measures the total magnetic moment of a material. To determine the M_s, it requires the precise evaluation of the sample volume, which is extremely difficult for thin films. Especially, the magnetic contributions of impurities, underlayers or substrates are subtle to assess using these techniques. In the following chapter, we will start our magnetic characterization by using VSM with special emphasis on the error bar estimation. Later on, we will introduce a recently developed new technology – polarized neutron reflectometry (PNR), which allows the direct determination of the in-depth profile of saturation magnetization of iron nitrides thin film samples. In this case, the giant saturation magnetization with $4\pi M_s$ value exceeds 3.0 T is directly observed and confirmed for the first time, which is significantly larger than that of FeCo alloy ($4\pi M_s$ ~ 2.45 T), providing an exciting new fundamental information on this topic that may draw immediate attention in the magnetic research community.

3.2 Determination of M_s using VSM

3.2.1 Evaluation of sample volume

1) Film thickness measurement

We applied three independent methods to measure the sample thickness. X-ray reflectivity (XRR) is used preliminary to resolve the layer structure and their corresponding thicknesses. In figure 3.1, we show a typical XRR data measured on a Pro X'pert x-ray difrractometer for a Fe/GaAs sample and a Fe-N/Fe/GaAs sample.

The data were fitted using instrument associated X'pert XRR software, the error bar of which was mainly attributed to the thickness fluctuation and can be determined by equation $\frac{\Delta t}{t} = \frac{1}{m}$ [43]; where *m* is the total number of visible fringes in the XRR curve, t refers to the thickness of the film and Δt gives the fluctuation of the thickness. This measurement typically yields an uncertainty of 3% in our samples.

To verify that the structural information, we have prepared cross section TEM sample using the same Fe-N film subjected to XRR measurement (figure. 3.1a). The low-magnification bright field image is shown in figure 3.2. The Fe and Fe-N layers can be distinguished by the morphology contrast. The measured thickness for each layer is consistent with the XRR analysis, which confirms its accuracy.

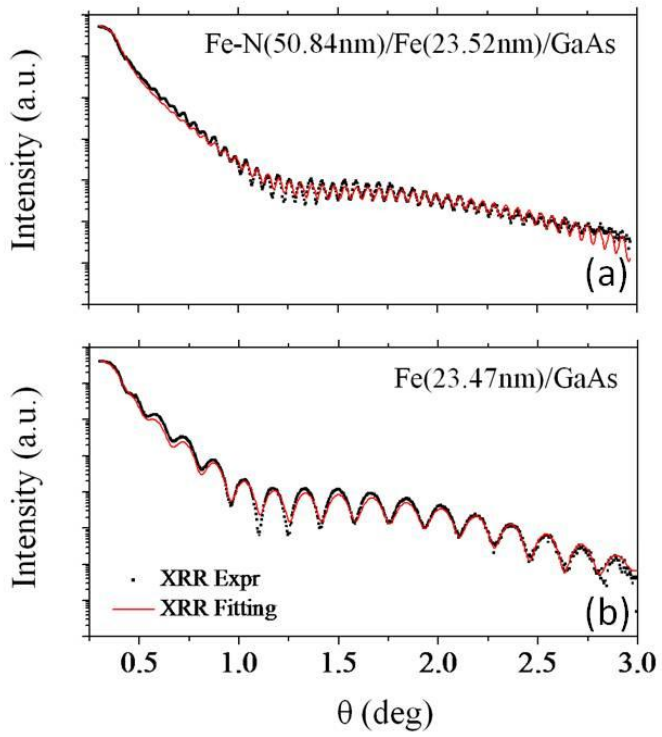

Figure 3.1 Fitted XRR curves for a Fe-N sample (a) and a Fe underlayer sample (b). Experimental data is shown in black dots and fitting data is shown in continues red lines.

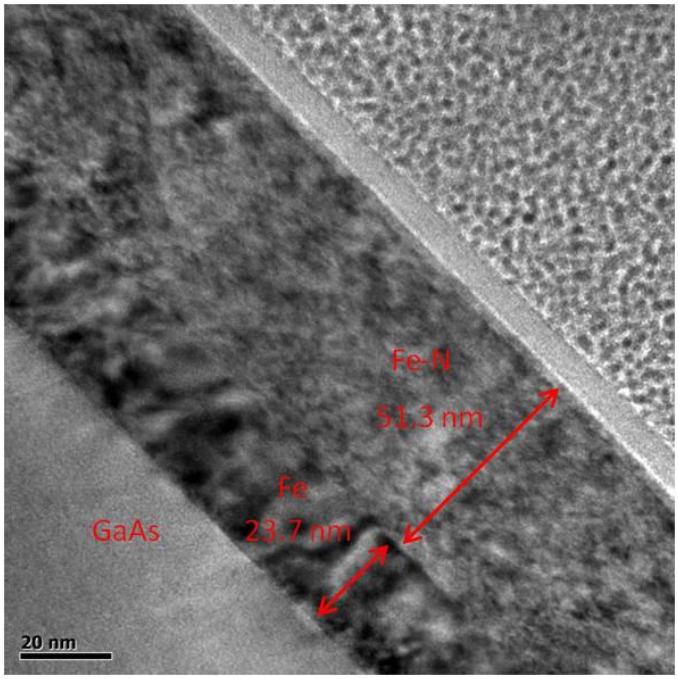

Figure 3.2 A cross-sectional TEM image prepared from the Fe-N sample subjected to XRR measurement in Figure 3.1(a). The layer structure determined here is consistent with the XRR observation.

Furthermore, we have used scanning electron microscopic (SEM) imaging to provide the estimation of the thickness for thicker samples. As the sample thickness exceeds 100 nm, the roughness could introduce large errors for the XRR measurement. In figure 3.3, we show a typical cross-section SEM image of a Fe-N sample. It is noticed that in this case only the total thickness of the sample is measured. The Fe and Fe-N layer structure can not be resolved directly. The error bar in this case is determined by averaging at least 5 measurement at different locations for one sample, which gives a typical deviation of 7%.

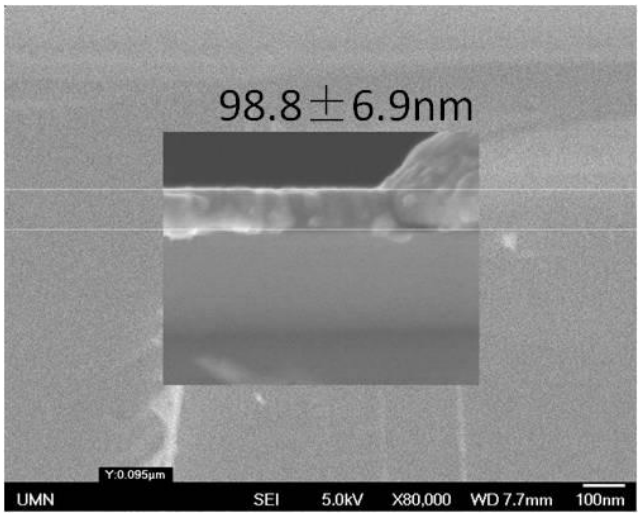

Figure 3.3 A typical cross sectional SEM image of Fe-N sample. The film and substrate can be distinguished by the contrast and therefore the thickness can be measured.

To consolidate the thickness measurement, we have systematically studied thickness dependence of the deposition time of Fe/GaAs films to calibrate the deposition rate. In figure 3.4, the Fe thickness is plotted as a function of deposition time. The sputtering power, Ar pressure and substrate temperature were kept constant during deposition. The trend expectedly shows a linear dependence. In some cases, the thickness of the same sample is cross-checked by both XRR and SEM, which further confirms the accuracy of the thickness measurement.

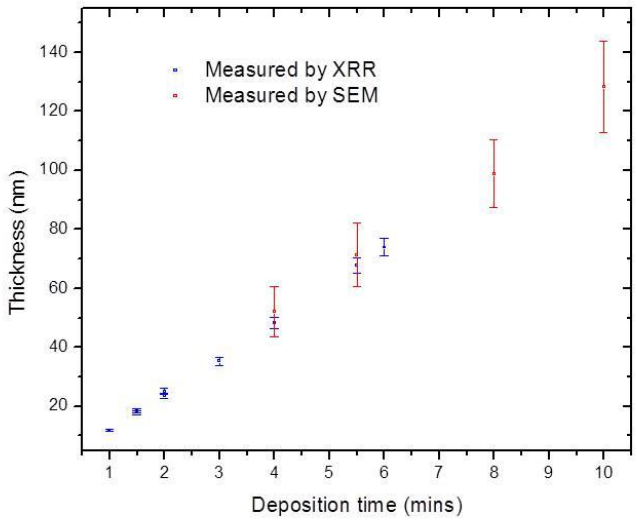

Figure 3.4 The thickness vs deposition time for Fe/GaAs samples. The sputtering power and Ar partial pressure were kept constant for all the samples here. Data labeled by different colors correspond to different measuring tools: XRR (blue) and SEM (red).

2) Sample area measurement

We applied two independent methods to measure the sample area. The difference obtained between these two methods was treated as the error bar of area measurement, which is less than~2%. 1) Samples subjected to VSM measurement were carefully cut into rectangular shape (typically ~5*5mm). Their side-lengths were examined by micrometer with uncertainty (<0.1mm). 2) The total masses of the samples were measured and compared with optical method calibrated GaAs substrate with known area ($1*1cm^2$) and weight. The area of the sample in question was then calculated by the relative weight ratio.

In addition, samples were selectively chosen for ICP testing, in which the samples after the VSM and area measurement are completely dissolved into chemical solution with known volume. By measuring the concentration of Fe atoms, the total amount of Fe atoms as well as the mass of the film was determined. The results are also consistent with the volume of samples measured by the above method

3.2.2 Evaluation of total magnetic moment

1) Sensitivity evaluation

We use the vibrating sample magnetometer (VSM) to measure the total magnetic moment of our thin film samples. The instrument is a Princeton Measurements Vibrating Sample Magnetometer, which allows the cryo options (operating temperature: 10~1025 K). The signal of the films we are measuring typically produce magnetic moment in the range of 10^{-3}~10^{-4}emu. The noise level of the VSM is in the order of 10^{-7}emu in our measurement set-up. The arrangements of

coils and standard calibration are handled by facility staff. The only artificial error introduced by operator is directional displacement which is typically less than 2%[44].

2) Magnetic measurement Calibration

Before measuring our samples each time, a standard Ni bulk sample with a known magnetic moment (44 memu) was used to calibrate the instrument to ensure the instrument is calibrated correctly. In order to subtract the diamagnetic contribution from the measured data and rule out the possibility of any additional magnetic contribution from the impurities within the substrate, M-H loops from a naked substrate were measured. This data was used to be subtracted from the corresponding raw data of the film. In figure 3.5b, we show a typical hysteresis containing both the substrate and film (Fe-N/Fe grown on GaAs) magnetic information measured by applying the external field parallel to the thin film plane. The VSM data of a naked substrate is shown in figure 3.5a, which confirms that the linear background originates from the substrate.

The background subtracted VSM data is shown in figure 3.6. In this case the saturation moment is determined by the maximum magnetic moment the sample reaches at high external field. It is interesting to notice a slope corresponding to a slow saturation of magnetization is seen on these iron nitrides samples, which will be discussed chapter 5 explicitly.

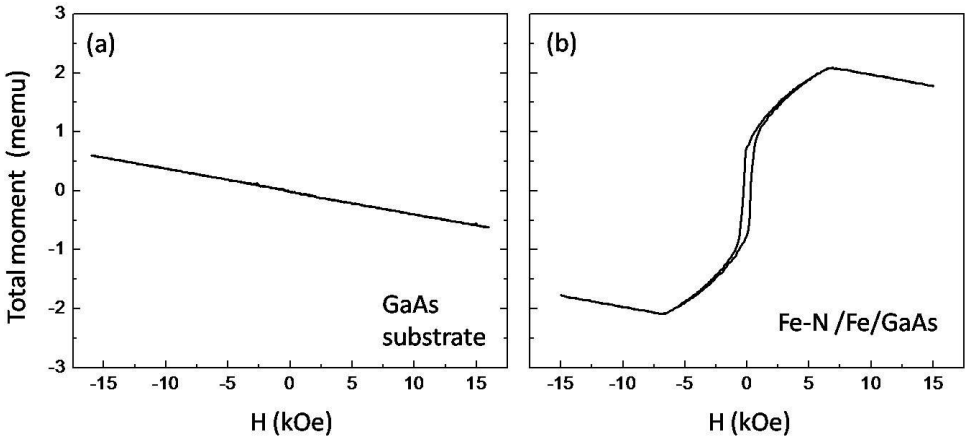

Figure 3.5 The raw hysteresis loops of GaAs substrate (a) and a Fe-N/Fe/GaAs sample (b). The linear background after saturation is attributed to the substrate. The measurement is performed with external magnetic field applied along film plane direction

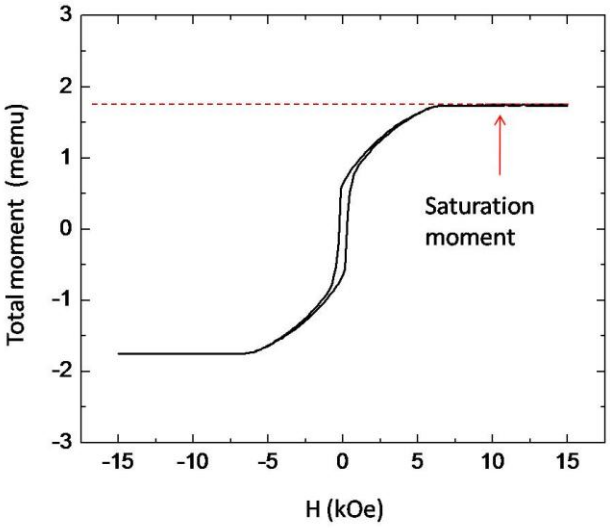

Figure 3.6 M-H loop measured in-plane after subtracting the GaAs substrate information. The saturation moment is defined as the value of the plateau region as highlighted in the figure.

Over all, this saturation magnetization measurement following the XRR+VSM approach will generate an error in the range of 6~7% in general, which is specified in the figure error bar for the magnetic data presented in the following.

3.2.3 The saturation magnetization of Fe buffer layer

As illustrated earlier, to develop high quality $Fe_{16}N_2$ with designated texture, it is essential to introduce an Fe underlayer. In this case, the evaluation of the M_s value for the underlayer crucially influences the M_s estimation of the Fe-N layer. Therefore, we start our characterization by systematically investigate the saturation magnetization of the Fe/GaAs system.

In figure 3.7a, we show a thickness dependent saturation magnetization of

pure Fe/GaAs sample. The $4\pi M_s$ value obtained after averaging different samples falls into the value of around 2.02 T, which is slightly less than the bulk magnetization of Fe metal (2.14 T). This is likely due to the formation of interfacial "dead layer" formed at the GaAs and Fe interface given the relatively high temperature process in preparing the Fe buffer layer. In figure 3.7b, we show the background subtracted hysteresis loop of a Fe/GaAs sample measured in-plane, which shows a typical soft magnetic material behavior.

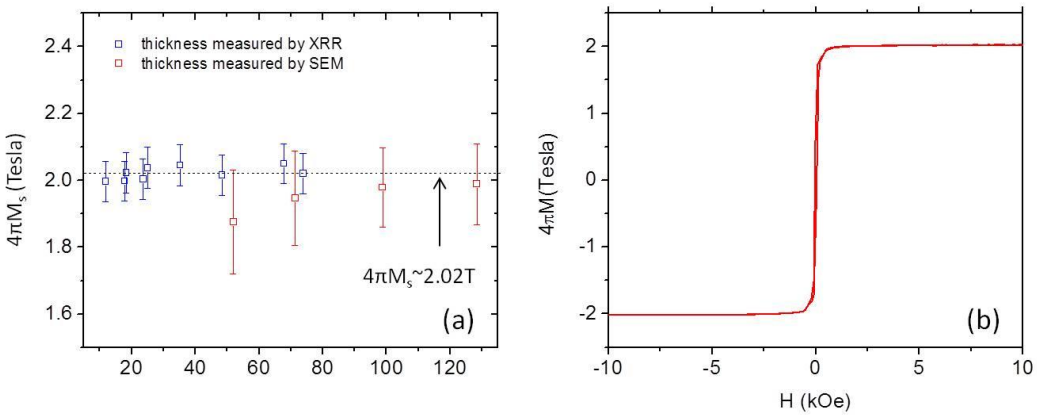

Figure 3.7 (a) 4πMs value of Fe/GaAs samples as a function of film thickness. Data with different colors are due to the different thickness measurement and corresponding to different error bars. (b) A typical M-H loop of a Fe/GaAs sample with Fe nominal thickness of 24 nm.

3.2.4 The saturation magnetization of Fe-N

1) M_s evaluation of various Fe-N phases without annealing

In the previous chapter, we have discussed that by using Fe (001) as buffer layer grown on GaAs (001), a series of Fe-N phases epitaxial films can be obtained. In figure 3.8, we show the saturation magnetization evaluated on as-deposited films with different Fe-N phases or their mixtures according to XRD and VSM results. To determine the saturation magnetization of the Fe-N layer, the saturation

magnetization ($4\pi M_s$) of the Fe buffer layer was assumed to be 2.02 T according to previous characterizations. It is seen that the saturation magnetization of Fe-N follow an interesting trend upon the doping of N in Fe. Starting from pure Fe, the 4πMs value initially drops slowly and followed by a bump at atomic ratio of Fe/N ~8/1, and then decreases. However, the highest $4\pi M_s$ value obtained here is only 2.2 T, which is similar to that of pure Fe.

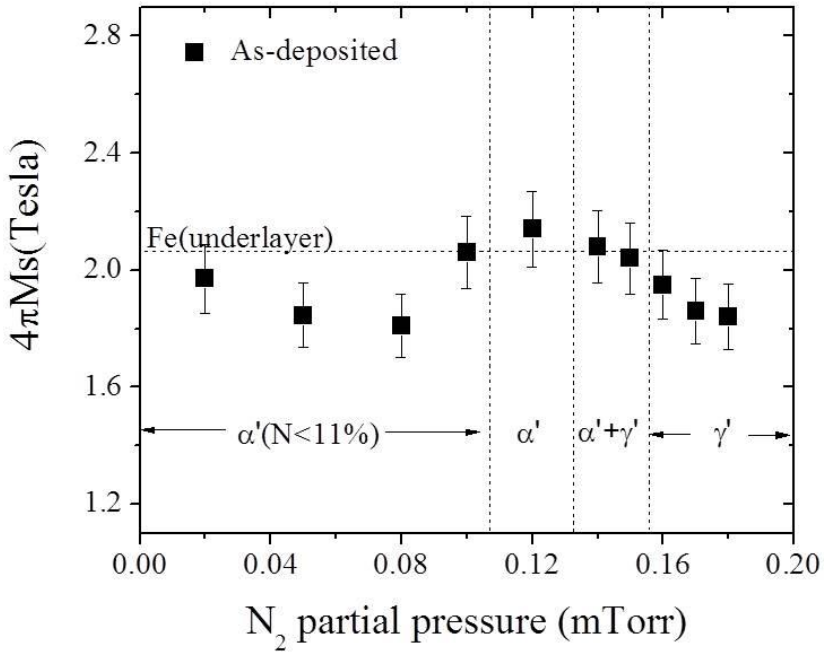

Figure 3.8 Saturation magnetization ($4\pi M_s$) of as-deposited Fe-N layer prepared under different N_2 partial pressure, their phases are separated by different zones according to XRD observation. The $4\pi M_s$ of the Fe underlayer is outlined by the horizontal dashed line. The thickness of Fe underlayer is kept at 24 nm for all the samples

2) Annealing effect

In the previous chapter, it is also demonstrated that by in-situ post-annealing the as-deposited samples at 120 ℃, the chemically ordered $Fe_{16}N_2$ can be achieved. In this case, the α' phases transfer into α" phase. In figure 3.9, we have compared the $4\pi M_s$ of annealed and as-deposited samples. It is clear that a robust enhancement of

the magnetization is observed, which is attributed to the presence of $Fe_{16}N_2$.

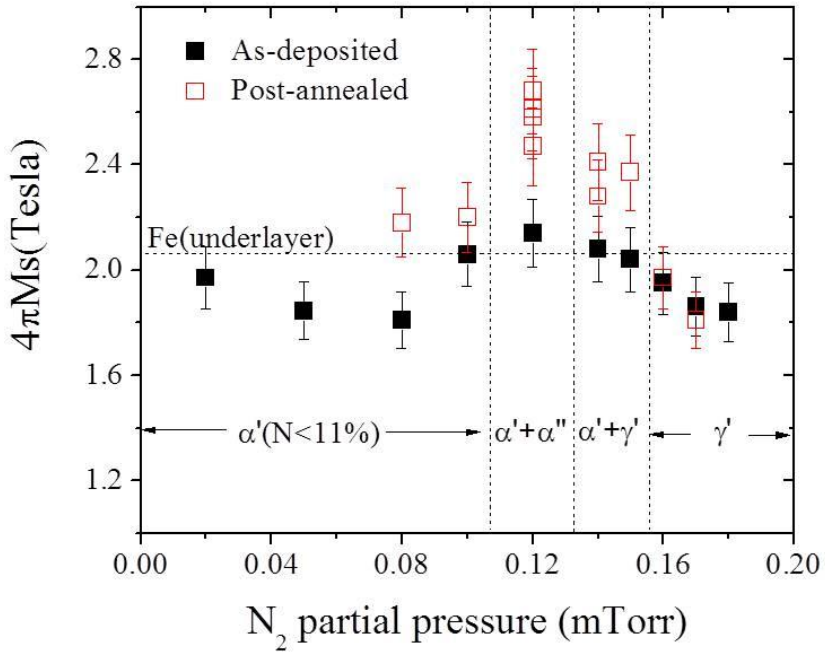

Figure 3.9 Saturation magnetization of as-deposited (black) and annealed (red open square) Fe-N layers prepared under different N_2 partial pressure. The $4\pi M_s$ of the Fe underlayer is outlined by the horizontal dashed line. The thickness of Fe underlayer is kept at 24 nm for all the samples

In particular, for the samples prepared at N_2 partial pressure of 0.12 mTorr. The $4\pi M_s$ value of all the annealed Fe-N layers ranges from 2.6 ~2.8 T, which is much larger than that of FeCo even considering the error bars.

3) N site ordering effect

In the previous chapter, it was illustrated that even α'-Fe-N with the correct atomic ratio Fe/N ~8/1 is achieved. The post-annealing process can only allow the N to be partially ordered with highest ordering parameter of D=0.36 determined from the XRD data. Here by controlling the post-annealing time, it is possible to control the ordering parameter. In figure 3.10, we show the ordering parameter (D) as a

function of annealing time, which has a increasing trend and saturates at around D ~ 0.35, even long time annealing (~40 hrs) is applied.

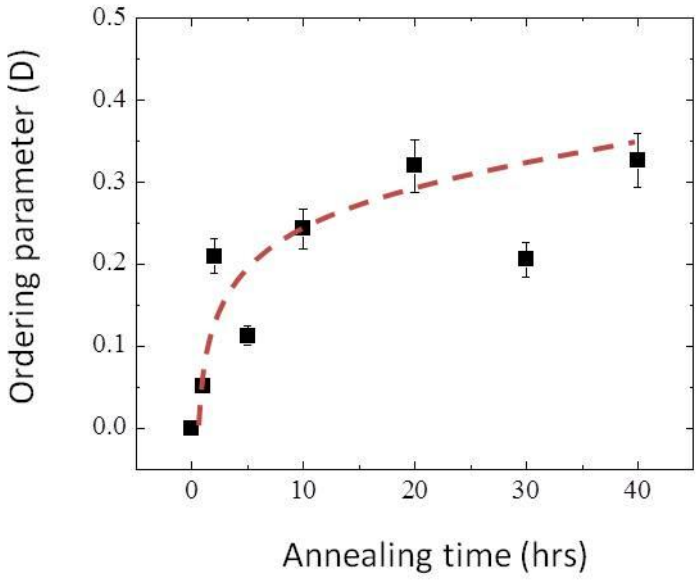

Figure 3.10 Ordering parameter (D) (defined in chapter II) as a function of annealing time. The dashed line is a guide to the eye.

To examine the relationship between the ordering parameter and saturation magnetization of the Fe-N layer, we have plotted a thickness dependent $4\pi M_s$ of annealed α'+α"-Fe-N samples with different degree of N ordering. As shown in Figure 3.11, it is seen as the ordering parameter increases, there is a systematic enhancement of the $4\pi M_s$.

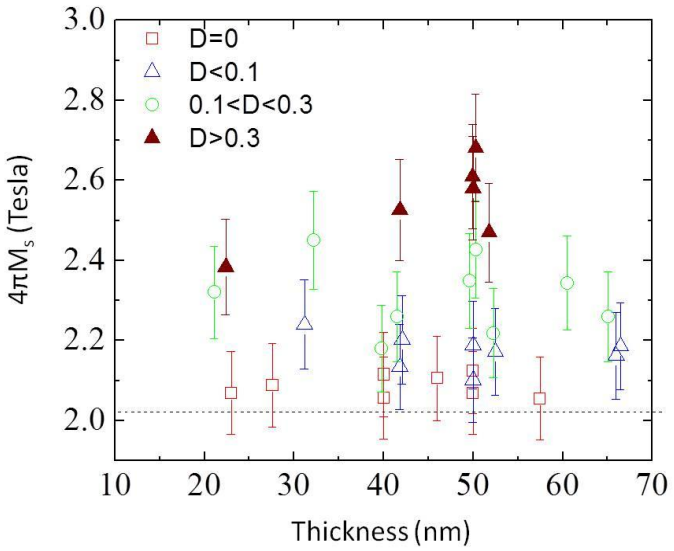

Figure 3.11 Saturation magnetization of partially ordered $Fe_{16}N_2$ with different degree of N ordering as a function of Fe-N layer thickness. he $4\pi M_s$ of the Fe underlayer is outlined by the horizontal dashed line. The thickness of Fe underlayer is kept at 24 nm for all the samples

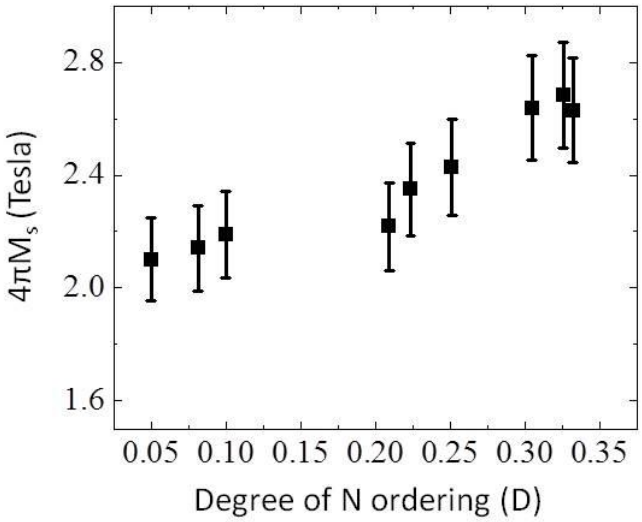

Figure 3.12 Saturation magnetization of partially ordered $Fe_{16}N_2$ with different degree of ordering but a fixed layer structure of Fe-N(50nm)/Fe-N(24nm)/GaAs

In addition, when fixing the Fe-N layer thickness and allowing the degree of

N ordering to progressively change (figure 3.12), a clear correlation between the N ordering and saturation magnetization presents, which suggests that a pure $Fe_{16}N_2$ is of even larger magnetization.

Furthermore, we have conducted a saturation magnetization measurement of annealed and as-deposited Fe-N with the same atomic ratio (Fe/N ~8/1) with different thicknesses. As shown in figure 3.13, an apparent enhancement of the magnetization was seen after annealing the samples for 20 hrs. Also, it is noticed that at the Fe-N thickness range of 40~50 nm. The annealed samples gave highest $4\pi M_s$.

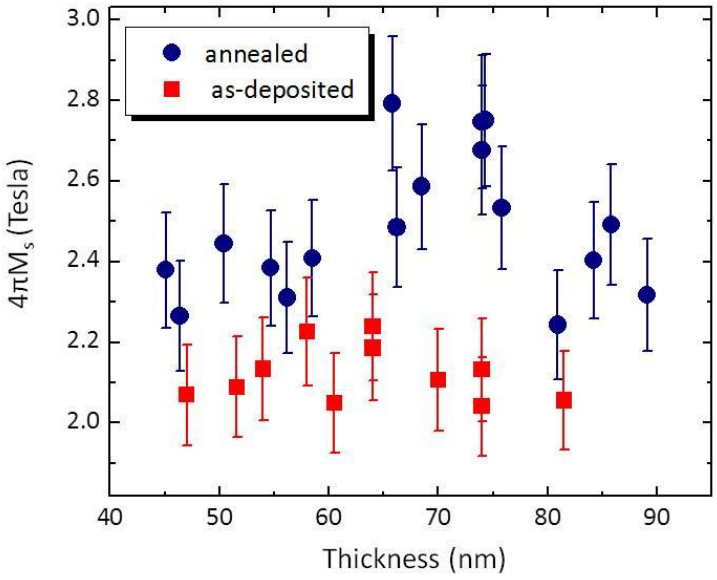

Figure 3.13 Thickness dependence of saturation magnetization of Fe-N layer prepared at optimized N_2 partialy pressure (PN_2 = 0.12 mTorr) before and after annealing for 20 hrs

3.3 Polarized Neutron Refelctometry (PNR)

3.3.1 Introduction of PNR

We first give an overview of the experiments conducted on our Fe-N thin film samples using polarized neutron reflectometry method, focusing mainly on

specular reflectivity geometry and only monitoring non-spin flip scattering events.

1) Working principle of polarized neutron reflectometry

The interaction of Neutrons with Matter

The propagation of a neutron radiation in a material/medium can be presented in according to optical formalism, in which the interaction between the radiation and the medium is described by the reflective index. In the Schrödinger equation, this interaction can be characterized by a potential *V,* which can be written as equation (1) and (2)

$$[-\frac{\hbar^2}{2m}(\Delta + k_0^2) + V]\Psi = 0 \quad (1)$$

$$\frac{\hbar k_0^2}{2m} = \omega \quad (2),$$

where m is the neutron mass, k_0 is the wave vector in vacuum, $\hbar\omega$ is its energy. Therefore, a refractive index can be defined as equation (3)

$$n^2 = 1 - V/\hbar\omega \quad (3)$$

In analogy to the light reflected and transmitted with a change in the direction of propagation at an interface between two media which have different optical properties, the radiation of neutrons also creates reflections at one or multiple interfaces. At each interface, the reflectivity at a potential step obeys Fresnel Equations as shown in Fig. 3.14.

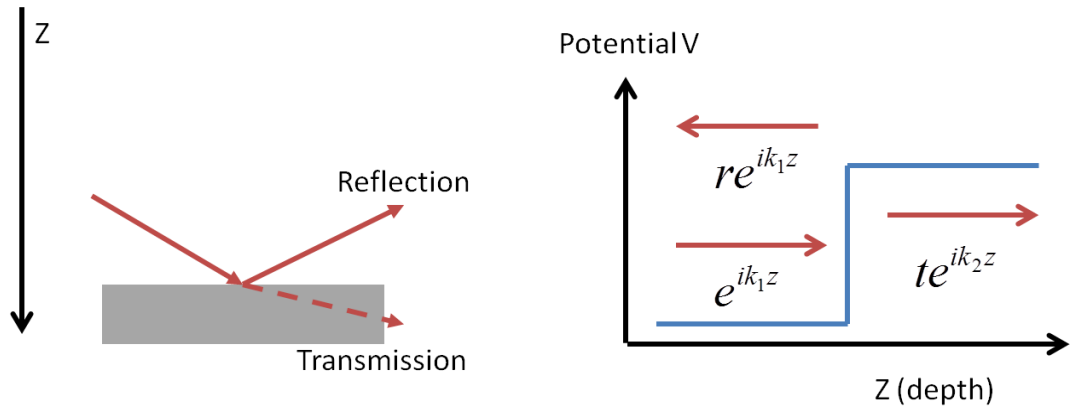

Fresnel Equation:

$$R = |r|^2 = |(k_1 - k_2)/(k_1 + k_2)e^{i2k_1z}|^2$$

$$T = |t|^2 = |2k_1/(k_1 + k_2)e^{i2(k_1 - k_2)z}|^2$$

Figure 3.14 A schematic illustration of neutron interacting with matters at the interface, obeys the Fresnel equations in analogy to the optical formalism.

Specular reflectivity of thin films

For bulk materials, after applying Snell-Descartes' Law, the reflection coefficient at a small incident angle can be written as a function of the wave-vector transfer *q*: (equation (4))

$$R(q) = \left| \frac{q_z - \sqrt{q_z^2 - q_c^2}}{q_z + \sqrt{q_z^2 - q_c^2}} \right|^2 \quad (4),$$

where q_c is the wave vector corresponds to critical angle of total external reflection. It is also easy to show that at high *q* limit, the reflectivity *R*, follows the $1/q^4$ power law. A typical example of the reflectivity curve is shown in Figure 3.15a.

In the case of thin films with a typical thickness of 1~1000 nm, since the neutrons are with wavelength (λ) of a few Å, there are constructive/destructive interference occurring, given the wave nature of the incident neutron beam.

Consequently, reflectivities with periodic oscillations are in presence as long as the Bragg diffraction Law ($2d\sin\theta=\lambda$) satisfies. A typical example of a reflectivity measured from a thin film is shown on figure 3.15b.

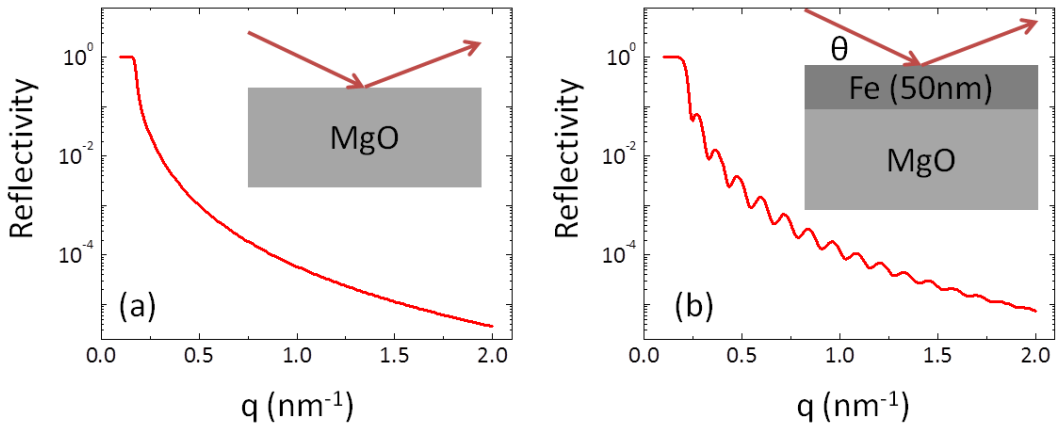

Figure 3.15 Simulated neutron reflectivity curves of (a) a flat MgO substrate and (b) a flat 50 nm thick Fe thin film grown on MgO substrate.

Polarized neutron reflectivity of magnetic thin films

When the incident neutron beams are spin polarized and the thin film material of interest carries the magnetic moment, two interactions, nuclei and magnetic interactions, are both strong enough to be taken into account.

Within the Born approximation, these interactions can be characterized by the Fermi pseudo-potential (equation (5))

$$V_{\pm} = \frac{2\pi\hbar}{m}\rho(b_n \pm b_m), \quad (5)$$

where $V_{\pm}$ denotes the interacting potential for spin-up and spin-down neutrons with mater, respectively; ρ represents number density of the material (atoms per volume), b_n and b_m denote the nuclei and magnetic scattering length. As a result, two different reflectivity curves are obtained as the polarization of the incident neutron beam are switched from spin-up to spin-down.

Figure 3.16 illustrates the scattering geometry of the polarized neutron reflectivity measurement. The spin-up (μ+) and spin-down (μ-) neutrons are defined as spins parallel and anti-parallel to the magnetization direction. The neutron beams impinges on the samples with a grazing incident geometry and generate reflectivities given the different scattering cross section for the film and substrate.

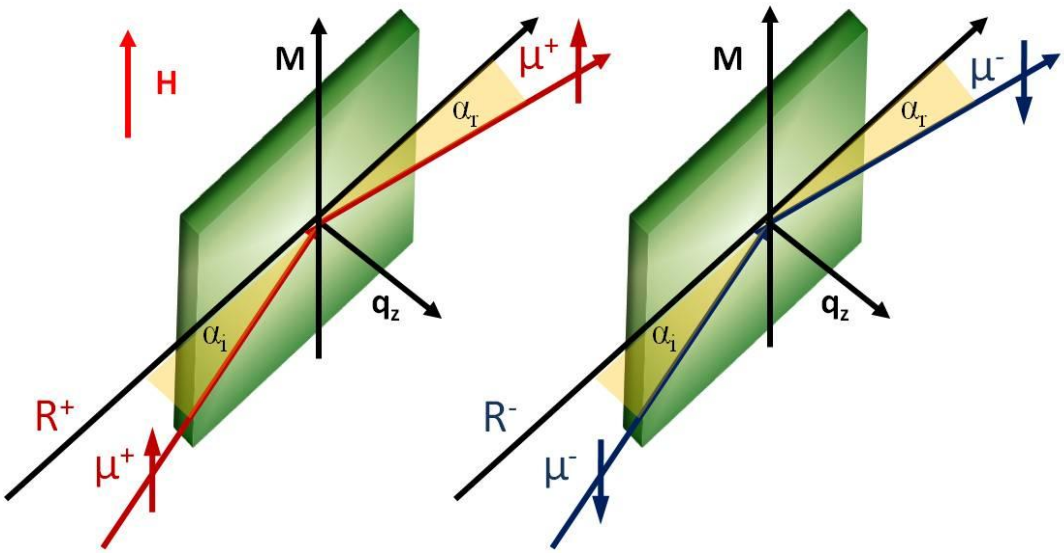

Figure 3.16 A sketch of the scattering geometry of polarized neutron reflectivity. The spin-up (μ+) and spin-down (μ-) neutrons are defined as spins parallel and anti-parallel to the magnetization direction of the sample.

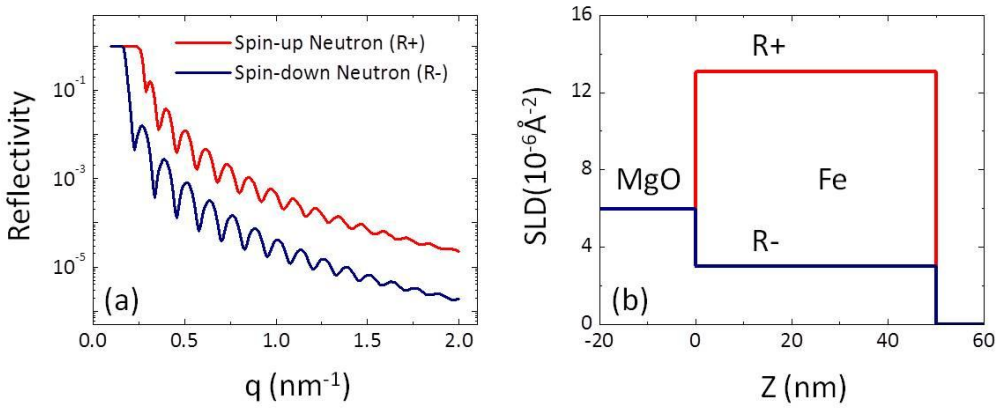

Figure 3.17 (a) The calculated reflectivity curves (R±) of spin-up (down) neutrons for a 50 nm thick Fe grown on MgO substrate in a magnetically saturated state. (b) The

depth-dependent scattering length density (SLD) ($\rho b_{n\pm m}$) according to the reflectivity curves in (a).

3.3.2 Experimental details

1) Experimental set-up

The polarized neutron reflectometry (PNR) experiments were conducted at the Magnetism Reflectometer on beamline 4A at Spallation Neutron Source, Oak Ridge National Laboratory at room temperature[45]. Figure 3.18 shows the image of the instrument. Neutrons from the moderator are guided to the sample position at a distance of 18.5 m via a combination of a short channel beam bender and a tapered neutron guide. A horizontal scattering plane has been chosen to allow more convenient operation of the instrument and auxiliary equipment. Neutrons that are reflected by the sample will be counted by a two-dimensional multidetector at a 20 m distance from the moderator. Polarizing neutron optical elements (polarizer, analyzer and spin flipper) determine the spin-state before and after scattering by the sample (Figure 3.18b). The wavelength is determined by time-of-flight. The instrument is designed for 60 Hz operation. Bandwidth choppers restrict the total bandwidth of neutrons that are incident onto the sample to 3.5 Å when the instrument is collecting data in every time frame. The highest intensity will be available in the second frame (3.5 Å - 7.0 Å). In the PNR, the two curves R+ and R- denote the spins of the neutrons either parallel (R+) or anti-parallel (R-) to the external magnetic field direction ($\mu_0 H$=1.0 T), which is applied in-plane and sufficiently large to saturate the samples.

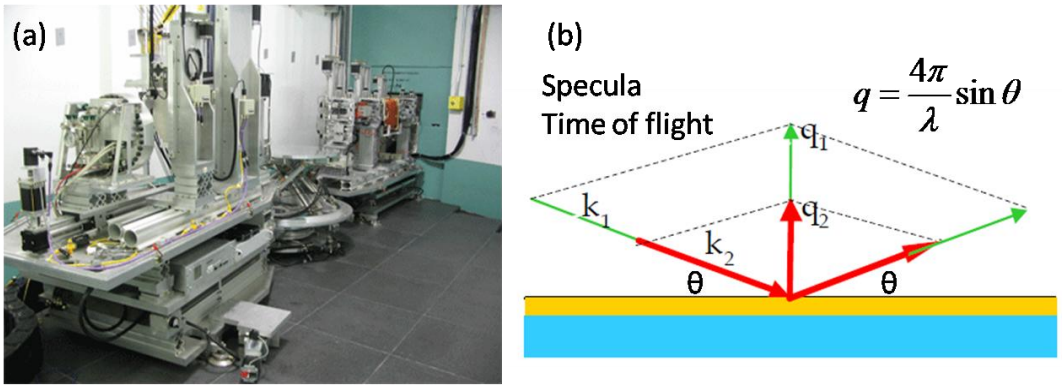

Figure 3.18 (a) A real image of the Magnetism Reflectometer located at beamline 4A at ORNL. (b) A sketch showing the geometry of specular reflectivity with time-of-flight source.

2) Data reduction

For the time-of-flight source, we measure the reflected intensity at several incident scattering angles in ordered to gain a large range in the momentum transfer. This allows us to use the highest intensity of the incident beam and obtain a high polarization. Also it requires the merging of several two-dimensional (2D) intensity maps of reflected and scattered neutrons measured at different incident scattering angles with different spin states for each scattering angle.

An experimental demonstration is shown in Figure 3.19. Using a pure Fe thin film grown on GaAs substrate, the PNR data is acquired in an external field of 1T along in-plane direction. By integrating the specular portion of the neutron intensity for both R+ and R- curves, a plot of reflectivity curves is collected[46].

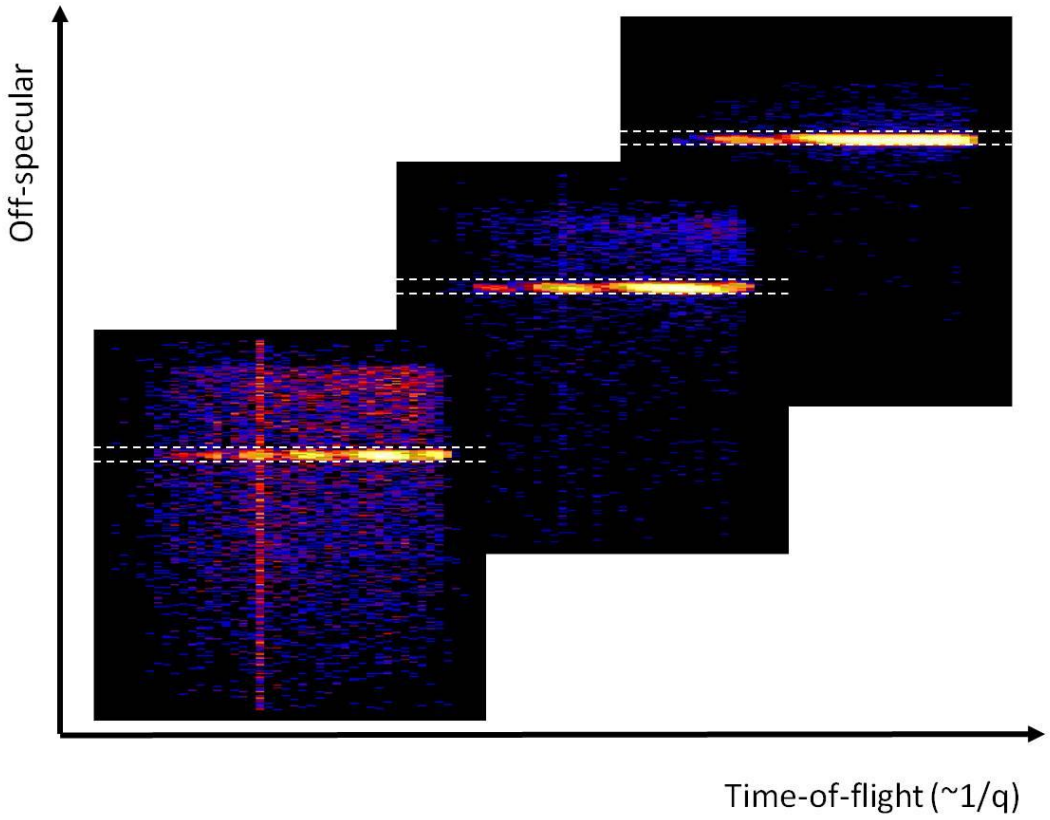

Figure 3.19 Experimental 2D intensity maps of neutrons reflected and scattered by a Fe/GaAs film in an external magnetic field of 1.0 T parallel to the surface of the sample. The intensities within the dashed lines regions are coming from specular reflectivity of spin-up polarized neutron (R+), in which the intensity oscillation are clearly resolved and are used to do the integration when calculating and plotting the reflectivity curves.

3) Reflectivity curves and data analysis

After taking the integral, we re-plotted the neutron specular reflectivity intensity as a function of momentum transfer (q). By fitting the reflectivity data, the depth-dependent structural and magnetic information can then be obtained. We utilized *SimuReflec* to calculate the reflectivity[47]. This program allows to simulate reflectivity curves and to fit experimental neutron data. The multi-layer system has to be described by a series of discrete layers which is performed using an exact recursive matrix calculation model as accurately as possible the physical system. The layers in this model can be characterized by the thickness, the density, the

scattering diffusion length, the magnetization, the direction of their magnetization, the roughness, the in-plane correlation length and a critical exponent describing the fractal dimension of the roughness.

3.3.3 Characterization of Fe samples using PNR

To set the stage for the discussion of iron nitride thin films, we first studied the depth-dependent saturation magnetization of pure Fe samples fabricated on GaAs substrate. The samples are prepared by facing target sputtering method[48] . The crystalline and texture quality are checked by x-ray diffraction, which show epitaxial relationship of Fe(001)/GaAs(001). The polarized neutron reflectivity curves (non-spin-flip) are collected at room temperature with an external field of 1.0T to ensure that it is in a saturated state as plotted in figure 3.20 (a). The scattering length density (SLD) model used to successfully fit the data is shown in figure 3.20 (b) with nuclei and magnetic SLD plotted as functions of film depth. In the simulated curves, four layers (specified in figure) are used to reproduce all the essential features of the obtained data. To further account for the non-uniformity due to the oxidation towards the surface, the film body part is sub-divided into three slabs in which the roughness, structural and magnetic SLD are allowed to modulate freely. As expected, the top and bottom interface show distinguished SLD in comparison to that of the film. In the thin film, as it approaches the top interface, both the NSLD and MSLD decreases gradually, due to the oxidation towards the surface. As it approaches the bottom interface, the magnetic SLD shows slow saturation and levels off at the value close to that bulk Fe metal.

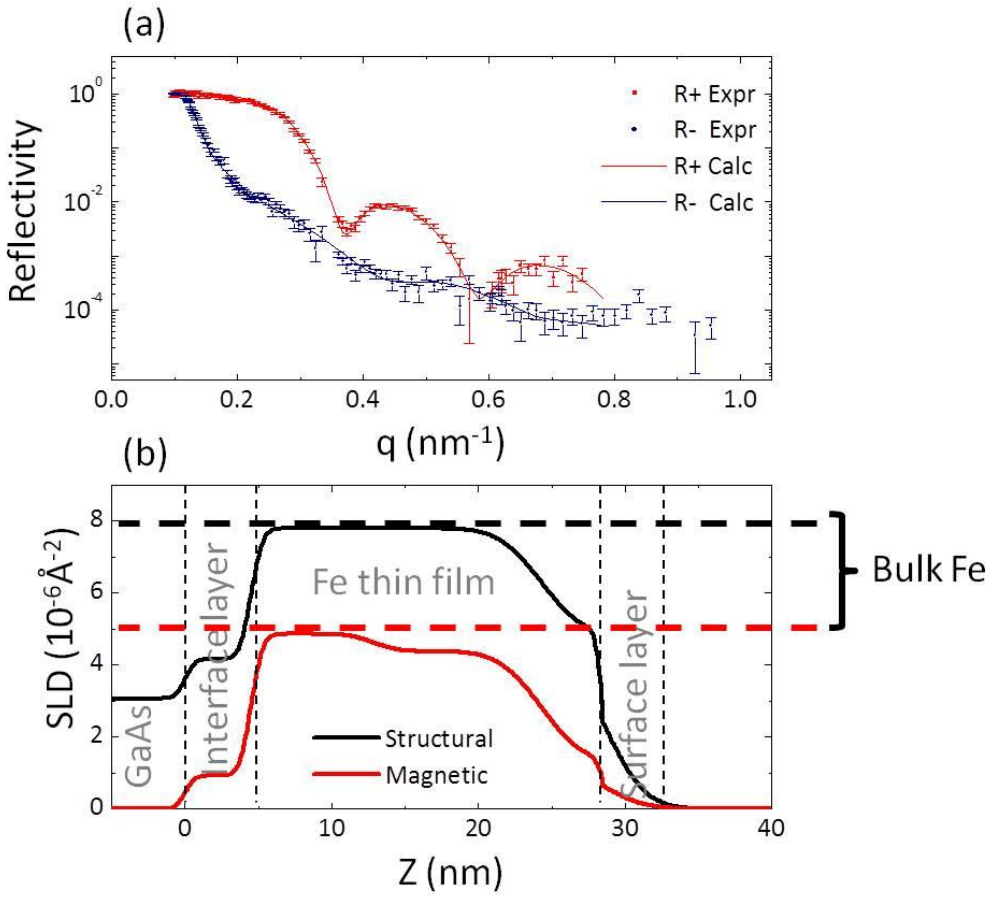

Figure 3.20 (a) Fitted (lines) and measured (dots) non-spin-flip polarized neutron reflectivities (R+ and R-). (b) Scattering length density models used for the fitting. The different layer structures are labeled in the figure. The horizontal dashed lines indicate the NSLD (black) and MSLD (red) of bulk Fe.

3.3.4 Direct observation of giant M_s in $Fe_{16}N_2$ thin films

The iron nitride samples for the PNR experiments were prepared by first depositing a thin Fe layer with nominal thickness of 2 nm on GaAs (001) single crystal substrate at an ambient temperature of ~300 ℃. The Fe-N layer was subsequently grown by sputtering thoroughly mixed Ar and N_2 gases at room temperature. The x-ray diffraction (XRD) and transmission electron microscopy studies reveal the formation of body-centered tetragonal Fe-N martensite epitaxially adopted on GaAs(001). Fine-tuning of the N_2 doping rate results in the formation of

stoichemtry Fe/N=8/1 as feedback from Auger electron depth profile. After an in-situ post-annealing treatment at substrate temperature of 120 ℃ on the as-grown samples, chemically-ordered $Fe_{16}N_2$ phase can be favored with its degree of N site ordering controlled by the amount of annealing time, which is varying from 5hrs to 20 hrs.

For the Fe-N films, the PNR experiments were performed under the same conditions as the reference Fe film. The results obtained for four samples with different annealing time treatment are shown in the figure 3.21a-d. Looking at the reflectivity curves of each sample, in addition to the difference of the periodicity of the fringes due to the thickness variation, it is noticed that as the annealing time progressively increases, the oscillation magnitude gradually evolves, which is especially robust for the R- curve. In particular, for the as-grown sample, the reflectivities show pronounced oscillations in contrast to that of the 20 hrs-annealed sample, where the reflectivities become very smooth and without well-defined oscillations. Because of this behavior, fits to the data reveal difference in the depth-dependent magnetic properties of these films.

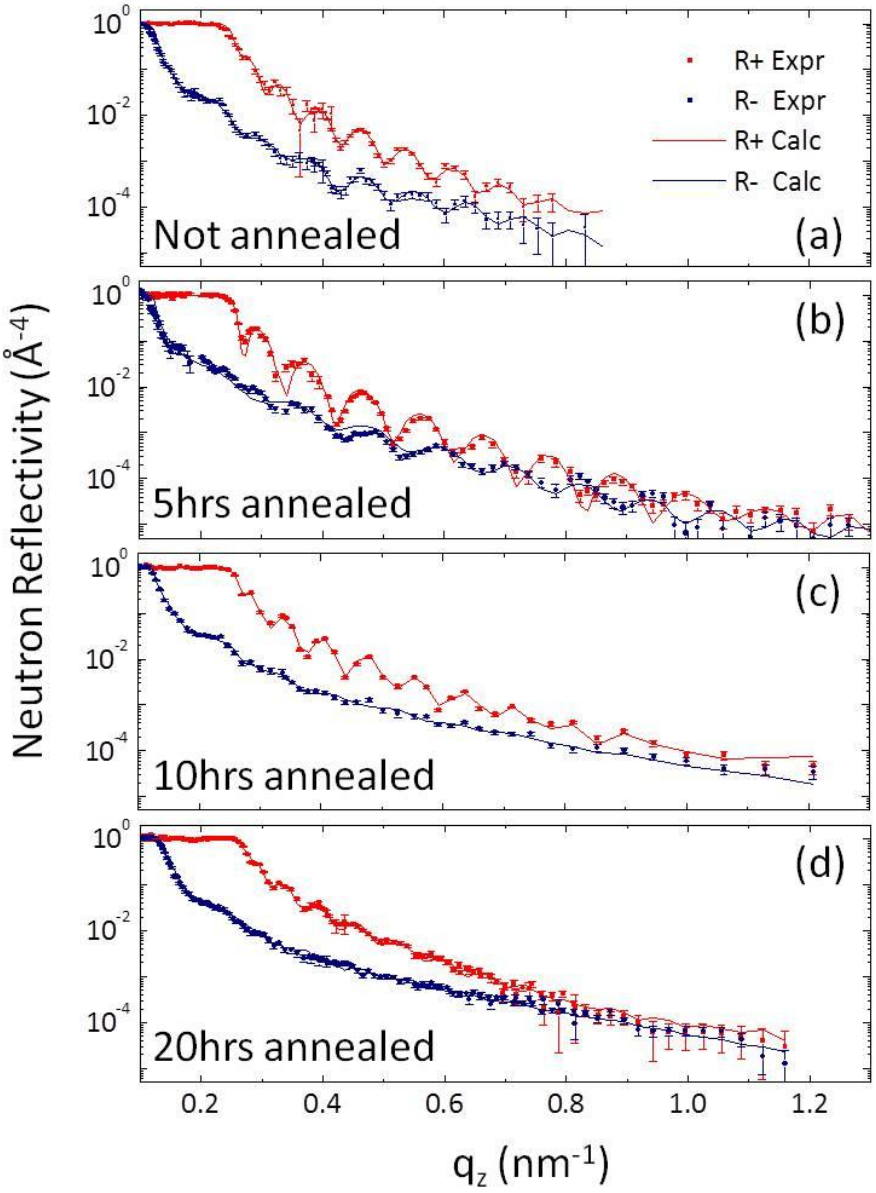

Figure 3.21 (a)~(d) Measured PNR reflectivities obtained from Fe-N samples after different annealing time treatment as outlined in the figure, along with fitting curves to the data. .

Figure 3.22 shows the fitted depth profile of the four samples with different amount of annealing time. The top panel shows the NSLD depth-profile as functions of the distance from the substrate of the four samples, the configurations of which is consistent with the structural analysis by XRD and are rather uniform through the thickness except a "bump" at the bottom interface between film and substrate, corresponding to the seed Fe layer.

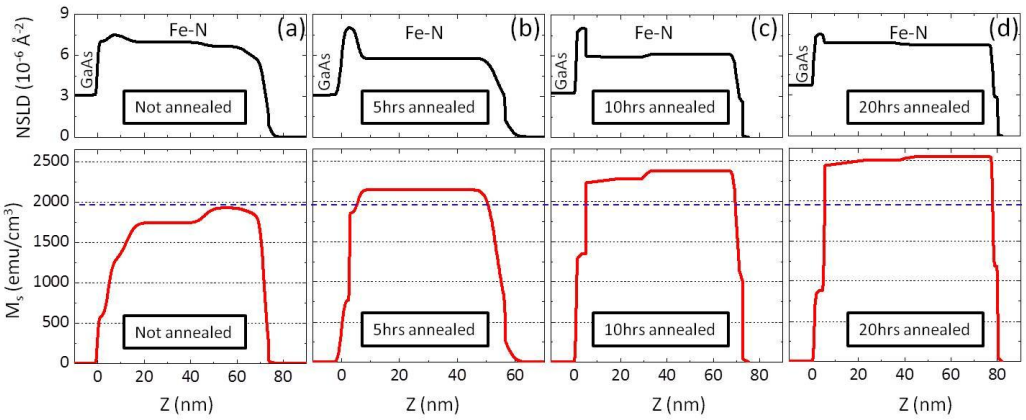

Figure 3.22 Nuclear (top panel) and magnetic (bottom panel) scattering length density depth-profiles as functions of the distance from substrate for each film after different annealing time. The MSLD is presented on the left hand side and the magnetization in cgs unit (emu/cm^3) is shown on the right hand side of the figures. The blue dashed line represents the reference M_s value of $Fe_{65}Co_{35}$ for comparison.

The striking results of the MSLD profiles are shown in the bottom panel of Fig. 3.22 bottom panel. For all the annealed samples, the M_s substantially exceed that of $Fe_{65}Co_{35}$ (~1900 emu/cm^3 outlined by dashed blue line). As we progressively increase the annealing time, the Ms of the bulk part of the samples enhance significantly and uniformly, reaching up to Ms ~ 2500 emu/cm^3. In our previous report[49], it is observed that the degree of N site ordering is correlated with the annealing time according to XRD analysis. Therefore, the obtained results prove that the enhancement of M_s after a longer annealing time is due to the increasing amount of chemically ordered $Fe_{16}N_2$ phase, which is consistent with the previous magnetometry analysis.

Furthermore, we compared our neutron results with the bulk magnetization data obtained using VSM magnetometry. As shown in figure 3.23, we have tested five samples of pure Fe film, as-prepared Fe-N film and three Fe-N films with different annealing time treatment. The extracted magnetizations from both measurements are in good agreement.

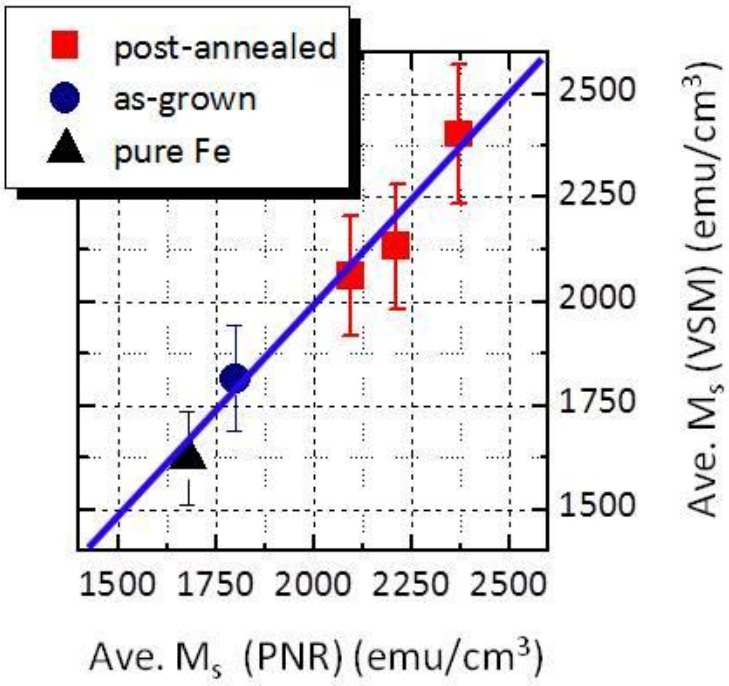

Figure 3.23 Comparison between VSM and PNR results on average saturation magnetization value obtained for five different samples: pure Fe film, as prepared Fe-N films, three Fe-N after different annealing time. The blue line plots the ideal case when the two measurements (PNR and VSM) yield same results.

3.3.5 N inter-diffusive effect of Fe-N magnetism

Since the PNR technique can allow the depth dependent magnetization characterization of thin films, we have purposely prepared the following samples to study, in which case, the $Fe_{16}N_2$ is prepared through a process of N inter-diffusion into crystalline Fe. In this case, part of the sample develops $Fe_{16}N_2$ phase with giant M_s up to 2360 emu/cm^3 directly observed.

In this case, we studied annealed Fe/FeN and $[Fe/FeN]_2$ samples on GaAs substrate. It was found that a giant M_s can be established, which is attributed to the ordered occupation of N in the interstitial sites upon N inter-diffusion and consequently, the formation of $Fe_{16}N_2$ phase at interfacial regions after a long time post annealing (20 hrs). Distinguished from any previously reported synthesis

processes of $Fe_{16}N_2$ films that involving heated substrates or phase-transformation of the as-deposited Fe_8N films into $Fe_{16}N_2$, here the N is purposely overdoped in FeN layer, which was found close to amorphous status before annealing. The subsequent annealing process allows the N diffusion into its adjacent strained Fe crystalline layer to form $Fe_{16}N_2$ phase (figure 3.24a).

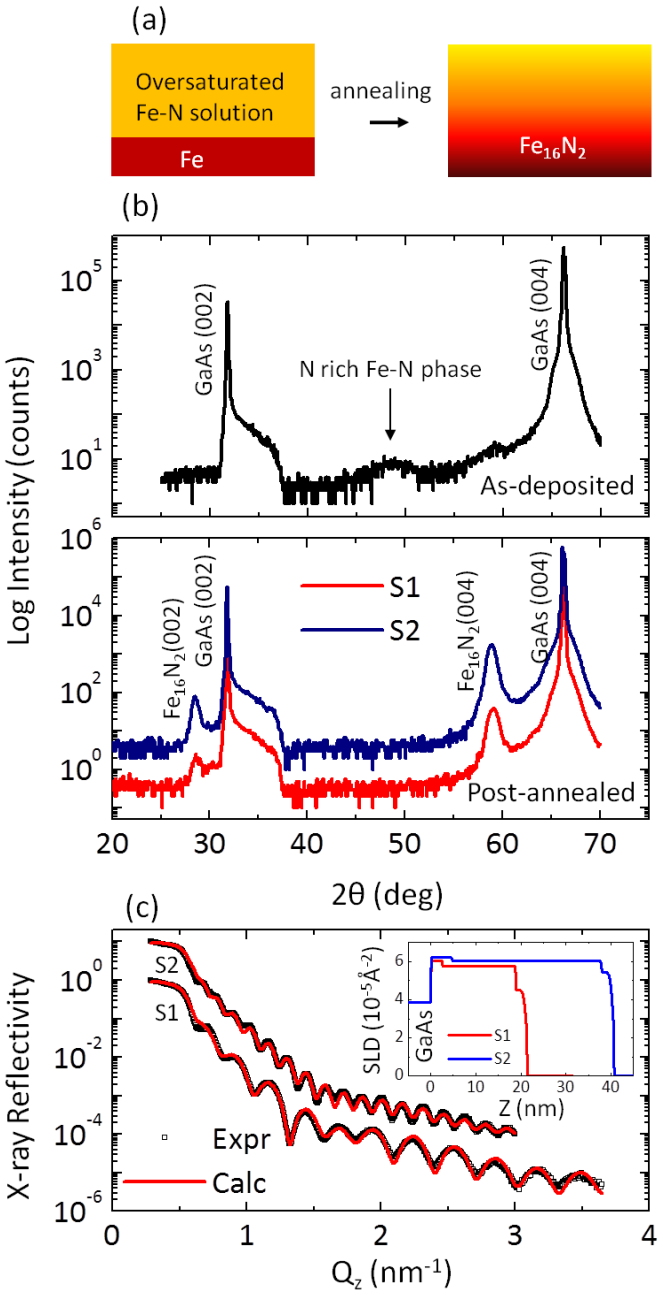

Figure 3.24 (a) A schematic illustration of the formation of $Fe_{16}N_2$ due to the N diffusive process. (b) XRD θ-2θ scans of sample S1 and S2 (c) Fitted GIXR data of sample S1 ad S2.

(Data vertically shifted one order of magnitude for clarity). The inset shows depth-dependent x-ray SLD used in fitting the experimental data

The bi-layer Fe/Fe-N structured sample (labeled as S1) was prepared by first depositing a 2 nm Fe on GaAs (001) surface at substrate temperature of 250 ℃, then cooling down to room temperature and adding another 12 nm Fe-N layer by sputtering Fe targets with thoroughly mixed $Ar+N_2$ with an excess of N_2 partial pressure.[50]. The four-layer (Fe/Fe-N)x2/GaAs structure sample (labeled as S2) was similarly obtained by first depositing a 2 nm Fe on GaAs (001) at 250℃, then adding sandwiched structure of Fe-N(12nm)/Fe(2nm)/Fe-N(12nm) when cooling down to room temperature. The x-ray diffraction (XRD) measured on the as-deposited bi-layer sample (Figure 3.24b top panel) reveals a broad bump ranging from 45°~ 52°. This can be attributed to the presence of N rich Fe-N phase and is nearly amorphous, which is similar to the previous report on amorphous Fe-N system[51]. After post-annealing the as-deposited films at substrate temperature of 120 ℃ for 40 hrs, the XRD results of the final products were shown in the bottom panel of Figure 3.24b. Both the annealed bi-layer (labeled as S1) and annealed four-layer (labeled as S2) samples develop similar XRD pattern and can be indexed to a partially ordered $Fe_{16}N_2$ phase.

The low-angle grazing incident x-ray reflectivity (GIXR) curves are shown in Fig. 3.24c for both samples (S1 and S2), which were subsequently analyzed to retrieve the in-depth structural information. The calculated reflectivity curves that best reproduce the experimental data are shown with their x-ray scattering length density (XSLD) depth profiles plotted in the inset. When fitting the reflectivity curves of both samples, a single layer model is used to successfully reproduce the experiment data, indicating a uniform chemical structural through the depth direction. The XSLD of the substrate is fixed to match up with that of a nominal GaAs ($3.84x10^{-5}Å^{-2}$), the SLD of the film expectedly reproduced that of bulk Fe ($5.88\ x10^{-5}Å^{-2}$)[52].

Figure 3.25 shows the non-spin-flip (NSF) specular reflectivity as a function of wave vector transfer [$Q= (4\pi/\lambda)\sin\theta$, where θ is the incident angle on the film and λ is the wave length in (nm) of the neutron beam] measured on samples S1 and S2 (the exact same pieces as measured by GIXR) at room temperature. In the PNR data, the two curves R+ and R- denote the spins of the neutrons either parallel (R+) or anti-parallel (R-) to the external magnetic field direction ($\mu_0 H$=1.0 T), which is applied parallel to the sample plane and sufficiently large to saturate the samples during the measurement.

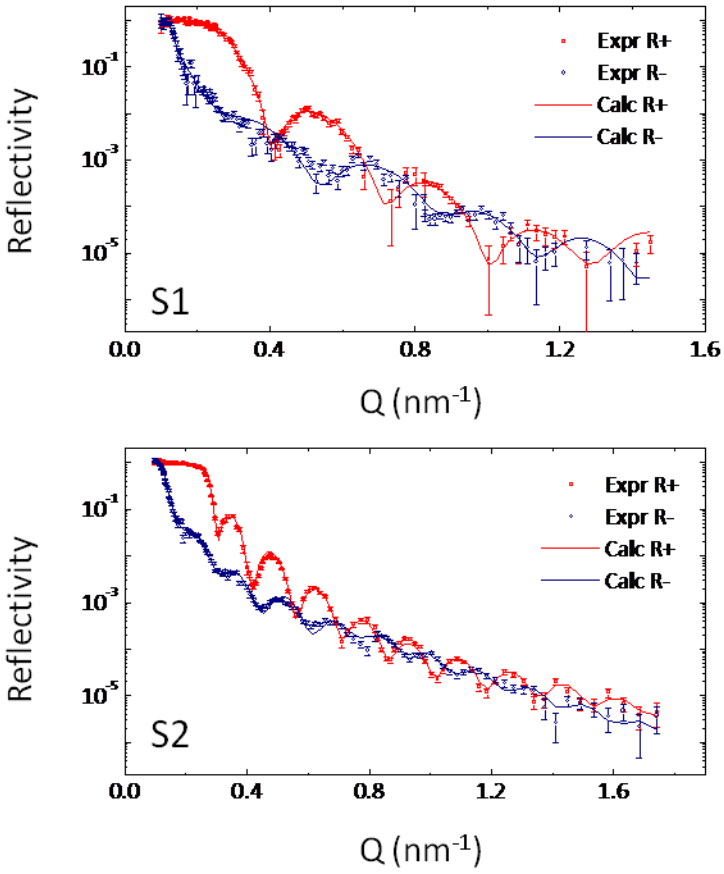

Figure 3.25 Fitted spin-up (R+) and spin-down (R-) polarized neutron reflectivity curves for sample S1 (top) and S2 (bottom), respectively

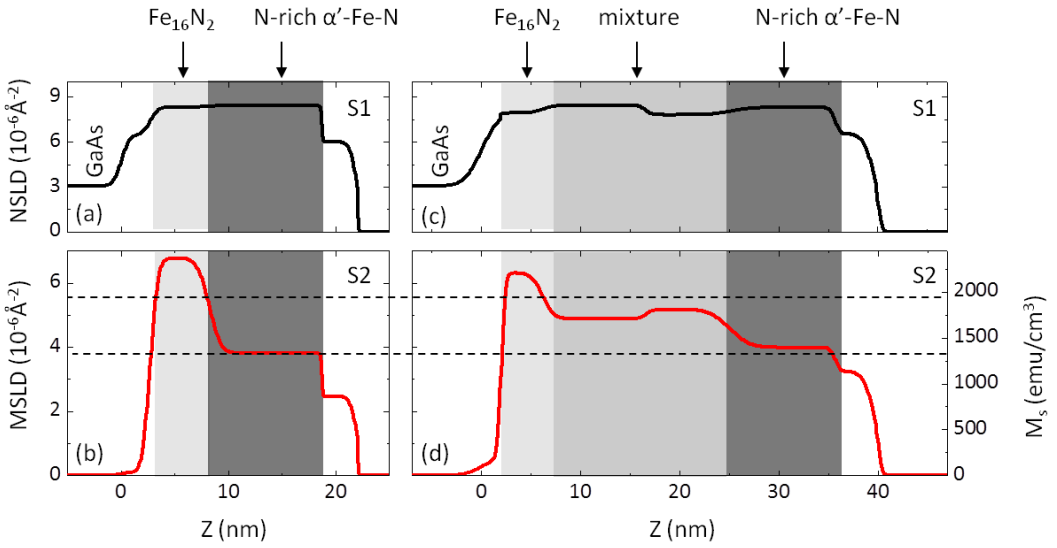

Figure 3.26 Magnetic (bottom) and structural (upper) SLD for sample S1 (a) (b) and S2 (c) (d). The dashed lines represent the Magnetic SLD of Fe65Co35 (currently known as the material with highest saturation magnetization so far). The regions correspond to different phases are outlined and explained in text

It is known that co-refining the x-ray and neutron reflectivity curves allows an unambiguous determination of magnetic depth profile[53, 54]. Therefore, in modeling the chemical part (nuclear scatter length density (NSLD)) of the PNR results, we set the initial structural information (two layer model for S1 and four layer model for S2) to be uniform and resemble that of the GIXR results, allowing marginal adjustment during fitting process. This finally gives minor but appreciable discrepancy of NSLD between layers (top panel in figure 3.26), which is expected due to the comparable scattering cross-section between N and Fe for neutron probe. In addition, the observation also suggests the N concentration at the layer interfacial region is lower than that in the Fe-N layers before annealing.

The key results are presented in the magnetic scattering length density (MSLD) depth profiles (green lines in Fig. 3a and b). There are several interesting features. It is clear that in sample S1, at the bottom interface between substrate and film, the MSLD reaches 6.76 $x10^{-6}$ $Å^{-2}$, corresponding to a M_s of 2360 emu/cm^3 [55]

and stabilizes within a thickness region of 50~70 Å, which is remarkable and substantially larger than that of $Fe_{65}Co_{35}$ (5.7 x10^{-6} $Å^{-2}$). Towards the top interface, the magnetization quickly drops and reaches a plateau with M_s calculated to be 1300 emu/cm^3. This value is much smaller than the bulk value of Fe which is about ~ 1700 emu/cm^3 and cannot be solely attributed to the disordering effect of N in the stoichiometry identical Fe_8N+$Fe_{16}N_2$ system, in which the M_s is in general at least larger than 1700 emu/cm^3. More likely, this reduction of M_s is due to the presence of some N-rich Fe-N phase that exists near the top interface given the synthesis procedure and enhancement of NSLD at corresponding regions. It is also appealing to notice that magnetic interface between high and low magnetization region is very sharp, suggesting two well separated iron nitride regions along the direction of surface normal, in which we ascribe them as $Fe_{16}N_2$ and N-rich Fe-N, respectively. In sample S2, similar magnetic configuration is also observed. A reduced but still "giant" magnetization resides at the bottom interface (MSLD =6.35x x10^{-6} $Å^{-2}$), corresponding to the M_s of 2200 emu/cm^3. However, different from sample S1, the transition region is much gradual and at the interface between Fe and Fe-N towards the top, a broad peak feature is seen for the magnetic SLD, showing the enhancement of magnetization at this region, accompanied with a slightly enhanced plateau with M_s = 1380 emu/cm^3 at the top interface. Since structural analysis based on x-ray diffraction suggest the only possible Fe-N phases are α"-$Fe_{16}N_2$ and α'-Fe-N martnesites on both samples, these observations can be only appreciated by considering the formation of mixture phases consisting of $Fe_{16}N_2$ and N-rich amorphous Fe-N in the region as highlighted, likely due to the complicated strain effect given the multiple interfaces in contrast to that in sample S1.

It is also worth mentioning that a single layer model with both MSLD and NSLD to be uniform throughout the film fails to describe the essential features of the reflectivity curves measured on the present samples. To further facilitate this discussion, we compared PNR data of sample S1 with that of a pure Fe reference sample, which is grown on GaAs substrate using the same method. Plotted in Fig.

3.27a are the fitted PNR curves for pure Fe film and sample S1. Besides the apparent difference of oscillation periodicity given the thickness deviation, an apparent discrepancy is seen at the R- reflectivity curves between these two samples. In the Fe-N sample, the fringe features of the R- curve are much robust in S1 in contrast to that in Fe sample. Since the magnitude of the oscillation is proportional to the contrast of SLD between film and substrate, these observations suggest that in the Fe film, for the R- curve, the SLD is similar for the film and substrate. However, this is not the case in the sample S1. As illustrated in Figure 3.27 b and c, a relatively uniform SLD with its value calculated to be close to that of GaAs substrate is seen from the R- SLD profile of the Fe sample. In contrary, a complicated structure is obtained in describing the R- reflectivity curve of sample S1.

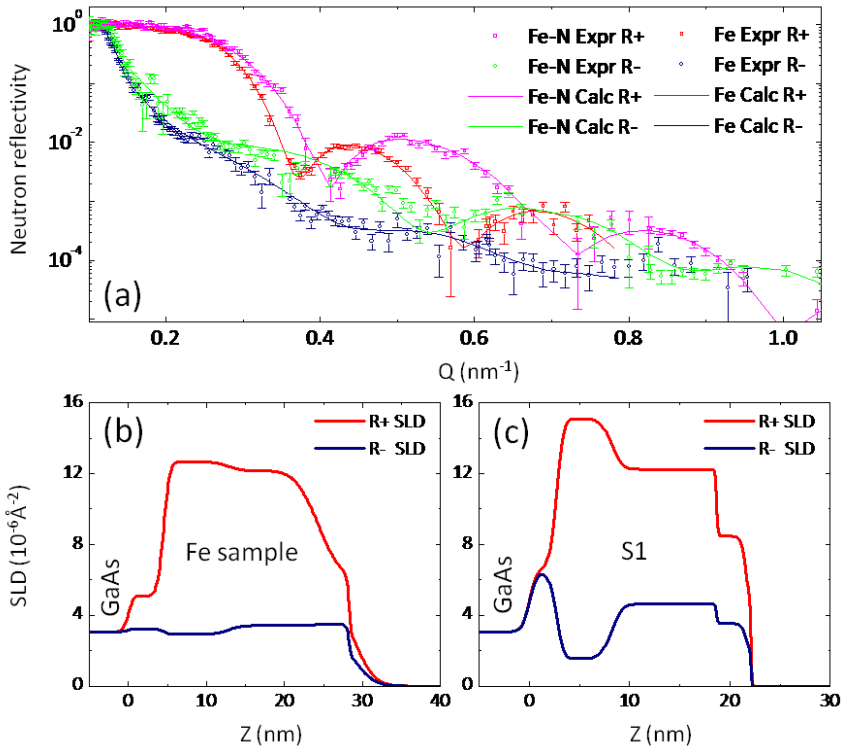

Figure 3.27 (a) Fitted spin-up (R+) and spin-down (R-) polarized neutron reflectivity curves for Fe reference sample and Fe-N sample (S1). (b) and (c) show calculated R+ (red) and R- (blue) SLD for Fe and Fe-N samples respectively.

3.3.6 Ex-situ annealing experiments of Fe-N samples

In all the previous annealing experiments, the analysis was performed by comparing different samples with and without in-situ annealing. In this section, we have compared the PNR data of the same iron nitride samples prepared on GaAs substrate before and after post-annealing treatment. All the measurement and heating treatment were carried out on the PNR stage. Similar non-spin-flip (NSF) PNR reflectivity curves are firstly collected on one sample with a nominal structure of Fe-N (50nm)/Fe (20nm)/GaAs prepared by facing target sputtering at room temperature as shown in Figure 3.28aa. After the initial measurement, the stage temperature gradually ramped up to 150℃ for 1 hour and cooled down to room temperature for the second PNR measurement (Figure. 3.28b). When this measurement is finished, we heated up the substrate to 150℃ and annealed the sample for another 4 hours (5 hours anneal in total). The Figure 3.28c shows the PNR data collected when cooling the sample back to room temperature again after all the above treatment. An external magnetic field of ~1.0 T was applied in-plane all the time, which is large enough to saturate the sample.

While the R+ reflectivity shows somewhat similar oscillations for both films, the three R- curves show relatively different features especially at the low q region. For the PNR data of the as-grown sample, the first fringe of the R- curve locates at the moment transfer close to that of the critical angle position of the R+ curve. By comparison, the data of the annealed sample shows a consistent shift of the fringe position towards the lower q value as the annealing time progressively increases. It is known that the reflection coming from the top interface (film/air interface) dominates the behavior of the reflectivity curves near the critical angle. Therefore, the observation suggests that the film top surface experienced substantial structural or magnetic modification after the annealing treatment.

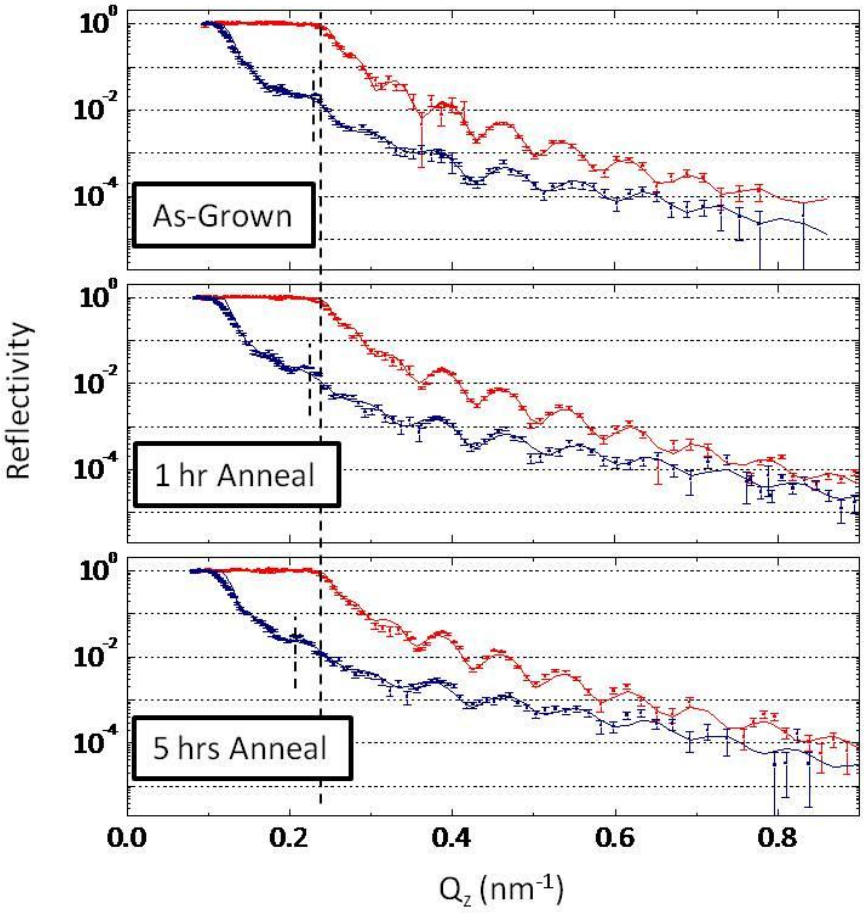

Figure 3.28 Measured NSF polarized neutron reflectivities for the as-grown, 1 hr annealed and 5 hrs annealed film, along with fits to the data from the corresponding SLD model.

The SLD models used to satisfyingly describe the data is shown in Figure 3.29. With nuclei and magnetic SLD plotted as a function of film depth, as suspected, it is immediately noticed that with nuclei SLD closely resemble each other, the magnetization of the top ~10 nm show dramatic enhancement after annealing treatment, with an initial value of ~2.3 T to 2.7 T after 5 hrs annealing. This is significantly larger than that of the material ($Fe_{65}Co_{35}$~2.45 T) with the highest saturation magnetization known so far. We attribute the observed high M_s to the presence of $Fe_{16}N_2$. This suggests the chemically ordered $Fe_{16}N_2$ can be favored towards the top interface after ex-situ annealing the chemically disordered Fe_8N.

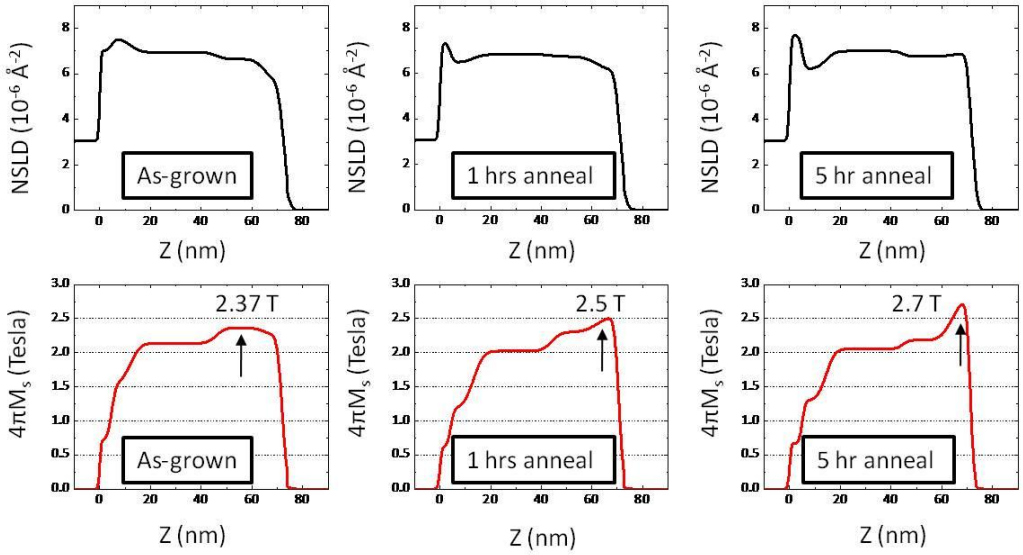

Figure 3.29 Nuclei (top) and magnetic (bottom) scattering length density models for the same film after each thermal treatment. The magnetization is proportional to the magnetic SLD and is shown in SI unit.

3.3.7 Epitaxy and lattice mis-fit effect on the saturation magnetization ($Fe_{16}N_2$ grown on MgO substrates)

In this section, we demonstrate that, using epitaxy and mis-fit strain imposed by an underlying substrate, the in-plane lattice constant of $Fe_{16}N_2$ thin films can be tailored to create favorable conditions for exceptionally large saturation magnetization. Combined studies using polarized neutron reflectometry and x-ray diffraction show that with increasing epitaxial strain at the interface, the M_s of these films can be changed over a broad range, from ~2.1T (non-high M_s) up to ~3.1T (high M_s). We suggest that this wide tunability of the magnetization is associated with the delicate choice of the ground state energy between high spin and low spin configuration, which can be adjusted by the sensitive modulation of the crystal lattice.

As shown in figure 3.30, MgO (100) substrate can provide epitaxy with a lattice misfit of 4.2% and creates a tensile strain in the Fe-N lattice. Therefore, by

tuning the Fe underlayer thickness, the strain condition of the $Fe_{16}N_2$ can be manipulated.

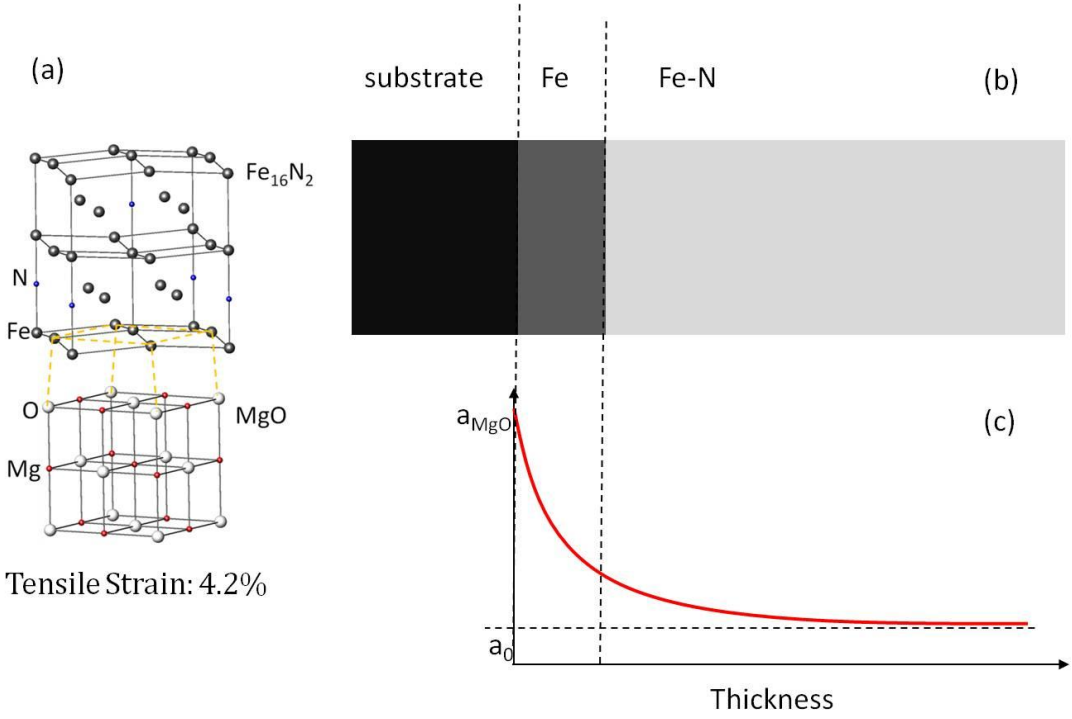

Figure 3.30 (a) Crystal structure and epitaxial relationship between $Fe_{16}N_2$ and MgO substrate. (b) and (c) show the lattice relaxation process through the in-depth direction. By tuning the underlayer thickness, the strain condition of the $Fe_{16}N_2$ can be controlled

Encouraged by this discussion, after massive trial, we have developed a recipe to grow epitaxial $Fe_{16}N_2$ on MgO substrate. The idea of controlling the stain is schematically shown in Figure 3.30 by growing $Fe_{16}N_2$ epitaxially on Fe buffered MgO substrate. Since the lattice mis-match between $Fe_{16}N_2$ and Fe is about ~(-0.3%), which is much smaller than that between Fe and MgO (4.2%). Therefore, by changing the thickness of Fe buffer, it is possible to *fine tune* the in-plane lattice as well as the strain in the $Fe_{16}N_2$. To demonstrate the strain effect, two samples with the following structures grown under otherwise same conditions are purposely studied, (labeled as S1 and S2) with nominal thickness structures shown below:

S1: *Fe-N (40nm)/ Fe (2nm)/ MgO*

S2: *Fe-N (40nm)/ Fe (20nm)/ MgO*

The *θ-2θ* XRD scan was shown in figure 3.31a. It is seen that both samples exhibit similar (00*l*) orientation, with an out-of-plane lattice constant of 6.28 Å. Other than diffractions from substrate and buffer layer Fe (002), the peaks developed at 58.8 ° and 28.6 ° can be indexed to $Fe_{16}N_2$ (004) and $Fe_{16}N_2$ (002), respectively. Consistent with previous reports on similar samples that the integrated area ratio of diffraction peaks from (002) and (004) planes does not reproduce what would be expect from single crystal pure phase $Fe_{16}N_2$. The current samples typically produce a degree of N site ordering (D) in range of 0.26±0.15. This is likely due to the relatively short range ordering of the (002) diffraction in contrast to that of (004) diffraction, which can be estimated from the rocking curve measurement figure 3.30b that the mosaic spreading of the (002) peak (Δθ~1.5°) is three times as large as that of (004) peak (Δθ ~0.6°).

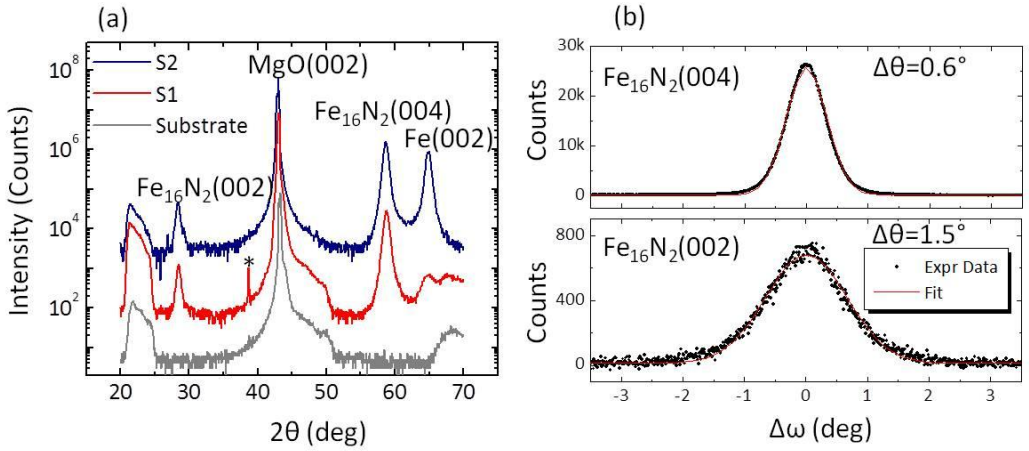

Figure 3.31 (a) High angle x-ray diffraction data on sample S1: Fe-N (40nm)/Fe (2nm)/MgO and S2: Fe-N (40nm)/Fe (20nm)/MgO. The peak labeled by (*) comes from the CuKα2. (b) Gaussian fitted Rocking curves measured on Fe16N2 (002) and (004) of sample S1 respectively.

To verify the idea of the strain control, grazing incident x-ray diffraction (GIXRD) was performed on both samples and plotted in Figure 3.32a. Aligning the

scattering vector along the MgO (200), the observed peak in the neighborhood of 44.8 ℃orresponds to $Fe_{16}N_2$ (220) and is coherent with the underlayer Fe (110). It is clear that the peak ($Fe_{16}N_2$(220)/Fe(110)) from thicker sample (S2) shows notable shift toward the higher angle with respect to that of the thinner one (S1), suggesting that the average in-plane lattice constant is longer in S1 than that in S2. Typical Φ scan (Figure. 3.32b) shows regularly distanced four peaks with 90 º spacing, suggesting an expected 4-fold cubic symmetry with the full width of half maximum (FWHM) of 1.16 ° (Inset in Figure. 3.31b), which is comparable to monocrystalline samples. The combination of out-of-plane and in-plane x-ray diffraction analysis reveals that the prepared films possess a body-center-tetragonal crystal structure (a=5.72 Å, c=6.28 Å), which coherently follows the epitaxy of MgO substrate with a substantial tensile strain developed at the bottom interface between the film and the substrate.

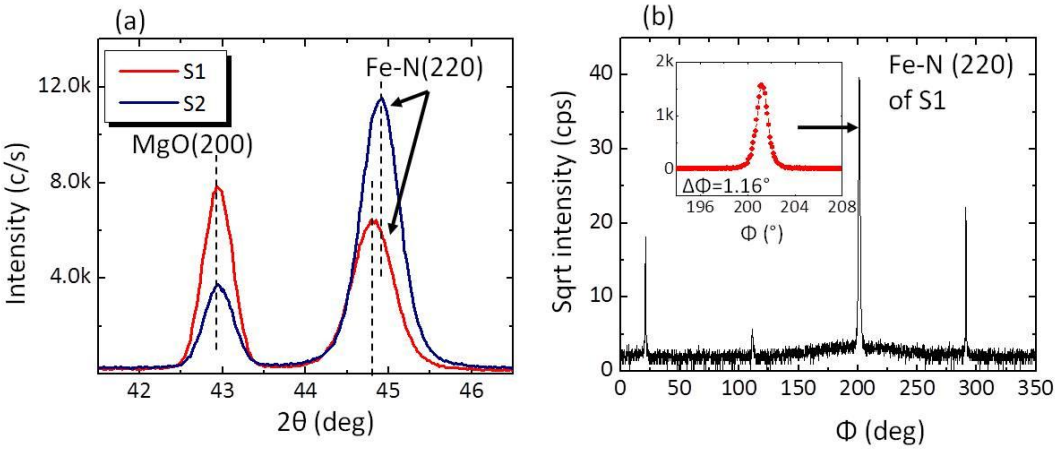

Figure 3.32 (a) Grazing incident x-ray diffraction with scattering vector aligned along MgO (2 0 0) on sample S1 and S2. The shift of the peak position upon underlayer thickness increase suggests the tensile strain developed at the bottom interface of the films. Dashed lines are guides to the eye. (b) Φ scan of $Fe_{16}N_2$ with scattering vector aligned on 2θ=$Fe_{16}N_2$ (220) of sample S1. The inset shows the zoom-in look of one peak (outlined by arrow)

Low angle x-ray reflectivity (XRR) curves (Figure 3.32a) were measured to obtain the structural information. The calculated reflectivity curve that best

reproduces the experimental data is also shown with its electron density depth profile plotted in Fig. 3.33b. When fitting the reflectivity curve of sample S1, a single layer model is used given the fact that the Fe seedlayer is very thin and its density is close to $Fe_{16}N_2$. At the bottom interface between the film and the substrate, an additional "transition layer" with increased electron density compared to MgO is detected, which *creates* the modulation of the oscillations in the reflectivity data and is consistently seen in modeling the data of sample S2. From the fit to the data with the bulk value of the electron density for MgO (~$3.1 \pm 0.1 \times 10^{-5}$ Å^{-2}), we obtained a uniform layer of $Fe_{16}N_2$ ($5.9 \pm 0.3 \times 10^{-5}$ Å^{-2}), suggesting a uniform chemical composition. The introduction of two layer model for describing the XRR of sample S2 only marginally improves the quality of the fit.

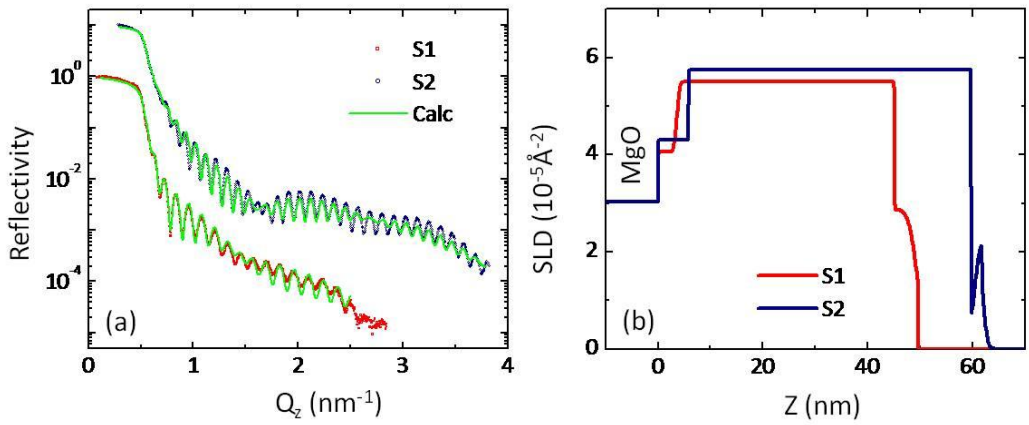

Figure 3.33 X-ray reflectivity characterization (a) The fitted x-ray reflectivity curves measured on sample S1 and S2 (vertically offset by a factor of 10. (b) Calculated depth-dependent x-ray scattering length density profiles.

Both samples were investigated by polarized neutron reflectometry, which were performed at room temperature in the saturation external field of H=1.0 T applied in-plane of the sample. The R+ and R- reflectivity data were fitted simultaneously. In data modeling process, the structural NSLD profile was constrained to closely match x-ray results. To account for the possibility that the film possess homogeneous chemical composition but potentially different magnetization,

the Fe-N layer was subdivided into three slabs where NSLD was fixed but thickness, roughness and MSLD were allowed to vary. Since all the parameters chosen for the top and bottom interfaces are preset in accordance to the x-ray results and are allowed for slight modulation during data analysis, the only free parameter is magnetic moment. The experimental reflectivity and calculated curves with best chi-squared fit for samples S1 and S2 are shown on Fig. 3.34a and b respectively. Their corresponding structural NSLD and magnetization depth profiles are plot in Fig. 3.34c and d. To compare XRR and PNR for the chemical SLD, the interface layer produces relatively large roughness in the PNR, which can be attributed to the lack of high q information or likely due to the non-magnetic nitrides (e. g. MgO:N) formed at the bottom interface accounting for the difference in scattering lengths for the neutron and x-ray probes on light elements such as N.

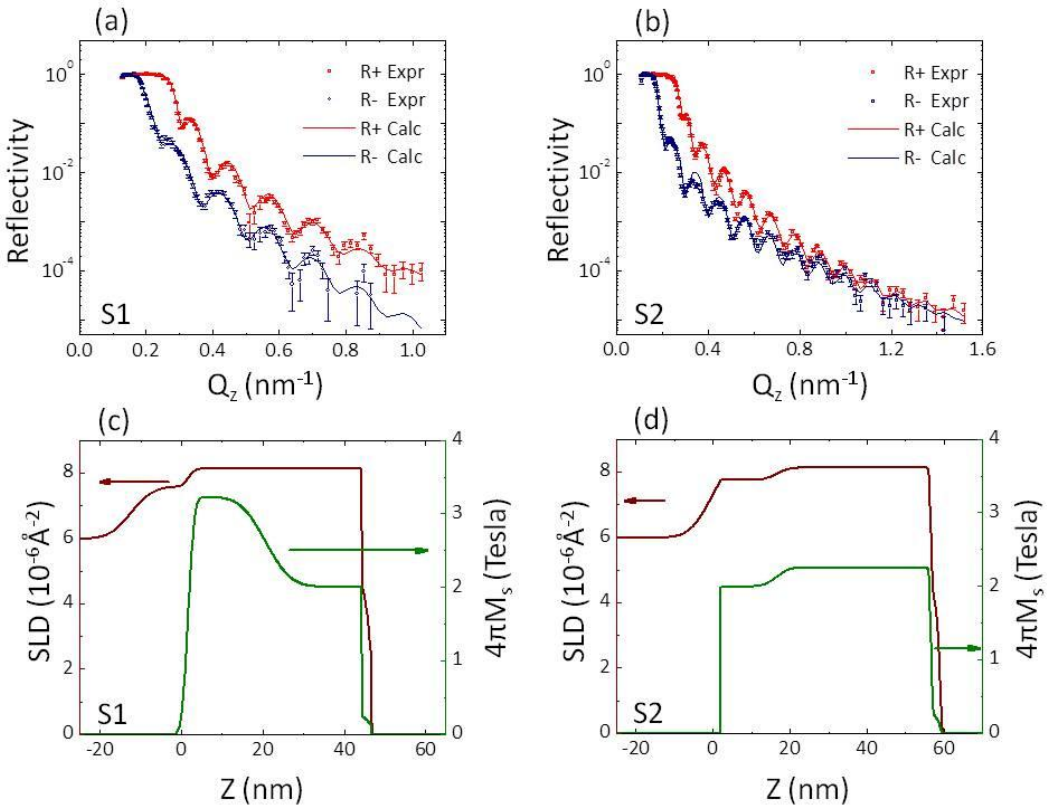

Figure 3.34 (a) and (b) Experimental polarized neutron reflectivities together with the fitted curves as functions of momentum transfer Q for sample S1 and S2 as labeled respectively. (c) and (d) structural (Brown) and magnetic (Green) depth profiles for samples S1 and S2 as

labeled correspondingly. (c) and (d) show the experiment (dots) and fitting (lines) data on sample S1 and S2, respectively. The difference of the high q (q>0.8nm-1) behavior suggests the large magnetization developed in sample S1 but not in S2

It is clear that for sample S1, an anomalously large magnetization is present at the thickness range of about 20 nm towards the bottom interface, where MSLD is in the range of 7.2~7.5x10^{-6}Å^{-2}, corresponding to a magnetization of 3.1~3.2T, which is 40~50% larger than that of bulk Fe and 20~30% higher than that of $Fe_{65}Co_{35}$. As it approaches to the film surface, the MSLD drops rapidly and levels off at 4.66x10^{-6}Å^{-2}, corresponding to a magnetization value of ~2.01T, closely resembling that of nominal Fe.

It is worth noting that a single layer model with both MSLD and NSLD to be uniform through the Fe-N layer or without introducing the transition layer failed to provide satisfying solutions. To illustrate this in detail, three models are used to fit the data, which are listed as A, B and C in the following.

A: uniform NSLD but non-uniform MSLD with a transition layer at the bottom interface

B: uniform NSLD but non-uniform MSLD without a transition layer at the bottom interface

C: Both uniform NSLD and MSLD

At first, the structural scattering length density (SLD) is constrained to be identical with x-ray results. To describe the non-uniformity, the Fe-N layer was subdivided into three slabs where thickness, roughness and magnetic SLD were allowed to vary independently. Both the NSLD and MSLD at the top and bottom interface are allowed to produce smooth modulation. The calculated curves with best chi-squared fit of each model are plotted in Figure 3.35. It is seen model B fails to describe the experiment curves concerning the substantial deviation of first fringe between theory

and experiment on both R^+ and R^- (Note that an unrealistically large magnetic SLD is inevitably produced based on this fitting). A robust improvement on the fitting quality is only obtained by considering an additional transition layer at the bottom interface (Model A) without significant alteration of structural SLD and film thickness. It is also noted that a single layer model with both MSLD and NSLD to be uniform through the thin film main body also fails to describe reflectivity curves. As plotted, when NSLD is restricted to its nominal value, a gradual increase of MSLD and roughness towards the top surface is seen during the iteration process of the calculation and finally stabilizes in current configuration, which does not reproduce any essential features as seen experimentally (Model C).

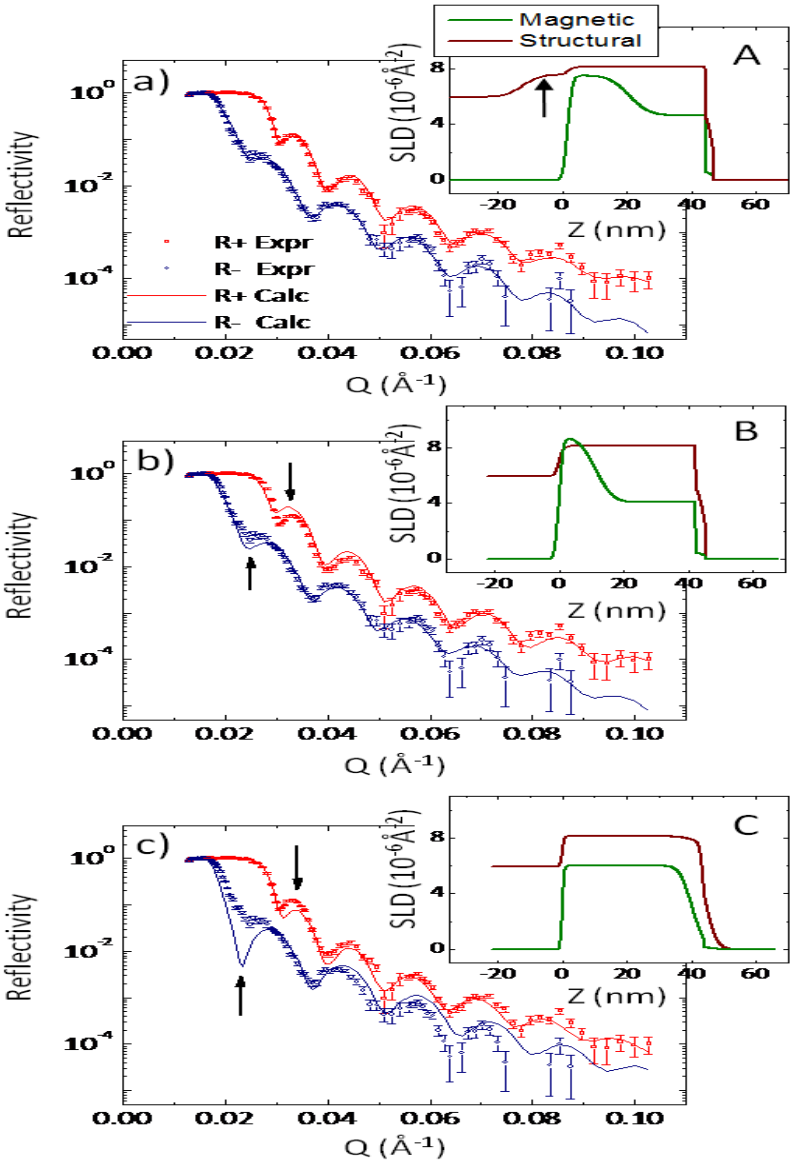

Figure 3.35 PNR data recorded on sample S1. The continues lines in (a) (b) and (c) represent the three fitting models used in analyzing the experiment data as described in the text. (Inset) shows the in-depth (Z: distance to substrate) structural (brown) and magnetic (green) scattering length density profile according to each model labeled as A, B and C in each figure.

For sample S2, following repeating analysis that co-refining PNR with XRR, the resulted MSLD is close to $5x10^{-6}Å^{-2}$ for the Fe-N layer, corresponding to M_s of 2.15T, which does not show the presence of giant M_s.

Further justification for the different magnetic structure upon Fe buffer thickness change comes from the spin asymmetry (SA) comparison between S1 and S2, which is defined as $(R^+-R^-)/(R^++R^-)$ and plot shown in Figure 3.36 a and b. In particular, the SA of the high M_s sample (S1) and normal M_s samples (S2) are plotted in the same scales. It is noticed that at high scattering vector ($q>0.8nm^{-1}$) region, when both the MSLD and NSLD at the bottom interface dominate the behavior of R+ and R- reflectivities, in contrast to sample S2, the SA of the S1 shows a clear tendency to go to unity, which is reflected in the actual reflectivity curves as marked by arrows. This is only possible when condition |MSLD-NSLD|>>MSLD is satisfied. Since NSLD is similar for both samples, this observed feature directly proves the substantial enhancement of MSLD in S1 comparing to S2 at the bottom interface.

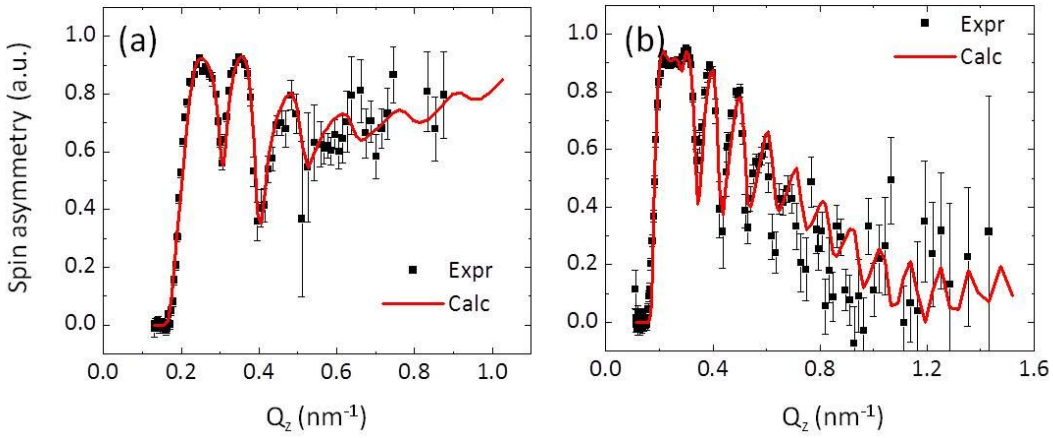

Figure 3.36 Spin Asymmetry plotting of sample S1 (a) and S2 (b). It is clear as it approaches high q, the trend of the curves are different for these two samples.

3.3.8 Role of N in N-deficient Fe-N films grown on MgO substrate

In this section, we used the PNR to investigate the depth-dependent saturation magnetization ($4\pi M_s$) of bi-layer structured N-deficient Fe-N/Fe grown on MgO substrates. These films are purposely annealed to study the N inter-diffusive effect in crystalline Fe. It is observed that by tuning the Fe layer thickness from 2 nm to 5 nm, the magnetic properties of the resulting product varies substantially. According to X-ray diffraction, an additional peak, indexed to $Fe_{16}N_2$(004), was developed in the sample with thinner (2 nm) underlayer. Its corresponding PNR study shows a $4\pi M_s$ of up to 2.82 T towards the substrate interface, which is 14% higher than the known limit ($Fe_{65}Co_{35}$~$4\pi M_s$ = 2.45T). We attribute this giant magnetization to be due to the presence of chemically ordered $Fe_{16}N_2$. We have seen evidence that the high M_s is favorably stabilized due to the lattice mis-fit. The thickness range over which is consistent with the strained region of the films.

We begin our discussion by presenting x-ray diffraction (XRD) data acquired on these two samples, which were performed on a D5005 diffractometer with Cu Kα x-ray source. We fist label the samples in this study in the following way.

S1: Fe-N(20nm)/Fe(2nm)/MgO

S2: Fe-N(20nm)/Fe(5nm)/MgO

As shown in Figure 3.37, both samples show a common peak at around 64.1 °, which can be indexed to α'-$Fe_{0.95}N_{0.05}$ martensite phase with (002) orientation. Comparing with that of α-Fe (002) (~65.8 ° dashed line), the peak position shifts towards a relatively lower 2θ value, suggesting an enhanced lattice constant along the out-of-plane direction for our films due to the interstitial doping of N atoms. Interestingly, for the sample with 2 nm Fe underlayer, an additional bump is seen at around 2θ~59.1° with a much broad peak width (FWHM~3°), suggesting the presence of rich doping Fe-N phases with relatively widely varying lattice constant along c-axis. This is consistent with previous observation that the c-lattice constant can present wide tunability upon different concentration of N doping into bcc Fe.

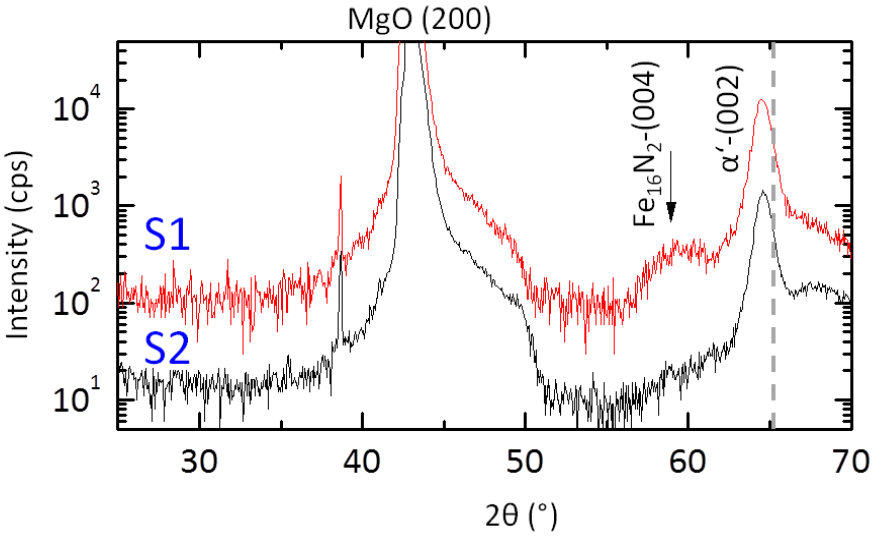

Figure 3.37 X-ray diffraction of sample S1 (Fe-N(20nm)/Fe(2nm)/MgO) and S2 (Fe-N(20nm)/Fe(5nm)/MgO). The 2θ of Fe(002) is outlined in grey dashed line. The data are vertically offset by one order of magnitude.

The PNR with the spin of the neutrons being either parallel (R+) or anti-parallel (R-) to the applied magnetic field (H=1.0T parallel to film plane) were

collected simultaneously at room temperature and are plotted as a function of wave-vector transfer Q in figure 3.38. To better accentuate their features, the reflectivities are multiplied by a factor of Q^4 and shown in logarithmic scale. It is immediately noticed that the oscillation period deviates between these two curves due to the total thickness difference between the two samples. In addition, while the intensity of the R- reflections show similar descending tendency, the intensity of R- curves of the thinner sample drops much faster than that of thicker sample by comparison as it going towards the high Q region. This indicates a larger magnetization fluctuation along depth direction for the thinner sample. Because of these behaviors, the fits to the data reveal differences in the depth dependent magnetic properties of the two films.

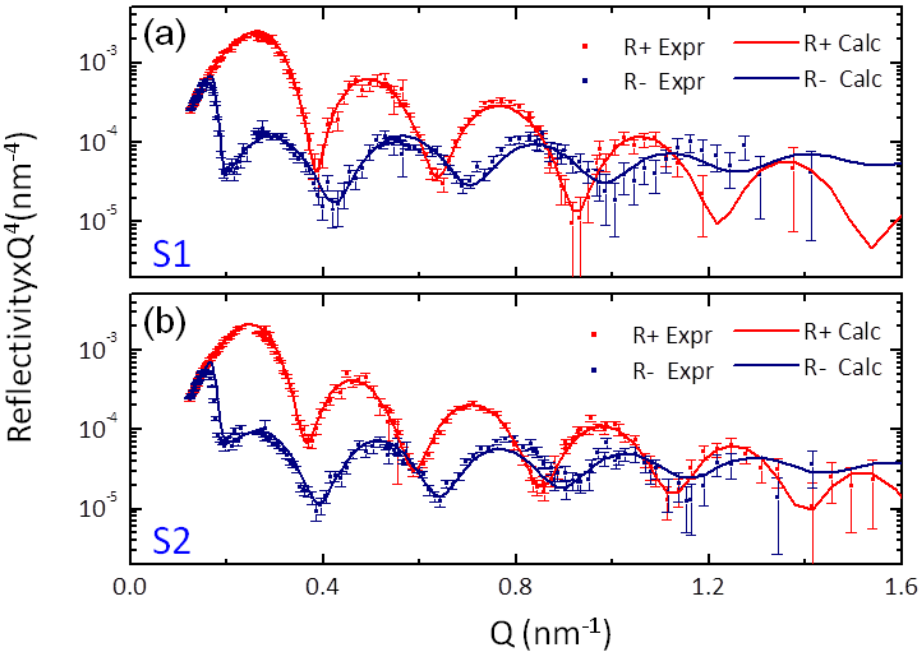

Figure 3.38 measured (dots) and fitted (continues line) non-spin-flip PNR reflectivity curves for sample S1 and S2 as described in text. The data were multiplied by Q4 to highlight their features.

From these data, the depth profiles of the scattering length density (SLD) of both nuclear and magnetic are obtained and shown in figure 3.39. The R+ and R-

reflectivity data were fitted simultaneously. In modeling the SLD, we used three-layer model considering the possible surface oxidation and interfacial reaction. To account for the non-uniformity, the film bulk region is sub-divided into 3 slabs and allows marginal adjustment during fitting process. Since the nuclear SLD of N is close to Fe, we set initial the structural parameter to resemble that of nominal Fe.

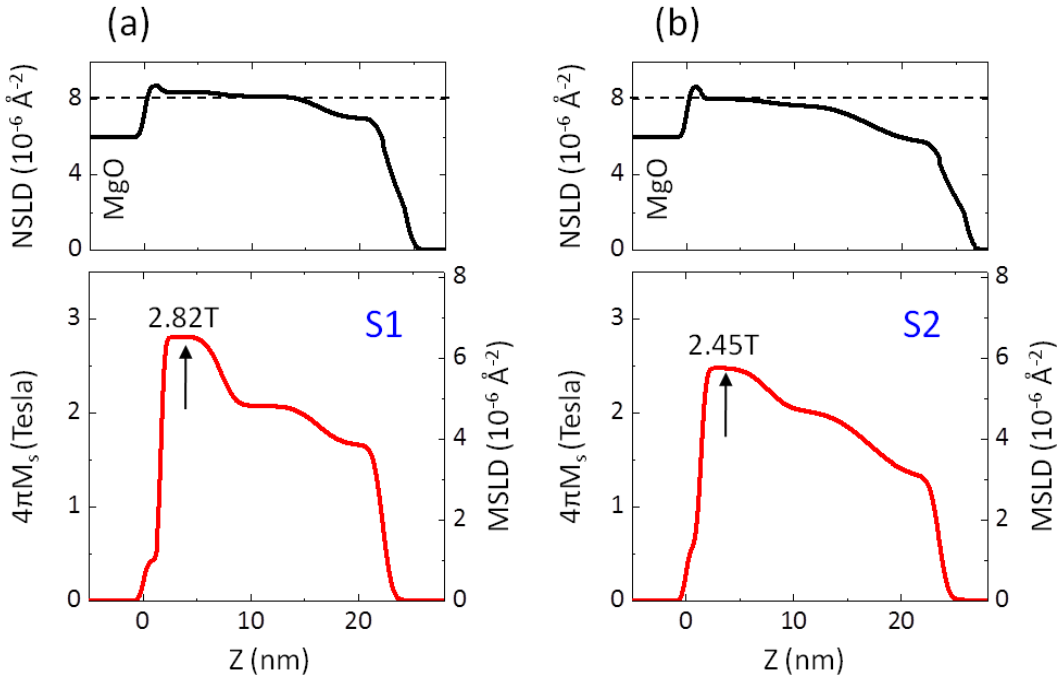

Figure 3.39 Scattering length density (SLD) models for sample S1 (a) and S2 (b) with film structures as described in text. Top panel: Nuclear SLD (NSLD), Bottom panel: Magnetic SLD (MSLD). The magnetization is proportional to the MSLD and is shown on the right. The dashed lines in both figures show the NSLD of nominal Fe.

Looking at the depth profile that best reproduces the experiments, the nuclear SLD of both samples expectedly show similar configurations, which is close to that of nominal Fe (dashed line). Starting at the substrate, the nuclear SLD of both samples decreases as the magnetization decreases, indicating a deep but gradual oxidation of the films. What is striking about these results is the absolute value of the magnetic SLD. From the top surface, the magnetizations of both samples gradually climb up. For the thicker sample, the highest $4\pi M_s$ already reaches 2.45 T

close to that $Fe_{65}Co_{35}$. For the sample with thinner underlayer Fe, the $4\pi M_s$ remarkably peaks at 2.82 T and preserves for about 60 Å towards the bottom interface.

To draw further comparison between the two samples, the diffusive effect of N is clearly revealed from the combined analysis of XRD and PNR. Due to the lattice mis-fit between Fe and MgO, tensile strain is developed at the bottom interface. Due to the N concentration gradient and post-annealing treatment, N atoms diffuse into the "virgin" Fe seedlayer, which produces N-rich Fe-N martensites. According to XRD, only thin Fe (2 nm) seed can allow the formation of N-rich Fe-N phase, suggesting its growth mechanism is indeed strain-related, concerning the strain relaxation of metal film are of ~5 nm. The giant magnetization (2.82 T) can be apparently attributed to the presence of $Fe_{16}N_2$ in consistent with the N-rich phase as observed by XRD.

To this extent, we have demonstrated that even structurally similar $Fe_{16}N_2$ can be synthesized, however, due to the different strain conditions, the saturation magnetization value can change drastically, the reason of which will be discussed in the following chapter.

Reference

[43] http://www1.chm.colostate.edu/Files/XRR.pdf

[44] Shau-Wei Hsu, Conference on Precision Electromagnetic Measurements Digest (1996)

[45] V. Lauter, et. al., Physica B 404, 2543 (2009)

[46] R+ and R- are spontaneously recorded. We only show R+ curve in the image

[47] http://www-llb.cea.fr/prism/programs/simulreflec/simulreflec.html

[48] N. Ji, Y. M. Wu and J. –P. Wang, J. Appl. Phys. 109, 07B767 (2011)

[49] N. Ji, et. al, *Appl. Phys. Lett.* 98, 092506 (2011)

[50] Comparing to previous experiments (N. Ji et al., J. Appl. Phys. 109, 07B767 (2011)), the optimized N_2 partial pressure to achieve high quality Fe_8N is at 0.12 mTorr, the Fe-N layers prepared here were grown at N_2 partial pressure of 0.18 mTorr with otherwise identical deposition conditions as the previous report.

[51] Ranu Dubey, Ajay Gupta, and J. C. Pivin, Phys. Rev. B 74, 214110 (2006)

[52] The x-ray scattering cross section of N is much smaller than that of Fe. Therefore, the SLD of the N doped Fe is similar to SLD of pure Fe for x-ray probe.

[53] G. P. Felcher, Phys. Rev. B 24 1595 (1981)

[54] C. F. Majkrzak, Physica B 173, 75 (1991)

[55]The MSLD (ρb_m) is the same physical parameter as the saturation magnetization (M_s), both of which are a measure of the magnetic density. In cgs unit, the conversion formulism is $3.5x10^8 \times \rho b_m$ ($Å^{-2}$) = M_s (emu/cm^3)

Chapter IV Magnetism in $Fe_{16}N_2$

4.1 Introduction

In calculating the saturation magnetization of $Fe_{16}N_2$, a variety of first principle approaches have been proposed and implemented previously, which all failed to describe the giant saturation magnetization and became one of the three missing pieces for this topic. Some attempts discussed the $Fe_{16}N_2$ system in a context of localized electron pictures. However, there is lack of convincing experimental evidence to support the speculation. In this chapter, we will discuss the magnetism of $Fe_{16}N_2$. A new model is proposed to rationalize the giant magnetism in $Fe_{16}N_2$ system. This is based on the ferromagnetism associated with partially localized electron states. We will also demonstrate that an unusual correlation effect is brought up within the Fe-N octahedral cluster region. The effective on-site 3d-3d Coulomb interaction increases due to a substantial 3d electrons charge density difference between the clusters and its surroundings, which leads to a partially localized electron configuration with a long range ferromagnetic order. First principle calculation based on LDA+U method shows that the giant saturation magnetization can be achieved at sufficiently large Hubbard U values. The feature of the coexistence of the localized and itinerant electron states plays a key role on the formation of the giant saturation magnetization. Finally, we will present experimental evidence of the charge transfer from N to Fe sites within the Fe_6N region, which provides supporting evidence on the proposed "(Fe_6N) cluster + (Fe) atom" model.

4.2 Band magnetism in Fe-N system

A general understanding of the magnetism in the iron nitrides is based on itinerant ferromagnetism. Shown in figure 4.1a is a plot of spin-resolved density of state (DOS) for pure Fe and one typical Fe-N compound γ'- Fe_4N. Comparing the shapes of these two DOS, it is clear that the major difference between Fe and Fe_4N

occurs near the bottom of the bands for both spin-up and spin-down states as highlighted. This is coming from the hybridization of N 2p and Fe 3d bands. For other iron nitride system, as the doping concentration of N progressively changes, the band hybridization between Fe3d and N2p provides gradual alteration of spin occupations in the imbalanced density of states and consequently results in the smooth modulation of the average magnetic moment. As a result, the calculated magnetic moment of various Fe-N compounds based on band magnetism can be appreciated by a generalized "Slater-Pauling" curve with elegant simplicity as shown in figure 4.1b

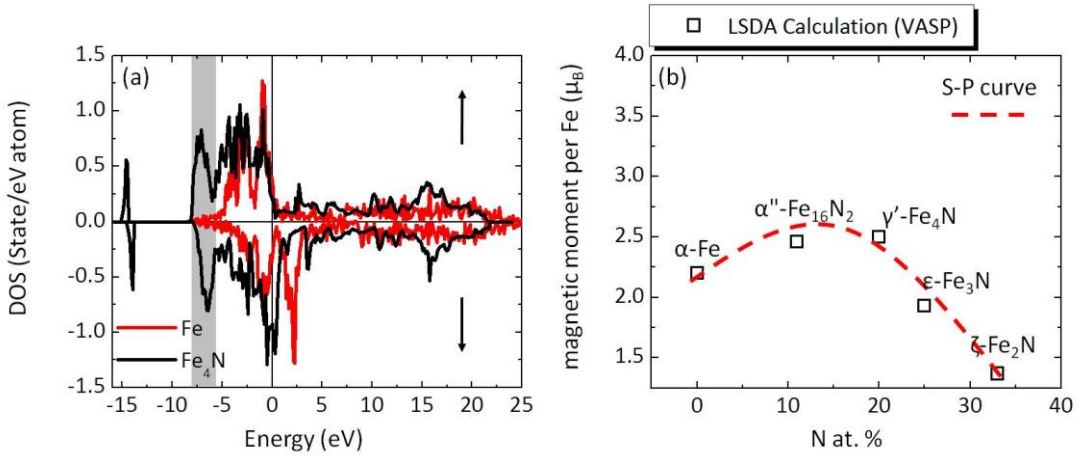

Figure 4.1 (a) Spin resolved density of state of Fe (red) and Fe_4N (black). The outlined region represents the DOS modulation due to the N2p and Fe3d hybridization. (b) (open squires) Calculated average magnetic moment per Fe as a function of N doping concentration based on LSDA on a variety of iron nitrides (from left to right: Fe metal, $Fe_{16}N_2$, γ-Fe_4N, ε-Fe_3N and ζ-Fe_2N). The dashed line here is a schematic drawing of Sater-Pauling curve, which is intended to describe the magnetization behavior of Fe-N based on the LSDA results.

4.3 "(Fe_6N) cluster + (Fe) atom" model

4.3.1 Historical efforts in rationalizing the high moment report

To rationalize the high moment reports, Lai *et al.*[56] postulated the existence of a strong correlation effect on all iron sites in $Fe_{16}N_2$ system and obtained the magnetic moment more closely resembling the high moment experimental data. However, it has been argued that whether the material system can maintain its metallic properties given the high on-site Coulomb U values and its inability to guide the experiment. A. Sakuma proposed another high moment scenario called the charge transfer model[57], inferring the existence of empty nitrogen orbitals near the Fermi level, which serve as charge hopping sites. This qualitative model predicts a high spin configuration of Fe and long range ferromagnetic order through an effective "double exchange" process in the context of highly localized spin interacting picture. However, no obvious evidence shows the N site is much more negatively charged relative to other iron nitrides.

4.3.2 Partial localization of electrons

The crystal structure of $Fe_{16}N_2$ contains Fe with local environment similar to both bct-Fe with (c/a~1.1) and fcc-Fe (Fe_4N). In both bct-Fe and fcc Fe_4N, a D4h symmetry Fe is formed due to the lattice expansion along [001] direction. However, in a real $Fe_{16}N_2$ system, the Fe sites with local D4h point group symmetry reduce to C4v and C1h symmetry due to the alternating occupancy of the N atoms. Unlike Fe_4N or bct Fe, the corner Fe sites within those distorted Fe-N octahedral clusters lose the mirror reflection symmetry along certain directions, experiencing less symmetric crystal field due to the center N. Therefore, an additional effect arises due to the symmetry break. Plotted in figure 4.2 is the total charge density for Fe_4N and $Fe_{16}N_2$ on the Fe-N plane perpendicular to the [001] direction based on local spin density approximation (LSDA) method. As illustrated in the figure, in Fe_4N, Fe-N octahedral clusters are connected through the corner Fe, which results in relatively uniform charge distribution along line CD. In the contrary, in $Fe_{16}N_2$, Fe-N octahedral clusters are geometrically isolated in the sense that each corner Fe site belongs to an individual Fe-N octahedral cluster. As a result, there appears a

significant charge density difference interior and exterior the Fe-N octahedral cluster region which originates from this reduced symmetry. These observations lead us to suggest 3d electron partial localization model for the strong ferromagnetism in this $Fe_{16}N_2$ material system.

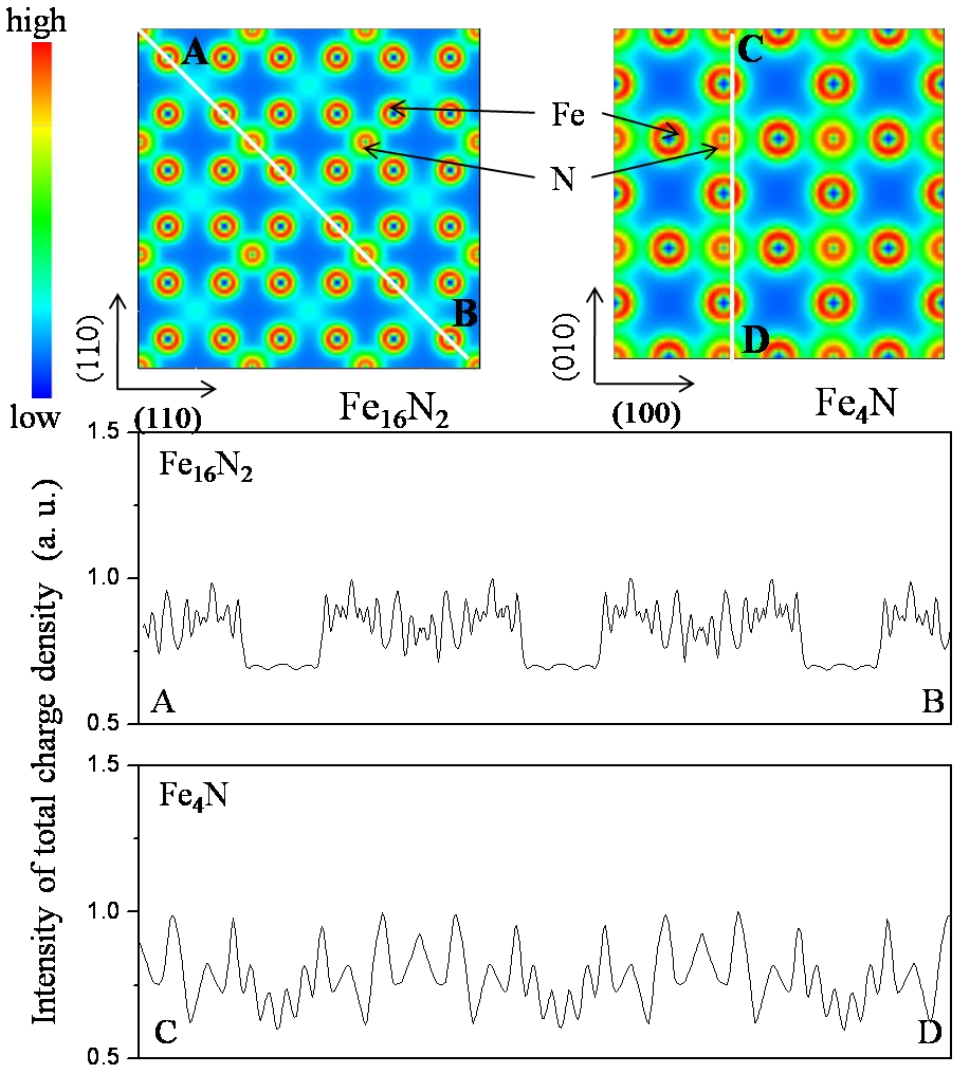

Figure 4.2 Total charge density distribution projected on Fe-N plane perpendicular to the [001] plane for $Fe_{16}N_2$ and Fe_4N based on LDA calculation results, the right figures shows intensity of charge density (logarithmic scale and normalized to their maximum intensities) along line AB and CD as marked in the charge figure is shown to illustrate the effect of the broken symmetry as explained in text.

The starting point for a discussion of the partial localization model is that there exists a considerable 3d electron charge density difference between iron sites inside and outside the Fe-N octahedral cluster. To illustrate the charge density effect on its magnetic properties, a model calculation is performed to capture the essential qualitative features. Considering a uniform and spherical 3d electron charge distribution within the Fe-N octahedral cluster as illustrated schematically in figure 4.3, the static potential difference between interior and exterior of the clusters can be obtained by solving Poison's equation. This potential can be written as $\frac{2\pi}{3}(\rho_{in}-\rho_{out})a_0 r_0^2 Ry$. With ρ_{in} and ρ_{out} represent the d electron charge density interior and exterior the sphere respectively, a_0 the Bohr radius and Ry as the Rydberg constant. This potential energy difference is created solely by the short-region repulsive electron interaction as a screened Coulomb energy in electron gases, which qualifies an on-site Coulomb interaction difference between the Fe-N octahedral cluster and its metallic environment (Fe4d). The U values found in metallic Fe are typically 1eV [58].

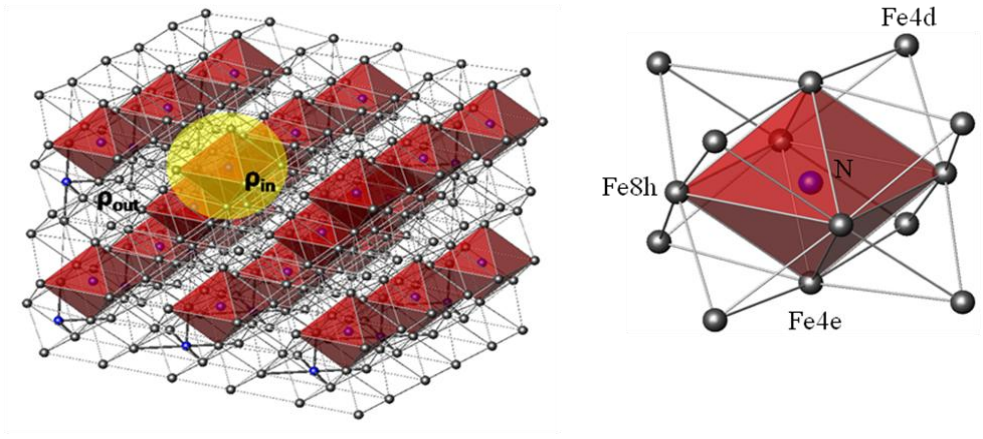

Figure 4.3 The crystal structure of $Fe_{16}N_2$. Fe-N octahedral clusters are highlighted in red color. The proposed charge density distribution is schematically drawn by yellow sphere. ρ_{in} and ρ_{out} as marked on the figure is to illustrate such difference. The right figure

shows chemical environment of the three iron sites, Fe8h and Fe4e are within the cluster region and Fe4d locates outside the cluster.

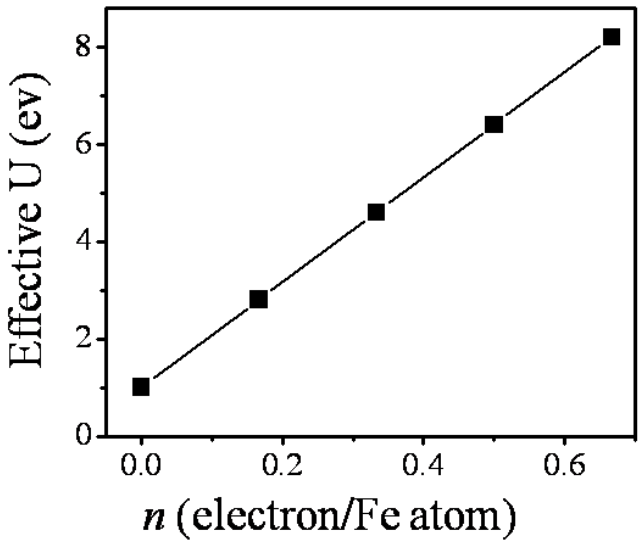

Figure 4.4 3d electron charge difference per iron site between interior and exterior the Fe-N octahedral cluster versus the effective on site Coulomb U.

According to our model, the average number (*n*) of 3d electron per Fe inside the Fe-N octahedral cluster, after subtracting that outside the cluster, increases linearly as U increases, reaching a value of *n*~0.5 at U around 7~8 eV (figure 4.4). In the LSDA picture, the number of 3d electrons per Fe on Fe4d, Fe4e and Fe8h sites calculated by He *et al*[59] is 6.65, 6.57 and 6.58, respectively. In our model, if ~0.4 3d electrons transfer from Fe4d site to its four neighboring Fe-N octahedral clusters, it will give rise to a number of 3d electrons per Fe of 6.25, 6.70 and 6.71 for Fe4d, Fe4e and Fe8h respectively and *n*~0.5 can be easily reached. At this point, the physical picture is clear. Certain amount of 3d electrons transfer from Fe4d site to Fe-N octahedral cluster and give rise to local potential energy fluctuation, which result in a large U difference between the Fe-N octahedral cluster and its surrounding iron atoms. To stabilize this charge transfer process, additional energy term is required to compensate the U increase. Therefore, the bonding between Fe

and N plays an important role. In analogy to the Stoner's ferromagnetism stability argument, a high U value leads to the reduction of the band overlapping between spin up and down and effectively increases the exchange energy. Ultimately, certain orbitals within the Fe-N octahedral cluster will possess localized feature with fully polarized spin configuration, where Hund's coupling dominates. On the other hand, the other orbitals remain broad bandwidth and less exchange splitting due to their spatial extension and strong hybridization with neighboring metallic Fe4d sites outside the Fe-N octahedral cluster. This condition helps to maintain their band-like features that favor long-range ferromagnetic coupling and metallic behavior. In that sense, the dual electron behavior and partial localization is realized.

To illustrate this idea quantitatively further, an electronic structure calculation with on-site Coulomb interaction corrections is performed to compute the magnetic moment in $Fe_{16}N_2$. To simulate partial localization, we used the LDA+U method used by Anisimov *et al*[60]. The U value of Fe outside (Fe4d) the cluster sphere was fixed at 1 eV and the magnetic moment change was then plotted for three Fe sites as the U inside the cluster (same U is assumed for both Fe4e and Fe8h) varied as shown in figure 4.5. The J parameter (Stoner parameter) was taken to be U/10. Calculation is performed by using the Vienna *ab initio* simulation package (VASP), with Projector Augmented Wave potential[61]. A plane wave cutoff corresponds to kinetic energy of 250ev was used. A k mesh of 8*8*8 was used to sample the supercell. The exchange correlation function is approximated with the fully localized limit of the local spin density approximation +U method[62]. The lattice constant is constrained according to its bulk value. The density of states (DOS) were calculated with fine k meshes using a tetrahedron method with Blöchl corrections as implemented in VASP. Both Fe4e and Fe8h sites are sitting inside the Fe-N octahedral cluster. As the U increases, they favor rapid polarization while for the Fe4d site, which sits outside the Fe-N cluster, exhibits slow decay of the moment from 2.9 to 2.6 μ_B/Fe and levels off at high U values. it is seen that when U is large enough, an average magnetic moment above 3 μ_B/Fe is obtained. It is important to

discuss the choice of U=1eV for the Fe4d sites. Recent study shows a U close 2~3eV is considered in metallic Fe[63]. According to our calculation, when U=1eV is applied to all three iron sites, the magnetic moments calculated coincide with those derived from standard LSDA calculation. This result implies U around 1eV should be sufficiently small to give rise to band theory based electrons picture. It is possible that U can be less than 1eV for the Fe4d site without jeopardizing its itinerant electron feature. In that case, a reduced average magnetic moment should be expected though the monotonic trend of magnetic moment versus U still remains. The U values considered in the Fe4e and Fe8h sites are up to 8eV. In reality, U~6eV is used for insulator FeO[64], in which the screening effect is expected to be weaker than that in $Fe_{16}N_2$. Therefore, though no first principle calculation on the U value can be retrieved, a reasonable estimation on the actual U value should be positioned in between metal Fe and FeO. However, in the model discussed here, at U = 4eV, the average moment reaches a value of ~2.8 μ_B/Fe, which already exceeds the known limit for the ferromagnetism (~2.6 μ_B/Fe in $Fe_{0.65}Co_{0.35}$).

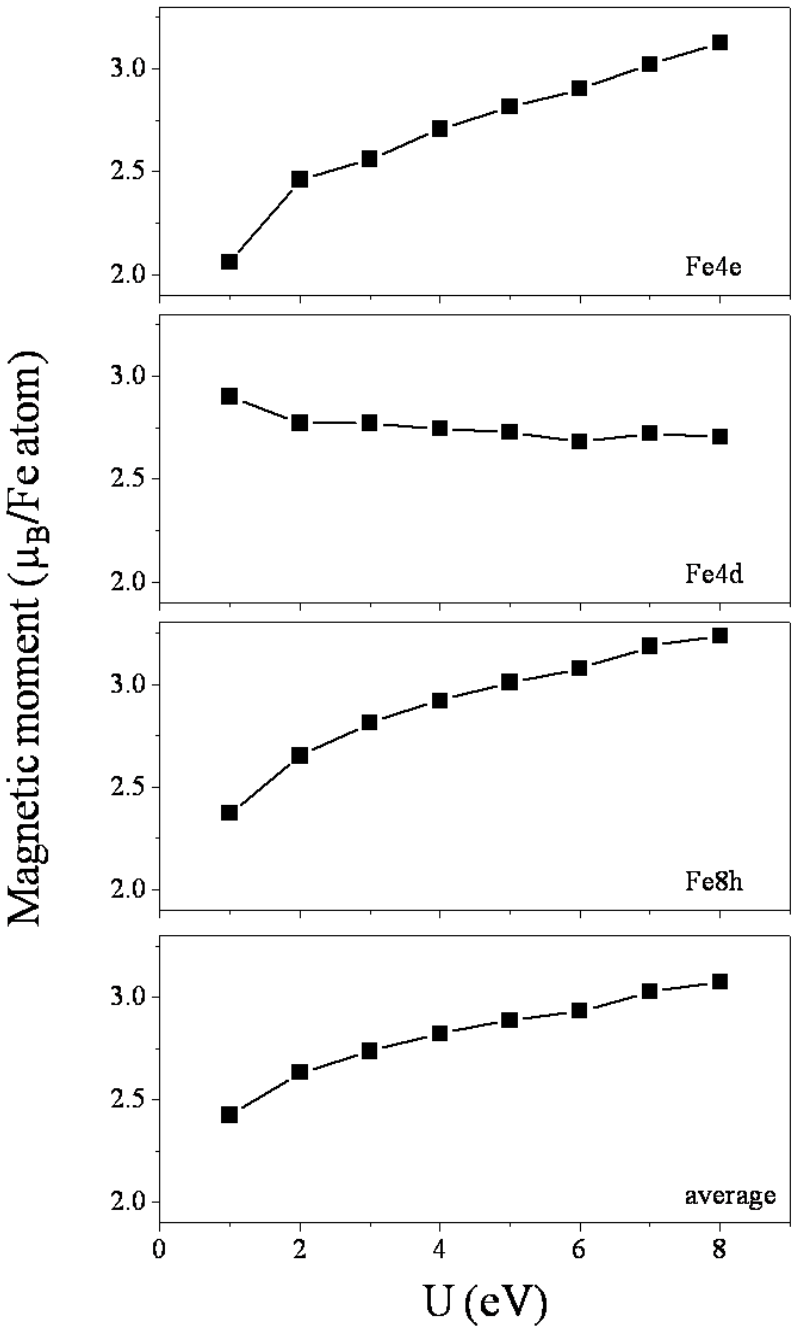

Figure 4.5 Local magnetic moment of three different Fe sites (Fe4d, Fe4e and Fe8h) in $Fe_{16}N_2$ versus Coulumb U change.

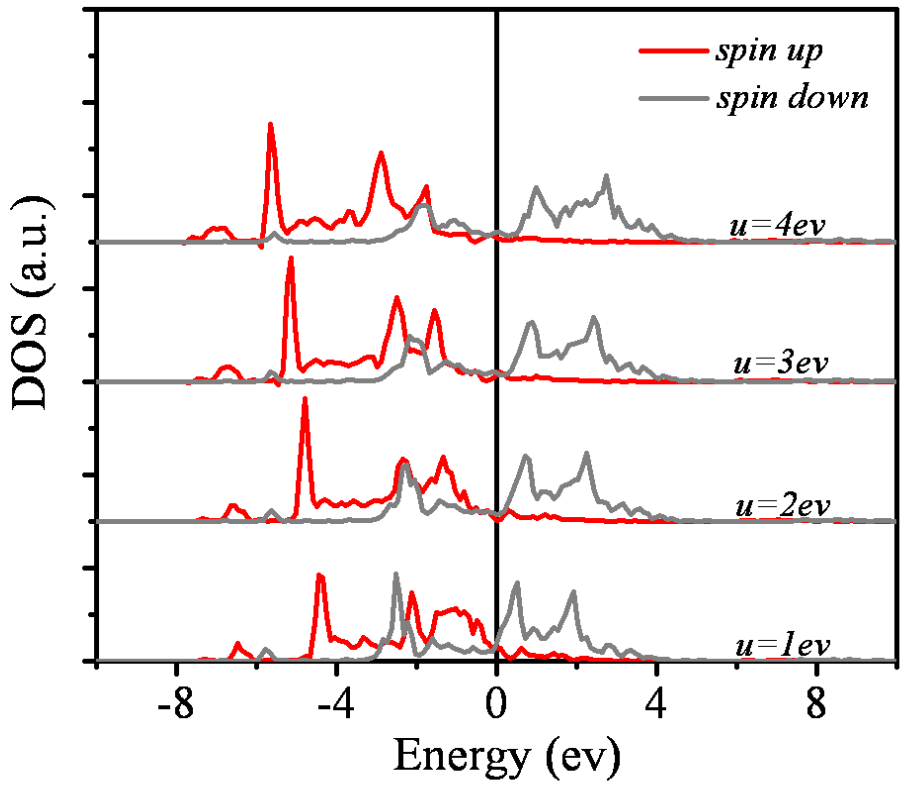

Figure 4.6 Partial density of states projected on (3dxz+3dyz)/2 of Fe4e site in $Fe_{16}N_2$ for different U values.

The effect of the d-d Coulomb interaction on the electronic structure can be explained in the following. Plotted in figure 4.6 is the partial DOS projected on double degenerate (dxz+dyz) orbital of Fe4e sites. As U begins to increase, the spin up band shifts downwards with more and more states occupied at the expense of spin down orbital in the process of self-consistency iteration. This orbital will eventually become fully occupied when U is sufficiently large. In that case, electrons on these orbitals exhibit nearly atomic configuration and the on-site magnetic coupling mechanism is dominated by Hund's rule, which gives rise to a high spin configuration of Fe. It is also interesting to notice that the Fe4d sites reduce their magnetic moment as U increases. This suggests that the electron distribution on different iron sites changes significantly in comparison with the LSDA calculation

results, in which case, the high magnetic moments on Fe4d sites are due to the charge transfer from Fe4d to the Fe sites closer to the N sites.

The essential difference between our model and others' is the idea of 3d electron partial localization. The LDA+U methods are initially developed to treat Mott insulator systems such as FeO. The earlier Lai's model considers a strong correlation effect on all three iron sites and achieves high magnetic moment. The U values used are calculated from the embed cluster method[65] by assuming a relatively small screening constant, which has been considered as "unrealistic" for a metal system[66]. Experimentally, low temperature transport properties suggest the legitimacy of treating $Fe_{16}N_2$ as a metal[67]. However, large residual resistivity is also explored relative to the pure metal Fe, implying the existence of defects-like localized electron states though single crystal samples are used for this study. Recently, our group has performed similar measurements that confirmed this observation[68]. In our model, we emphasize that the unusual correlation occurs within the Fe-N octahedral clusters due to the introduction of the center N atom. The metallic behavior of the system still stands as the U on the Fe4d sites remain metal like. More importantly, the difference of the on-site Coulomb U for the three iron sites distinguishes the material into two subsets, namely, Fe-N octahedral clusters (Fe8h and Fe4e) and metallic Fe atoms (Fe4d). Within the Fe-N octahedral clusters, Fe8h and Fe4e possess a partially localized electron behavior due to the enhancement on U. Outside the Fe-N octahedral clusters, Fe4d maintains its metal like behavior. The macroscopic giant ferromagnetic order is formed through the interplay between localized oribitals and itinerant band. Therefore, to rationalize the giant saturation magnetization report, a dual electron behavior seems to be a necessity in a fundamental level. This opens up the direction on identifying promising candidates for many applications that demand high M_s.

Roughly speaking, the model proposed here is to examine the magnetism in $Fe_{16}N_2$, which is viewed as a non-conventional ferromagnetic metallic system. Since

for Fe in metal, a pure band theory description is not capable of yielding such large moments given the fact that exchange and correlation included in the standard LSDA approach are usually underestimated. Therefore, parametrized many-body approaches (LDA+U) was explicitly applied in the completely localized electron scheme. In this case, the high local magnetic moment correlates well with the Hund's rule prediction.

4.4 Experimental evidence of localized 3d Fe states in $Fe_{16}N_2$

One essential feature of the proposed model is the presence of localized 3d states. This can be investigated by X-ray magnetic circular dichroism (XMCD) experiments[69], which were carried out on a series of well textured Fe-N samples grown on single crystal (001) GaAs substrate.

Experiments were performed on beam line X13A of the national synchrotron light source (NSLS) at Brookhaven National Lab. Spectra were recorded in a total electrical yield (TEY) mode using circular polarized light with 75% polarization at room temperature. A magnetic field of up to 0.2T were used to magnetize the samples at $\theta = 0°$ and 30° with respect to surface normal. The incident beam was chosen at 8 °with respect to sample surface.

Plotted in Figure 4.7 are the total-electron-yield mode iron $L_{2,3}$ edges XMCD spectrum for single phase Fe_3N, Fe_4N, Fe_8N and partially ordered $Fe_{16}N_2$ samples, which were normalized to the L_3 edge peak position. Similar to L edge XMCD data collected on pure iron metal , it is seen that the main excitation threshold occurs at the photon energy 708 ± 1 ev and 721 ± 1 ev for all these iron nitrides samples, which is attributed to band-like states of the 3d electrons. Unexpectedly, it is obvious and interesting to notice, for the XMCD spectra of Fe_8N (α' phase) and partially ordered $Fe_{16}N_2$ samples, there appear additional features on both edges. As shown in this figure, this feature can be numerically reproduced[70] by considering a spectrum of atomic-like Fe $3d^6$ to $2p^5$ $3d^7$ multiplet transition in a D4h crystal symmetry

superimposing with the band-like Fe, which provides solid evidence that two electron states (band-like and atomic like) coexist in Fe_8N and $Fe_{16}N_2$.

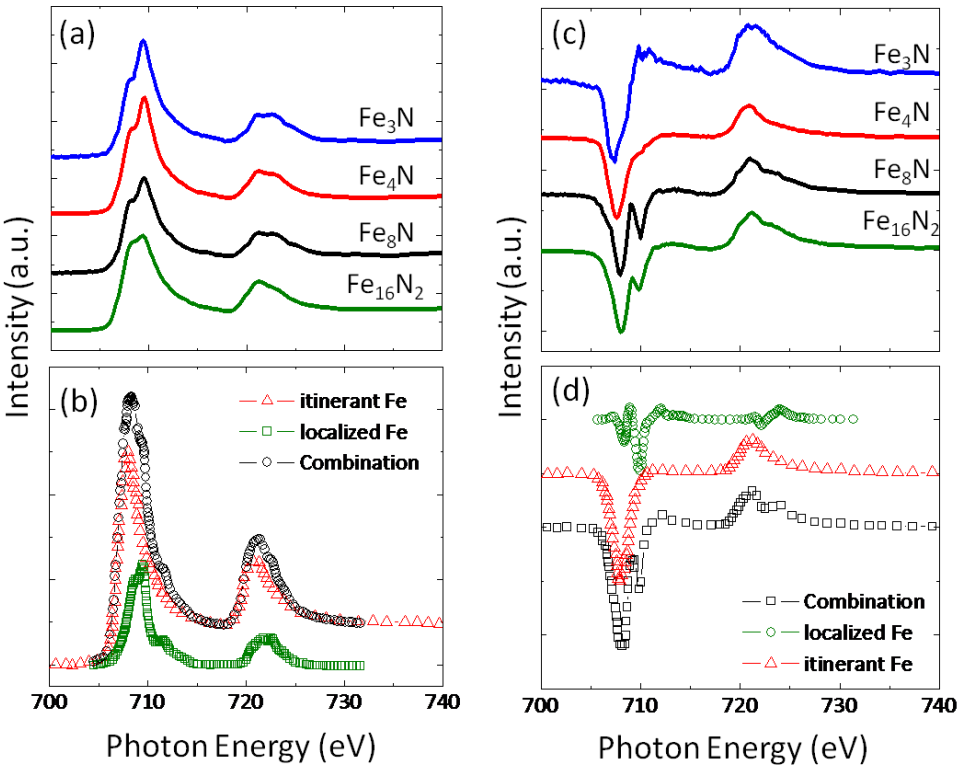

Figure 4.7 (a) Fe L edge XAS for varies Fe-N phases thin film samples. (b) XAS simulation on localized and itinerant Fe L edge spectra. (c) Fe L edge XMCD measured on varies Fe-N thin films. (d) XMCD simulation on localized and itinerant Fe L edge spectra.

We also conclude that the ionic Fe contribution in the Fe_8N and $Fe_{16}N_2$ samples are not attributed to the presence of surface oxidizes. In the XAS data, it is seen that spectra for all these samples have metallic and ionic Fe signals due to surface native oxides. However, in the XMCD spectra, the ionic Fe signals are significantly reduced in Fe_3N and Fe_4N case and can be safely neglected. While for the spectra of $Fe_{16}N_2$ and Fe_8N, the XMCD of the ionic signals are strong and is in contrast to Fe_3N and Fe_4N cases.

4.5 Experimental evidence of charge transfer within Fe_6N cluster in $Fe_{16}N_2$

An immediate predication of the "Cluster (Fe_6N) + Atom (Fe)" model is the presence of directional charge transfer from Fe to N site, in which case, an effective "double exchange" mechanism can be facilitated and consequently, a high-spin configuration and long-range ferromagnetic order can be stabilized to develop high moment (figure 4.8). The XPS experiment presented in chapter II suggests the existence of multiple Fe valance 3d electron states in $Fe_{16}N_2$, which already provides evidence for treating this Fe-N system in the localized picture. To further verify this essential feature, we investigated the nature of Fe-N bond from individual Fe sites using polarization-dependent x-ray absorption near edge spectroscopy (XANES), which allows the evaluation of the local structure with element specificity[71, 72, 73, 74].

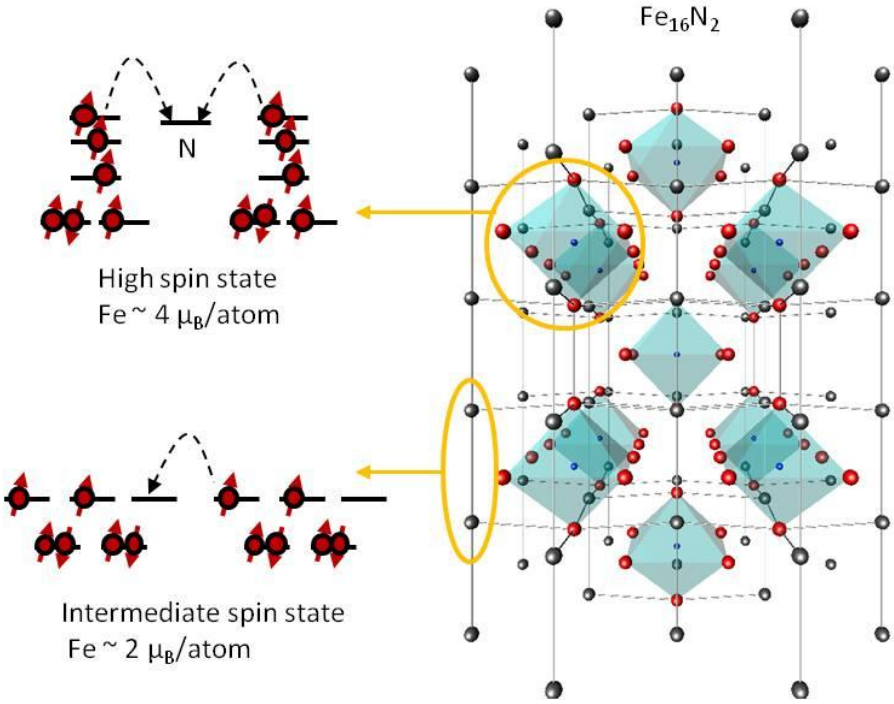

Figure 4.8 An illustration of the "atom+cluster" model to realize the giant moment in $Fe_{16}N_2$, within the Fe_6N octahedron, the charge transfer facilitates the high spin configuration and double exchange ferromagnetic coupling. Exterior the Fe_6N cluster, the intermediate spin state is energetically favorable. Multiple Fe valance electron states are expected from this model.

The Polarization dependent X-ray Near Edge Spectroscopy (XANES)

measurements were performed at room temperature at the bending magnet beamline 20-BM-B of the Advanced Photon Source (APS), Argonne National laboratory. In particular, a toroidal mirror was used to focus the beam to 400 um^2, allowing 5 degree glancing angle measurements with x-ray polarization parallel and perpendicular to the (002) surface plane, given the samples of $Fe_{16}N_2$ are epitaxial along the (002) orientation. The samples were spinning about the surface normal during the measurement to eliminate possible Bragg diffractions. An Fe metal foil was used as an online reference for all of the measurements to check the monochromator energy calibration. The absorption edge positions for Fe metal was taken as 7110.75 eV. The scattering geometry is shown in figure 4.9 with x-ray polarization parallel (E//surface) and perpendicular (E⊥surface) to the $Fe_{16}N_2$ (002) surface plane.

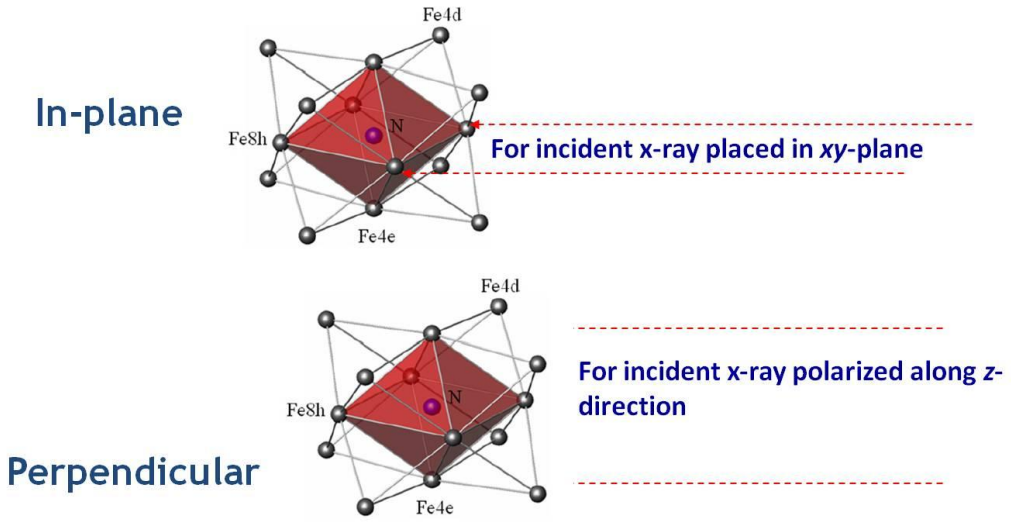

Figure 4.9 Scattering geometry of the XANES experiment

The analysis was done by comparing the simulated spectra with ($Fe_{16}N_2$) and without ($Fe_{16}N_0$) N occupying the octahedral center to extract the role of N using the *ab initio* FEFF8.4 code[75, 76]. The experimentally obtained XANES data were shown in figure 4.10a. The simulated polarization-dependent XANES based on two structural models of $Fe_{16}N_2$ and $Fe_{16}N_0$ are shown in figure 4.10b and c, respectively.

The simulated XANES spectra of $Fe_{16}N_2$ reproduce all essential features as observed experimentally, as marked using the vertical blue dashed lines, which is in contrast to that of $Fe_{16}N_0$. Therefore, we used the simulated XANES spectra from individual Fe sites to investigate the role of N in the $Fe_{16}N_2$. As shown in figure 4.10e and f for the E//(002) surface plane, the only substantial spectra modification upon removing N is seen on Fe8h (figure 4.10e), which is attributed to its large influence on the in-plane Fe-N bonds. In comparison, the XANES spectrum from the Fe4e site shows a slight change (figure 4.10f) for the E//(002) surface plane direction. Likewise, a similar conclusion can be drawn for the case of Fe4e and the E⊥(002) surface plane, which results from the out-of-plane Fe-N bonds. The Fe4d site, which is the most distant Fe atom from the N site, undergoes the least spectra modification with N occupation status change.

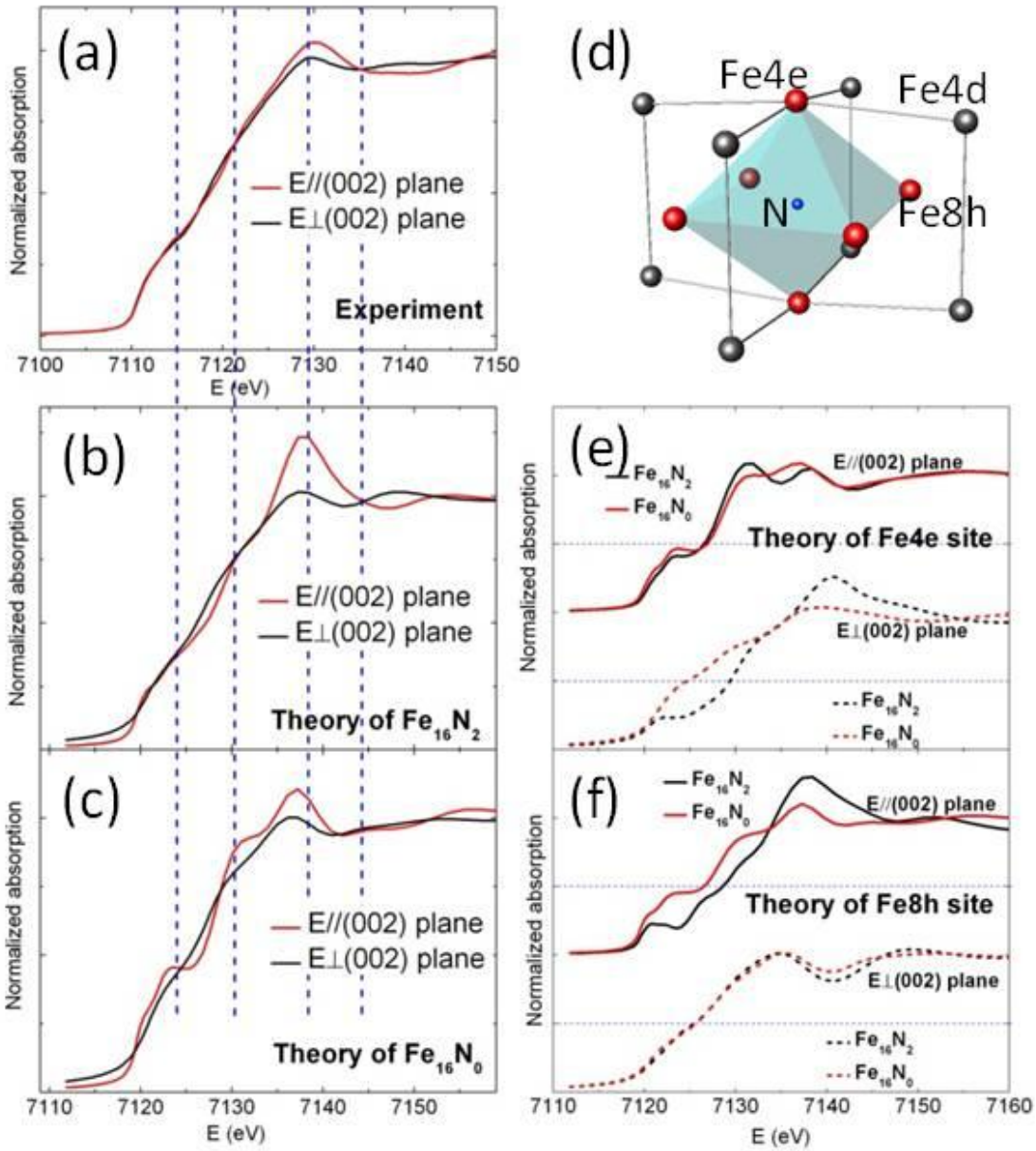

Figure 4.10 XANES analysis of $Fe_{16}N_2$ experimental (a) $Fe_{16}N_2$ calculated (b) and $Fe_{16}N_0$ calculated (c) spectra with polarization direction of X-ray perpendicular (red) and parallel (black) to the sample surface. (d) The crystal structure of $Fe_{16}N_2$ and each individual site. The calculated XANES spectra on of $Fe_{16}N_2$ and $Fe_{16}N_0$ on both Fe4e and Fe8h sites are shown in (g) and (f), respectively. The horizontal dash blue line refers to the normalized absorption value as 0.5. The absolute K-edge of XANES simulation of Fe metal is shifted 10.5 eV higher compared to that of Fe metal XANES measurement.

Most importantly, it is found that the absorption edges of Fe4e for E⊥(002) surface plane and Fe8h for E//(002) surface plane with N ($Fe_{16}N_2$) consistently shift to higher absorption energies as compared to absorption edges of $Fe_{16}N_0$. These polarizations correspond to the directions of Fe-N bonds. It is well established that the absorption edge is consistently shifted to higher energies with higher Fe valance states (figure 4.11), indicating that the energy shift in the Fe absorption edge is associated with the charge transfer from Fe to N.

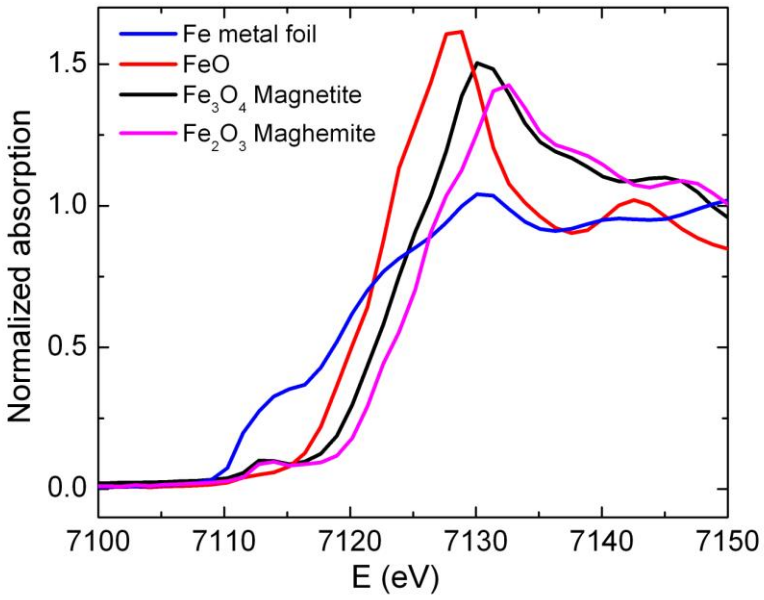

Figure 4.11 The reference XANES spectra of Fe with various valance states. These show the correlation between energy shifts and charge transfer. It is well established that the absorption edge is consistently shifted to higher energies with higher Fe valance states, indicating that an energy shift in the Fe absorption edge is associated with the charge transfer from Fe to ligand.

Bearing the present "cluster + atom" model in mind, it is possible to explain some of the experiments such as N site ordering effect and strain effect as observed previously.

4.6 N site ordering effect

In the previous chapters, we have explicitly studied the relationship between the magnetization and the degree of N site ordering. Here we provided a model discussion based on the "cluster+ atom" model to illustrate how it affects the magnetism in this Fe-N system. As shown in figure 4.12a, the chemically ordered $Fe_{16}N_2$ possess a crystal structure that the N occupies every other interstitial site. In this case, the Fe_6N are spatially isolated from each other in the sense that there are no corner-sharing or edge-sharing cases. This will cause the Fe sites interior the clusters to produce localized features and provide a high spin state.

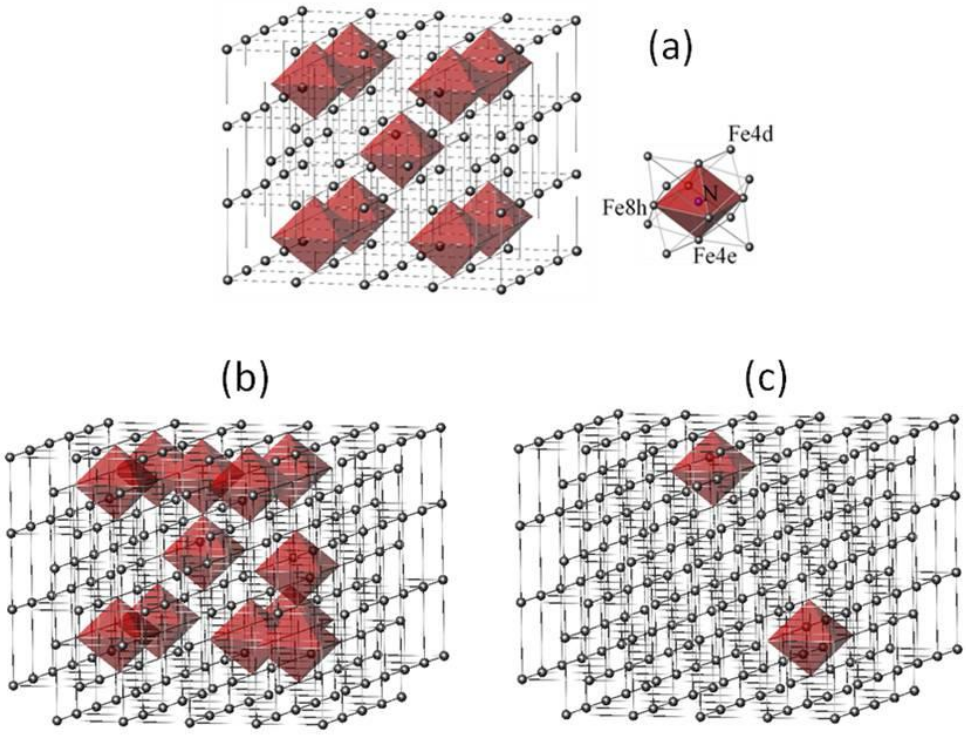

Figure 4.12 (a) $Fe_{16}N_2$ crystal structure; (b) N rich local region in Fe_8N; (c) N poor local region in Fe_8N

In that case, strong Coulomb interaction is brought up due to the charge difference interior and exterior to the cluster region, and consequently leads to the appearance of localized electrons on Fe sites within the Fe-N clusters (Fe4e and

Fe8h), and itinerant band-like electrons on the rest of the Fe sites (Fe4d) outside the clusters. In the atomic limit, a magnetic moment of $4\mu_B$/Fe is realized given Hund's first rule for highly localized electrons, and ~ $2.0\mu_B$/Fe is considered for band-like electrons according to metallic Fe behavior. This will produce an average magnetic moment of ~$3.5\mu_B$/Fe for the chemically ordered $Fe_{16}N_2$. However, in Fe_8N, due to the N random occupation, there exists both N-rich and N-poor local regions, as schematically shown in figure 4.12(b) and (c). In the N-rich case, the redundancy of Fe-N clusters inevitably causes the appearance of "connected" neighboring Fe-N clusters, in which the corner-shared or edge-shared Fe atoms are present. These Fe atoms closely resemble the local chemical environment of Fe sites in N-rich phases such as Fe_4N or Fe_3N; in which case, the significant charge difference brought up in a "separated cluster" scenario disappears. Consequently, electrons residing on these sites evolve from highly localized atomic-like states to itinerant band-like states, again due to the reduction of Coulomb interaction. In the N-poor case, though the "cluster separation" is still maintained, the dominant population of Fe sites is metallic-like, which also leads to the reduction of average magnetic moment. To give a quantitative estimation, in α"-$Fe_{16}N_2$, 75% of iron sites (Fe4e and Fe8h) have only one N as the nearest neighbor (NN). The remaining 25% consists only of Fe4d with no surrounding N . However, in α'-Fe_8N, the percentage of iron sites with 0, 1, 2 and 3 N atom(s) as NN was calculated under the binomial distribution assumption using the following equation. The result is summarized below

$$P_m = \frac{6!}{(6-m)!m!}\left(\frac{1}{8}\right)^m\left(1-\frac{1}{8}\right)^{n-m}$$

m	0	1	2	3	Total
P_m(%)	44.88	38.47	13.74	2.61	0.997

where P_m is defined as the percentage of the iron sites that have m N atoms as NN. Similarly, we consider that highly localized Fe sites (m=1 case) possess a magnetic

moment of $4\mu_B$ and band-like Fe sites (m=0, 2 and 3) possess a moment of $2\mu_B$. The average magnetic moment of $2.6\mu_B$/Fe is obtained, which is substantially lower than that of $Fe_{16}N_2$. As for the N partially ordered case, a non-trivial scenario could occur if Fe-N clusters are interconnected in a macro scale, say a few hundreds of atoms, the assumption of the magnetic moment of 4 μB/atom for the m=1 case would be no longer valid. From the perspective of bond percolation theory, the threshold impurity concentration P_c is 0.12 for an fcc lattice[77], which is less than that in Fe/N=8/1 case (p=0.125). This suggests a random distribution of the N in this lattice system would cause a global connection of Fe-N octahedral clusters and give rise to band-like iron behavior. From a broader perspective, to rationalize the giant magnetic moment, it is essential to consider the formation of localized electron states where Hund's rule can be suitably applied. The present "cluster+atom" model considers the electron localization and explicitly discusses the evolution from localized to itinerant electron states of Fe due to the local chemical environment change, in which the N site ordering effect can be interpreted.

4.7 Strain effect on the magnetization of $Fe_{16}N_2$

In the previous chapter, the polarized neutron reflectivity study told us that when $Fe_{16}N_2$ was epitaxially grown on MgO substrate, which has a relatively large lattice mis-match (4.2%). By tuning the underlayer thickness, the magnetization of $Fe_{16}N_2$ could vary in a wide range, changing from high $4\pi M_s$ up to 3.1 T to normal magnetization of $4\pi M_s$ 2.1 T. This observation already suggests that even chemical ordering is achieved, the formation of giant M_s requires suitable strain condition for epitaxial films.

It is known that the SP curve describes the variation of average magnetic moment with the electron concentration in the framework of itinerant electron bands. To rationalize the giant M_s which is beyond the SP curve, it is essential to require the electrons of interest to possess localized feature. As schematically illustrated in figure 4.13a, the spin configuration of a Fe atom in solids is determined by the

interplay between the crystal field (Δ), the kinetic energy (k) and on-site Coulomb interaction (U). As the inter-atomic distance progressively increases, the 3d electrons residing on Fe sites have tendencies to possess localized features, accompanying the reduction of both the kinetic energy (k) and crystal field (Δ), but enhancement of Coulomb interaction (U). Interesting scenario occurs when equilibrium inter-atomic distance (lattice constant) "sits" in the neighborhood of the crossover point between Δ+k and U. Namely, at equilibrium lattice constant a_0, if the condition $|\Delta+k-U| \ll U$ is satisfied, a crystal field with small perturbation due to the lattice distortion (Δ', $|\Delta-\Delta'| \ll \Delta$) can induce a modification of kinetic energy (k') and Coulomb interaction (U'), which substantially influence the spin configuration of Fe sites as long as conditions $\Delta+k-U>0$ and $\Delta'+k'-U'<0$ are spontaneously satisfied. In the case of $\Delta+k-U>0$, intermediate spin (IS) state is energetically favorable, which predicts a non-high M_s scenario and is consistent with reports based on bulk $Fe_{16}N_2$ samples in which the lattices are known to be fully relaxed[78]. However, in strained epitaxial films, a modulation of the lattice constant is anticipated, in which the proposed scenario ($\Delta'+k'-U'<0$) becomes possible and subsequently yields a giant M_s. Though local spin density approximation (LSDA) based calculation show insensitive dependence of the lattice constant[79] and favor an intermediate spin configuration, it is generally accepted that Coulomb U is underestimated in the LSDA, which may produce large discrepancy given the delicate requirement of the onset of the high spin ground state. The previous reported M_s value of Fe-N epitaxial films sensitively depends on the choice of substrate, buffer layers and processing techniques, though careful x-ray and electron diffraction results on these samples all show "similar" crystal structure of $Fe_{16}N_2$ phase as proposed by Jack et al[80], implying the subtle correlation between the magnetism and straining in this material system.

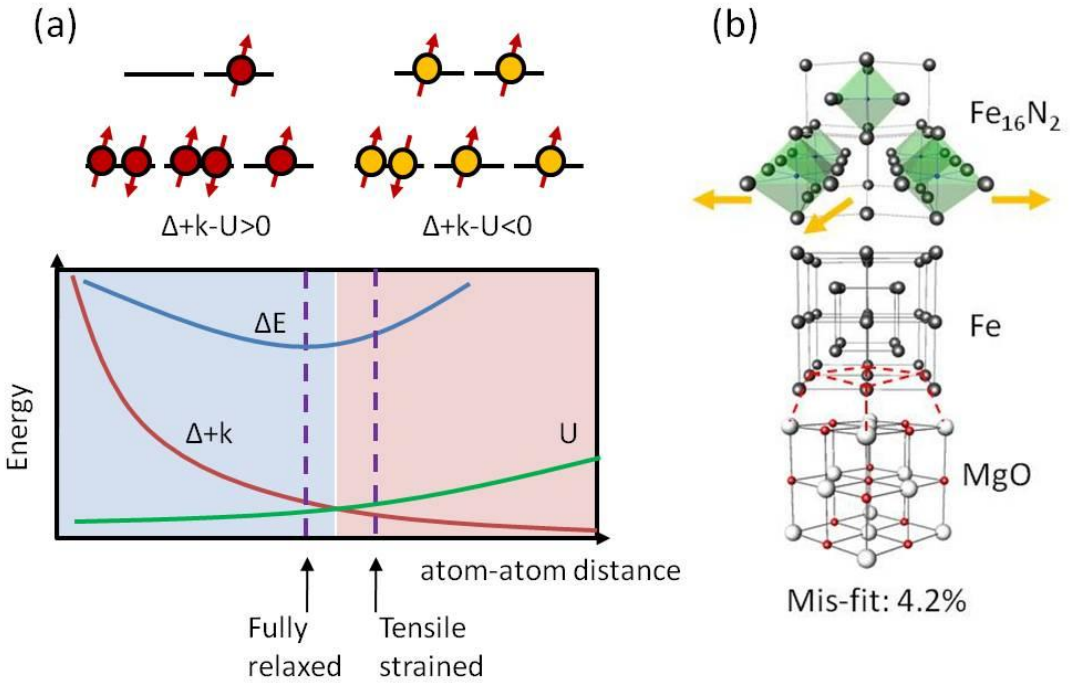

Figure 4.13 (a) A schematic drawing of the behaviors of different energy terms of the 3d electrons of Fe in solids as a function of inter-atomic distance. ΔE: total energy; Δ+k: sum of crystal field and kinetic energy; U: Coulumb energy. The dashed lines show the equilibrium position (left) and tensile strained position (right). Zones with different colors indicate the different spin configurations of Fe sites (top) due to the interplay between Δ+k and U. (b) A sketch of epitaxial relationship of $Fe_{16}N_2$/Fe/MgO with (001) orientation. Due to the lattice mis-fit, the $Fe_{16}N_2$ is under tensile strain, which can be tuned by adjusting the thickness of Fe buffer.

4.8 Outlook on the "cluster + atom" model

Finally, we provide a speculative outlook on synthesizing materials with giant saturation magnetization. Usually, large inter-atomic distance is necessary to favor electron localization, which effectively increases the volume and reduces the magnetization in macroscopic scale even locally, high moment is achieved. Encouraged by the observation in the $Fe_{16}N_2$ system, the configuration of individual clusters + atoms provides local potential fluctuation and offers an alternative to realize electron localization without sacrificing the volume. As is clearly seen, the

key feature for a material to exhibit giant saturation magnetization is the coexistence of localized electrons and itinerant electrons, in which giant local moment and collective ferromagnetism can be realized at the same time. More specifically, the "spatially isolated Fe_6N" clusters behave as quantum dots in matrix due to the charge density difference with highly localized electron orbitals, which serve as the fundamental building blocks. Based on this concept, we proposed some other structures that are structurally relevant to the ideal of "cluster + atom" and consequently, may produce material with unique magnetic properties (Figure 4.14)

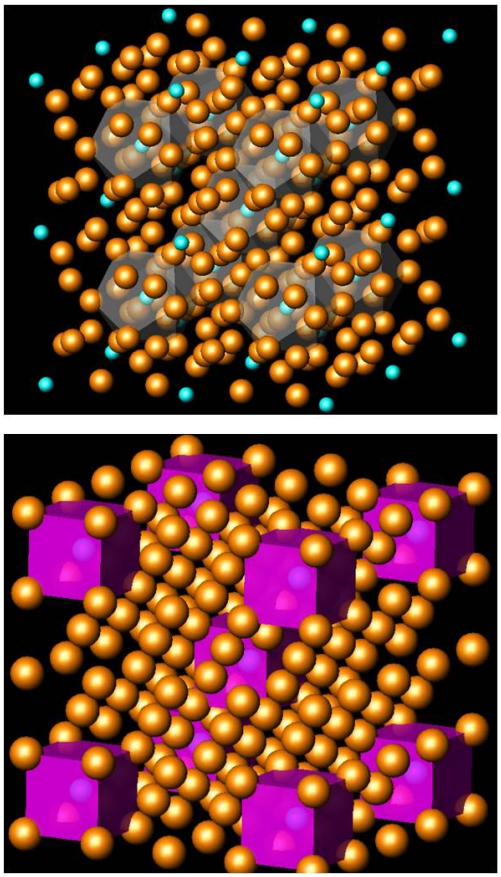

Figure 4.14 Structures that may exhibit unique magnetic properties given the "spatial isolation of the octahedrons"

Reference

[56] W Y Lai, Q Q Zheng and W Y Hu, *J. Condens. Matter* 6 L259 (1994)

[57] A. Sakuma, *J. Appl. Phys.* 79 5570 (1996)

[58] F. Janak, Phys. Rev. B 16, 255 (1977)

[59] Jingsong He, Yumei Zhou, Wuyan Lai and C. Y. Pan, *Phys. Rev.* B 52 6193 (1995)

[60] V. I. Anisimov, J. Zaanen and O. K. Anderson, *Phys. Rev.* B 44 943 (1991)

[61] P.E. Blöchl, *Phys. Rev.* B 50, 17953 (1994)

[62] V. Anisimov, F. Aryasetiawan, and A. Lichtenstein, *J. Phys.: Condens. Matter* 9, 767 (1997)

[63] J. Sánchez-Barriga et al., *Phys. Rev. Lett.* 103 267203 (2009)

[64] V. I. Anisimov, J. Zaanen and O. K. Anderson, *Phys. Rev.* B 44 943 (1991)

[65] R. S. Han, Z. Z. Gan, D. L. Yin and Q. Liao, Phys. Rev. B 41 6683 (1990)

[66] G. W. Fernando, R. E. Watson, M. Weinert, A. N. Kocharian, A. Ratnaweera and K. Tennakone, *Phys. Rev*. B 61 375 (2000)

[67] H. Takahashi, M. Komuro, M. Hiratani, M. Igarashi and Y. Sugita, *J. Appl. Phys.* 84 1493 (1998)

[68] Jian-Ping Wang, et. al., IEEE Trans Magn (In press)

[69] The XMCD principle is shown in detail in appendix

[70] A Ligand field theory based multiplet calculation using Cowan software[70] has been performed to simulate these satellites as shown in fig.2c and d. For a reasonable estimation, we used the spectrum of pure iron thin film sample collected by C. T. Chen et al[70] as the band like part signals. For the additional parts, our simulation takes into account the atomic Fe $3d^6$ to $2p^53d^7$ multiplet transition with D4h crystal symmetry. The 3 parameters X_{400}, X_{420} and X_{220}[70] which are used to manipulate D4h crystal field are set to be 3.286, 0, 2 respectively. This corresponds to a 1ev crystal field with explicit inclusion of lattice distortion along c-axis. With and without considering the spin-orbital coupling in the final states does not show significant change through the calculation. A reducing factor on the Slater integral is applied to take care of the absorbing ions and ligands. It also considers the experimental broadening due to the core-hole life time (Lorentzian broadening) and

instrumental resolution (Gaussian broadening).

[71] D. E. Sayers et al., Phys. Rev. Lett. 27, 1204 (1971)

[72] J.J. Rehr et al., Rev. Mod. Phys 72, 621 (2000)

[73] J. Stöhr, NEXAFS Spectroscopy, Springer (1992)

[74] A. Bianconi et al., Phys. Rev. B 26, 6502 (1982)

[75] A. L. Ankudinov, et al., Phys. Rev. B 67, 115120 (2003).

[76] To construct the $Fe_{16}N_2$ crystal, a space group of I4/mmm and experimental lattice constants were used. a cluster of atoms with a size of 5.47 Å is applied for the calculation of full-multiple scattering (FMS), a cluster of atoms with a size of 4.0 Å is used for the calculation of the self-consistent-field (SCF) muffin-tin atomic potential, the Hedin–Lundqvist self-energy is used by default. To calculate the XANES of $Fe_{16}N_0$, the crystal structure and lattice constant were chosen to be identical to single crystal $Fe_{16}N_2$. The sites that originally occupied by N in $Fe_{16}N_2$ were left empty on purpose when constructing the dummy structure $Fe_{16}N_0$.

[77] C. D. Lorenz and R. M. Ziff`, Phys. Rev. E 57`, 230–236 (1998)`, for a bct structured Fe-N`, the crystal structure viewed along 110 direction closely resembles the fcc lattce matrix.

[78] J. M. D. Coey, et. al., J. Phys. Con. Mater. 6, L23 (1994)

[79] H. Tanaka, et. al., Phys. Rev. B 62, 15042 (2000)

[80] K. H. Jack, Proc. R. Soc. 208 (1093), 200 (1951)

Chapter V Perpendicular magnetic anisotropy in $Fe_{16}N_2$

5.1 Introduction

In the previous three chapters, we have focused on the saturation magnetization of $Fe_{16}N_2$. Here we present another magnetic property – magnetic anisotropy of this material system. We will first demonstrate a general framework for realizing and modulating perpendicular magnetic anisotropy in a rare-earth-element and heavy-metal -free material system. Using GaAs(001)/Fe(001) template, we have developed a synthesis scheme to produce epitaxial body center tetragonal Fe-N with (001) texture. By varying the N doping concentration, the crystal tetragonality (c/a) can be tuned in a relatively wide range. It is found that the Fe-N layer developed a strong perpendicular magnetic crystalline anisotropy (MCA) as it approaches the iron nitride interstitial solubility limit. Further annealing process significantly improves the MCA due to the formation of chemically ordered $Fe_{16}N_2$. In addition to realize an MCA up to 10^7 erg/cm3 , the spin polarization ratio (P~0.52), as probed directly by a Point Contact Andreev Reflection (PCAR) method, even shows a moderate increase in comparison with normal metal Fe (P~0.45). These combined properties make this material system a promising candidate for applications in spintronic devices and also potential rare-earth-element free magnets.

5.2 Iron nitrides for future perpendicular spintronic devices

Giant magnetoresistive devices with perpendicular magnetic anisotropy have drawn increased attention due to their potential for higher storage densities in magnetic memory applications[81,82,83]. To fabricate such devices, one essential component, the ferromagnetic electrode, which serves as a polarized electron source, has to satisfy two criteria: 1) High value of spin polarization; 2) Magnetic easy axis points out of the film plane. The focus of most efforts has been on transition metal (TM) and heavy elements based multilayers, which are proven structures with high perpendicular magnetic anisotropy (PMA). However, concerns such as large

damping due to the heavy elements and poor compatibility with the common barrier material prevent them from being realized in practical applications. For magnetic tunnel junction (MTJ) device, the recently developed ultra thin FeCoB layer with PMA offers a new route to tackle the problem, in which a high tunneling magnetoresistance (TMR) (>100%) and an easy axis perpendicular to the film plane are simultaneously realized[84]. However, the utilization of interface anisotropy that produces out-of-plane easy axis demands precise and critical control of layer thicknesses (less than 1.3 nm) and interface conditions.

Iron nitrides are known to form various phases. Much attention was focused on their saturation magnetization due to the debatable claim of giant M_s ($4\pi M_s$~3.0T) observed on the $Fe_{16}N_2$ phase decades ago.. However, the magnetic anisotropy of this material system has received less attention since most of the known iron nitride phases only possess low magnetocrystalline anisotropy (MCA). In principle, $Fe_{16}N_2$ and its relevant Fe-N martensite form a tetragonal distorted Fe lattice As a consequence, due to the reduced crystal symmetry, a large MCA is expected to develop, given the reduced energy separation between the two orbitals d_{x2-y2} and d_{xy}, which are located below and above the Fermi level, respectively[85]. Since its a-lattice constant (in-plane lattice constant) closely matches that of bcc Fe, this allows the epitaxial control and consequently the realization of an MCA perpendicular to thin film plane if Fe (001) substrate is provided.

Following this idea, we grew epitaxial Fe-N martensite thin films. We systematically controlled the stoichiometry of Fe-N films using a facing-target sputtering method, which is secondary electron free from substrate with the confined plasma just between the targets. A structural characterization based on x-ray diffraction (XRD) and transmission electron microscopy (TEM) imaging reveal the crystal quality and film morphology, which shows that the c-axis of the Fe-N layer is perpendicular to the film plane and is coherently adapted on the Fe(001)/GaAs(001) template. A complementary study of magnetometry and polarized neutron

reflectometry show that an MCA perpendicular to the film plane is developed in the Fe-N layer. Moreover, a subsequent post-annealing process facilitates the formation of chemically-ordered $Fe_{16}N_2$ phase and further enhances the MCA, which is evaluated to exceed 10^7 erg/cm^3. The combination of the large magnetocrystalline anisotropy and its giant saturation magnetization may point a new direction for the synthesis of rare-earth-element free magnets in future. In addition, we measured the spin polarization ratio of partially ordered $Fe_{16}N_2$ thin films using a Point Contact Andreev Reflection (PCAR) method [86], which shows a relatively large spin polarization ratio (P~0.52). These combining properties make the $Fe_{16}N_2$ and Fe-N martensites a promising candidate for the ferromagnetic electrodes for future spintronic devices.

5.3 Tunable tetragnality and magnetic characterization of Fe-N martensites

It is known that the α'-Fe-N martensites form interstitial solid and can accommodate N concentration up to ~13 at.% [87]. In our previous study, we demonstrated that with an Fe buffer layer providing (001) epitaxial constraint and allowing the increase of the N_2 partial pressure during Fe-N growth, it is possible to epitaxially support the Fe-N martensites with (001) texture. As schematically shown in figure 5.1a, in principle, by controlling the dopant concentration (N at. %), the c-lattice constant can be adjusted while the a-lattice is constrained by the underneath Fe buffer layer. As a result, the tetragnality can be fine-tuned. In light of these discussions, we systematically fabricated samples with Fe-N layer thicknesses in the range of 45~50 nm using a facing-target sputtering method. Prior to the growth of Fe-N layer, an Fe layer with a fixed thickness of 22 nm is deposited on GaAs (001) substrate at temperature of 250℃ to encourage (001) epitaxy at an Ar pressure of 5 mTorr. The subsequent Fe-N layer is prepared by sputtering Fe targets with thoroughly mixed Ar and N_2 working gases (~1% N_2).

In figure 5.1b, the XRD peaks (measured by Philips X'Pert Pro X-ray Diffractometer with Cu Kα radiation) from Fe-N (002) showed a consistent shift

towards the lower 2θ values, indicating an elongated d-spacing along the (001) direction with a typical texture deviation of 0.88 ° (Figure 5.1c) according to the rocking curve measured on the Fe-N (002) diffraction peak. This suggests the c-lattice constant substantially enhances (>10%) as the increase of N interstitial solubility given the progressively higher N_2 partial pressure (Figure 5.1d) used in depositing these samples.

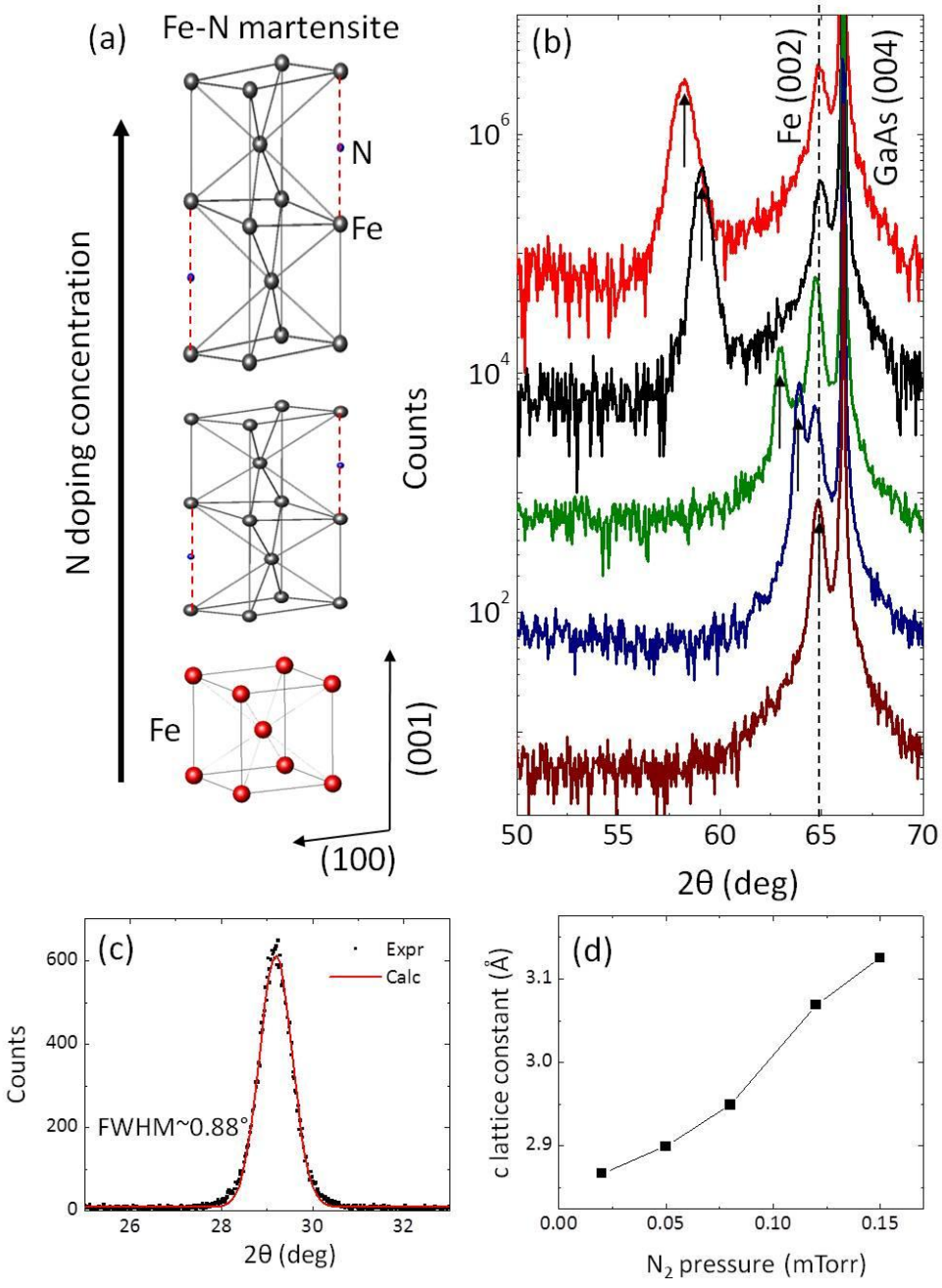

Figure 5.1 (a) A sketch of different stages of Fe-N tetragonality (c/a) due to the N interstitial doping. (b) XRD of as-deposited Fe-N martensite thin films with different c-lattice constant. Data from different samples are consistently vertically shifted by a factor of 10 in log scale. The substantial horizontal shift of Fe-N (002) diffraction peak (labeled by arrows) is due to the different N_2 partial pressure used in the growth of each sample. (c) Rocking curve measured on Fe-N (002) peak of the sample with largest c-lattice constant. (d) C-lattice constant calculated from XRD in (b) as a function of N_2 partial pressure in the growth of each sample (all other deposition conditions are kept the same).

To further examine the crystal quality and epitaxial relationship of the present films, we used high resolution (HR) transmission electron microscopy (JEOL 2200FS) (TEM) to study a cross-sectional sample that may possess the largest c-lattice constant according to the XRD. Figure 5.2a shows a high-angle annular dark-field TEM image with low magnification. In addition to the GaAs substrate, Fe and Fe-N layers as outlined in the figure, Cr cap layer (~8 nm) and carbon (~1 μm) layer are deposited *ex-situ* for protection of further oxidation. The brightness contrast between two layers is clearly seen, which is due to the presence of light element N in the Fe-N layer. Aberration-corrected lattice images with nominal resolution of <0.1nm were recorded at the Fe/Fe-N interface (Figure 5.2b) to reveal the epitaxy of both layers. To analyze the periodicities, a diffractogram from a 128 x 128 pixels region (i.e. region A) was computed, and the X and Y scan directions calibrated so that the diffraction spots positions closely matched the known d-spacings for the α-Fe structure, as shown in figure 5.2c. The calculated d-spacing matches with a [110] zone axis (axis that parallel to the observation direction) for both Fe and Fe-N. In addition, the in-plane direction only presents one periodicity, suggesting perfect lattice matching along that direction. Two periodicities are seen in the interface region (box A), indicating the presence of two types of d-spacing along film normal. Similar periodicity analysis in region of Fe-N layer (box B) shows an expected single d-spacing and is coherent with the longer distanced d-spacing obtained in analyzing box A. These observations demonstrate

the effect of doping N atoms in the crystalline Fe causes a directional expansion of the crystal lattice along c-axis perpendicular to the film plane while the in-plane lattice constant (a) is maintained and coherent with the Fe underlayer. The calculated d-spacing reasonably matches with that observed by XRD.

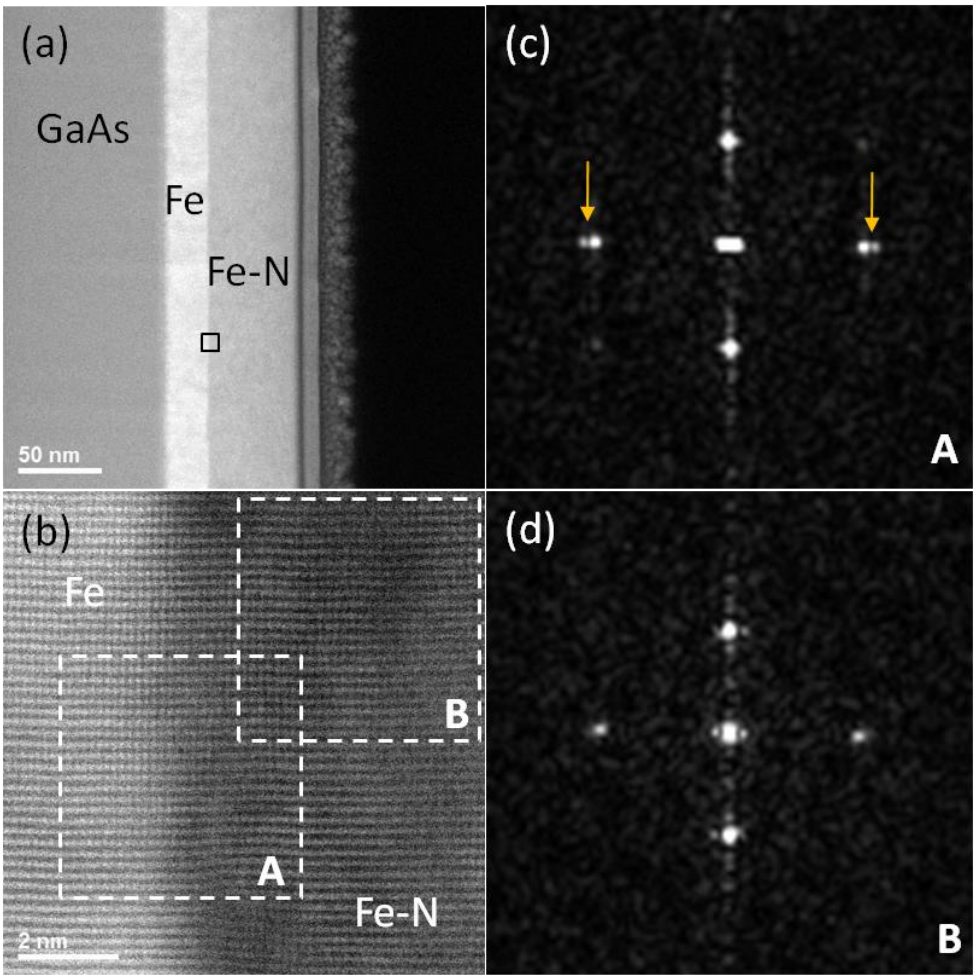

Figure. 5.2 (a) Low-mag HAADF image of a cross-section epitaixial Fe-N martensite thin film. The layered structure at the top interface is due to the Cr and C capping as described in the text. (b) A zoom-in look of the lattice image acquired at the Fe/Fe-N interface (outlined as a box in (a)) with a [110] zone axis. The images with in the boxes labeled as A and B are processed by diffractogram as shown correspondingly in (c) and (d). A clear "double peak" is shown in A (highlighted by yellow arrows) corresponding to the lattice periodicity from Fe and Fe-N, respectively. Only one type of lattice periodicity is shown in (d), corresponding to only one d-spacing in Fe-N layer.

To systematically study the magnetic properties of these films, first we investigated the in-plane M-H hysteresis loops (Figure 5.3a) measured by a Princeton Measurements Vibrating Sample Magnetometer at room temperature, which clearly reveal a correlation between the saturation magnetic field (H_s, defined in Figure 5.3b) and the average c-lattice constant as determined from XRD. The selective M-H loops (normalized to saturation magnetization) of these samples are shown in Figure 5.3b. An evolution from typical easy axis to hard axis loop is expectedly seen as c-lattice constant of the Fe-N layer progressively increases, with its highest H_s larger than 4 kOe, suggesting a MCA developed in the film due to the presence of Fe-N layer. However, the small but notable M_r suggests the film possess both in-plane and out-plane magnetization components due to the existence of soft Fe underlayer and its strong exchange coupling with the Fe-N layer.

To facilitate the discussion of the magnetic contribution of Fe underlayer, we studied the thickness dependence of in-plane M-H loops for samples prepared at N_2 partial pressure of 0.12 mTorr, (deposition condition to fabricate Fe-N films with largest c/a ratio). As shown in Figure 5.4a and 4b, by increasing the thickness of Fe-N layer, the saturation field saturates rapidly and levels off at around H_s~7 kOe, suggesting the films possess a remanent (external field H=0) magnetic configuration as shown in the inset. In particular, as the thickness of Fe-N layer increases, the magnetic contributions from the underlayer (Fe) and interfacial (Fe/Fe-N) regions become progressively weak. In that case, the saturation field is determined by the crystalline anisotropy of the hard layer towards the top interface. The presence of the typical hard axis loop measured in-plane show a clear reversible magnetization rotation process, which provides the evidence of out -of-plane oriented magnetization domains in the Fe-N layer.

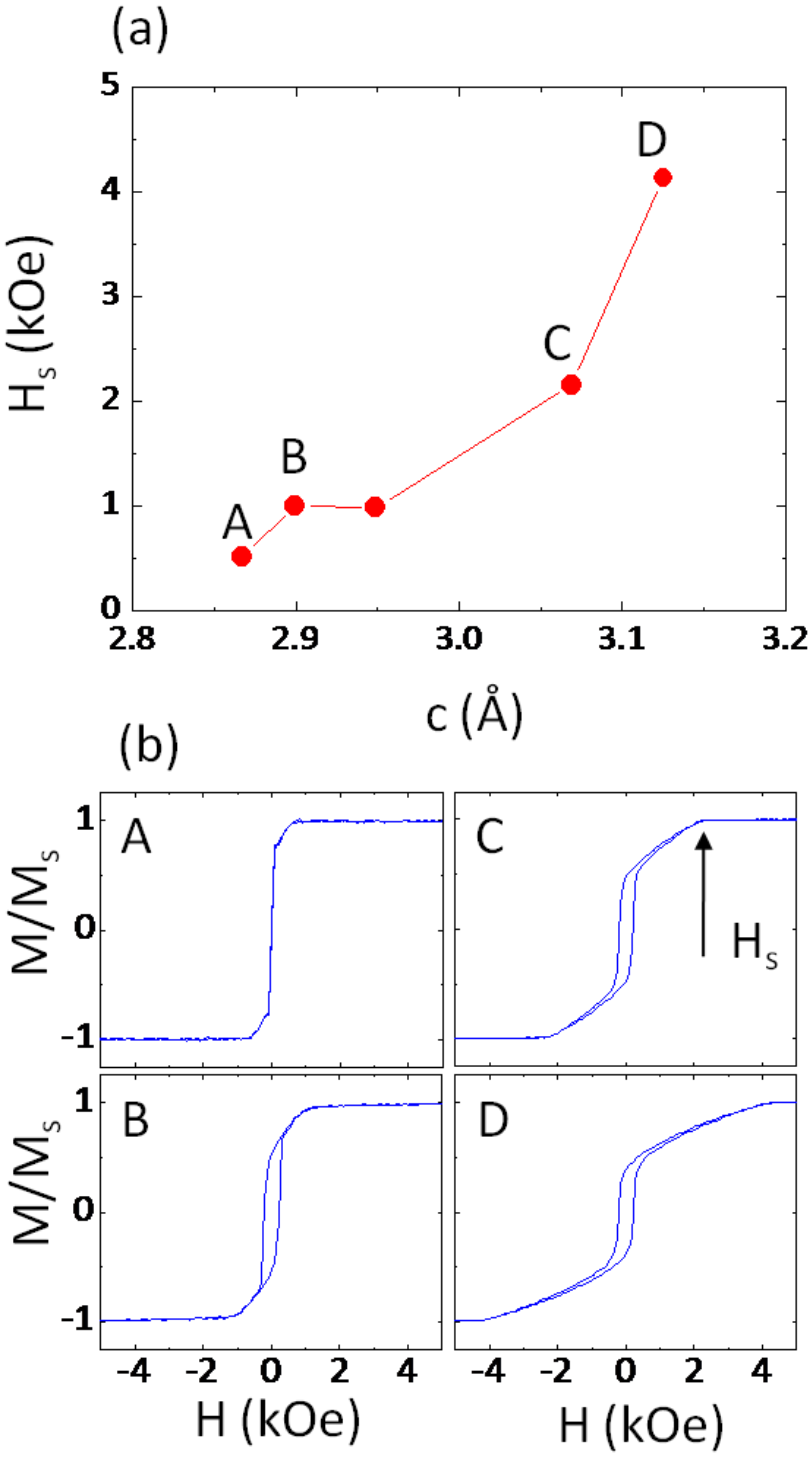

Figure 5.3 (a) In-plane saturation field (H_s) as a function of c-lattice constant according to XRD results in FIG. 1. (b) Selective M-H loops measured in-plane for samples labeled A-D in accordance with that presented in (a). The magnetic field of the point as marked by the arrow in C is the saturation field (H_s) defined in this study.

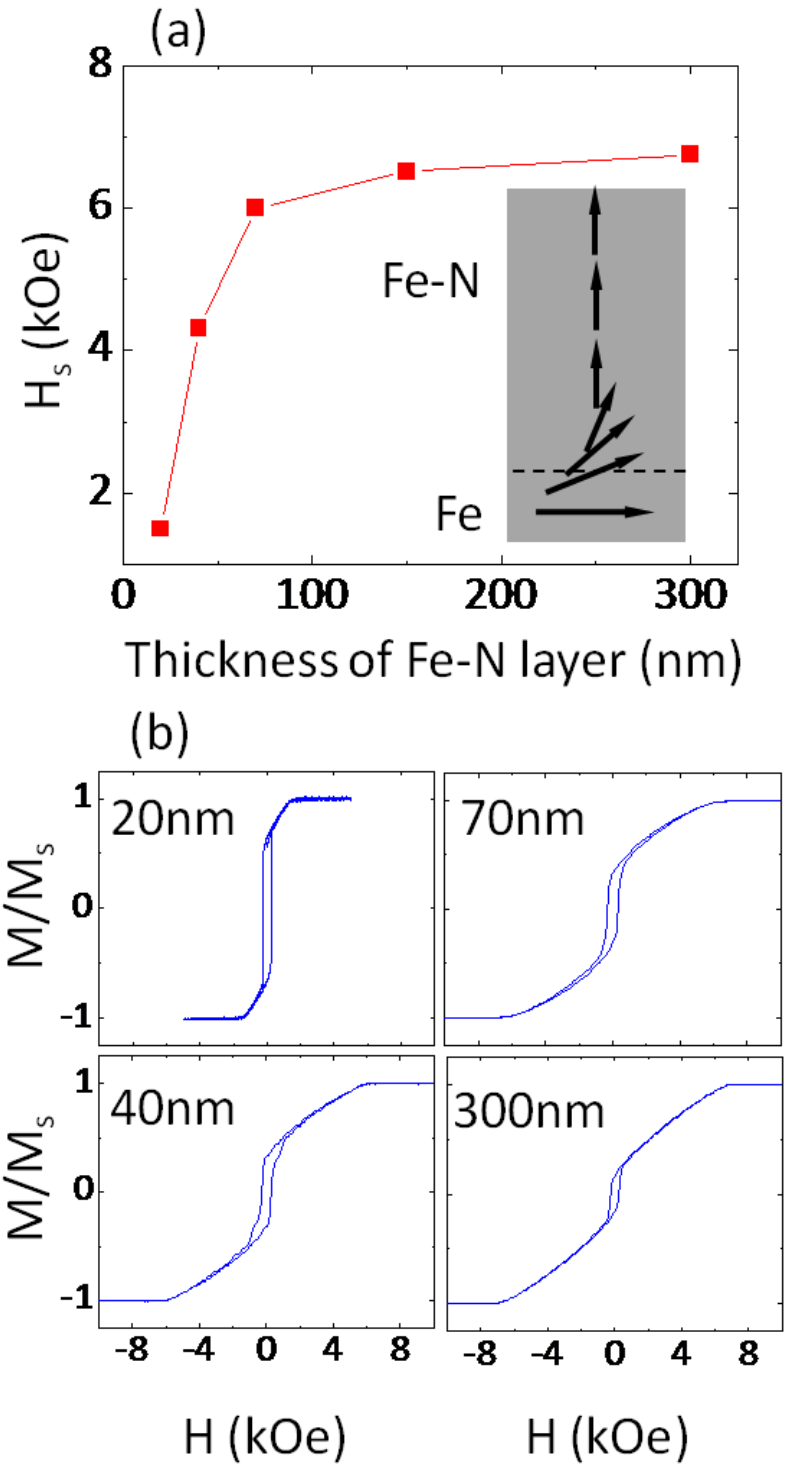

Figure 5.4 (a) In-plane saturation field (H_s) as a function of thickness of Fe-N layer with same tetragonality (c/a). Inset shows the schematic drawing of magnetization configuration at remanence as explained in the text. (b) Selective M-H loops measured in-plane for samples with different Fe-N layer thickness as outlined in each figure.

5.4 Perpendicular magnetic anisotropy in $Fe_{16}N_2$

Furthermore, in a previous chapters, we showed that a dramatic increase of saturation magnetization was observed after in-situ post-annealing the as-deposited Fe-N films, which is attributed to the presence of chemically ordered $Fe_{16}N_2$ and is associated with the increase of N site ordering (D).Here, by systematically analyzing M-H loops of optimally annealed (120 ℃ for 40 hrs) samples with same bilayer structure, we show that the H_s also increases monotonically.

In figure 5.5a, the XRD patterns of an as-deposited and an annealed sample with the same nominal structure (Fe-N(48nm)/Fe(22nm/GaAs)) were compared. The main difference occurs at $2\theta=28.6°$, where the XRD pattern of the annealed sample develops a robust peak and can be indexed to $Fe_{16}N_2$(002), originated from the superlattice diffraction given the alternating occupancy of N in crystalline $Fe_{16}N_2$ (inset of figure 5.5a). By analyzing the integrated intensity ratio between (002) and (004) peaks, it is possible to estimate the volume fraction of the $Fe_{16}N_2$ in Fe-N layer. To facilitate the discussion, we introduced a parameter D, which describes the degree of N ordering as shown in detail previously. The in-plane M-H loops of both samples are compared in figure 5.5b. It is seen the H_s increased substantially in the annealed sample. More samples with different D value are compared in figure 5.5c, in which a correlation between D and H_s is clearly seen.

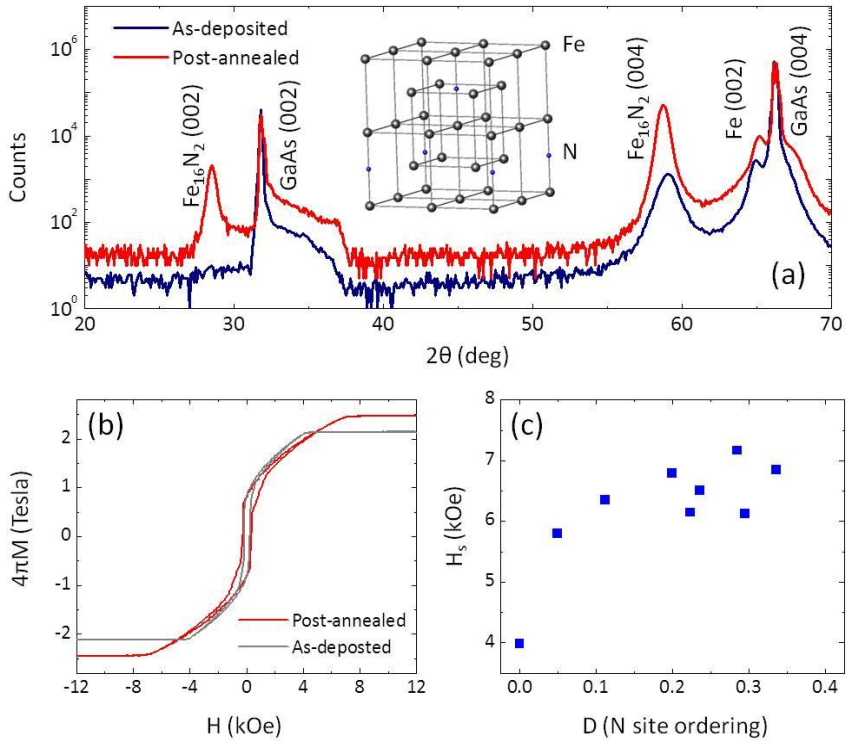

Figure 5.5 (a) X-ray diffraction pattern of as-deposited and annealed samples with similar structure (Fe-N(48nm)/Fe(22nm)GaAs). The inset shows the crystal unite cell of $Fe_{16}N_2$. The ordered site occupation of the N atoms causes the diffraction of $Fe_{16}N_2$(002), which is not seen in as-deposited sample. (b) M-H loops measured in-plane for the two samples shown in (a). (c) in-plane saturation field (H_s) as a function of N site ordering D as defined in chapter II

To further evaluate the magnetic configuration in more details, both in-plane and out-of-plane M-H loops for a partially ordered sample (D=0.32) are shown in Figure 5.6a. As for the out-of-plane loop, as stated above, due to the magnetic contribution of the Fe layer, the samples develops both in-plane and out-plane magnetization components at remanence state as schematically shown in the inset of Figure 5.6a. As a result, the in-plane magnetization component causes the large demagnetization linear background up to about 16 kOe in order to fully saturate the sample along the out-plane direction. However, at applied field of H~5.7 kOe, a switching is clearly seen which is originated from the magnetization flip of the

out-of-plane component in the Fe-N layer. For a rough estimation, the H_s measured in-plane coincides with the larger switching point measured out-of plane, suggesting the anisotropy field H_k is close to H_s with crystalline anisotropy (K_u) aligning perpendicular to film plane. Therefore, we can calculate[88] the crystalline anisotropy in the Fe-N layer as a function of N site ordering after knowing the saturation magnetization (M_s) of Fe-N layer (Figure 5.6b). The highest K_u is seen around ~10^7erg/cc, which agrees well with the previous reported value determined by torque curve measurements[89]. It is worth mentioning that the present synthesis process (deposition and post-annealing) does not produce fully ordered $Fe_{16}N_2$ from the structural analysis. In particular, the highest volume fraction of the $Fe_{16}N_2$ in the Fe-N layer, which is consisted of $Fe_{16}N_2$and Fe_8N, has been obtained to be ~39% according to the XRD analysis using the current sputtering fabrication process. However, the increasing trend of the K_u upon the degree of N ordering increases clearly shows that the anisotropy should be much higher for pure phase $Fe_{16}N_2$.

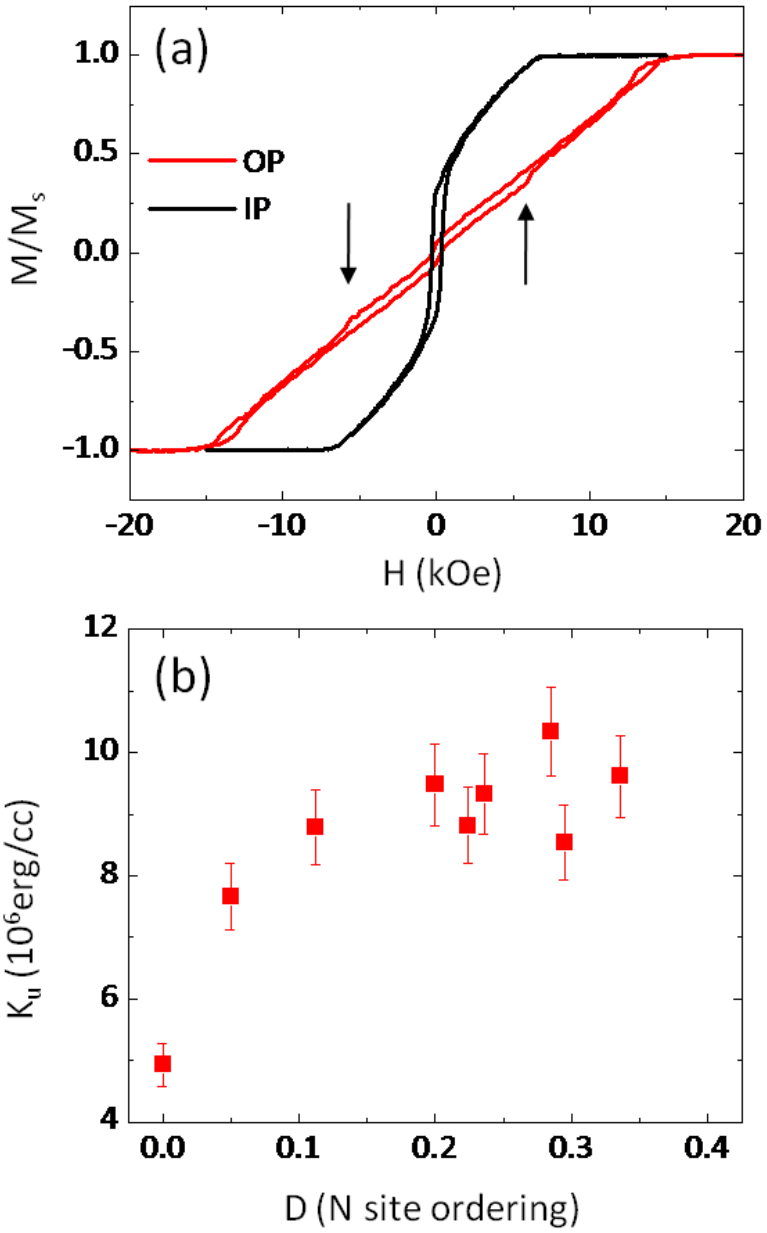

Figure 5.6 (a) In-plane (solid) and Out-of-plane (dash) M-H loops measured on one partially ordered $Fe_{16}N_2$ sample (D~0.32). The Fe-N layer switches at Hc~5.7kOe (black arrows). (b) Calculated K_u as a function of degree of N site ordering (D) in partially ordered $Fe_{16}N_2$ thin film samples as described in text. The dashed line here is a guide to the eye. All the samples have the same nominal thickness structure: Fe-N(48nm)/Fe (22nm)/GaAs.

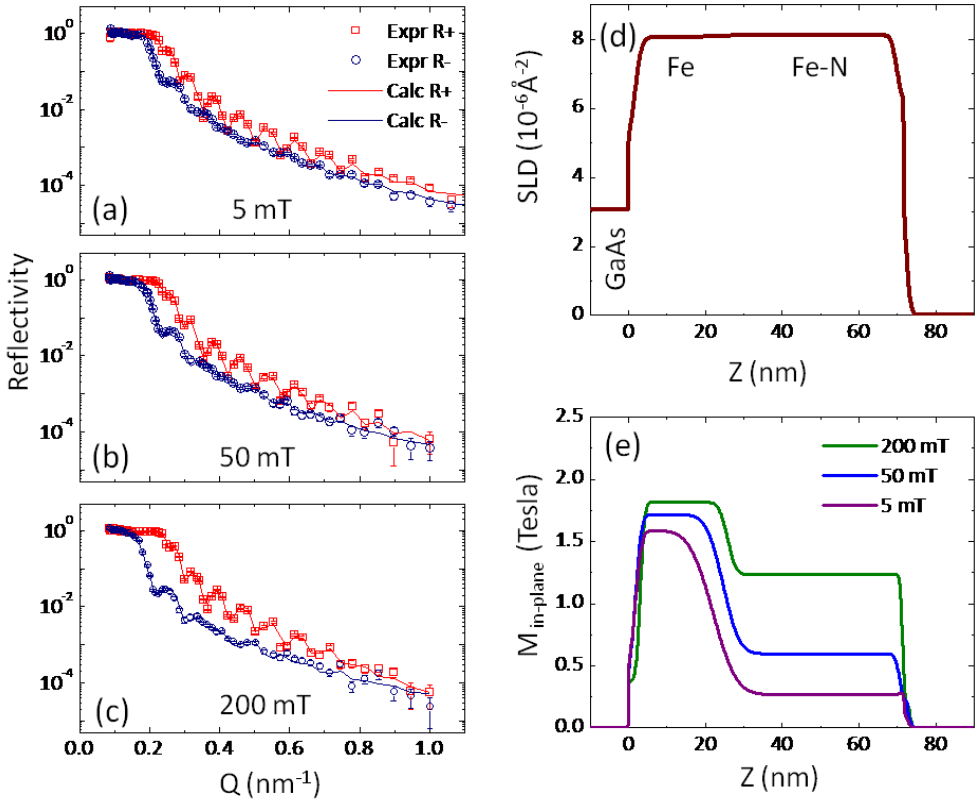

Figure 5.7 (a)~(c) Fitted polarized neutron with spin-up (R+) and spin-down (R-) reflectivity curves for an annealed sample at external field of 5, 50, and 200 mT. (d) Nuclear scattering length density and (e) Field dependent in-plane magnetization depth profiles as functions from the distance from the substrate

To confirm the magnetic configuration based on the hysteresis loop analysis, in-depth and field-dependence Polarized Neutron Reflectometry (PNR) experiments were performed using the Magnetism Reflectometer on beamline 4A at Spallation Neutron Source, Oak Ridge National Laboratory. When conducting the PNR experiments, an external magnetic field was applied parallel to the thin film plane. The non-spin-flip reflectivity curves of spin up and spin down neutrons were spontanously recorded. Representative fitted PNR spectra for one partially ordered sample are shown in figure 5.7a~c, in which three different in-plane fields smaller than the H_s are purposely chosen after saturating the sample at around H_s = 20 kOe. With the nuclear scattering length density (NSLD) closely matching the nominal

value (Figure 5.7d), the spontaneously fitted in-plane projection of the magnetization depth profile ($M(z)_{in\text{-}plane}$) was retrieved (Figure 5.7e). It is seen that in contrast to that of the Fe layer, the in-plane component of the magnetization vector $M(z)_{in\text{-}plane}$ of the Fe-N layer goes down drastically with decreasing in-plane external field. This can have two scenarios. In the first one, the Fe-N film forms in-plane nearly antiferromagnetic in-plane domains. In the second one, the film magnetization turns out-of-plane due to the out-of-plane easy-axis. The first scenario is possible only if the Fe-N film would have uniaxial in-plane anisotropy, which is not the case. In addition in the first scenario, a strong magnetic off-specular scattering would appear. However we did not record an increase in the off-specular scattering. In the second scenario, no additional off-specular scattering is expected, because the out-of-plane component of the magnetization vector is parallel to the momentum transfer Q and the in-plane parallel component contributes to the specular reflection. Hence the reduction of the in-plane magnetization originates from the evolution of the out-of plane magnetization component along the perpendicular easy axes. It is worth mentioning that the oscillation magnitude of the R^- curve is relatively small comparing to R^+. Since the oscillation magnitude is directly related to the SLD contrast between the film and the substrate. This observation is likely due to the SLD of the R^- is very close to that of the substrate in contrast to the SLD of R+. This effect is especially robust as it approaches the bottom interface (GaAs/Fe) interface, in which case the scattering behavior of that region is dominated by the reflectivity at high q_z and consequently results in the "smearing out" of the oscillation magnitude.

5.5 Spin polarization ratio measurement using PCAR

Encouraged by the magnetic characterization, we performed a *direct* measurement of the transport spin-polarization (SP) using PCAR on a partially ordered $Fe_{16}N_2$ sample in figure 5.8. A superconducting (Nb) tip was gently pressed into the sample to minimize the effect of surface oxidation. At least 10 such different

contacts were created and tested at a temperature of 1.6K. Figure 5.8a and b show normalized conductance $G(V)/G_n$ versus V/V_Δ, in which G_n is the conductance at applied voltage $V >> V_\Delta$ and V_Δ is the superconducting gap of Nb. The PCAR experimental curves were fitted by the modified[90, 91] BTK model[92] with the fitting parameters spin polarization, P, and barrier strength, Z. The superconducting gap, Δ, was fixed to the value for Nb. An effective temperature (3.5K) was used to improve the quality of the fit for low Z junctions (Figure 5.8 (b)) suggesting that electron heating was occurring. The noise observed in the data is relatively large, which is attributed to the weak signal produced as the SP is close to 0.5. Fits based on a ballistic model reproduces the experimental data reasonably well producing an apparent dependence of P on Z. As a result, intrinsic spin polarization value was obtained by extrapolating the result to Z=0.[93, 94, 95, 96] Figure 4 (c) shows the linear fit of P versus Z, which intercepts Z=0 at 0.52, namely the spin polarization of our sample approximates 52%. In comparison with reported values of ~45% on Fe samples using similar probing approaches[97], the present results show moderate enhancement.

5.6 Summary

In conclusion, we have spontaneously realized perpendicular mangetocrystalline anisotropy (MCA) and high spin polarization ratio (SP) by a simple scheme, namely, tuning the c-lattice constant of bcc Fe by interstitial doping of N. The in-plane lattice parameter of the present Fe-N films is close to bcc Fe, allowing a direct epitaxial adaption with a MgO barrier for MTJ and a Ag spacer for GMR applications. Furthermore, utilizing light-element (e. g. B, C, N) and ferromagnetic (e. g. Fe, Co, Ni) interstitial alloys to develop magnetic material with strong perpendicular MCA without using any *rare earth* elements offers promising approaches of searching and identifying new magnet materials for clean energy applications.

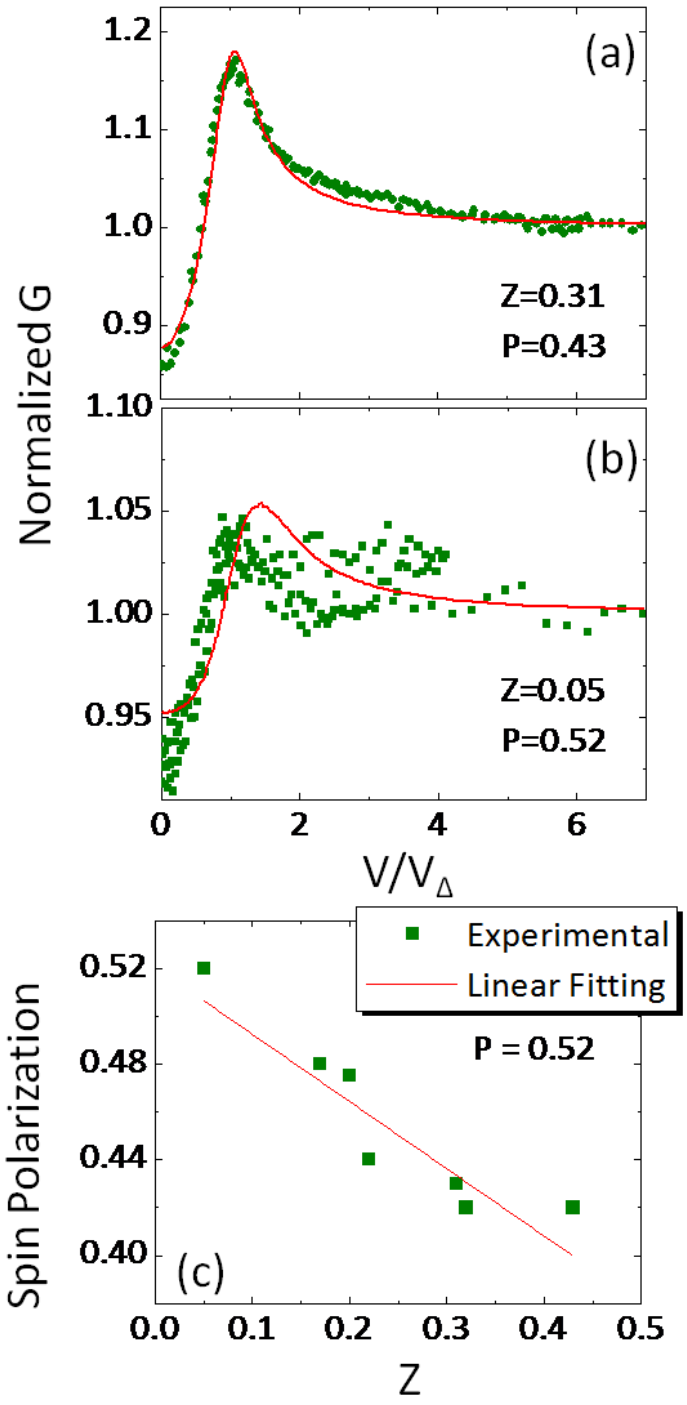

Figure 5.8 PCAR measurement on partially ordered $Fe_{16}N_2$ with structure Fe-N(48nm)/Fe(22nm)/GaAs. (a) and (b) Normalized conductance as a function of applied voltage (V) divided by superconducting gap (V_Δ). Experimental data is shown in dots (green) and fitting is shown in continues curve (red), (c) Spin Polarization as a function of Z (described in text), the experiment data (green dots) is fitted linearly (straight line).

Reference

[81] H. Meng and J.-P. Wang, Appl. Phys. Lett. 88, 172506 (2006)

[82] S. Mangin, D. Ravelosona1, J. A. Katine, M. J. Carey, B. D. Terris and Eric E. Fullerton, Nat. Mater. 5, 210 (2006).

[83] T. Seki, S. Mitani, K. Yakushiji, and K. Takanashi, Appl. Phys. Lett. 88, 172504 (2006).

[84] S. Ikeda,K. Miura, H. Yamamoto, K. Mizunuma, H. D. Gan, M. Endo, S. Kanai, J. Hayakawa, F. Matsukura and H. Ohno, Nat. Mater. 9, 721 (2010)

[85]P. Bruno, Phys. Rev. B 39, 865 (1989).

[86] R. J. Soulen, Jr., J. M. Byers, M. S. Osofsky, B. Nadgorny, T. Ambrose, S. F. Cheng, P. R. Broussard, C. T. Tanaka, J. Nowak, J. S. Moodera, A. Barry and J. M. D. Coey, Science 282 85 (1998)

[87] K. H. Jack, Proc. R. Soc. London. Ser. A 208 200 (1951)

[88] To calculate the K_u, we used the equation: $K_u=H_k*M_s/2$, where M_s is the saturation magnetization of the Fe-N layer and H_k is H_s as defined in text.

[89] H. Takahashi, M. Igarashi, A. Kaneko, H. Miyajima, Y. Sugita,, IEEE Trans. Magn.. 35 (5), 2982 (1999)

[90] I. I. Mazin, A. A. Golubov, and B. Nadgorny, J. Appl. Phys. 89, 7576 (2001).

[91] G. T. Woods, R. J. Soulen, Jr., I. Mazin, B. Nadgorny, M. S. Osofsky, J. Sanders, H. Srikanth, W. F. Egelhoff, and R. Datla, Phys. Rev. B 70, 054416 (2004)

[92] G. E. Blonder, M. Tinkham, and T. M. Klapwijk, Phys. Rev. B 25, 4515 (1982).

[93] Y. Ji, C. L. Chien, Y. Tomioka, and Y. Tokura, Phys. Rev. B 66, 012410 (2002);

[94] Y. Ji, G. J. Strijkers, F. Y. Yang, C. L. Chien, J. M. Byers, A. Anguelouch, G. Xiao, and A. Gupta, Phys. Rev. Lett. 86, 5585 (2001);

[95] P. Raychaudhuri, A. P. Mackenzie, J. W. Reiner, and M. R. Beasley, Phys. Rev. B 67, 020411 (2003);

[96] C. H. Kant, O. Kurnosikov, A. T. Filip, P. LeClair, H. J. M. Swagten, and W. J. M. de Jonge, Phys. Rev. B 66, 212403 (2002).

[97] B. Nadgorny, R. J. Soulen, Jr., M. S. Osofsky, I. I. Mazin, G. Laprade, R. J. M. van de Veerdonk, A. A. Smits, S. F. Cheng, E. F. Skelton, and S. B. Qadri , Phys. Rev. B 61, R3788 (2000).

Chapter VI Conclusion and Outlook

6.1 Conclusion

In this work, we developed a process to synthesize metastable $Fe_{16}N_2$ thin films using a unique facing target sputtering technique. This approach opens up the opportunity to utilize this material for industrial applications. From the viewpoints of thin film material processing, magnetic characterization and fundamental magnetism, we have provided a systematic investigation in this material system, which may offer new insight on this topic after 40-years' debate since the first claim of its giant saturation magnetization.

We clearly identified the growth mechanism and controlled the key parameters to favor and stabilize this metastable phase. The use of GaAs (001) or MgO (001) substrate and the subsequent Fe (001) buffer layers, provides a template to realize the directional doping of N atoms and allow the growth (001) textured $Fe_{16}N_2$ epitaxial films.

We systematically investigated the crystal structure of the prepared films using a series of thin film characterization tools including multiple x-ray diffraction and transmission electron microscopy techniques. Experiments involving energy dispersion spectroscopy (EDS), Auger electron spectroscopy (AES) depth profiling, x-ray photoemission spectroscopy (XPS) were also carried out to study the chemical composition of this Fe-N material system.

We have measured the saturation magnetization of the Fe-N films by using vibrating sample magetometry, with a special emphasis on the error bar estimation, which proves the presence of giant saturation magnetization in $Fe_{16}N_2$. Further investigation using polarized neutron reflectometry (PNR) provided a direct measure of the saturation magnetization in our $Fe_{16}N_2$ films, which were significantly larger than the currently known limit ($Fe_{65}Co_{35}$). In addition to provide independent

evidence for the giant magnetization, we revealed the correlation between the giant M_s and epitaxial constrain.

We proposed a "Fe_6N cluster + Fe atom" model to rationalize the giant saturation magnetization. One of the features in this model, the partial localization of the 3d electrons was observed by carrying out x-ray magnetic circular dichroism (XMCD) experiments. Also based on this model, we predicted the directional charge transfer from Fe to N site within the Fe_6N cluster, which was successfully confirmed from the analysis of the x-ray absorption near edge spectroscopy (XANES) data. Further magnetic effects due to the N site ordering and epitaxial strain were both found to be supportive within the context of the discussion of the proposed model.

We also provided a discussion regarding the perpendicular magneto-crystalline anisotropy in Fe-N martensites and $Fe_{16}N_2$, which may be one of potential candidates for rare-earth free permanent magnets, due to their large anisotropy and large magnetization. The spin polarization ratio of $Fe_{16}N_2$ was directly measured by point contact Andreev reflection (PCAR), which shows a moderate enhancement comparing to metal Fe. This property allows the $Fe_{16}N_2$ to be a potential electrode for highly demanded MTJ or GMR spintronic devices with perpendicular anisotropy.

6.2 Outlook

There are still questions open in this field. For example, the famous Mössbauer experiments conducted by the Hitachi's group only show one type of hyperfine (HF) field in their $Fe_{16}N_2$ films, which presumably should have three. The value of their HF is similar to that of pure Fe, which makes this result even more mysterious. Others claimed the observation of three sets of HF in $Fe_{16}N_2$ and is consistent with the chemical and structural environment of this material. However，these samples do not show giant magnetization. It is suggested the electron localization plays a key role on understanding the Mössbauer results. However,

more systematic effort is demanded in the future investigation of the HF. Another example is the transport properties such as temperature dependent resistivity measurement. This has been studied in Hitachi group's earlier report. A large residual resistivity is seen at low temperature for $Fe_{16}N_2$ thin films comparing to Fe metal and other Fe-N nitrides compounds. The reason on why there is a robust increase of this residual resistivity is still not answered yet.

With these unclear points in mind, future investigations should be focused on a more consistent and systematic experiment to explore the hyperfine field and the transport properties of this material system.

Exploring the Giant Magnetism in Novel Magnetic Nanoparticles

Introduction

In bulk and thin film systems, for iron nitrides, it was demonstrated that to realize giant magnetization, it is essential to allow the electrons to possess localized features, in which case, the spatial chemical ordering (N ordering) is required. To obtain the electron localization in more general itinerant ferromagnetic systems, one promising approach is to build/engineer materials with lower dimensionality. In the extreme case, an isolated Fe atom (a zero dimension system) can provide giant magnetic moment as governed by Hund's first rule. In addition to the presence of spin magnetic moment, orbital moment can also produce significant magnetic contribution.

Following this discussion, we have picked up a typical high moment Fe-Co alloy system to study its magnetism in nano-particle scale, which is near zero-dimension. By using a unique deposition tool, we successfully fabricated FeCo nano-particles with core-shell configurations. To directly explore its magnetic behavior with element specificity, X-ray magnetic circular dichroism (XMCD) experiments are performed on FeCo-FeCoO and FeCo-Au core-shell type nanoparticles. The core-shell coupling magnetism as well as spin and orbital magnetic moments on each 3d magnetic element (Fe and Co) are determined. The main discoveries are the following.

(1) For FeCo-FeCoO nanoparticles, the spin canting coupling magnetism on the oxidized shell are observed and proposed to be induced by the magnetic metallic core material.

(2) For the FeCo-Au nanoparticles, strong spin-orbital coupling is found, which substantially modifies the spin configuration and occupation, providing

uncompensated orbital magnetic moments on both Fe and Co sites. Further experimental investigation is proposed to address the origin of the strong spin-orbital coupling. It is also tempted to reproduce the Slater-Pauling curve at nanoscale. Discrepancies are expected given the substantial change in the spin band structure in nanoscale.

Purpose of this study

Magnetic nanoparticles with biocompatible coating surface offer great opportunities in applications such as contrast agents in magnetic resonance imaging [98], magnetically controllable drug delivery [99] and bio sensor related devices[100], etc. All these applications require high magnetic moment in order to have better performance. Therefore, the understanding on the fundamental magnetism of such magnetic system are of particular importance.

Though Hund's rule predicts large spin and orbital moments for a ground state isolated atom, when they approach metal bulk states, both these magnetic moments are gradually quenched due to the hybridization and cubic crystal field. For Fe-Co 3d alloy system, the underlying physics for its bulk can be appreciated the famous Slater-Pauling curve. As for magnetic nanoparticles, they can be viewed as a bridge between atomic and bulk states. Their magnetic behaviors can neither be a simple reminiscent of Hund's rule nor be safely considered as a reproduction of Slater-Pauling curve. Roughly speaking, in magnetic nanoparticles, the interaction of the orbital and spin parts of the total magnetic moment becomes important due to the non-negligible orbital magnetic moment arising from the broken symmetry and non-cubic crystal structure near the interface and surface. These contributions become especially important in small size nanopaticles. For example, 50% of all the atoms in a 3 nm nanoparticles are surface atoms. Therefore, the investigation of the nanomagnetism of such FeCo alloy based nanoparticles system is of particular importance for not only technical application but also fundamental research purpose.

A direct and efficient approach to experimentally study the spin and orbital magnetic moment as well as the magnetic coupling nature with elemental specificity is X-ray magnetic circular dichroism (XMCD) technique. Here, we performed XMCD study on high quality FeCo alloy based core-shell type nanoparticles. This section is organized in the following manner.

Firstly, we present the fabrication and characterization results of the FeCo-FeCoO and FeCo-Au core-shell type nanoparticles, followed by a brief introduction on the X-ray absorption spectra and X-ray magnetic circular dichroism technique. Then, the spectra analysis on both types of samples are discussed separately. Special emphasis is made on the core-shell coupling mechanism in FeCo-FeCoO nanoparticle system and the orbital magnetism induced spin configuration change on the FeCo-Au nanoparticle system. Finally, a series of future experiments are proposed to systematically investigate the nanomagnetism of FeCo based metallic high-moment system.

Sample fabrication and characterization

Due to the rapid progress on the synthesis methods, many kinds of magnetic nanoparticles have been successfully fabricated. Some of them involve the synthesis by a seed-growth approach by wet methods[101] or followed by a chemical vapor deposition (CVD) process[102]. However, these solution-based methods make it difficult to obtain contamination-free interfaces and surfaces as well as to be integrated into many vacuum-based micro- and nano-electronics fabrication processes. On the other hand, the gas phase technique offers the intrinsic merit of producing core-shell nanoparticles with clean interface and surface.

In our work, we chose the gas phase synthesis method by using a gas condensation source equipped with sputtering guns. Sputtering alloy target with ferromagnetic elements (Fe and Co) and another target with a combination of elements (Fe,Co and Au) are used separately to fabricate FeCo-FeCoO and FeCo-Au

nanoparticles. Similar to sputtering methods used in fabricating thin film materials, high purity Argon is used as sputtering gas to vaporize the target atoms at plasma region. Figure A1 shows the schematic setup for our fabrication system. At deposition early stage, high energy "hot" target atoms are cooled down by colliding with inlet Ar gas, during which a super-saturation condition can be achieved. Thermodynamically, nucleation process occurs in order to lower the free energy and atom condensation is realized.

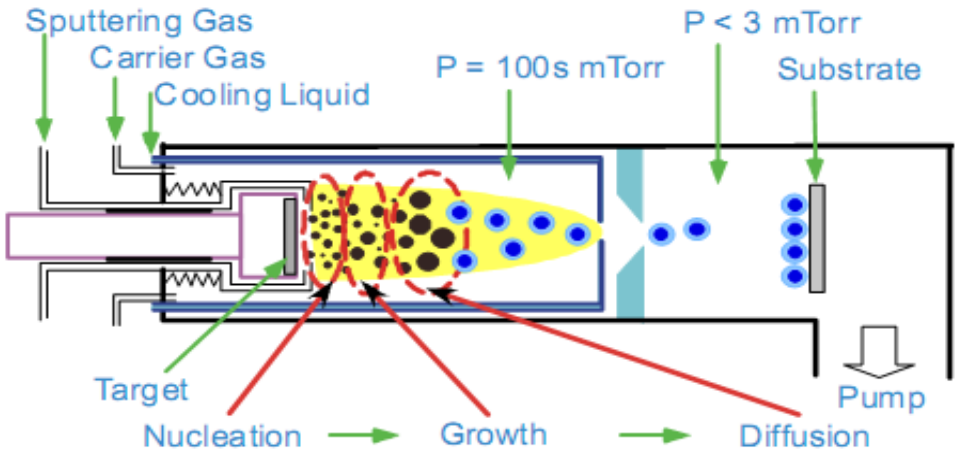

Figure A1 Physical vapor deposition system for the fabrication of the samples discussed in this paper. Picture source: Dr. Yunhao Xu's Ph.D thesis (http://gradworks.umi.com/32/92/3292994.html).

Followed by the growth and diffusion process, high quality core-shell type nanoparticles are obtained for FeCo-Au. The FeCo nanoparticles are directly fabricated and their oxidized shells are naturally formed after the exposure to the atmosphere. Figure A2 shows the TEM image of nanoparticles that discussed here. Both types of samples establish cubic shape. For the FeCo-FeCoO samples, the side length are ~20nm and 2.5nm for core and shell, respectively. For the FeCo-Au sample, ~4 nm shell Au is coated on the ~20nm core. As the diffraction pattern shows, FeCo core material is of body centered cubic in both samples. Figure A3a shows the energy dispersive spectra (EDS) analysis on a single FeCo-Au nanoparticle that shows the spatial distribution of Fe, Co and Au elements, providing

a direct evidence of the fact that these nanoparticles are consisted of FeCo core and Au shell. HR-TEM (figure A3b) shows the epitaxial relationship of FeCo core and Au shell, suggesting a high crystal quality and well defined interface.

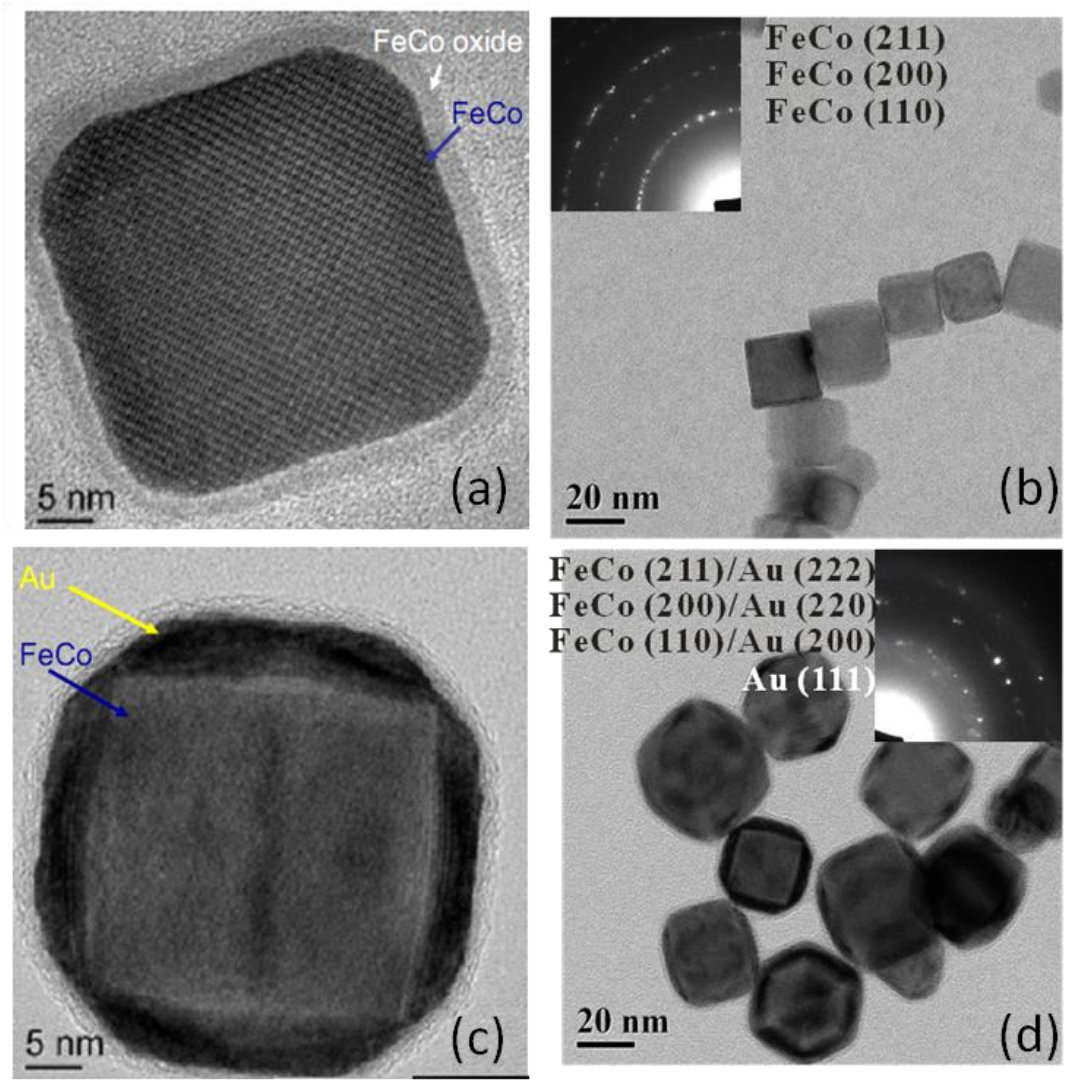

Figure A2 TEM image on two sets of FeCo based nanoparticle samples. (a) and (b) are the high resolution and large scale images of FeCo=FeCo-O core-shell NPs. (c) and (d) are high resolution and large scale images of FeCo-Au core-shell NPs. The inset in (d) are the diffractions patterns, the indices are outlined correspondingly. Picture source: Dr. Yunhao Xu's Ph.D thesis (http://gradworks.umi.com/32/92/3292994.html).

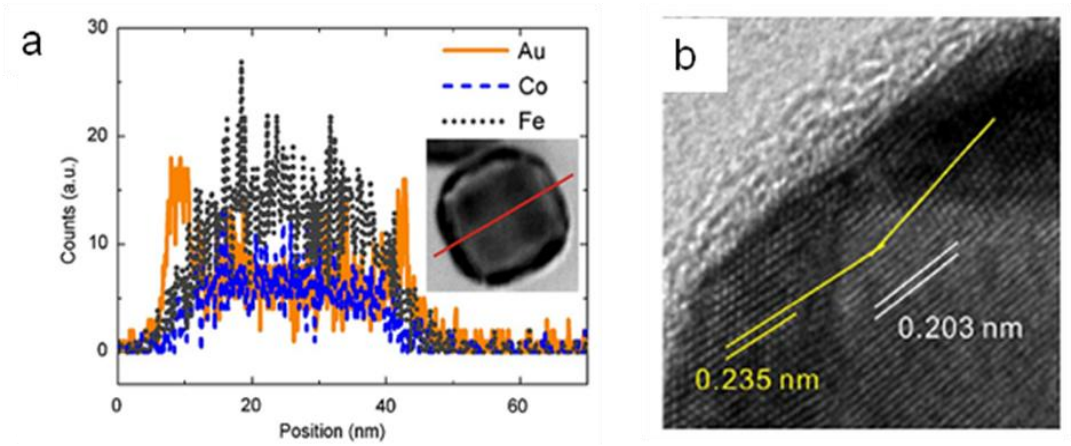

Figure A3 (a) EDS scan of Fe, Co and Au elements on single FeCo-Au core shell nanoparticles; b, HR-TEM image on FeCO/Au interface. Picture source: Dr. Yunhao Xu's Ph.D thesis (http://gradworks.umi.com/32/92/3292994.html).

X-ray absorption and X-ray magnetic circular dichroism

X-ray magnetic circular dichroism (XMCD) is a technique based on the X-ray absorption spectroscopy. Dichroism is the polarization dependence of the absorption. To understand the principle of XMCD, a two-step model is adapted[103]. In the first step, the photons in a circular polarized X-ray radiation transfer their angular momentum to the excited photoelectron. The electrons carry the momentum either by spin or orbital degree of freedom. At L_3 edge (p3/2), the orbital moment (m_l) and the spin moment (m_s) are parallel. The transfer of the angular momentum (+ħ) by right circularly polarized light excites more (62.5%) spin-up than (37.5%) spin-down electrons. The reverse holds for left circularly polarized light. At L_2 edge (p1/2), m_l and m_s are anti-parallel. The right circularly polarized light preferentially couples to the spin-down electrons (75% spin-down and 25% spin-up). In this step, the "spin-up" and "spin-down" are defined relative to the photon spin direction. In the second step, the valence shell acts like detector for the spin polarization of the photoelectrons. In experiments, switching the polarization of X-ray radiation or equivalently switching the magnetization direction of the sample will generate different absorption spectra (I+ and I-) for light with different helicities (+ħ and -ħ).

In general, $I_+ + I_-$ is referred as XAS and $I_+ - I_-$ is referred as XMCD.

Due to the different 2p→3d dipole transition energy required by different elements, XMCD is able to measure element specific signals in samples containing multiple elements. In metallic system, by applying sum rules[104], orbital moment and spin moment of each element can be calculated based on the measured data. Recent developments in the field also enable the detection in electron microscopy as well as the dynamic behavior of magnetic materials and structures[105].

Due to the weak signal of XMCD, strong intensity of radiation is required. Most measurements are carried out at synchrotron radiation source. The results reported in this study were obtained at the Beamline U4B at the National Synchrotron Light Source (NSLS), Brookhaven National Laboratory. Circular polarized light with 90% polarization is used at room temperature. A magnetic field of up to 1T was applied along θ=0 degree with respect to surface normal to magnetize the sample. MCD data were taken by alternating between two opposite directions of the field. The incident beam was chosen to be perpendicular to the sample surface. Each spectrum reported here was averaged over multiple measurements to reduce the noise level. Magnetization independent spectra of substrates were also measured in order to obtain relative absorption cross sections (μ) by using equation $\mu_{\pm}(\omega) \propto -\ln[I_{\pm}(\omega)/I_s(\omega)]$ [104]. Sample substrates subject to the measurement was carbon coated Cu grid used in TEM measurement.

Results and discussion of FeCo-FeCoO system

Figure A4a and b showed typical XAS and XMCD results on Fe $L_{2,3}$ edges. Besides the main signals of metallic Fe from the core material, satellites (marked by arrows) were observed in the XAS spectra, corresponding to the Fe states from oxidized shell. Metallic Fe bulk XMCD collected by C.T. Chen[104] was also shown and normalized to the main peak position at L_3 edge in Fig. A4b for comparison. In the spectra for our core shell NPs, there appears a satellite near the L_3 edge tail at

energy of 708eV, which implies the atomic like Fe^{3+} states with Oh symmetry crystal field[106] as shown in the inset. Standard sum rule was applied to determine the spin-to-orbital magnetic moment ratio for Fe element, which is ~0.01 with 2% error bar. This value is significantly reduced compare to iron bulk (0.043)[104]. Plotted in Fig. 4c and d are XAS and XMCD results on Co $L_{2,3}$ edges. Oxidized Co features (marked by arrows on XAS) were also observable given the shell material. The spin-to-orbital moment ratio is determined to be ~0.134 according to the Co XMCD spectra, which is much larger than its metallic bulk value (0.099 for hcp Co and 0.078 for fcc Co).

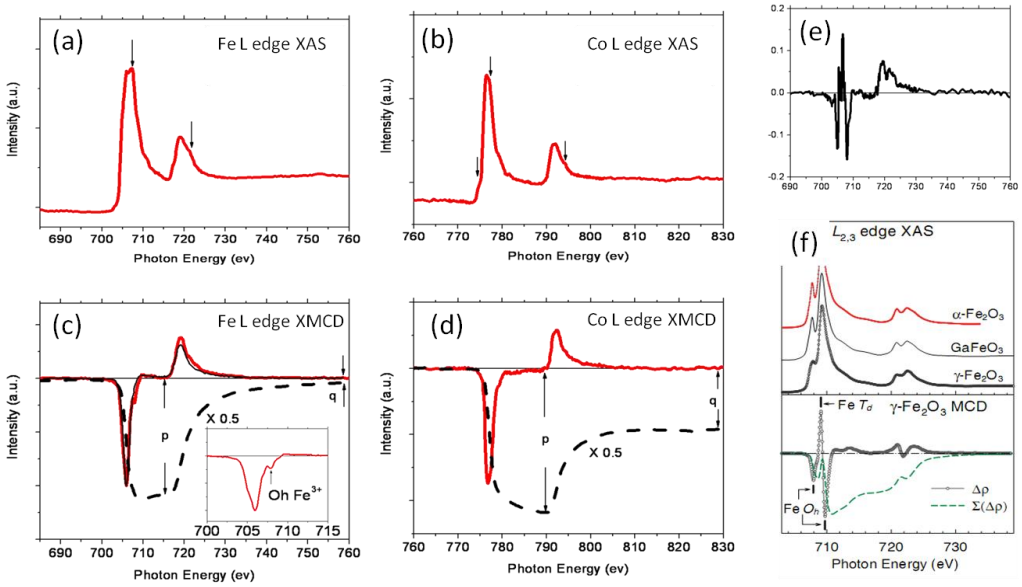

Figure A4 XAS and XMCD on Fe and Co L edge for FeCo/FeCo-O core shell nanoparticles. (a) and (b) are Fe and Co L edge XAS. (c) and (d) are the corresponding XMCD of FeCo-FeCO-O NPs. the dashed lines are integrated lines to calculate the spin and orbital moment contribution according to sum rule. (e) shows the metallic background subtracted XMCD spectra as discussed in the text, which resembles that of typical Fe oxides as shown in the reference data (f). Data source of (f) is from reference 107.

It is known that corundum structured α-Fe_2O_3, rocksalt structured FeO and CoO are all anti ferromagnetic ordered materials with the anti-coupled magnetic

sites possess equivalent chemical environment. In principle, such system will not give rise to XMCD signals even with the appearance of the absorption signals given simply by the fact that the left and right polarized X-ray absorption cross sections will have no difference under such circumstances. Ferrimagnetic phases such as γ-Fe_2O_3 and Fe_3O_4, which contain magnetic sites with different crystal fields may generate MCD signals due to the non cancellation of the spectra from these sites. The appearance of the MCD signals coming from oxidized Fe states indicates the existence of these oxidized iron phases. By assuming the itinerant electrons signals coming from the FeCo core is roughly the same as that in pure Fe metal, we obtained the spectra of oxidized Fe states in these NPs after subtracting the black curve from the red one as shown in figure.4e. It shows a spectra configuration similar to that reported on γ-Fe_2O_3 (Ref. 107) but sizable discrepancies are found on the relative intensities for different peaks. This indicates the existence of Fe^{3+} states with Oh symmetry ferromagnetically coupled with the core magnetization, while Td symmetry Fe^{3+} antiferromagnetically coupled with both of them, which is in analogy to the magnetic configuration in γ-Fe_2O_3.

The intensity difference could be due to the poor assumption on the itinerant electron signals. More importantly, it also opens up the possibility that these oxidized magnetic sites are not completely antiferromagnetically (AFM) ordered or more precisely form spin canted states, which is more likely to happen in such native oxidized states given its poor crystallized nature. The increase on the spin-to-orbital moment ratio for Co can be attributed to the presence of the uncompensated or spin canting Co states near the core shell interface as pointed out by U. Wiedward *et. al*[108] on their Co/CoO core shell nanoparticles system, which provides a clear indication on the spin configuration of the samples discussed here. In order to justify the formation of such canting couple mechanism, which is coming from the competing AFM and FM coupling between neighboring magnetic sites, a model is proposed as shown on Fig. A5 to illustrate our basic concept. The AFM can be easily realized due to the super-exchange mechanism. However, the possible

mechanism to realize a FM in such system is through the s-d exchange which requires the existence of a spin polarized conduction band. In our core shell nanoparticle system, during the oxidization, large amount of defects are created which form an impurity band near the Fermi level. Since the core materials are conducting, the electrons can be easily filled into that impurity band and Stoner criteria can be reached to favor polarized configuration. The static electrical potential energy created for transferring δe (0.1) per atom to this band is $\frac{(\delta e)^2}{4\pi\epsilon a^2}$, where *a* is the radius of the nanoparticle. This is on the order of 10~100mev. The s-d coupling strength J_{sd}, on the other hand, is on the order of 1~10ev. Therefore, it is energetically favorable for the charge transfer from the core to the shell to lower the total energy. Considering the AFM super-exchange mechanism which is in the order of several ev, ultimately the spin configuration in the shell part will become spin canted, which explains the observation on the XMCD spectra of both Fe and Co L edges. The SQUID hysteresis loop measured at room temperature shows ferromagnetic order (Hc and reminisce) which is unexpected for nanoparticles at such diameter range. Loop of similar size FeCo nanoparticle with Au coating gives superparamagnetic behavior which confirms this ferromagnetism is coming from the presence of the oxidized FeCo-O shell while the core may still remain superparamagnetic.

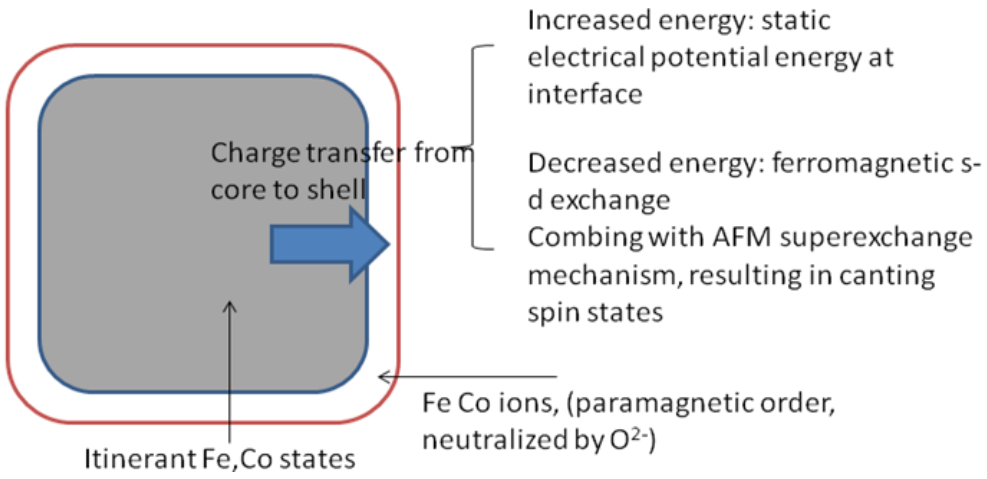

Figure A5 Proposed coupling mechanism in FeCo-FeCoO nanoparticles

Results and discussion of FeCo-Au system

Fe and Co L edges XAS and XMCD are shown in Figure A6. The concentration of Fe and Co is determined to be 76.3% and 24.7% respectively, obtained from comparing total integrated intensity between Fe and Co L edges, which is in excellent agreement with previous EDS scan results. XAS and XMCD reveals single peak at each edge for both Fe and Co, which corresponds to typical metallic configurations and excludes the existence of any sizable signals coming from oxidized 3d states. A more quantitative analysis of the data is achieved by means of sum rule. A voigt function with known linewidth and experimental resolution is applied to remove edge jumps. For unoccupied 3d electron states ($10-n_{3d}$), we assumed 3.34 and 2.55 for Fe and Co respectively[109] Values of effective spin moment m_s^{eff} including also the dipole term are calculated to be $2.52\,\mu_B$ per Fe atom and $1.47\,\mu_B$ per Co atom, respectively. The orbital magnetic moments are also determined to be $0.13\ \mu_B$ per Fe atom and $0.29\,\mu_B$ per Co atom. The experimental errors bars of the MCD results are estimated to be 8% for m_s and m_l and 4% for m_s/m_l.

Comparing with the neutron experiment[110] results on bulk FeCo alloy with similar element composition, the spin magnetic moments (~$2.8\,\mu_B$/atom and $1.6\,\mu_B$/atom for Fe and Co respectively) show relatively larger disagreement among the individual elements which are substantially reduced in our NPs system. Despite the fact that these experiments are carried out at room temperature, it can be attributed to the discrepancies in the n_{3d} obtained from the reports on thin film FeCo when we performed the sum rule calculation in our NPs system. Notably, closer spin magnetic moments (~$2.1\,\mu_B$ for Fe and $1.5\ \mu_B$ for Co) are obtained from XMCD sum rule for lattice distorted ultrathin FeCo films. The other feature observed in the XMCD spectra Fe L edge XMCD at photon energy range between 710 to 715 ev, where a near zero flat signal is uniquely presented though most of Fe metallic configuration exhibit a positive shoulder at that range. Such spectra difference is

associated with structural modification of 3d empty bands. Similar feature is also found in L_2 and L_3 transition region of Co edge spectra in comparison with other metallic Co signals. More importantly, such feature contributes significantly on the enhancement of orbital to spin magnetic moment ratio calculated by sum rule.

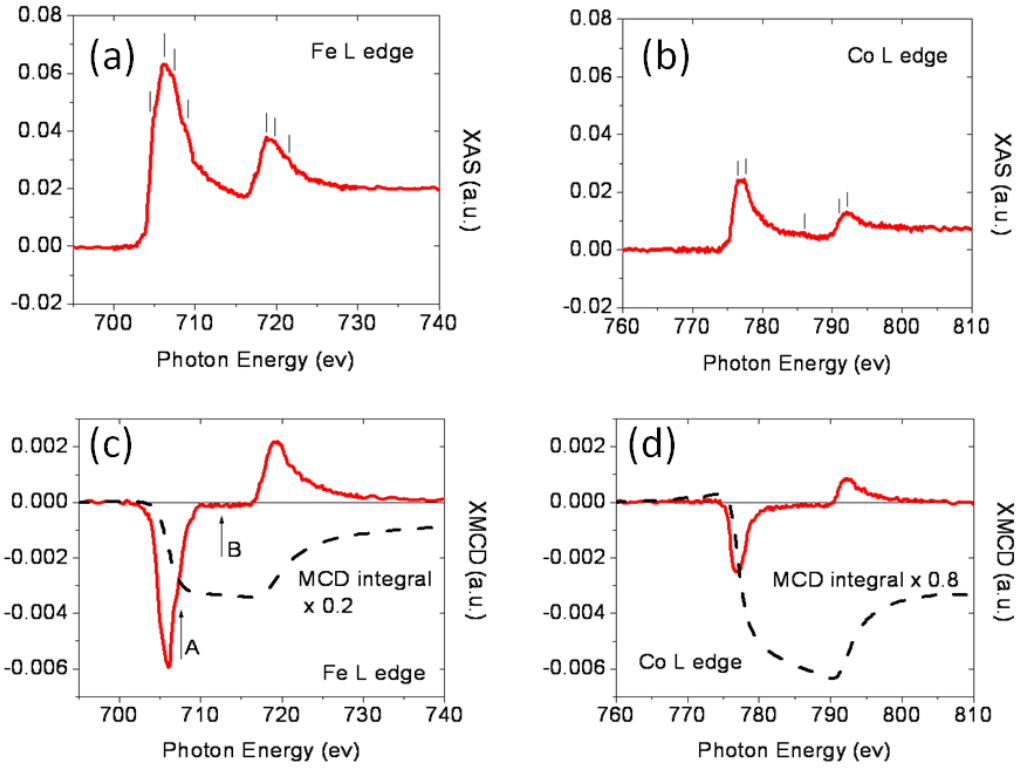

Figure A6 XAS and XMCD on Fe and Co L edge for FeCo-Au core shell nanoparticles. (a) and (b) are Fe and Co L edge XAS. (c) and (d) are the corresponding XMCD of FeCo-Au NPs. the dashed lines are integrated lines to calculate the spin and orbital moment contribution according to sum rule.

The discrepancy of the orbital and spin moment and spectra configuration between bulk and our nanoparticle system are explained as the following. Traditionally, orbital magnetism can be safely neglected when investigating 3d metals. Though Hund's rule predicts large orbital magnetic moment when elements in questions approach atomic limit, it is drastically quenched in the presence of cubic crystal field. Exceptional cases can be found in systems such as 3d impurities

embedded in noble metal matrix[111], where hybridization at site is extremely small. Little has been discussed on orbital magnetism in heterostructured nanoparticle system when the dominant effects can be a combination of finite size, broken symmetry and small interface hybridization. The observation of giant orbital magnetic moment, reduced spin magnetic moment, the notable modification 3d empty bands suggests the necessary correction of band structure and spin configuration due to sizable spin orbital coupling in our NPs system. A toy model is proposed to illustrate the spin orbital coupling effect. In a cubic system with negligible orbital magnetic moment, 3d states characterized by the same modulus of ml should be degenerate. However, this degeneracy is broken in the presence of term $-\alpha\, L{\cdot}s$. As figure A7a shows, initially degenerated bands will be shifted in different energy directions depending on the signs of both spin and orbital states. Specifically, for spin up band, positive m_l states are dropped down and negative m_l states are lifted up. Conversely, for spin down band, positive m_l states possess lower energy and negative m_l states possess higher energy. The combing effect would results in a reduced exchange splitting between spin up and spin down bands but uncompensated orbital moment states on them. In our FeCo nanoparticle system, based on the spin and orbital magnetic moment measured on Fe and Co and assuming the 3d total electrons merely changes from bulk to nanoparticle. We schematically draw the spin occupation of Fe and Co 3d electrons in figure A7b, which explains the difference on the orbital magnetic moments observed on Fe and Co though a similar band structure is presumed for both elements.

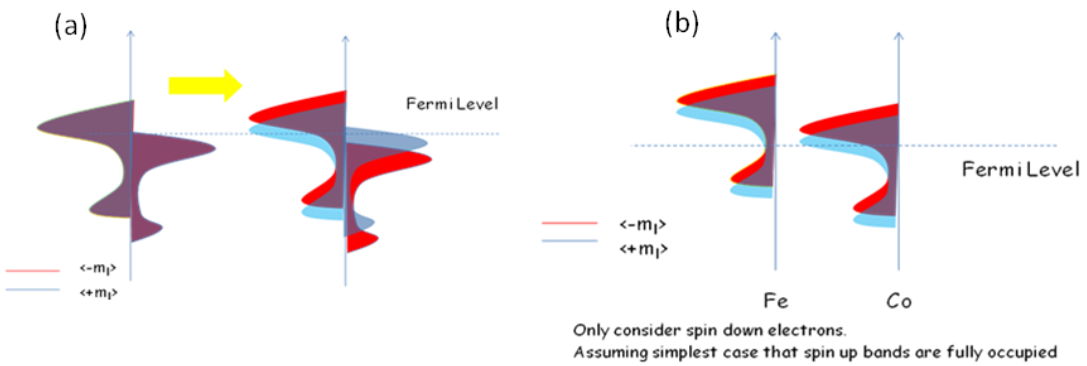

Figure A7 (a) The schematic drawing of the density of states of 3d electrons showing degeneracy. (b) A sketch showing the orbital contribution due to the symmetry breaking.

Future plan

The direct consequence for such modified band structure is that the Slater Pauling curve obtained from bulk FeCo may or may not applicable in nanoparticle system. Therefore, it is necessary and interesting to experimentally explore the spin and orbital magnetic moments on Fe and Co with varying composition, separately and elemental specifically. Therefore, at first, targets with varying Fe and Co concentration will be used on synthesis FeCo-Au core shell nanoparticles with different alloy atomic composition. In the mean time, to understand the hybridization nature between the FeCo core and Au shell. Particles with different sizes will be fabricated to vary the relative portion of surface atoms. A systematic XMCD and XAS study are required for further research from the experiment aspect.

Summary

High quality FeCo-FeCoO and FeCo-Au core-shell type cubic shape high-magnetic-moment nanoparticles are fabricated directly through a physical vapor deposition method. X-ray magnetic circular dichroism technique with elemental specificity is used to explore nanomagnetism of 3d electron states of Fe and Co in these nanoparticle systems. In FeCo-FeCoO nanoparticle, spectroscopic evidence shows localized Fe states, corresponding to signals from its oxidized shell. Fe L edge XMCD spectra show a configuration similar to that reported on γ-Fe_2O_3. The sizable enhancement obtained on the orbital to spin magnetic moment ratio on Co L edge as well as the discrepancy observed on the relative intensity of the oxidized Fe XMCD signals provide the direct evidence on the spin canting configuration of the oxidized shell material, which could be due to the competing mechanism between ferromagnetic s-d exchange and anti-ferromagnetic super-exchange. In FeCo-Au nanoparticles, spin and orbital magnetic moments are determined respectively on both

Fe and Co atoms. Comparing to the bulk, unusually large orbital moment is observed on Co atoms. The spin magnetic moments on both Fe and Co atoms are somewhat reduced, which implicates the necessary correction on the 3d electron band structure due to the strong spin orbital coupling effect in this nanoparticle system. A series of further experiments are designed to address the questions regarding the origin of the strong spin orbital coupling. By purposely modifying the composition of Fe and Co in our FeCo-Au nanoparticle system, it is tempted to reproduce Slater-Pauling curve in such nanoscale, which is expected to be different from that observed in bulk metal given the modified 3d electron band.

Reference

[98] Suh, WH; Suh, YH, Stucky, GD, Nano today 4, 27 (2009) ; Gao, JH, Xu, B, Nano Today 4, 37 (2009); Kim, J; Piao, Y, Hyeon, T, Chem. Soc. Rev. 38, 372 (2009); De, M; Ghosh, PS, Rotello, VM, Adv. Mater. 22, 4225 (2008)

[99] Namdeo, M; Saxena, S; Tankhiwale, R, et al., J. Nanosci. Nanotech. 8, 3247 (2008)

[100] Wang, SX, Li, G, IEEE Trans. Magn. 44, 1687 (2008) ; Berven, CA, Dobrokhotov, VV, Int. J. Nanotech. 5, 402 (2008)

[101] H. Yu, M. Chen, P. M. Rice, S. X. Wang, R. L. White and S. H. Sun, Nano Lett. 5, 379 (2005); J. Lin, W. L. Zhou, A. Kumbhar, J. Wiemann, J. Y. Fang, E. E. Carpenter and C. J. O'Connor, J. Solid State Chem. 159, 26 (2001); M. Chen, S. Yamamuro, D. Farrell and S. A. Majetich, J. Appl. Phys. 93, 7551 (2003); Y. P. Bao and K. M. Krishnan, J. Magn. Magn. Mater. 293, 15 (2005); M. A. Willard, L. K. Kurihara, E. E. Carpenter, S. Calvin and V. G. Harris, Int. Mater. Rev. 49, 125 (2004)

[102] L. J. Lauhon, M. S. Gudiksen, C. L. Wang and C. M. Lieber, Nature 420, 57 (2002); W. S. Seo, J. H. Lee, X. M. Sun, Y. Suzuki, D. Mann, Z. Liu, M. Terashima, P. C. Yang, M. V. McConnell, D. G. Nishimura and H. J. Dai, Nature Mater. 5, 971 (2006)

[103] S. W. Lovesey and S. P. Collins, X-ray scattering and absorption by magnetic

materials (Clarendon Press; Oxford University Press, Oxford, New York, 1996); J. Stohr, J. Magn. Magn. Mater. 200, 470 (1999)

[104] C. T. Chen, Y. U. Idzerda, H. J. Lin, N. V. Smith, G. Meigs, E. Chaban, G. H. Ho, E. Pellegrin and F. Sette, Phys. Rev. Lett. 75, 152 (1995)

[105] P. Schattschneider, S. Rubino, C. Hebert, J. Rusz, J. Kunes, P. Novak, E. Carlino, M. Fabrizioli, G. Panaccione and G. Rossi, Nature 441, 486 (2006); B. Van Waeyenberge, A. Puzic, H. Stoll, K. W. Chou, T. Tyliszczak, R. Hertel, M. Fahnle, H. Bruckl, K. Rott, G. Reiss, I. Neudecker, D. Weiss, C. H. Back and G. Schutz, Nature 444, 461 (2006)

[106] J.-Y.Kim, T. Y.Koo, and J.-H. Park, Phys. Rev. Lett. 96, 047205 (2006)

[107] J.-Y. Kim, T. Y. Koo, and J.-H. Park, Phys. Rev. Lett. 96, 047205 (2006)

[108] U. Wieldwald et al., Phys. Rev. B 68, 064424 (2003)

[109] R. Wu and A. J. Freeman, Phys. Rev. Lett. 73, (1994)

[110] Collins. M. F., Forsyth J. B., Philos. Magn. 8 (1963) 401

[111] B. Nonas et al., Phys. Rev. Lett. 86, 2146 (2001); I. Cabria et al., Phys. Rev. B 65, 054414 (2002)

Comprehensive bibliography

[1]H. Beckmann and G. Bergmann, Phys. Rev. Lett. 83, 2417 (1999)

[2] http://en.wikipedia.org/wiki/Hund%27s_rules

[3] http://dpwww.epfl.ch/cours/ansermet/magweb/crystal_field.pdf

[4] J. C. Slater, J. Appl. Phys. 8, 385 (1937).

[5] L. Pauling, Phys. Rev. 54, 899 (1938)

[6] R. M. Bozorth, Phys. Rev. 79, 887 (1950)

[7] T. K. Kim, and M. Takahashi, Appl. Phys. Lett., 20 492 (1972)

[8] In CGS unit, the magnetization is expressed in emu/cm^3. For ferromagnetic material, this is equivalent to the value of magnetization inductance ($4\pi M_s$) in Tesla (T). In this thesis, we have used both magnetic units but they represent the equivalent measure of the same physical parameter

[9] Y. Sugita, et al., *J. Appl. Phys.* 70 (10), 5977 (1991)

[10] The papers were published in J. Appl. Phys. 79 5564-5581 (1996)

[11]K. H. Jack, Proc. R. Sot. London, Ser. A 208,200 (1951)

[12] J. M. D. Coey, Phys. World 6 (August) 25

[13] R. M. Metzger, X. H. Bao and M. Carbucicchio, J. Appl. Phys. 76 (10), 6626 (1994) and references therein

[14]S. Okamoto, O. Kitakami and Y. Shimada, Journal of Applied Physics 79 (3), 1678-1683 (1996).

[15]D. C. Sun and et al., Journal of Physics: Condensed Matter 7 (18), 3667 (1995)

[16] M. A. Russak, C. V. Jahnes, E. Kiohkolm, J.-W. Lee, M. E. Re, and B. C. Webb, J. Appl. Phys. 70, 6427 (1991).

[17]C. Gao, W. D. Doyle, and M. Shamsuzzoha, J. Appl. Phys. 73, 6579 (1993).

[18] X. Bao, R. M. Metzger, and W. D. Doyle, J. Appl. Phys. 73,6734 (1993)

[19] Huang, M. Q., Wallace, W. E., Simizu, S., Pedziwiatr, A. T., Obermyer, R. T., and Sankar, S. G. (1994a). J. Appl. Phys. 75, 6574.

[20] Coey, J. M. D. (1994). *J. Appl. Phys.* 76, 6632.

[21] M. Takahashi, H. Shoji, H. Takahashi, H. Nashi, T. Wakiyama, M. Doi and M. Matsui, Journal of Applied Physics 76 (10), 6642-6647 (1994).

[22] C. Ortiz, G. Dumpich and A. H. Morrish, Applied Physics Letters 65 (21), 2737-2739 (1994).

[23] Lai, W. Y., Zheng, Q. Q., and Hu, W. Y. (1994). *J. Phys.* C 6, L259

[24]Sakuma, A. (1996). J. Appl. Phys. 79, 5570

[25]Ishida, S., Kitawatase, K., Fujii, S., and Asano, S. (1992). *J. Phys.* C 4, 765.

[26]Min, B. I. (1992). *Phys. Rev.* B 46, 8232.

[27] Matar, S. (1992). *Z. Phys.* B 87, 91.

[28] Coehoorn, R., Daalderop, G. H. O., and Jansen, H. J. F. (1993). *Phys. Rev.* B 48, 3830.

[29] Miura, K., Imanaga, S., and Hayafuji, Y. (1993). *J. Phys.* C 5, 9393.

[30] Sawada, H., Nogami, A., Matsumiya, T., and Oguchi, T. (1994). *Phys. Rev.* B 50, 10004

[31] Huang, M. Z., and Ching, W. Y. (1995). *Phys. Rev.* B 51, 3222.

[32] Umino, K., Nakajima, H., and Shiiki, K. (1996). *J. Mag. Magnet. Mater.* 153, 323.

[33]J. P Wang, INSIC Meeting 2010; APS Meeting 2010; ScienceNOW March 19th 2010; PMRC 2010

[34]Y. Nimura and M. Naoe. J. Vac. Sci. Technol. A **5** 109 (1987)

[35] Z. H. Qian, Geng Wang, J. M. Sivertsen, J. H. Judy; *IEEE Trans. Magn.*, 33, 3748 (1997)

[36]In-plane lattice constant of $Fe_{16}N_2$ a= 5.72Å, the lattice constant of GaAs is a=5.65Å.

[37] N. Ji, Y. Wu, and J.-P. Wang, *J. Appl. Phys.* **109**, 07B767 (2011)

[38]S. Okamoto, et. al., J. Magn. Magn. Mater., 208 102 (2000)

[39] M. Takahashi, et. al., J. Appl. Phys. 79 (8), 5576 (1996).

[40] C. Ortiz, G. Dumpich, and A. H. Morrish., Appl. Phys. Lett., **65,** 2737 (1994)

[41] M. A. Brewer, K. M. Krishnan and C. Ortiz, J. Appl. Phys. **79,** 5321 (1996)

[42]N. Ji, et. al, Appl. Phys. Lett. 98, 092506 (2011)

[43] http://www1.chm.colostate.edu/Files/XRR.pdf

[44] Shau-Wei Hsu, Conference on Precision Electromagnetic Measurements Digest (1996)

[45] V. Lauter, et. al., Physica B 404, 2543 (2009)

[46] R+ and R- are spontaneously recorded. We only show R+ curve in the image

[47] http://www-llb.cea.fr/prism/programs/simulreflec/simulreflec.html

[48] N. Ji, Y. M. Wu and J. –P. Wang, J. Appl. Phys. 109, 07B767 (2011)

[49] N. Ji, et. al, *Appl. Phys. Lett.* 98, 092506 (2011)

[50] Comparing to previous experiments (N. Ji et al., J. Appl. Phys. 109, 07B767 (2011)), the optimized N_2 partial pressure to achieve high quality Fe_8N is at 0.12 mTorr, the Fe-N layers prepared here were grown at N_2 partial pressure of 0.18 mTorr with otherwise identical deposition conditions as the previous report.

[51] Ranu Dubey, Ajay Gupta, and J. C. Pivin, Phys. Rev. B 74, 214110 (2006)

[52] The x-ray scattering cross section of N is much smaller than that of Fe. Therefore, the SLD of the N doped Fe is similar to SLD of pure Fe for x-ray probe.

[53] G. P. Felcher, Phys. Rev. B 24 1595 (1981)

[54] C. F. Majkrzak, Physica B 173, 75 (1991)

[55]The MSLD (ρb_m) is the same physical parameter as the saturation magnetization (M_s), both of which are a measure of the magnetic density. In cgs unit, the conversion formulism is $3.5x10^8 \times \rho b_m$ ($Å^{-2}$) = M_s (emu/cm^3)

[56] W Y Lai, Q Q Zheng and W Y Hu, *J. Condens. Matter* 6 L259 (1994)

[57]A. Sakuma, *J. Appl. Phys.* 79 5570 (1996)

[58] F. Janak, Phys. Rev. B 16, 255 (1977)

[59] Jingsong He, Yumei Zhou, Wuyan Lai and C. Y. Pan, *Phys. Rev.* B 52 6193 (1995)

[60] V. I. Anisimov, J. Zaanen and O. K. Anderson, *Phys. Rev.* B 44 943 (1991)

[61] P.E. Blöchl, *Phys. Rev.* B 50, 17953 (1994)

[62] V. Anisimov, F. Aryasetiawan, and A. Lichtenstein, *J. Phys.: Condens. Matter* 9, 767 (1997)

[63] J. Sánchez-Barriga et al., *Phys. Rev. Lett.* 103 267203 (2009)

[64] V. I. Anisimov, J. Zaanen and O. K. Anderson, *Phys. Rev.* B 44 943 (1991)

[65] R. S. Han, Z. Z. Gan, D. L. Yin and Q. Liao, Phys. Rev. B 41 6683 (1990)

[66] G. W. Fernando, R. E. Watson, M. Weinert, A. N. Kocharian, A. Ratnaweera and K. Tennakone, *Phys. Rev*. B 61 375 (2000)

[67] H. Takahashi, M. Komuro, M. Hiratani, M. Igarashi and Y. Sugita, *J. Appl. Phys.* 84 1493 (1998)

[68] Jian-Ping Wang, et. al., IEEE Trans Magn (In press)

[69] The XMCD principle is shown in detail in appendix

[70] A Ligand field theory based multiplet calculation using Cowan software[1] has been performed to simulate these satellites as shown in fig.2c and d. For a reasonable estimation, we used the spectrum of pure iron thin film sample collected by C. T. Chen et al[1] as the band like part signals. For the additional parts, our simulation takes into account the atomic Fe $3d^6$ to $2p^53d^7$ multiplet transition with D4h crystal symmetry. The 3 parameters X_{400}, X_{420} and $X_{220}{}^1$ which are used to manipulate D4h crystal field are set to be 3.286, 0, 2 respectively. This corresponds to a 1ev crystal field with explicit inclusion of lattice distortion along c-axis. With and without considering the spin-orbital coupling in the final states does not show significant change through the calculation. A reducing factor on the Slater integral is applied to take care of the absorbing ions and ligands. It also considers the experimental broadening due to the core-hole life time (Lorentzian broadening) and instrumental resolution (Gaussian broadening).

[71] D. E. Sayers et al., Phys. Rev. Lett. 27, 1204 (1971)

[72] J.J. Rehr et al., Rev. Mod. Phys 72, 621 (2000)

[73] J. Stöhr, NEXAFS Spectroscopy, Springer (1992)

[74] A. Bianconi et al., Phys. Rev. B 26, 6502 (1982)

[75] A. L. Ankudinov, et al., Phys. Rev. B 67, 115120 (2003).

[76] To construct the $Fe_{16}N_2$ crystal, a space group of I4/mmm and experimental lattice constants were used. a cluster of atoms with a size of 5.47 Å is applied for the calculation of full-multiple scattering (FMS), a cluster of atoms with a size of 4.0 Å is used for the calculation of the self-consistent-field (SCF) muffin-tin atomic

potential, the Hedin–Lundqvist self-energy is used by default. To calculate the XANES of $Fe_{16}N_0$, the crystal structure and lattice constant were chosen to be identical to single crystal $Fe_{16}N_2$. The sites that originally occupied by N in $Fe_{16}N_2$ were left empty on purpose when constructing the dummy structure $Fe_{16}N_0$.

[77] C. D. Lorenz and R. M. Ziff`, Phys. Rev. E 57`, 230–236 (1998)`, for a bct structured Fe-N`, the crystal structure viewed along 110 direction closely resembles the fcc lattce matrix.

[78] J. M. D. Coey, et. al., J. Phys. Con. Mater. 6, L23 (1994)

[79] H. Tanaka, et. al., Phys. Rev. B 62, 15042 (2000)

[80] K. H. Jack, Proc. R. Soc. 208 (1093), 200 (1951)

[81]H. Meng and J.-P. Wang, Appl. Phys. Lett. 88, 172506 (2006)

[82] S. Mangin, D. Ravelosona1, J. A. Katine, M. J. Carey, B. D. Terris and Eric E. Fullerton, Nat. Mater. 5, 210 (2006).

[83] T. Seki, S. Mitani, K. Yakushiji, and K. Takanashi, Appl. Phys. Lett. 88, 172504 (2006).

[84] S. Ikeda,K. Miura, H. Yamamoto, K. Mizunuma, H. D. Gan, M. Endo, S. Kanai, J. Hayakawa, F. Matsukura and H. Ohno, Nat. Mater. 9, 721 (2010)

[85] P. Bruno, Phys. Rev. B 39, 865 (1989).

[86] R. J. Soulen, Jr., J. M. Byers, M. S. Osofsky, B. Nadgorny, T. Ambrose, S. F. Cheng, P. R. Broussard, C. T. Tanaka, J. Nowak, J. S. Moodera, A. Barry and J. M. D. Coey, Science 282 85 (1998)

[87] K. H. Jack, Proc. R. Soc. London. Ser. A 208 200 (1951)

[88] To calculate the K_u, we used the equation: $K_u=H_k*M_s/2$, where M_s is the saturation magnetization of the Fe-N layer and H_k is H_s as defined in text.

[89] H. Takahashi, M. Igarashi, A. Kaneko, H. Miyajima, Y. Sugita,, IEEE Trans. Magn.. 35 (5), 2982 (1999)

[90] I. I. Mazin, A. A. Golubov, and B. Nadgorny, J. Appl. Phys. 89, 7576 (2001).

[91] G. T. Woods, R. J. Soulen, Jr., I. Mazin, B. Nadgorny, M. S. Osofsky, J. Sanders, H. Srikanth, W. F. Egelhoff, and R. Datla, Phys. Rev. B 70, 054416 (2004)

[92] G. E. Blonder, M. Tinkham, and T. M. Klapwijk, Phys. Rev. B 25, 4515 (1982).

[93] Y. Ji, C. L. Chien, Y. Tomioka, and Y. Tokura, Phys. Rev. B 66, 012410 (2002);

[94] Y. Ji, G. J. Strijkers, F. Y. Yang, C. L. Chien, J. M. Byers, A. Anguelouch, G. Xiao, and A. Gupta, Phys. Rev. Lett. 86, 5585 (2001);

[95] P. Raychaudhuri, A. P. Mackenzie, J. W. Reiner, and M. R. Beasley, Phys. Rev. B 67, 020411 (2003);

[96] C. H. Kant, O. Kurnosikov, A. T. Filip, P. LeClair, H. J. M. Swagten, and W. J. M. de Jonge, Phys. Rev. B 66, 212403 (2002).

[97] B. Nadgorny, R. J. Soulen, Jr., M. S. Osofsky, I. I. Mazin, G. Laprade, R. J. M. van de Veerdonk, A. A. Smits, S. F. Cheng, E. F. Skelton, and S. B. Qadri , Phys. Rev. B 61, R3788 (2000).

[98] Suh, WH; Suh, YH, Stucky, GD, Nano today 4, 27 (2009) ; Gao, JH, Xu, B, Nano Today 4, 37 (2009); Kim, J; Piao, Y, Hyeon, T, Chem. Soc. Rev. 38, 372 (2009); De, M; Ghosh, PS, Rotello, VM, Adv. Mater. 22, 4225 (2008)

[99] Namdeo, M; Saxena, S; Tankhiwale, R, et al., J. Nanosci. Nanotech. 8, 3247 (2008)

[100]Wang, SX, Li, G, IEEE Trans. Magn. 44, 1687 (2008) ; Berven, CA, Dobrokhotov, VV, Int. J. Nanotech. 5, 402 (2008)

[101] H. Yu, M. Chen, P. M. Rice, S. X. Wang, R. L. White and S. H. Sun, Nano Lett. 5, 379 (2005); J. Lin, W. L. Zhou, A. Kumbhar, J. Wiemann, J. Y. Fang, E. E. Carpenter and C. J. O'Connor, J. Solid State Chem. 159, 26 (2001); M. Chen, S. Yamamuro, D. Farrell and S. A. Majetich, J. Appl. Phys. 93, 7551 (2003); Y. P. Bao and K. M. Krishnan, J. Magn. Magn. Mater. 293, 15 (2005); M. A. Willard, L. K. Kurihara, E. E. Carpenter, S. Calvin and V. G. Harris, Int. Mater. Rev. 49, 125 (2004)

[102] L. J. Lauhon, M. S. Gudiksen, C. L. Wang and C. M. Lieber, Nature 420, 57 (2002); W. S. Seo, J. H. Lee, X. M. Sun, Y. Suzuki, D. Mann, Z. Liu, M. Terashima, P. C. Yang, M. V. McConnell, D. G. Nishimura and H. J. Dai, Nature Mater. 5, 971 (2006)

[103] S. W. Lovesey and S. P. Collins, X-ray scattering and absorption by magnetic

materials (Clarendon Press; Oxford University Press, Oxford, New York, 1996); J. Stohr, J. Magn. Magn. Mater. 200, 470 (1999)

[104] C. T. Chen, Y. U. Idzerda, H. J. Lin, N. V. Smith, G. Meigs, E. Chaban, G. H. Ho, E. Pellegrin and F. Sette, Phys. Rev. Lett. 75, 152 (1995)

[105] P. Schattschneider, S. Rubino, C. Hebert, J. Rusz, J. Kunes, P. Novak, E. Carlino, M. Fabrizioli, G. Panaccione and G. Rossi, Nature 441, 486 (2006); B. Van Waeyenberge, A. Puzic, H. Stoll, K. W. Chou, T. Tyliszczak, R. Hertel, M. Fahnle, H. Bruckl, K. Rott, G. Reiss, I. Neudecker, D. Weiss, C. H. Back and G. Schutz, Nature 444, 461 (2006)

[106] J.-Y.Kim, T. Y.Koo, and J.-H. Park, Phys. Rev. Lett. 96, 047205 (2006)

[107] J.-Y. Kim, T. Y. Koo, and J.-H. Park, Phys. Rev. Lett. 96, 047205 (2006)

[108] U. Wieldwald et al., Phys. Rev. B 68, 064424 (2003)

[109] R. Wu and A. J. Freeman, Phys. Rev. Lett. 73, (1994)

[110] Collins. M. F., Forsyth J. B., Philos. Magn. 8 (1963) 401

[111] B. Nonas et al., Phys. Rev. Lett. 86, 2146 (2001); I. Cabria et al., Phys. Rev. B 65, 054414 (2002)